8 Diffusional Phase Transformations in the Solid State

W.A. Soffa, Department of Materials Science and Engineering, University of Virginia, USA
David E. Laughlin, Department of Materials Science and Engineering, Carnegie Mellon University, Pittsburgh, PA, USA

8.1 Introduction

8.1.1 General Concepts: Classification of Phase Transformations

This chapter is about diffusional phase transformations. It is appropriate to first define the terms **phase** and **phase transformation**. A phase is a physically distinct homogeneous portion of a thermodynamic system delineated in space by a bounding surface, called an interphase interface, and distinguished by its state of aggregation (solid, liquid or gas), crystal structure, composition and/or degree of order. Each phase in a material system generally exhibits a characteristic set of physical, mechanical and chemical properties and is, in principle, mechanically separable from the whole.

A phase transformation in a material system occurs when one or more of the phases in a system changes their state of aggregation, crystal structure, degree of order or composition resulting from a reconfiguration of the constituent particles (atoms, molecules, ions, electrons, etc.) comprising the phase. This reconfiguration is a change in the thermodynamic state leading to a more stable condition described by appropriate thermodynamic potentials such as a decrease in the Gibbs free energy (G) at constant temperature (T) and pressure (P). Whether describing the freezing of a metal or the onset of ferromagnetism in iron (Fe), a change in phase is indicated when small changes in relevant thermodynamic variables produce marked changes and sometimes dramatic qualitative changes in the nature of the system. These changes can occur abruptly (discontinuously) or gradually (continuously) at critical values of certain thermodynamic variables. The decrease in free energy accompanying the reconfiguration is often referred to as the thermodynamic "driving force" for the phase change.

In his well-known collected works Gibbs formulated the fundamental conditions for equilibrium of phases in a thermodynamic system based on a simple principle of mathematics. If a system has a total of x variables which are related by r equations, the number of independent variables which can be altered without changing the state of equilibrium is $x - r$. We call the parameter $F = x - r$ the *variance* or *degrees of freedom of the system*. If the state of an individual phase is completely determined by its temperature, pressure and composition then the total number of variables associated with a system

composed of P phases is $P(C+1)$ wherein $(C-1)$ composition variables must be specified to describe the composition of a phase. If the temperature and pressure are uniform throughout the system and the chemical potentials of the individual chemical species are equal within the coexisting phases, the number of equations relating the variables is $(P-1)(C+2)$; thus, the variance of the system is $F = P(C+1) - (P-1)(C+2) = C+2-P$. This is the famous *Gibbs phase rule* which is usually written as $P+F=C+2$. Care must be exercised in properly specifying the number of components C; it is not always simply the number of elements present in the system. The variance or degrees of freedom can be understood as the number of thermodynamic variables that can be changed arbitrarily (within limits) by an experimenter without causing the disappearance of phases or the appearance of new phases while probing the system. It should be mentioned that if the chemical species are reactive and there are R independent reaction equilibria among the N species, the variance is then given by $F = C-R+2-P$. Finally, it should be clear that the phase rule $P+F=C+2$ will be altered if other thermodynamic variables are essential in the description of a phase such as electric and magnetic fields as well as stress.

8.1.2 Diffusional and Nondiffusional Transformations

Phase transformations in the solid state may be divided into two broad categories: (1) those requiring the movement of atoms over distances of the order of atomic spacings or greater effected by essentially stochastic thermally activated jumps down a chemical potential gradient often accompanied by significant redistribution of solute and composition changes and (2) those whose atoms at the boundary of the new growing phase are displaced in a synchronous and coordinated fashion, over fractions of atomic spacings. The former are called diffusional transformations and are the subject of this chapter. The latter are often called displacive transformations (or sometimes martensitic). Following Frank, Professor Christian has referred to the former type of transformations as civilian (they occur with little or no atomic coordination) and the latter as military transformation, since the atomic motions occur cooperatively and in step with each other.

8.1.3 Replacive and Reconstructive Transformations

Diffusional transformations can be classified as either replacive or reconstructive (Buerger, 1948, 1951). In the former, the atomic jumps merely rearrange the positions of the species on the underlying lattice whereas in the latter the new phase that arises generally has a very different crystal structure. Replacive diffusional transformations are of two types: those in which the solute atoms cluster together to form a solute-enriched phase and those in which the solute and solvent atoms form an atomically ordered arrangement which is crystallographically related to the parent phase. (Of course, ordering of the phase could occur after the clustering step or vice versa. See Section 8.6.3 subsequently.) Replacive transformations may occur with complete coherency between the new phase and its matrix phase. On the other hand, reconstructive diffusional transformations involve an atom by atom disassembling of the parent phase and an atom by atom assembling of a new phase. The new phase generally forms with an interface that is incoherent with that of the matrix. An incoherent interface is one in which there is no systematic matching of atomic planes at the interface boundary.

Diffusional transformations can differ from each other with respect to their thermodynamic character, resultant microstructures and kinetics. In the following section we give an overview of such classifications.

8.1.4 Discontinuous and Continuous Transformations: Gibbs (1875, 1876, 1877, 1878)

In well-known (but seldom read) papers Gibbs (1875, ff) distinguished between two fundamentally distinct types of phase transformations, namely those that are initiated by fluctuations that are large in degree but small in spatial extent and those that are initiated by fluctuations that are small in degree and relatively large in spatial extent.

(A phase) "…may be capable of continued existence in virtue of properties which prevent the commencement of *discontinuous* changes. But a phase which is unstable in regard to *continuous* changes is evidently incapable of permanent existence on a large scale except in consequence of passive resistances to change…" (Gibbs, 1875, ff, our emphasis).

Here, Gibbs contrasts changes in what we call today an order parameter, such as the difference in composition, atomic order or magnetization within a phase, with changes that result in the formation of an *entirely* new phase. A single phase may not be able to continuously change via infinitesimal fluctuations of order parameter, but could change if a large enough fluctuation in the order parameter were to appear. This kind of transformation is called by Gibbs a *discontinuous change* (transformation). This kind of transformation contrasts with *continuous* changes or *transformations*. Continuous transformations require only infinitesimal changes in order parameter to proceed and initially occur within the existing phase. *Discontinuous transformations* are those which require large fluctuations in order parameter and hence they form a new phase clearly distinguishable from the initially existing one.

Thus, Gibbs introduces two types of phase transformations: those which are initiated by fluctuations that are small in spatial extent but large in degree (*discontinuous*) and those which are initiated by fluctuations that are small in degree but large in spatial extent (*continuous*).

From the time of this article by Gibbs, until 1956, nearly all research on the initiation of phase transformations was done in terms of *discontinuous transformations*, the so-called nucleation and growth transformations. In 1956, Mats Hillert, working on his graduate degree at MIT, ushered in the spinodal era by discussing decomposition by a *continuous transformation* which was later termed by Cahn as "spinodal decomposition" (Cahn, 1961).

The distinction between continuous and discontinuous transformations includes aspects of thermodynamics, kinetics and microstructure. **Thermodynamics** is included in the use of such terms as stable and unstable for the phases under consideration. Also, the changes in the thermodynamic functions may be continuous or discontinuous with the advancement of the transformation. The **kinetics** of the two types of transformation are different in the sense that in a continuous transformation there is no sharp change in the kinetics as a function of time, whereas for discontinuous transformations (those that are diffusional) the reaction often starts off slowly and speeds up with time. See Section 8.3 subsequently. The **microstructural differences** are included in the idea of the extent of the spatial range of the fluctuations. For continuous changes the initiation of the change occurs within a single phase, that is, there is no sharp interface between two incipient phases. Also it occurs in all regions of the sample, not just localized regions as in nucleation events.

8.1.5 Homogeneous and Heterogeneous Transformations: Christian (2002)

Another classification of phase transformations has been given by Professor J. W. Christian in his classic treatise (Christian, 2002). *Heterogeneous* transformations involve the spatial partitioning of the system into regions that *have transformed* and regions which *have not transformed*. Such regions are separated by an interphase interface. *Homogeneous* transformations occur uniformly throughout the entire system

and the changes occur continuously in time as well as uniformly in space. Therefore, all *homogeneous* transformations are *continuous according to this viewpoint*.

This classification is similar to that of Gibbs discussed earlier. All nucleation and growth processes are heterogeneous transformations, just as they are discontinuous transformations. It should be noted that homogeneous nucleation is a heterogeneous transformation. Homogeneous transformations are continuous.

8.1.6 First- and Higher Order Phase Transitions: Ehrenfest (1933)

In the early 1930s, Ehrenfest (1933) suggested a very useful scheme for distinguishing different types of phase transformations/transitions based on the behavior of certain thermodynamic variables in the vicinity of the phase change. The ORDER of a phase transition in this thermodynamic classification is defined according to the lowest differential/derivative of the relevant thermodynamic potential such as the Gibbs free energy which is discontinuous. The discontinuous first derivatives of the Gibbs free energy which define a FIRST-ORDER transition are as follows:

$$\left(\frac{\partial G}{\partial T}\right)_P = -S \quad \left(\frac{\partial G}{\partial P}\right)_T = V \quad \left(\frac{\partial\left(\frac{G}{T}\right)}{\partial\left(\frac{1}{T}\right)}\right)_P = H$$

for which it emerges that the entropy S is discontinuous at the transition temperature T_t and the phase change occurs isothermally with a discontinuity in H and a so-called latent heat of transformation ΔH_t. It follows from the basic definition of a heat capacity that the heat capacity or specific heat C_P will exhibit an infinite discontinuity at the transition temperature. The following second derivatives of the free energy are discontinuous at the onset of a SECOND-ORDER transition:

$$\left(\frac{\partial^2 G}{\partial T^2}\right)_P = -\frac{C_P}{T} \quad \left(\frac{\partial^2 G}{\partial P^2}\right)_T = -\beta V \quad \left(\frac{\partial H}{\partial T}\right)_P = C_P$$

where $-\frac{1}{V}\left(\frac{\partial^2 G}{\partial P^2}\right)_T = \beta$ is the compressibility. Such transitions have no latent heat nor coexistence of phases at the transition temperature. The specific heat/heat capacity at the transition temperature shows a finite discontinuity according to the Ehrenfest thermodynamic classification. SECOND-ORDER transitions are rare in nature: however, the transition from the normal state to the superconducting state in zero magnetic field is the textbook example of such a transition. The majority of phase changes in materials are FIRST ORDER but there is a plethora of transitions which are clearly *not* FIRST ORDER or SECOND ORDER; that is, they are third order or higher. However, in practice, it is extremely difficult to analyze behavior explicitly associated with these higher order derivatives; thus, we find it useful to talk about FIRST-ORDER, SECOND-ORDER and HIGHER ORDER transitions (sometimes called λ transitions). All higher order transitions occur without a latent heat similar to second-order behavior but display markedly different behaviors with respect to their signature discontinuities in C_P. The nature of these singularities is yet to be fully resolved theoretically.

8.1.7 Landau Classification

In Section 2.5 a detailed discussion of the Landau approach and classification of phase transitions will be presented. In the Landau method the free energy is written as a Taylor series expansion with respect

to one or more order parameters which characterize the system and from this analysis two distinct types of transformation behavior become evident: those in which the curvature of the free energy of the high-temperature phase becomes zero at the transition temperature T_C and negative immediately below and those for which the curvature is positive at the transition temperature but may become negative at temperatures well below the equilibrium transition temperature. The former are identical to the second-order (continuous) transitions of Ehrenfest whereas the latter are the same as first-order (discontinuous) transitions discussed earlier. Far below the equilibrium transition T_C the first-order transition may exhibit thermodynamic (and kinetic) behavior associated with a continuous transformation under these nonequilibrium conditions since at a temperature $T_i^- < T_C$ the curvature of the free energy functional of the disordered phase becomes negative rendering the disordered state unstable. The temperature T_i^- is an instability temperature and it should be noted that for second-order transitions $T_C = T_i^-$.

8.1.8 Summary

This chapter deals with solid-state transformations in which atomic diffusion plays a major role. In this brief introductory summary we have distinguished between transformations that are continuous and homogeneous and those which are discontinuous and heterogeneous in nature. More details of these transformation modes will be discussed in the following sections. All second/higher order transitions are expected to proceed continuously and homogeneously. All first-order transitions might be expected to occur discontinuously and heterogeneously at and in the vicinity of the equilibrium transition temperature. However, well below the equilibrium transition temperature the intrinsically first-order transition can occur continuously and homogeneously under these nonequilibrium conditions.

8.2 Energetics

In the thermodynamics of phase stability the Gibbs free energy is of major importance and utility. This thermodynamic state function generally defined by

$$G = E + \mathrm{PV} - \mathrm{TS} = H - \mathrm{TS} \tag{1}$$

provides a tool for evaluating the relative stability of competing phases and quantitatively evaluating the thermodynamic "driving forces" for phase transformations as a function of relevant thermodynamic parameters such as temperature (T), pressure (P), composition (X) and, in some instances, can be generalized to include applied electric and/or magnetic fields. The internal energy (E) and entropy (S) of a phase can often provide a direct connection with factors relating to atomic structure and interatomic interactions. Initially, we will restrict ourselves to $G = G(T,P,X)$. If $G(T,P,X)$ is known then virtually all the thermodynamic properties of a material system can be deduced, in principle, from familiar derivatives of the Gibbs free energy and related quantities. For this reason the free energy is often called the characteristic function of the system. (The Helmholtz free energy $F = E - \mathrm{TS}$ differs from the Gibbs free energy by the familiar PV term which is only significant at relatively high pressures in the case of condensed phases). At constant T and P systems tend to evolve toward a state of lower free energy and stable equilibrium is characterized by a minimum in the free energy functional. Of course, local minima in the free energy of the system can occur, producing metastable states.

8.2.1 Allotropic/Polymorphic Transformations

One can write the Gibbs free energy of a solid crystalline phase α as

$$G^{\alpha}(T,P) = G^{\alpha}(T_0,P_0) + \int_{P_0}^{P} V^{\alpha}\mathrm{d}P + \int_{T_0}^{T} S^{\alpha}\mathrm{d}T \tag{2}$$

using the thermodynamic identities, $\left(\frac{\partial G^{\alpha}}{\partial P}\right)_T = V^{\alpha}$ and $\left(\frac{\partial G^{\alpha}}{\partial T}\right)_P = -S^{\alpha}$ where V^{α} and S^{α} are the molar volume and entropy of the α phase, respectively; both molar quantities generally are a function of T and P. G^{α} (T_0, P_0) is the free energy of the α phase in some arbitrary reference state defined by T_0 and P_0. This free energy functional can be used to calculate a free energy surface in the thermodynamic space $G(T.P)$ for the α phase and similarly for the vapor and liquid phases as well as an alternative solid phase β. These free energy surfaces intersect and that portion of each surface which represents the lowest free energy corresponds to the stable phase in a particular P–T range. The intersection of these surfaces produces two or more phases in equilibrium shown in the familiar P–T diagram such as the coexistence of a liquid and solid phase over a range of temperature and pressure along the melting curve. See Figure 1.

Along this curve/line in the P–T the free energy of the solid phase $G^S = G^L$, that is, the molar free energies of the solid and liquid phases are equal. Thus, $\mathrm{d}G^S = \mathrm{d}G^L$ for any movement along the melting curve giving $\mathrm{d}G^S = V^S\mathrm{d}P - S^S\mathrm{d}T = V^L\mathrm{d}P - S^L\mathrm{d}T = \mathrm{d}G^L$ resulting in the well-known Clapeyron equation

$$\frac{\mathrm{d}P}{\mathrm{d}T} = \frac{S^{\mathrm{L}} - S^{\mathrm{S}}}{V^{\mathrm{L}} - V^{\mathrm{S}}} \tag{3}$$

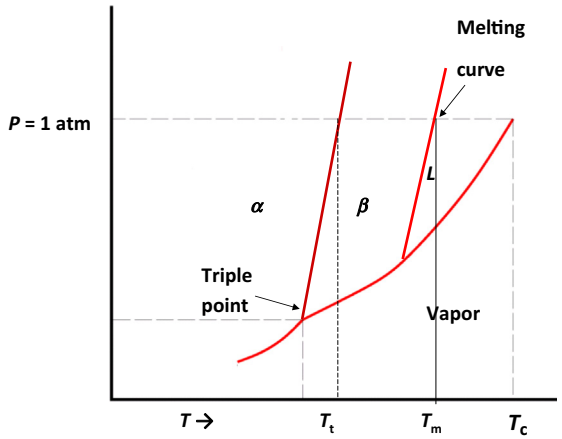

Figure 1 Schematic Pressure–Temperature phase diagram of a material displaying two allotropic solid phases. T_t is the transition temperature from the low-temperature α phase to the higher temperature β phase and T_m is the melting point of β at $P = 1$ atm.

where $(S^L - S^S)$ is the entropy of melting (fusion) and for any point on the curve can be written as

$$\Delta S^{S\to L} = \frac{\Delta H^{S\to L}}{T_m} \tag{4}$$

where $\Delta H^{S\to L}$ is the latent heat of melting (fusion) at the melting point T_m; The quantity $(V^L - V^S)$ is the volume change $\Delta V^{S\to L}$ accompanying the phase change. Clearly, the slope of the melting curve is determined by the relative molar volumes or densities of the liquid and solid phases along the coexistence curve. A similar analysis can be applied to the line representing two-phase equilibrium between allotropic or polymorphic modifications in the $P-T$ diagram as discussed subsequently as well to the sublimation and vaporization curves giving rise to the Clausius–Clapeyron equation.

If we restrict our discussion to isobaric conditions, say $P = 1$ atm, we can write the Gibbs free energy of a phase as a function of temperature as follows:

$$G(T) = H(T) - TS(T) = H_0 + \int_0^T C_P dT - T\int_0^T \frac{C_P}{T} dT \tag{5}$$

or

$$G(T) = H_0 - \int_0^T \left[\int_0^T \frac{C_P}{T} dT\right] dT$$

using the thermodynamic relationship $(\partial G/\partial T) = -S$ with H_0 essentially an integration constant. Of course, H_0 is the enthalpy of the phase at $T = 0$ K which for a solid phase is related to the cohesive energy recalling that $H \approx E$ for condensed phases. It is evident that various contributions to the heat capacity or specific heat play a central role in determining the variation of the free energy of a phase with temperature and thus the relative stability of the phases of the system.

Many materials including a number of important pure metals can exist in different stable crystalline forms at different temperatures and pressures. This phenomenon is called *polymorphism* or *allotropy* and the various crystalline forms are called *polymorphs* or *allotropes*. When the substances are pure elements (Ti, Zr, Sn, Fe, C) the terms allotropy and allotropes are preferred whereas when referring to compounds (SiO_2, ZrO_2, TiO_2, BN) the terms polymorphism and polymorphs are more appropriate. *Allotropic* and *polymorphic transformations* are important in a wide variety of engineering materials but, of course, from a technological point of view the occurrence of allotropy in iron (Fe) is most prominent giving rise to the eutectoid reaction in Fe–C–X alloys which is the basis for the heat treatment of engineering steels. Our discussion of allotropy/polymorphism will deal primarily with pure metals but we shall arrive at a number of important general conclusions.

Let us start our thermodynamic analysis of allotropy with a metal like zirconium (Zr) which is rather straightforward compared with iron (Fe) which will be addressed subsequently because magnetic effects are essentially absent in Zr. At one atmosphere pressure ($P = 1$ atm), pure Zr exhibits a stable hcp (α) structure from 0–1143 K and transforms to a bcc structure (β) which is stable from 1143 K to its melting point at 2125 K. The heat of transformation $\Delta H_t^{\alpha\to\beta}$ is 1040 cal mol^{-1} and the heat of fusion ΔH_f is approximately 4900 cal mol^{-1}. These latent heats are characteristic of the first-order nature of the $\alpha \to \beta$ and $\beta \to L$ transformations. In this one-component system the α, β and L phases are essentially

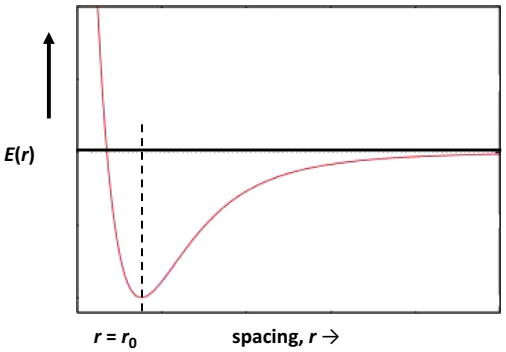

Figure 2 Schematic of the energy vs. atomic separation for an assembly of atoms showing a minimum in the energy at r_0, the equilibrium spacing. This curve is the result of long-range attractive interactions and short-range repulsive interactions.

the thermodynamically "competing" phases; we shall focus our attention on the relative stability of the solid α (hcp) and β (bcc) phases. Using the foregoing results for the free energies of the solid phases we write

$$G^{\alpha}(T) = H_0^{\alpha} + \int_0^T C_P^{\alpha}\,\mathrm{d}T - T\int_0^T \frac{C_P^{\alpha}}{T}\,\mathrm{d}T \tag{6}$$

and

$$G^{\beta}(T) = H_0^{\beta} + \int_0^T C_P^{\beta}\,\mathrm{d}T - T\int_0^T \frac{C_P^{\beta}}{T}\,\mathrm{d}T \tag{7}$$

for the α and β allotropes, respectively. The lead terms are the enthalpies $H_0^{\alpha} \approx E_0^{\alpha}$ and $H_0^{\beta} \approx E_0^{\beta}$ at 0 K of these phases and are related to the cohesive energy of the solids. Imagine that the atoms of the metal are placed on the lattice sites of a bcc lattice with a lattice spacing that is so large that the atoms do not interact. If the lattice spacing is then progressively reduced to the order of the size of the atoms themselves, the energy of the assembly will vary essentially like that shown in Figure 2 and a minimum will appear in the energy versus interatomic spacing which will determine the equilibrium spacing of the crystal in the bcc arrangement; similarly, for the hcp structure. In general, the nature of the energy versus spacing curve is determined by long-range attractive and short-range repulsive interactions and can often be described by an expression of the form

$$E(r) = -\frac{A}{r^n} + \frac{B}{r^m} \tag{8}$$

where r is a interatomic spacing and A, B, m and n $(m > n)$ are constants; $E(r)$ is the change in energy relative to the noninteracting assembly. The minimum in the curve $E(r = r_0) = E_C$ is approximately the

cohesive energy of the solid related to the energy required to vaporize the solid into its constituent atoms. The energy of the solid at $T = 0$ K given earlier also includes a zero point vibrational energy, thus

$$E_0 = E_C + E_0^{VIB}$$

where E_0 is a composite term of the cohesive energy term (negative) and the zero point vibrational energy (positive). The cohesive energy of zirconium is approximately 125–150 kcal mol^{-1} and the zero point vibrational energy is estimated to be less than one percent the cohesive or binding energy.

When considering the thermodynamics of allotropy in a metal like Zr, it is clear from the foregoing formulation of the free energies of the α and β phases that the heat capacity of a particular phase is critical in determining the variation of its free energy with temperature. The heat capacity of a solid phase, in general, can be considered to be composed of three parts: C_P^L the so-called lattice heat capacity associated with the thermal vibrations of the constituent atoms or ions about their equilibrium positions, C_P^e the electronic heat capacity arising from thermal excitation of free or conduction electrons in the vicinity of the Fermi level of a metallic solid and C_P^m the magnetic contribution associated with disordering or decoupling of electron spins in ferromagnetic or antiferromagnetic solids. Thus, the total heat capacity of the α and β phases can be written as

$$C_P = C_P^L + C_P^e + C_P^m$$

with the different components varying in a manner specific to the phase in question (α or β). In a paramagnetic metal such as zirconium (Zr), the magnetic contribution to the heat capacity or free energy is considered to be negligible ($C_P^m = 0$).

For our purposes, the lattice or vibrational component of the heat capacity is adequately described by the Debye theory of the specific heat or heat capacity. Theoretical approaches to the vibrational heat capacity generally calculate C_V rather than C_P but they are readily related through the thermodynamic relationship

$$C_P - C_V = \frac{\alpha^2 VT}{\beta}$$

where α is the coefficient of thermal expansion, β the compressibility and V the molar volume, and to a good approximation can be written as

$$C_P = C_V\left(1 + 10^{-4}\ \mathrm{T}\right)\mathrm{cal\ deg^{-1}\ mol^{-1}}.$$

According to the Debye theory the expression for the lattice heat capacity C_V^L as a function of temperature is given as follows

$$C_V^L = 9R\left(\frac{T}{\theta_D}\right)^3 \int_0^{x_m} \frac{x^4 e^x}{(e^x - 1)^2}\,dx \tag{9}$$

where $x = \dfrac{h\nu}{k_B T}$ and $x_m = \dfrac{h\nu_{max}}{k_B T}$ where ν is a vibrational frequency and ν_{max} is the "cut-off" frequency or maximum vibrational frequency in the vibrational or phonon spectrum of the normal modes characterizing the solid; the parameter $\theta_D = \dfrac{h\nu_{max}}{k_B}$ is called the Debye characteristic temperature and h, k_B

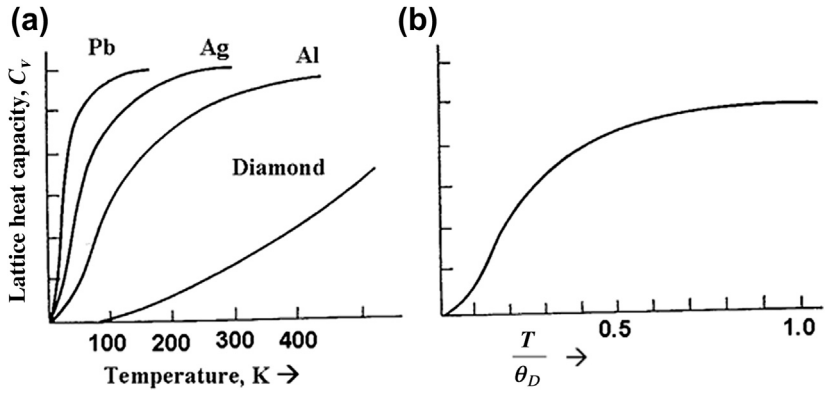

Figure 3 (a) Lattice heat capacity, C_V as a function of the temperature for different materials with different Debye temperatures. For Pb, $\theta_D = 88$ K; Ag, $\theta_D = 215$ K, Al, $\theta_D = 385$ K and Diamond, $\theta_D = \sim 2000$ K. (b). Master lattice heat capacity curve. After Smallman (1963).

and R have their usual meanings. This integral cannot be evaluated analytically; however, extensive tables have been computed numerically for C_V^L as a function of $\frac{T}{\theta_D}$. Also, values of the Debye energy, entropy and free energy have been compiled as a function of $\frac{T}{\theta_D}$. Figure 3a and b shows the Debye heat capacity as a function of the temperature for different materials with different Debye temperatures and versus reduced temperature, $\frac{T}{\theta_D}$. When plotted as a function of $\frac{T}{\theta_D}$ the data essentially lie on a master curve in this approximation. At low temperatures $T < 0.02\ \theta_D$, the lattice heat capacity is to a very good approximation given by

$$C_V^L = 234R\left(\frac{T}{\theta_D}\right)^3 \tag{10}$$

in agreement with experiment. This T^3 law is a major triumph of the Debye theory. At high temperatures C_V^L approaches the classical Dulong–Petit limit of $3R$. Note that at the Debye temperature, C_V^L essentially reaches the classical limit (about 0.96 the value of $3R$). Also, it is readily shown that the zero point vibrational energy in the Debye approximation is given by $\frac{9R\theta_D}{8}$.

The Debye frequency $\nu_{max} = \nu_D$ ($\sim 10^{12}$ to 10^{14} s^{-1}) and the Debye temperature $\theta_D = \frac{h\nu_D}{k_B}$ are related to the strength of the bonding and the elastic properties of the solid. If one thinks roughly in terms of the atoms of atomic mass m being coupled by springs of stiffness λ, the characteristic vibrational frequency might be expected to vary as $\left(\frac{\lambda}{m}\right)^{1/2}$. Carbon, which is elastically stiff and composed of relatively light atoms, has a Debye temperature of about 1860 K whereas lead is soft and heavy with a Debye temperature of 102 K. We will see that the Debye temperatures of different allotropic forms can

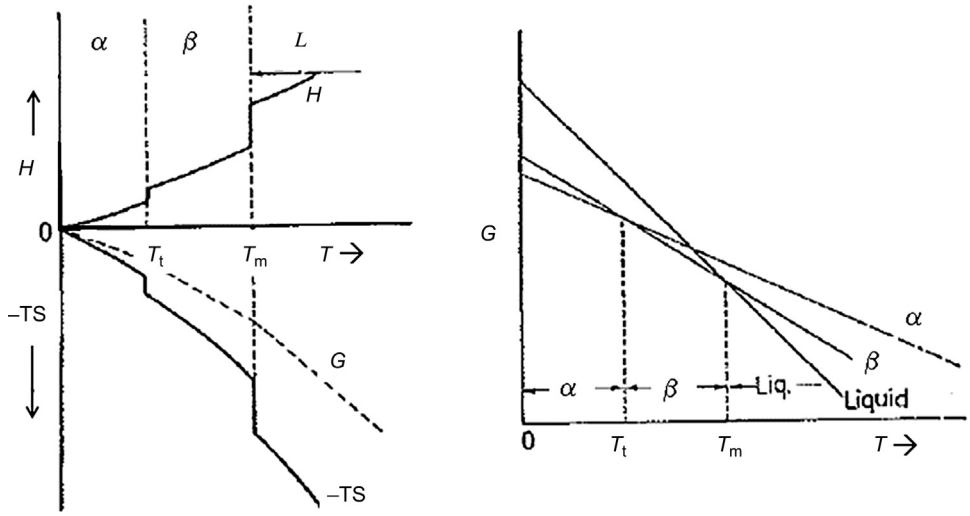

Figure 4 Schematic diagram showing the variation of *G*, *H* and –TS as a function of temperature for the α, β and liquid phases in a system exhibiting an allotropic phase change at $T = \mathrm{Tt}$. After Smallman (1963).

play a central role in the relative stability of phases. The Debye temperatures for the allotropes of Zr are approximately θ_D (hcp) = 260 K and θ_D (bcc) = 212 K.

The electronic contribution to the heat capacity for a metallic solid deriving from thermal excitation of the conduction electrons is predicted from the quantum theory of solids to be dependent on the density of states near the Fermi level and given by $C_V^e = \Gamma T$ where Γ is a constant and for most metals is typically about 10^{-3} to 10^{-4} cal deg^{-2} mol^{-1}. Transition metals generally show somewhat higher values because of their relatively high density of states. For example, Γ for Cu and Ag is about 1.5×10^{-4} whereas for γ-Fe and α-Fe, Γ is 8×10^{-4} and 12×10^{-4}, respectively. For zirconium (Zr; 4 d^2 5 s^2), Γ_α(hcp) is 7.1×10^{-4} and Γ_β(bcc) is 4.4×10^{-4} cal deg^{-2} mol^{-1}. It should be clear that the electronic contribution is expected to be important only at very low and very high temperatures.

With the thermodynamic machinery and data described briefly here it is possible to plot the energies (E, H), entropies (S) and free energies (G) of the α and β phases as a function of temperature as shown schematically in Figure 4. The thermodynamic properties of the liquid phase can also be computed (the heat capacity of the liquid phase is approximately $C_P = 8.0$ cal mol^{-1} deg^{-1}). The reader is reminded that the slopes of the free energy curves are directly related to the entropies of the competing phases, S^α, S^β and S^L through the thermodynamic identity $\left(\frac{\partial G}{\partial T}\right)_P = -S$. It is left to the reader to show how one can estimate the cohesive energy of the β phase in the thermodynamic analysis described earlier.

This thermodynamic analysis of phase stability and allotropy in zirconium (Zr) leads to some very important general conclusions. At low temperatures the more close-packed (hcp) α phase with stronger bonding (greater cohesive energy) tends to be favored because of the relative importance of the energy and entropic terms in the expression for the free energy $G = E + PV - TS$. The more open (bcc) β phase with higher internal energy is the phase of higher vibrational entropy as the temperature is increased. This is made clear by examining Figure 5a where the relative heat capacities of the bcc (β) and hcp (α) phases are shown schematically. The heat capacity of the more weakly bonded β phase with its lower

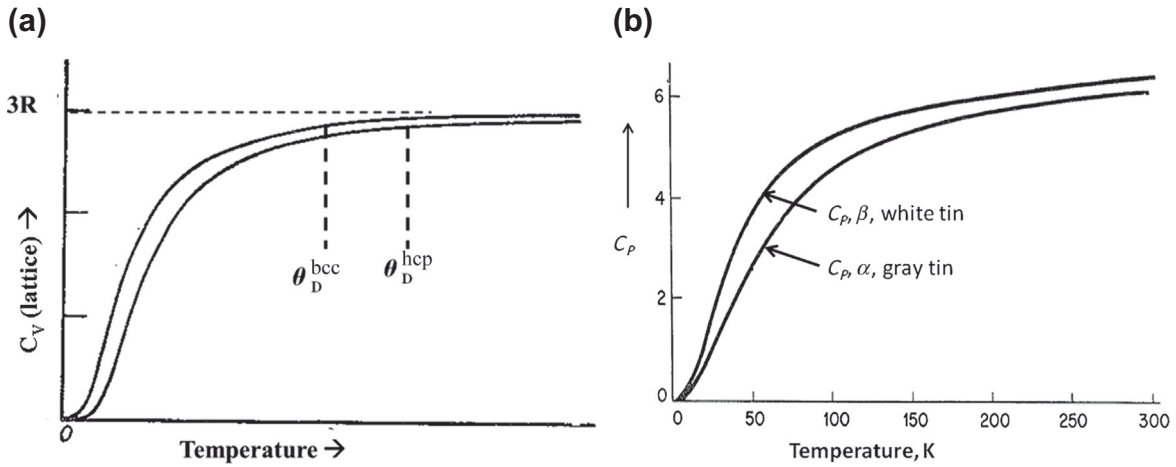

Figure 5 (a) Schematic showing relative lattice heat capacities and Debye temperatures for α (hcp) and β (bcc) allotropes in metals such as titanium (Ti) and Zirconium (Zr). (b) Schematic of the relative heat capacities of gray tin ($\theta_D = 260$ K) and white tin ($\theta_D = 212$ K)

characteristic temperature θ_D (and lower ν_D) lies above that of the more strongly bonded α phase (higher θ_D and ν_D) as they approach the Dulong–Petit limit. The leads to a higher entropy of the β phase eventually stabilizing it as its steeper G versus T curve falls below that of the α phase at high temperatures. Indeed, in many cases, the structure (in metals and nonmetals) of closest packing is favored at low T and a more open structure, one with weaker bonding and greater vibrational entropy, becomes stable at high T. See Th, Ti, Sr, Hf, Tl, Li, Na as well as NaCl-type to CsCl-type transformations. Importantly, these general conclusions cannot be applied in such a straightforward manner when directional bonding and magnetic effects become major considerations.

An interesting case in this regard is allotropy in tin (Sn) where at one atmosphere pressure ($P = 1$ atm) below about 286 K this element is stable in a diamond cubic structure called gray Sn (α) and above this transition temperature the stable form is ordinary Sn (β) possessing the usual metallic properties and exhibiting a body-centered tetragonal structure. The gray Sn is quite brittle and is a semiconductor. The densities of these two allotropes are quite different with $\rho(\alpha)$ and $\rho(\beta)$ being about 5.75 g cm^{-3} and 7.28 g cm^{-3}, respectively; therefore, there is a large volume expansion (approximately 27%) accompanying the $\beta \rightarrow \alpha$ transformation. This large volume expansion renders the transformation very sluggish. Importantly, the lower density diamond cubic form has a Debye temperature $\theta_D(\alpha) = 230$ K compared with $\theta_D(\beta) = 200$ K for the higher density metallic white Sn. See **Figure 5b**. The gray Sn with a coordination $z = 4$ is more strongly bonded than the white Sn $z = 6$; the nearest-neighbor distance in the directionally bonded diamond cubic structure is 0.280 nm compared with 0.302 nm in the metallic bct phase with space group $I\frac{4_1}{a}md$. The metallic phase is the phase which is stabilized by the vibrational entropy above 286 K. The difference in bonding is of central importance here.

The allotropic behavior of iron (Fe) is of paramount importance not only because of its technological significance—it might be said to essentially form the basis of an entire industrial and technological era—but also because it represents a most important example of where magnetic contributions to the free energy have a profound effect on the stability of the competing phases. At one atmosphere pressure, Fe is stable as a body-centered cubic (bcc) structure from 0 K to about 1183 K where it

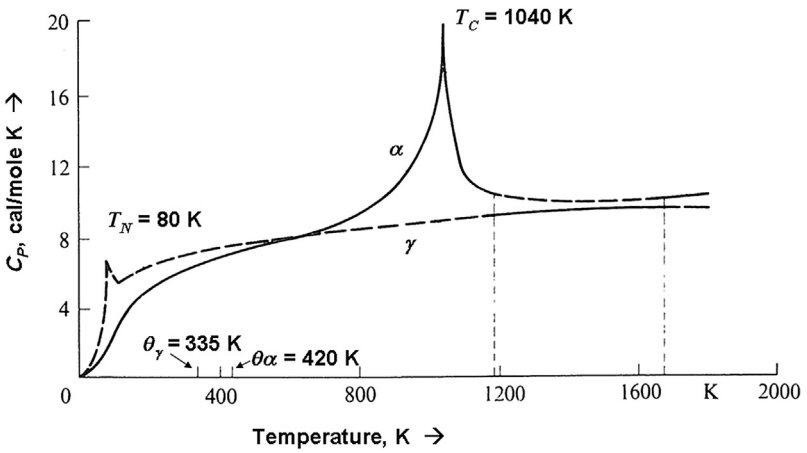

Figure 6 Schematic of the heat capacities of the competing phases in Fe at 1 atm pressure. After Haasen (2001). Note the peak of the γ phase heat capacity at low temperature represents its Neel temperature.

transforms to a face-centered cubic (γ) allotrope which is stable to approximately 1673 K wherein it reverts back to a stable bcc (δ) structure before melting at about 1808 K.

Zener (1955) was one of the first to attempt rigorously to understand the allotropy of Fe in terms of the physical properties and behavior of the solid phases emphasizing the importance of magnetism (C_P^m). Weiss and Tauer (1956) refined these ideas emphasizing the division of the heat capacity explicitly into lattice (C_P^L), electronic (C_P^e) and magnetic (C_P^m) components as discussed earlier. **Figure 6** shows a representation of the heat capacities of the competing phases in Fe at one atmosphere pressure. These authors then took the existing data and calculated the thermodynamic properties (H,S and G) of the α(bcc) and γ(fcc) phases. (Of course, the high temperature δ(bcc) phase is the reemergence thermodynamically of the α phase.) This was followed by an elaborated analysis by Kaufman et al. (1963) emphasizing a more rigorous description of the magnetic properties, particularly of the suggested low-temperature magnetic properties of the γ(fcc). These two works represent the seminal approaches to the subject. At low temperatures where entropy effects are expected to be less important, the ferromagnetic α(bcc) is the phase of lowest internal energy, the magnetic ordering lowers the energy by $\approx RT_C$ ($\approx$2000 cal mol^{-1}), where T_C is the Curie temperature (1141 K) of the ferromagnetic phase, but as the temperature increases a magnetic transition ($\sim$50–80 K) occurs in the competing γ(fcc) phase associated with the antiferromagnetic → paramagnetic state at an Néel temperature T_N or a Schottky-like two-level (high-spin/low-spin) specific heat anomaly. This magnetic effect in the γ(fcc) imparts significant entropy to the phase and the –TS term in the free energy stabilizes the γ(fcc) phase with respect to the magnetically ordered ferromagnetic bcc phase above 1183 K (this effect dominates differences in Debye temperature or electronic contributions to the heat capacity). However, between about 775 and 1141 K disordering of the spins in the ferromagnetic state leads to a ferromagnetic → paramagnetic transition in the α-Fe and this increased magnetic entropy stabilizes the α phase with respect to the γ phase at elevated temperatures to the melting point. The thermodynamic results are summarized schematically in the Gibbs free energy versus temperature curves depicted in **Figure 7**. Importantly, it is the magnetic disordering or Schottky-like anomaly in the γ phase at low temperatures which is postulated to give rise to a stable fcc allotrope over a restricted temperature range and if it were not for this transition the γ phase would not appear. The range of stability of γ-Fe is determined by

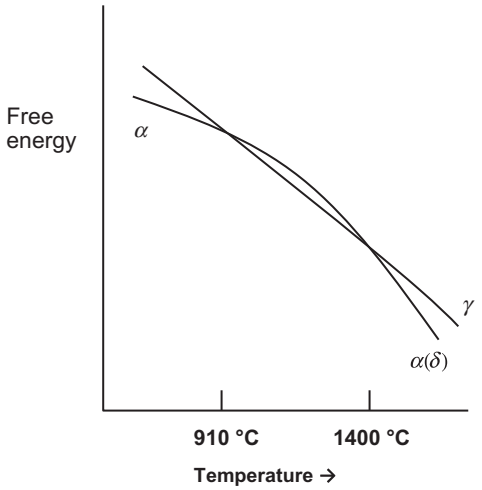

Figure 7 Schematic of the free energies of α and γ iron vs. temperature showing the return of α at higher temperature.

a delicate balance of relatively large contributions to the thermodynamics of the phases and the maximum value of $(G^{\alpha} - G^{\gamma})$ is only about 15 cal mol^{-1}; thus, it is not surprising that alloying elements can selectively stabilize the α and γ phases as is well known in ferrous physical metallurgy. More recent investigators (Massalski and Laughlin, 2009) have focused on elucidating and amplifying these conclusions with the latter discussing the old "β-iron" controversy and the definition of a phase and phase transition. Finally, the $T - P$ for Fe is shown in Figure 8 showing that allotropic phase

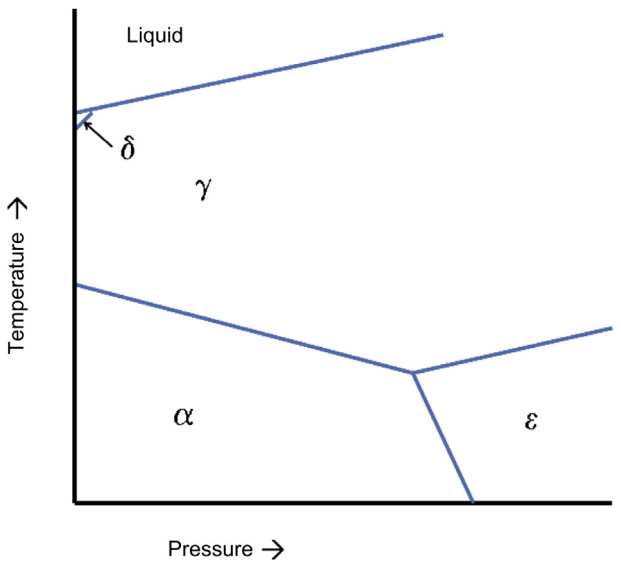

Figure 8 Schematic plot of the temperature vs. pressure phase diagram of iron. Note that at low pressure only the α,γ,δ and liquid phases are stable, whereas at high pressures ε (hcp) becomes a stable phase.

changes can be induced in the system by pressure as exemplified by the appearance of ε-Fe at high pressures.

8.2.2 Thermodynamics of Alloys: Energetics and Stability of Solutions

The Gibbs free energy of an alloy phase at constant temperature (T) and pressure (P) can be written as

$$G' = \sum_{i}^{n} \mu_i n_i \tag{11}$$

where G' is the extensive free energy and n_i is the number of moles of species i contained in the phase and μ_i is the chemical potential of species i in solution defined by

$$\mu_i = \left(\frac{\partial G'}{\partial n_i}\right)_{T,P,n_j} \tag{12}$$

wherein μ_i is also called the partial molar free energy $\overline{G}_i$. This fundamental definition applies to substitutional and interstitial solute elements in crystalline phases. From basic solution thermodynamics the chemical potential of a species in solution also can be written as

$$\mu_i(T,P) = \mu_i^0(T,P) + RT \ln a_i \tag{13}$$

where $\mu_i^0(T,P)$ is the chemical potential in a specified standard state (e.g. the free energy per mole of pure i at the given T and P) and a_i is the activity of the species i in solution. The chemical potential or partial molar free energy defined above can be understood as the free energy per mole of species i contributed to the total free energy of a solution of given composition or as the change in free energy when one mole of i is added to a large quantity of solution at constant composition. Partial molar quantities related to the enthalpy ($\overline{H}_i$) and entropy ($\overline{S}_i$) can be defined in a similar fashion and we can write $\overline{G}_i = \overline{H}_i - T\overline{S}_i$.

In multicomponent and polyphase systems we will find it convenient to write the free energy of a solution as a molar quantity, that is, G^α is taken to be the free energy per mole of the α phase and given by

$$G^\alpha(T,P) = G\left(T,P,X_A^\alpha,X_B^\alpha,\ldots X_M^\alpha\right) \tag{14}$$

with X_M^α referring to the mole fractions of the components A, B, …M, wherein $\sum_{i}^{M} X_M^\alpha = 1$, that is, only $M-1$ mole fractions specifying the composition of a phase are independent. Thus, at constant T and P,

$$G^\alpha = X_A^\alpha \mu_A^\alpha + X_B^\alpha \mu_B^\alpha + \ldots \tag{15}$$

A binary or two-component system A–B can be described thermodynamically by G^α (T,P,X) where X is the mole fraction of B in the α phase, and at constant T and P we can write

$$G^\alpha = (1-X)\mu_A^\alpha + X\mu_B^\alpha \tag{16}$$

In a multicomponent polyphase system composed of α, β, γ, … phases, the criterion for chemical equilibrium is that $\mu_i^\alpha = \mu_i^\beta = \mu_i^\gamma = \ldots$ for all components $i = 1,2,\ldots,C$ across the system. (Note that the

number of components may be less than the number of species in systems exhibiting ionic or covalent bonding.) For two phases α and β in thermodynamic equilibrium in a binary system ($C = 2$), $\mu_A^\alpha = \mu_A^\beta$ and $\mu_B^\alpha = \mu_B^\beta$. A material system is composed of C components when $(C - 1)$ composition variables are required to describe a phase.

The activity of a chemical species introduced in Eqn (13) is more rigorously defined as the ratio of fugacities $a_i = \frac{f_i}{f_i^0}$ where f_i is the fugacity of the species in solution and f_i^0 is the fugacity in a specified standard state such as the pure component at a given temperature (T) and total pressure (P). In this case, the activity of the pure substance is taken as unity. The fugacity f_i of component i is, to a good approximation, equal to the partial vapor pressure p_i of i over the solution. Thus, the activity of component i can be written as $a_i = \dfrac{p_i}{p_i^0}$ where p_i^0 is the vapor pressure of pure i. Other standard states can be invoked for convenience such as the infinitely dilute solution of species i. An ideal solution is defined by setting $a_i = X_i$ (Raoult's law) where X_i is the mole fraction or atomic fraction of i in solution, as discussed earlier. Thus, for an ideal solution

$$\mu_i - \mu_i^0 = RT \ln X_i \tag{17}$$

at constant total pressure P. Generally, solutions are not ideal and the deviation from ideal behavior is taken into account by writing $a_i = \gamma_i X_i$ where γ_i is called the activity coefficient. Dilute solutions often obey Henry's law and $\gamma_i = \gamma_o =$ constant over a restricted composition range. The deviation from ideality expressed by γ_i can be greater or less than unity depending on the atomic interactions of the various species in solution, as will be discussed subsequently.

Let us consider forming a binary liquid or solid solution by dissolving B in A and consider the energetics of this process or reaction, namely,

$$A(\text{pure}) + B(\text{pure}) \rightarrow (A, B)_{\text{solution}}$$

The free energy change accompanying the formation of the solution is called the free energy of mixing, $\Delta G_M = \Delta H_M - T\Delta S_M$, where ΔH_M is the heat (enthalpy) of mixing and ΔS_M is the entropy of mixing. In this brief review of the thermodynamics of alloys we will make extensive use of an approach often called **graphical thermodynamics** (Gibbs, 1873), particularly the use of free energy–composition diagrams in numerous contexts. Figure 9 shows schematically the free energy per mole of solution, G, as a function of composition, X, for a binary system exhibiting complete solubility in the liquid and/or solid state. The prominent dashed line shows the free energy of a mechanical mixture of the components A and B as a function of composition and the free energy of mixing, ΔG_M, is indicated graphically with respect to the mixture of the components. The free energy per mole of solution can be written as

$$G = (1 - X)G_A + XG_B + \Delta G_{\text{M}} \tag{18}$$

where $G_{\text{A}} = \mu_A^0$ and $G_{\text{B}} = \mu_B^0$ are the free energies per mole of the pure components A and B, respectively, and ΔG_M is the change in the free energy on mixing.

For an ideal solution,

$$\Delta G_M^{\text{id}} = RT\{(1 - X)\ln(1 - X) + X \ln X\} \tag{19}$$

whereas, in general, ΔG_M can be expressed as

$$\Delta G_M = RT\{(1 - X)\ln a_A + X \ln a_B\} = RT\{(1 - X)(\mu_A - \mu_A^0) + X(\mu_B - \mu_B^0)\} \tag{20}$$

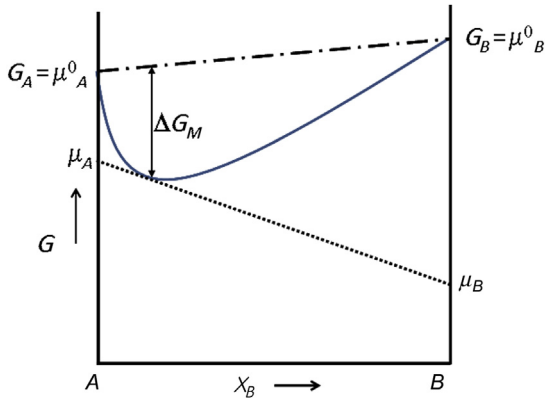

Figure 9 Free energy vs. composition curve of a binary system showing the chemical potentials of the *A* and *B* components in the alloy phase as well as those in their pure state.

or

$$\Delta G_M = RT\{(1-X)\ln \gamma_A + X \ln \gamma_B\} + RT\{(1-X)\ln(1-X) + X \ln X\} \tag{21}$$

It is readily shown that if the solute of a dilute solution obeys Henry's law ($a_B = \gamma^0 X_B$), then the solvent obeys Raoult's law ($a_A = X_A$) using the Gibbs–Duhem equation $(1-X)\mathrm{d}\mu_A + X\mathrm{d}\mu_B = 0$ which stems from the property that the Gibbs free energy is homogeneous function of first order. Writing $G = (1-X)\mu_A + X\mu_B$ for a binary solution and differentiating with respect to X and employing the Gibbs–Duhem relation leads to two very important relations widely used in the graphical thermodynamics of solutions:

$$\mu_A = G - X\frac{\mathrm{d}G}{\mathrm{d}X} \tag{22}$$

and

$$\mu_B = G + (1-X)\frac{\mathrm{d}G}{\mathrm{d}X} \tag{23}$$

as shown in Figure 9. We shall see that this provides a basis for the common tangent construction which illustrates graphically chemical equilibrium in phase mixtures. If the binary *A*–*B* phase represented by the *G* vs. *X* in Figure 9 is a solid phase then clearly the stable components *A* and *B* have the same crystal structure.

If we employ a ΔG_M vs. X curve to denote the energetics of the solid solutions, the intercepts represent relative partial molar quantities $\mu_A - \mu_A^0$ and $\mu_B - \mu_B^0$. See Figure 10. Since

$$\Delta G_M = \Delta H_M - T\Delta S_M \tag{24}$$

one can write the heat of mixing as

$$\Delta H_M = (1-X)\left(\overline{H}_A - H_A^0\right) + X\left(\overline{H}_B - H_B^0\right) \tag{25}$$

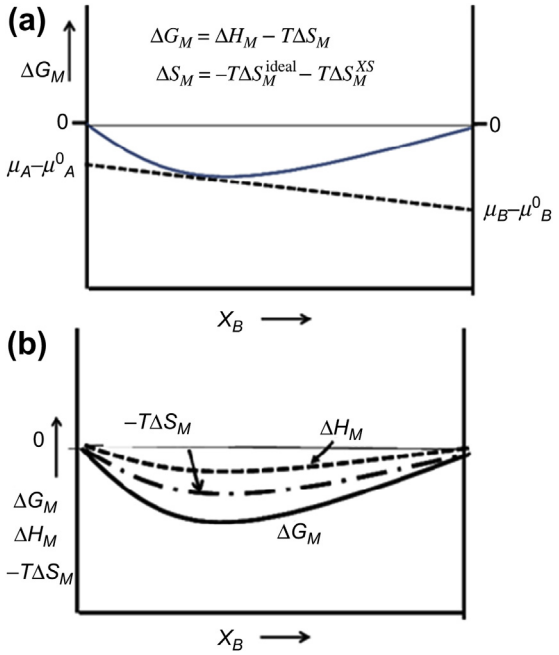

Figure 10 (a) ΔG of mixing plot for a binary solution. (b) Plot showing ΔG, ΔH and ΔS of mixing of the solution phase.

where $\overline{H}_A$ and $\overline{H}_B$ are the partial molar enthalpies of A and B in solution; H_A^0 and H_B^0 are the enthalpies of pure A and B per mole, respectively. Here we extend our definition of an ideal solution wherein

$$\Delta H_M = 0 \quad \text{and} \quad \Delta S_M = \Delta S_M^{\text{id}} = -R[(1-X)\ln(1-X) + X\ln X] \tag{26}$$

The later of which is called the ideal entropy (configurational) of mixing, calculated using elementary statistical thermodynamics applied to the random placement of the A and B atoms on the lattice sites. The ideal entropy of mixing has a maximum value of 1.38 cal mol^{-1} at $X = 0.5$ and is symmetric about this value. A reference state or solution model for the energetics of the A–B solution is the *regular solution* wherein ΔH_m is taken to be non-zero and $\Delta S_M = \Delta S_M^{\text{id}}$ (which has a built-in contradiction as discussed subsequently).

If the energetics of the solid solution are modeled in terms of short-range pairwise interactions or interatomic bonds between the A and B atoms on the lattice sites (assuming in the zeroth approximation interactions between first nearest-neighbors only (see Figure 11) described by bond energies E_{AA}, E_{BB} and E_{AB} (taken to be negative), then assuming random occupation of the N lattice sites ($N = N_{\text{A}} + N_{\text{B}}$, N_{A} and N_{B} being the number of A and B atoms, respectively) one finds that the heat of mixing ΔH_m can be written in a straightforward manner as

$$\Delta H_M = (n_{\text{AA}}E_{\text{AA}} + n_{\text{BB}}E_{\text{BB}} + n_{\text{AB}}E_{\text{AB}}) - N\frac{z}{2}[(1-X)E_{\text{AA}} + XE_{\text{BB}}] \tag{27}$$

where $n_{\text{AA}}, n_{\text{BB}}$ and n_{AB} are the number of A–A, B–B and A–B bonds in a random solid solution (statistical distribution) and z is the first nearest-neighbor coordination of a lattice site. Clearly, the first

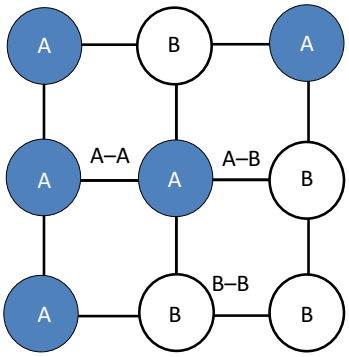

Figure 11 Schematic showing A–A, B–B and A–B first nearest-neighbor bonds.

term represents the enthalpy/energy of the solution and the second term is the enthalpy/energy of a mechanical mixture of the pure components. Importantly, it can be shown that ΔH_M can also be expressed as

$$\Delta H_M = NzX(1-X)\left[E_{AB} - \frac{(E_{AA}+E_{BB})}{2}\right] = NzX(1-X)V \tag{28}$$

indicating that if $\Delta H_M > 0$ ($V > 0$) A–A and B–B bonds are favored (there is a tendency for the atoms to surround themselves with like nearest-neighbors or clustering; if $\Delta H_M < 0 (V < 0)$, A–B first nearest-neighbor bonds are favored indicating a tendency for ordering.

At high temperatures the configurational entropy will tend to produce a random distribution of the species in solution; however, as the temperature is lowered the mutual interactions of the A and B atoms will give rise to clustering ($\Delta H_M > 0$) or ordering ($\Delta H_M < 0$) effects referred to earlier. In the case of $\Delta H_M > 0$ the atomic interactions can lead to the appearance of a miscibility gap and phase separation below a temperature critical T_C as shown in Figure 12a. In the simple regular solution model developed here, $T_C = 2\dfrac{\Delta H_M}{R}$ (at $X = 0.5$). The two-phase field derives from the appearance of a double-well free energy $G(X) = H(X) - TS(X)$ versus composition (X) curve depicted in Figure 12b showing a common tangent construction establishing chemical equilibrium between two phases α_1 and α_2 having different compositions but the same crystal structures. We call attention to the two inflection points $\left(\dfrac{\partial G^2}{\partial X^2} = 0\right)$ in the $G(X)$ vs. X curve since it can be shown that supersaturated solutions lying between these points where $\dfrac{\partial G^2}{\partial X^2} < 0$ are thermodynamically unstable with respect to diffusional processes leading to phase separation. Supersaturated solutions on the $G(X)$ vs. X curve where $\dfrac{\partial G^2}{\partial X^2} > 0$ between the inflection points (the so-called chemical spinodes) and the equilibrium compositions are metastable with respect to phase separation. Small composition fluctuations in a metastable solution tend to decay because they entail a local increase in free energy whereas fluctuations in unstable solutions will tend to amplify spontaneously (see the chord construction in Figure 12c) and lead to phase separation. Furthermore, the diffusion coefficient in

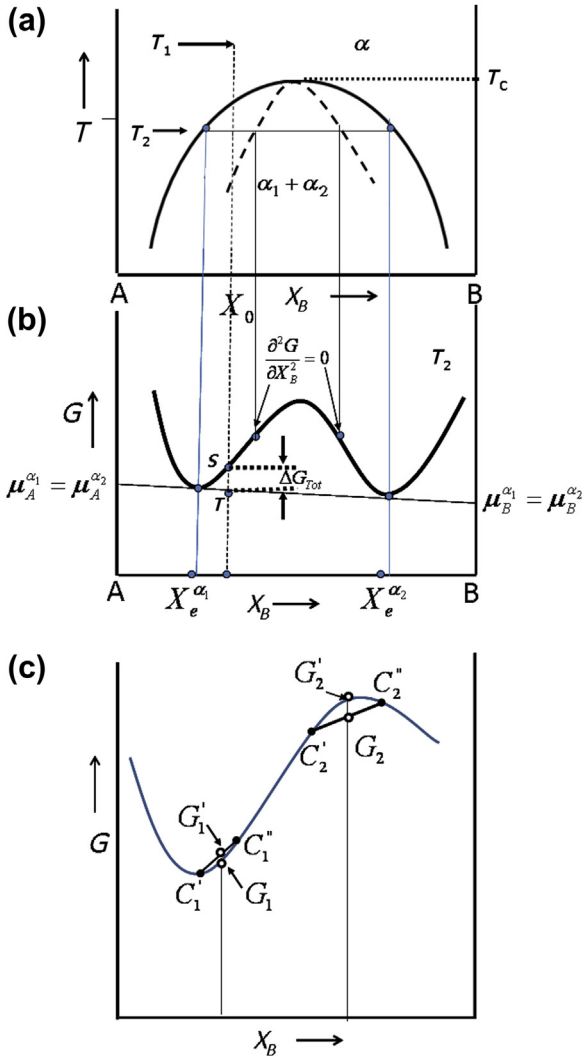

Figure 12 (a) Symmetric miscibility gap of an A–B alloy. (b) Free energy vs. composition curve of the alloy shown in (a) at temperature T_2. (c) Free energy vs. temperature curve for an alloy with an asymmetric miscibility gap, displaying by the cord construction the stability at 1 and instability at 2.

a binary system is proportional to $\frac{\partial G^2}{\partial X^2}$ which indicates that diffusive flow will occur up the concentration gradient (uphill diffusion) leading to spontaneous unmixing in thermodynamically unstable supersaturated solid solutions. This diffusional instability is often referred to as spinodal decomposition of the supersaturated state.

For the simple case of a miscibility gap let us explore further the properties of the $G(X)$ vs. X curve and introduce the concept of the overall "thermodynamic driving force" for a precipitation reaction

within a metastable supersaturated solid solution, that is, the free energy change ΔG_{Total} for the phase reaction:

$$\alpha_0(X_0) \rightarrow \alpha_1\left(X_e^{\alpha_1}\right) + \alpha_2\left(X_e^{\alpha_2}\right) \tag{29}$$

wherein the supersaturated α_0 phase of composition X_0 quenched from temperature T_1 to T_2 decomposes or phase separates within the miscibility gap into an equilibrium phase mixture of phases α_1 and α_2 of compositions $X_e^{\alpha_1}$ and $X_e^{\alpha_2}$, respectively, the relative proportions given by the lever rule. Within the graphical thermodynamics of Figure 12b the decrease in the free energy accompanying phase separation can be shown to be the segment –ST (free energy change per mole of solution α_0) where S is a point on the tangent to the G vs. X curve at X_0 and T is the point on the common tangent at the overall composition X_0. However, during the initial stages of formation of the two-phase mixture in a supersaturated matrix of composition X_0 (nucleation), the formation of a small region of composition X^N (nucleus) is accompanied by a release of free energy per mole of the nucleus indicated by $-$PQ in Figure 13. The matrix is effectively infinite in extent with respect to a small fluctuation and acts as a chemical potential reservoir, that is, the small fluctuation forming a potential nucleus occurs without disturbing the matrix composition or chemical potential. The free energy change (per mole of the nucleus or embryo) $-$PQ is given by

$$\Delta G = X^N\left[\mu_{\text{B}}^{\text{N}} - \mu_{\text{B}}^{M}\right] + \left(1 - X^N\right)\left[\mu_{\text{A}}^{N} - \mu_{\text{A}}^{M}\right] \tag{30}$$

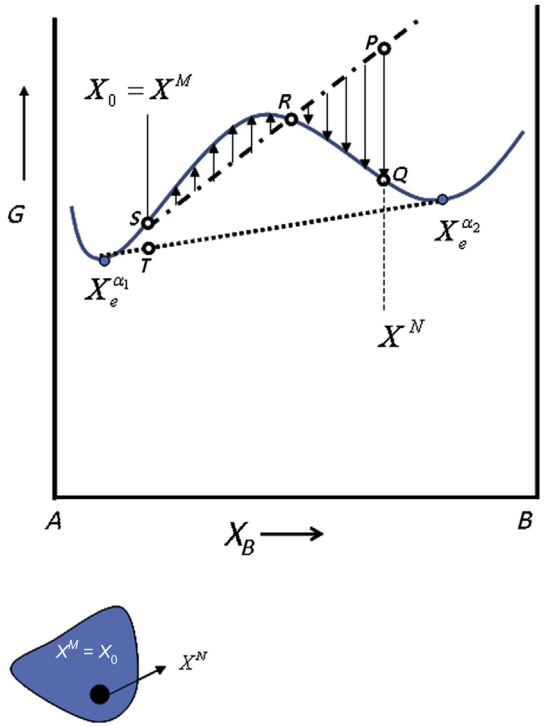

Figure 13 Free energy vs. composition diagram of an alloy with a miscibility gap, showing the driving force (PQ) for the nucleation of *B*-enriched phase from an alloy of composition X_0. X^M is the composition of the initial nuclei.

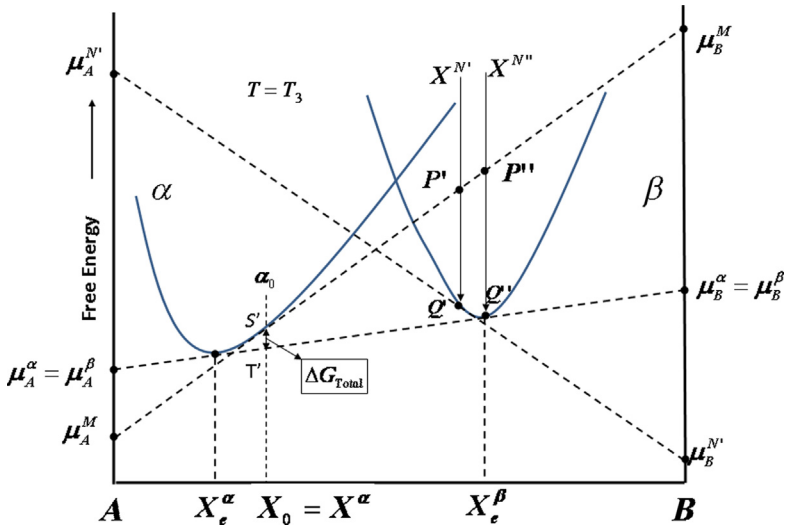

Figure 14 Free energy vs. composition diagram of an alloy with α and β phases of different crystal structure, showing the driving force for the nucleation of β phase from an alloy of composition X_0. See text.

where μ_B^N and μ_A^N refer to the chemical potentials of B and A in the nucleus/embryo of composition X^N and μ_B^M and μ_A^M refer to the chemical potentials of B and A in the matrix of composition X_0. The free energy release is the "effective" thermodynamic driving force for the formation of a nucleus/embryo of second phase of composition X^N within the supersaturated matrix. It should be noted that a fluctuation beyond R where the tangent to the free energy vs. composition (G vs. X) curve at the matrix composition intersects the G vs. X curve is needed to release free energy; smaller fluctuations than R actually increase the free energy locally and tend to decay.

Two-phase equilibrium between phases of different crystal structures is depicted in Figure 14 using the graphical thermodynamic representation and common tangent construction. The common tangent construction establishes the equilibrium compositions of the conjugate phases X_e^α and X_e^β and the equality of the chemical potentials $\mu_A^\alpha = \mu_A^\beta$ and $\mu_B^\alpha = \mu_B^\beta$. If a solid solution α of composition $X^\alpha = X_0$ is rapidly cooled/quenched from to T_3 to produce a supersaturated state α_0, there is an overall thermodynamic driving force ΔG_{Total} (per mole of solution) for the precipitation reaction:

$$\alpha_0(X_0) \rightarrow \alpha_e\left(X_e^\alpha\right) + \beta_e\left(X_e^\beta\right) \tag{31}$$

which is the free energy release accompanying the formation of the equilibrium two-phase mixture as discussed earlier and represented graphically by $-S'T'$ in the associated G vs. X diagram. Again the segment $-P'Q'$ is the effective driving force or free energy released per mole of a small β nucleus or embryo of composition X^N which might form during the initial stages of precipitation (as above) and $P''Q''$ is the free energy released if the nucleus/embryo has the composition X_e^β.

Assuming Henry's law is obeyed by the solute (X) and that Raoult's law is obeyed by the solvent, the expression for the overall free energy change (ΔG_{Total}; see Figure 14) for the precipitation reaction

$$\alpha_0 \rightarrow \alpha_e + \beta_e$$

can readily be shown to be

$$\Delta G_{\text{Total}} = RT\left[X^{\alpha}\ln\frac{X_e^{\alpha}}{X^{\alpha}} + (1-X^{\alpha})\ln\frac{(1-X_e^{\alpha})}{(1-X^{\alpha})}\right] \tag{32}$$

However, the free energy released per mole of a β nucleus of the equilibrium composition X_e^{β} $(-P''Q'')$ is shown to be

$$\Delta G_N = RT\left[X_e^{\beta}\ln\frac{X_e^{\alpha}}{X^{\alpha}} + (1-X_e^{\beta})\ln\frac{(1-X_e^{\alpha})}{(1-X^{\alpha})}\right] \tag{33}$$

If the β nucleus is dilute in A, $(1-X_e^{\beta})\approx 0$ and thus the effective driving force governing the formation of a β nucleus can be approximated by

$$\Delta G_N = -RT\ln\frac{X^{\alpha}}{X_e^{\alpha}} = -RT\ln(SS) \tag{34}$$

where SS is the supersaturation of the α_0 matrix.

It should be pointed out that in an in-depth treatment of the nucleation problem in supersaturated solid solutions ΔG_N is related to the important parameter ΔG_V which is the free energy released per unit volume of the nucleus or embryo and given by $\Delta G_V = \Delta G_N/V_N$ where V_N (V^{β}) is the molar volume of the nucleus.

8.2.2.1 Coherent Phase Equilibria

The effect of elastic stress on phase equilibria in coherent multiphase systems represents an important but complex problem in the thermodynamics of solids. Cahn (1962b) in his seminal work on spinodal decomposition clearly showed the major influence that stress and elastic misfit can have on thermodynamic stability and microstructural evolution in cubic crystals leading to the concept of a coherent spinodal and a fundamental understanding of the occurrence of crystallographically aligned modulated structures in spinodally decomposing systems. Importantly, he recognized that the thermodynamics of stressed solids had not been addressed rigorously and essentially represented an inadequately solved problem in phase equilibria. Larche and Cahn (1973) and Robin (1974) in the early 1970s revealed that to describe the thermodynamics of coherent phase equilibria some fundamentally new questions had to be addressed and some basic concepts modified to properly describe the nature of the conjugate phases comprising metastable phase mixtures with elastic strain energy as a major contribution to the free energy of the system. Williams (1980, 1984) addressed the problem in a rather straightforward manner combining elasticity and solution thermodynamics applying his analysis to basic free energy–composition schemes showing clearly that the elastic energy of coherent phase mixtures can lead to novel and sometimes subtle changes in our thermodynamic description of heterogeneous phase equilibria. For example, two-phase fields are found to contract markedly and sometimes disappear completely as well as showing discontinuities in volume fraction as phase boundaries are crossed. Furthermore, the study of coherent phase equilibria has shown that thermodynamic equilibrium within a phase does not require the uniformity of the individual chemical potentials of the components but a constant so-called diffusion potential related to the difference in chemical potentials $\mu_A - \mu_B$. One also finds the equilibrium compositions of the metastable phases can be greater or less than the compositions of the unconstrained incoherent phases. This pioneering work mentioned earlier was

followed by rigorous generalized treatments of the thermodynamics of elastically stressed crystals exemplified by the work of Voorhees and Johnson (2004), Pfeifer and Voorhees (1991), Johnson and Voorhees (1987), Johnson and Mueller (1991) and Ardell and Maheshwari (1995). A perusal of this literature shows that many of the results are strongly dependent upon the model used to represent the two-phase mixture, boundary conditions and assumptions regarding the variation of lattice parameters with composition in the conjugate phases. Khachaturyan in his classic treatise (1978) and subsequent work (1983) has developed a formalism emphasizing the central role of elastic energy in phase transformations occurring in the solid state.

For pedagogical reasons let us look at some relatively simple analyses which illustrate many of the salient and novel effects alluded to above. Essentially following Williams (1980, 1984), consider two cubic phases α and β with lattice parameters a_α and a_β within an incoherent two-phase state which are isotropically strained to have identical lattice parameters in a coherent metastable phase mixture; the lattice parameters are assumed composition independent. In this first approximation the compositions of the metastable conjugate phases remain the same as the unstressed equilibrium compositions established by the common tangent construction. The total free energy of the coherent phase mixture is written as a sum of the chemical free energies of the α and β phases in the unstressed state plus an elastic coherency strain energy which is a quadratic function of both the misfit strain and the volume fraction of the β phase. These free energies are shown graphically in **Figure 15**a. The nonlinear elastic term extends from point A to B passing through the intersection points X' and X''. Clearly a two-phase mixture is only stable between X' and X'' but the lever rule is applied to compositions A and B in this case. The elastic energy has contracted the extent of the coherent two-phase field compared with the incoherent equilibrium state and results in discontinuities in the metastable volume fractions of α and β phases as the compositions X' and X'' are crossed. If the elastic energy curve rises above the point W the metastable two-phase region disappears. This point W is called the Williams point. A more general case is shown in **Figure 15**b which allows for a composition dependence of the lattice parameters and a variation in the compositions of the metastable coherent conjugate phases. The metastable coherent two-phase field is contracted to the region between X' and X'' and the metastable phases are X'_α and X'_β, respectively; the lever rule is applied using these compositions. (Note: the morphology assumed has been a random array of spheres.)

The case of a miscibility gap can be addressed applying the same methodology. Allowing the lattice parameters of the conjugate phases to vary linearly with composition and assuming constant elastic properties yields a modified suppressed miscibility gap similar to result in the earlier work of Cahn (1962b). See **Figure 15**c. Here the metastable equilibrium compositions of the phases in the coherent state are delineated by the tangency of the elastic energy curve to the free energy–composition curve.

8.2.2.2 Magnetism:Phase Equilibria and Phase Diagrams

In our discussion of the allotropy of iron (Fe) we called attention to the critical role of magnetism (ferromagnetism and antiferromagnetism) in the relative stability of phases and cited early seminal papers on the subject. Here we wish to briefly examine a general approach to describing the contribution of magnetic effects to the heat capacity or specific heat specifically related to the occurrence of ferromagnetism in metals and alloys due primarily to Hillert and Jarl (1978) and extended by Inden (1976, 1981). Although the exact nature of the singularity of the heat capacity C_p^{mag} in the vicinity of the higher order ferromagnetic → paramagnetic transition is yet to be resolved theoretically, Inden introduced an accurate semiempirical operational description of the magnetic contribution to the heat

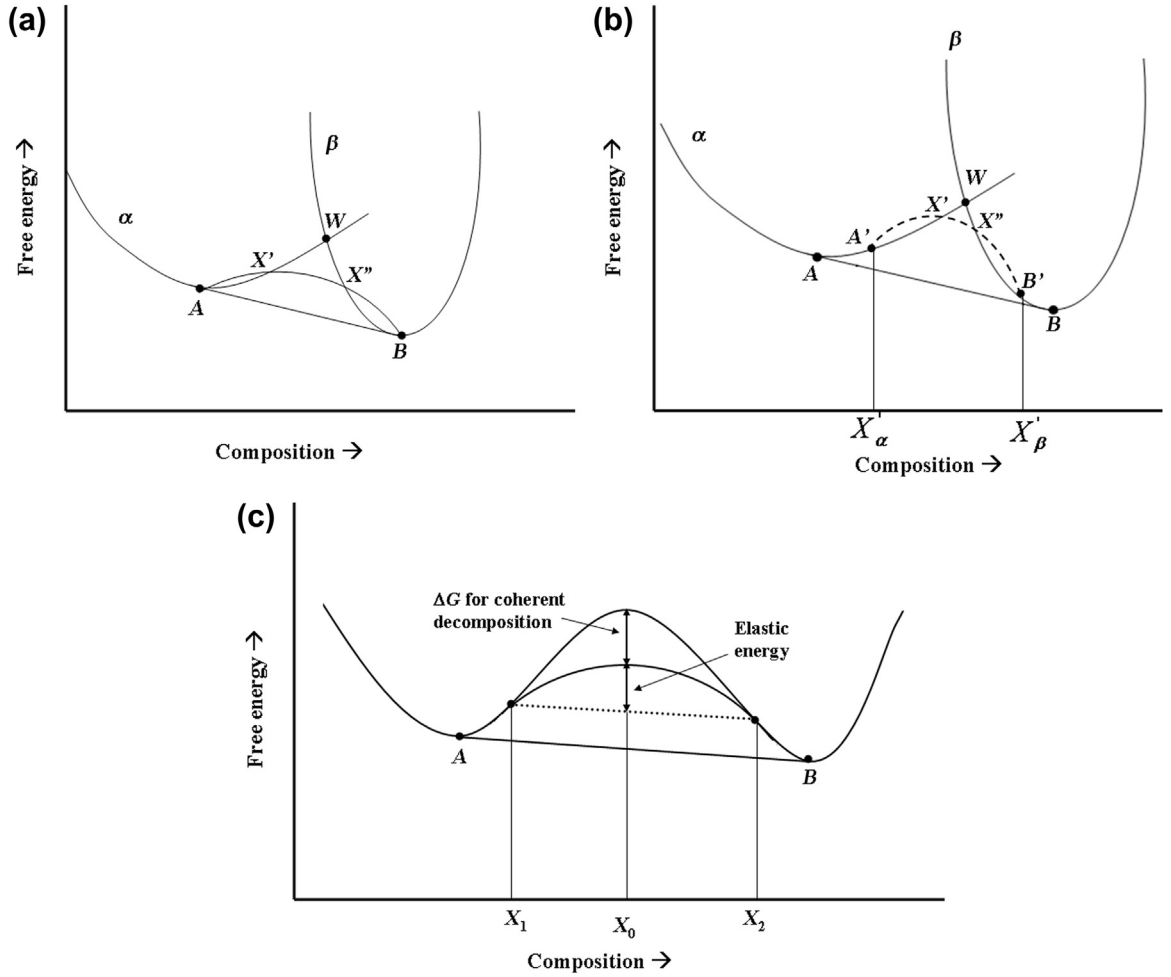

Figure 15 (a) Free energy–composition scheme showing superposition of elastic energy extending from A to B wherein the compositions of the conjugate phases remain the same as in the unstressed state. The coherent two-phase field has contracted to X'–X'' but the lever rule is applied to the compositions A and B of the conjugate phases. The point W where the coherent two-phase field would disappear is called the Williams point. (b) More general case of coherent two-phase equilibrium where the compositions of the conjugate phases are changed to A' and B' and the two-phase field has contracted to X'–X'' with the lever rule applied to compositions A' and B'. (c) Coherent two-phase equilibrium with attendant elastic energy applied to a miscibility gap.

capacity or specific heat taking into account the thermal disruption of both the LRO and SRO of the spins associated with the phase transition which is written as

$$C_P^{\text{mag}}(\text{LRO}) = K^{\text{LRO}} R \ln\left(\frac{1+\tau^3}{1-\tau^3}\right) \quad \text{for} \quad \tau = \frac{T}{T_{\text{C}}} \leq 1. \tag{35}$$

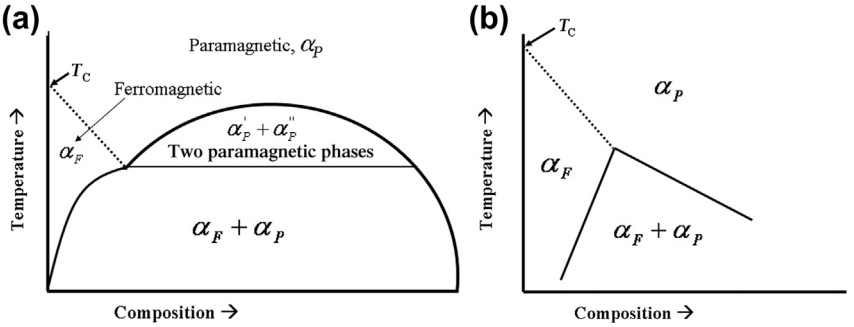

Figure 16 (a) Schematic phase diagram showing the intersection of a line of critical points (Curie temperature) with a simple miscibility gap delineating different magnetic phases α_P, α'_P, α''_P and α_F. (b) A line of critical points in a binary phase diagram showing the emergence of a tricritical point and two-phase region.

and

$$C_P^{\text{mag}}(\text{SRO}) = K^{\text{SRO}} R \ln\left(\frac{1+\tau^{-5}}{1-\tau^{-5}}\right) \quad \text{for} \quad \tau \geq 1 \tag{36}$$

where T_C is the Curie temperature with K^{LRO} and K^{SRO} being two constants characterizing the ferromagnetic and paramagnetic states, respectively. With several simplifications and the aid of series expansions the magnetic contribution to the free energy can be approximated by

$$G^{\text{mag}} = RTf(\tau, p)\ln(\beta + 1) \tag{37}$$

where $f(\tau. p)$ is a complex function of τ and includes a parameter p which is a constant defined as the fraction of the total spin disordering enthalpy absorbed above the Curie temperature (destruction of short-range order/SRO) and is given as $p = .28$ for fcc metals and 0.40 for bcc metals; β is the average magnetic moment (Bohr magnetons) of the atoms comprising the system. To effectively apply this formalism to alloys the salient parameters must be carefully evaluated as a function of composition. This remains an important and challenging problem in alloy physics and computational thermodynamics (Lukas et al., 2007).

Meijering (1963a) analyzed the interaction of a line of higher order transition such as a Curie temperature locus within a binary phase diagram with a miscibility gap as shown in **Figure 16**a. The magnetic transition can significantly distort the shape of the miscibility gap compared with the usual topology but also can markedly distort the associated spinodal curve. Later Nishizawa et al. (1979) discussed similar effects specifically in ferromagnetic α–Fe systems including the technologically important Fe–Cr system. Later Inden (1981 and 1982) analyzed the general behavior of second-/higher order lines in binary phase diagrams including atomic ordering. An important feature of the analysis is that a higher order line can terminate at a sharp critical point (tricritical point) within the interior of the binary diagram giving rise to a two-phase region, for example equilibrium between ferromagnetic and paramagnetic phases of different compositions in a two-phase region. See **Figure 16**b.

8.2.3 Metastability

A phenomenon of major importance in the thermodynamics and kinetics of phase transformations, particularly in the area of precipitation from supersaturated solid solution, is the formation of

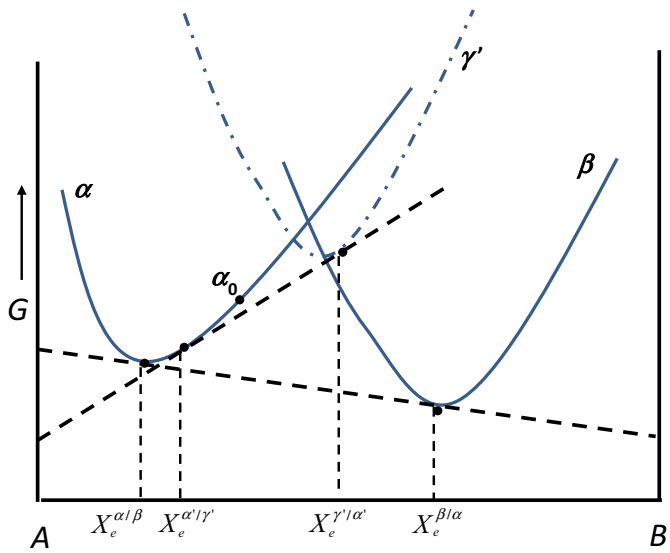

Figure 17 Free energy vs. composition curve of an alloy that has α and β as equilibrium phases at the temperature shown, but also has a metastable phase γ'. The compositions of the stable and metastable equilibria are shown.

metastable phases in the phase reaction in preference to the nucleation and growth of the thermodynamically stable precipitate. Indeed, in the heat treatment of age hardening alloys we find that the decomposition of the supersaturated state often proceeds through a series of metastable states before the emergence of the stable equilibrium precipitate and the optimum physical and mechanical properties invariably develop in association with the formation of fine-scale metastable precipitates within the parent matrix. We will see subsequently that this occurs as a result of favorable nucleation kinetics despite the fact that the thermodynamic driving forces discussed earlier are greatest for the formation of the equilibrium second phase. In Figure 17 we show a rather straightforward graphical representation of a competing γ' phase that can form in a supersaturated α_0 establishing a metastable equilibrium phase mixture composed of α' and γ'; stable equilibrium is the $\alpha + \beta$ two-phase mixture. The metastable equilibrium gives rise to a metastable solvus shown in Figure 18 deriving from a metastable common tangent construction with respect to the γ' phase. We see that the metastable γ' phase has a greater solubility in the α phase than the equilibrium precipitate. Furthermore, it is clear from the graphical thermodynamics that the overall driving force ΔG_{Total} is less for the phase reaction $\alpha_0 \rightarrow \alpha' + \gamma'$ than for the formation of the stable equilibrium phase mixture $\alpha + \beta$. Also, it can be shown by graphical thermodynamic construction that the "effective driving force" for nucleation of the β is greater than that for the nucleation of the metastable phase, γ'.

8.2.3.1 Eutectoid Decomposition

An important solid-state transformation in alloys is the case of eutectoid decomposition which has played a central role in governing the heat treatment of engineering steels. Also the proeutectoid reaction (a precipitation reaction) has been engineered to tailor the microstructure of hypoeutectiod compositions to achieve extraordinary combinations of properties (strength, ductility, etc.) for a wide range of technological applications. The eutectoid reaction per se is associated with a phase diagram configuration as shown in Figure 19 and can be written generally as $\gamma \rightarrow \alpha + \beta$, that is,

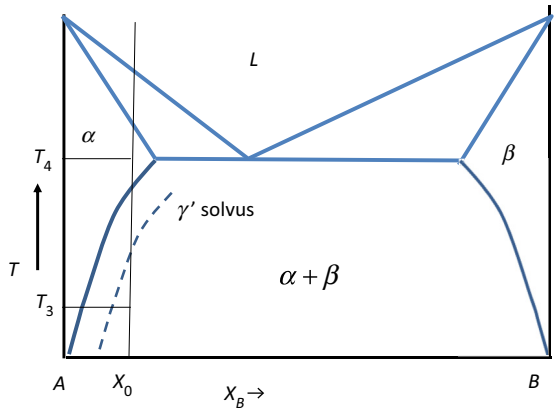

Figure 18 A simple eutectic phase diagram of a binary A–B alloy. The dotted line represents the metastable solvus line for the metastable γ' solid phase.

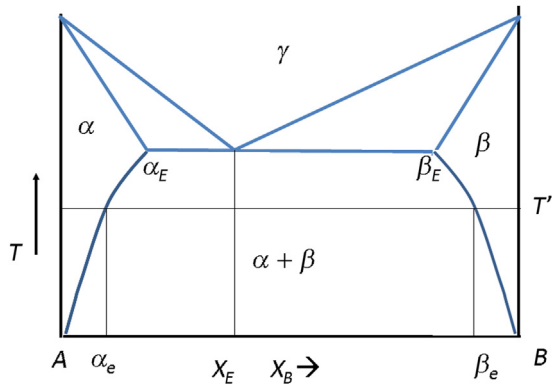

Figure 19 A simple eutectoid phase diagram for the alloy A–B. On cooling, the γ phase transforms to α and β at the invariant temperature.

a high-temperature γ phase decomposes into two phases α and β having different crystal structures. A schematic free energy–composition diagram for the eutectoid decomposition of an undercooled γ phase of eutectoid composition X_E at some temperature below the equilibrium eutectoid reaction isotherm is depicted in Figure 20 where $\Delta G = \Delta G_{\text{Total}}$ for the eutectoid reaction is given by SE. The eutectoid reaction involves a codeposition of two phases often exhibiting a characteristic morphology. The eutectoid microconstituent in carbon and low-alloy steels generally exhibits a classic lamellar morphology similar to that arising in eutectic freezing and this mode of transformation is often called cellular phase separation as will be discussed later.

An interesting feature of the free energy scheme depicted in Figure 20 is that a γ composition of S' can lower its free energy by transforming to a metastable α' phase without a change in composition. This alternative reaction path can involve either of two transformation mechanisms, namely, the well-known diffusionless martensitic transformation or diffusional massive transformation. The free energy change $S'E'$ is the thermodynamic driving force for these compositionally invariant transformation

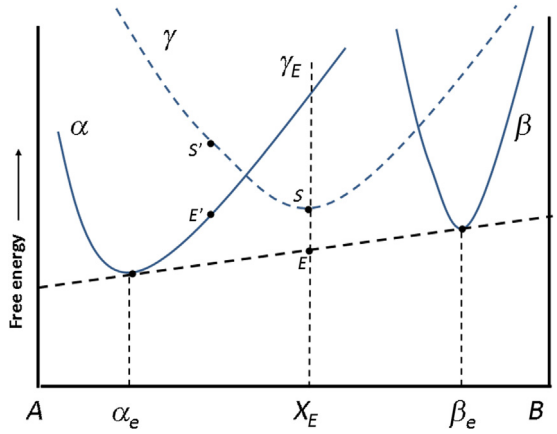

Figure 20 Free energy vs. composition curves for the three phases α, β and γ at the temperature T'.

modes. The *martensitic transformation* involves a characteristic distortion or strain which converts the parent phase (γ) to the product phase (α') often at very high velocities. The atoms within the unit cell of the parent phase generally move small distances relative to the unit cell dimensions essentially shearing from one crystal structure to another in the absence of thermally activated atomic jumps of individual atoms but rather involving a cooperative or synchronous shearing of groups of atoms. The *massive transformation* on the other hand occurs by a diffusional nucleation and growth mechanism involving short-range thermally activated and uncorrelated atomic jumps across a migrating transformation front or interphase interface (Massalski, 1958, 1970).

8.2.4 Atomic Ordering in Alloys: Superlattices

Solid solution formation is a basic phenomenon in modern physical metallurgy and materials science. The introduction of different atomic species onto the sites of a crystalline solid to form an alloy gives rise to a structural modification which can markedly influence the properties of the metallic material. (Note: the solute may enter the solid solution interstitially or substitutionally; in this discourse we will focus our attention on atomic arrangements in subtitutional solid solutions.)

The mixing of atomic species on the sites of a solid solution may not be random even under equilibrium conditions, that is, the probability of a pair of sites being occupied by specific atoms is not simply equal to the probability obtained by multiplying their respective atomic fractions. These nonrandom distributions of atomic species derive from different interatomic interactions between, say, A–A, B–B and A–B pairs of atoms in a binary solution. Indeed, randomness is the exception rather than the rule in real alloy systems. When the *A* and *B* atoms in a binary alloy have a preference for like atoms, that is, A–A and B–B pairings, the behavior is termed **clustering**. If the energetics of the solution favor unlike A–B pairings, the deviation from randomness is called **ordering**. If the preference for A–B pairs persists only over a few to several interatomic distances, the solid solution is said to exhibit **short-range order (SRO)**; whereas, if these correlations persist over large distances compared with the unit cell dimensions, the ordering is denoted **long-range order (LRO)** and the crystal structure and atomic arrangements can be described in terms of interpenetrating sublattices occupied preferentially by *A* and *B* atoms creating an ordered solid solution or superlattice. See Figure 21. In this figure the gray atoms represent average occupancy by white and black atoms: that is, the disordered binary phase.

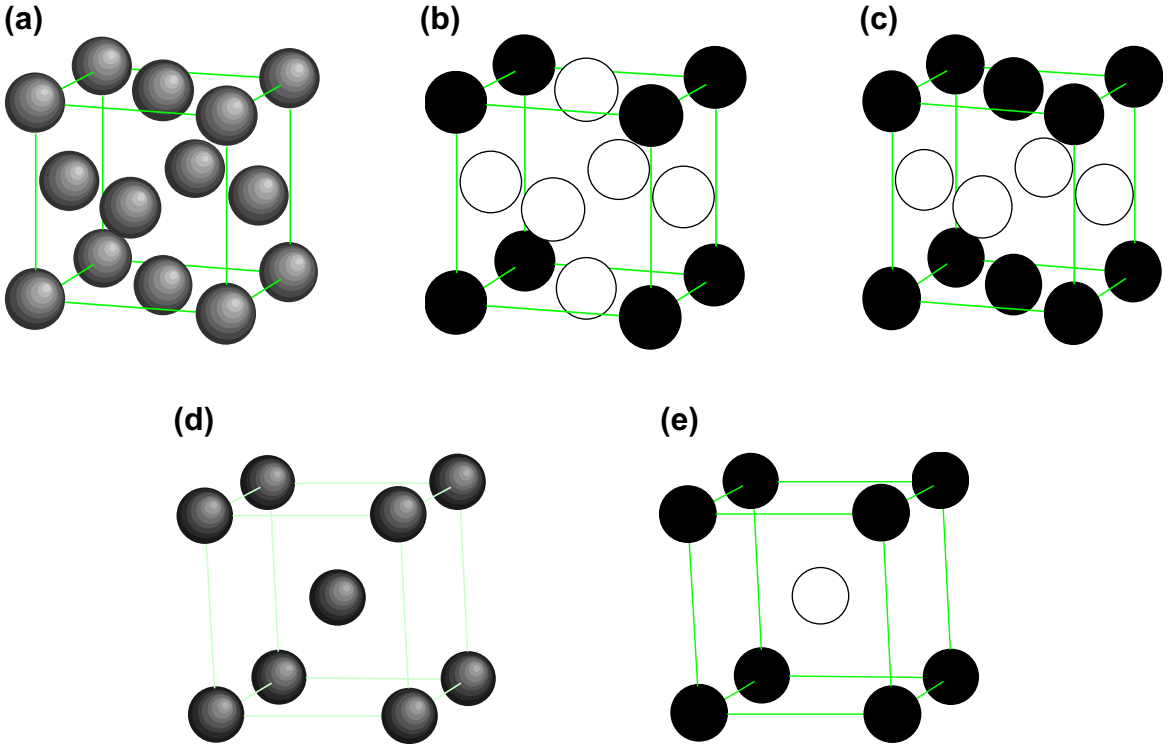

Figure 21 Disordered atomic structures and ordered atomic structures. (a) A1 (fcc, Cu), (b) $L1_2$ (Cu_3Au), (c) $L1_0$ (CuAu), (d) A2 (bcc, W), (e) B2 (CsCl).

These superlattices tend to form in the vicinity of stoichiometric ratios, for example, A_3B, AB, and are often referred to as intermetallic compounds, particularly when the ordered phase melts congruently or when the intermediate solid solution exists over a narrow composition range. We are going to be most interested in ordered (LRO) solid solutions which become disordered at elevated temperatures, that is, the LRO breaks down above a critical temperature but some SRO may persist. In the ordered state, the degree of LRO is not necessarily perfect, but is disrupted by thermal energy (temperature) and deviations from stoichiometry. Subsequently we shall quantify the description of the degree of order in a solid solution, but before doing this let us look briefly at the history of this phenomenon.

Tammann (1919) suggested that LRO could develop in a substitutional metallic solid solution. Earlier work by Kurnakow et al. (1916) indicated intriguing behavior in Cu–Au alloys of properties such as electrical resistivity in the vicinity of Cu_3Au and CuAu compositions, depending on the thermal treatment of these alloys. Bain (1923) and Johannson and Linde (1925) first reported "superlattice diffraction lines" in X-ray powder diffraction patterns. Indeed, because new periodicities appear in the structure of the ordered solution compared with the "disordered" parent phase, new "reflections" appear in the diffraction pattern. For example, in the A_3B superlattice viewed as a *crystallographic derivative* of a parent disordered FCC solid solution wherein the atomic sites are statistically occupied by "average" atoms, the distance between identical planes is doubled along the $\langle 100 \rangle$ directions as a result

of the atomic or chemical ordering. New superlattice lines appear as a result of the new and larger d-spacings. The disordered FCC solid solution is properly viewed as a crystal based on an FCC Bravais lattice with the basis being a "statistical" or "average atom" occupying the points of the Bravais lattice. The A_3B ($L1_2$) superlattice is a crystal structure based on the simple cubic Bravais lattice with an A_3B arrangement decorating the lattice points. See **Figures 21** a, b. Importantly, this change in Bravais lattice constitutes a thermodynamic phase change or phase transformation.

These exciting new ideas and results percolated in the 1920s and stimulated a great deal of theoretical attention. In the 1930s a truly classic paper by Bragg and Williams (1934) appeared based on a rather simple statistical thermodynamic approach defining the underlying energetics of the solid solution in terms of an ordering energy related to the work done, W, in interchanging A and B atoms in an ordered structure from "right" sites to "wrong" sites among the sublattice sites characterizing the superlattice. They introduced an LRO parameter based on the occupancy of the appropriate sublattices and formulated the underlying energetics of the solution in terms of an ordering energy due to unspecified long-range forces acting on the individual atoms, the strength of which is proportional to the degree of atomic order; the (configurational) entropy of the ordered solution was formulated assuming random mixing of the different atomic species on the aforementioned sublattices of the emerging ordered structure. Importantly, the original Bragg–Williams theory makes no explicit use of short-range forces or pairwise interaction energies as incorporated later in the so-called quasichemical approaches. The assumption of random mixing on the sublattices fails to account for any local correlations or SRO. The degree of ordering is defined solely in terms an occupancy of the sublattices or the LRO parameter defined explicitly below. However, as we shall see the Bragg–Williams approach captured salient features of the ordering transformation in AB (CuZn) and A_3B (Cu_3Au) compositions in cubic solid solutions and is referred to as the zeroth approximation in the scheme of quasichemical descriptions, which generally write the solution energetics in terms of AA, BB and AB bond energies (pairwise interaction energies) (Bethe, 1935; Guggenheim, 1952). Indeed, the original Bragg–Williams formulation of the problem is found to be basically equivalent to a quasichemical approach incorporating AA, BB and AB bond energies in its underlying physics when the assumption of random mixing on the sublattices (regular solution) is invoked and is essentially homologous to the Weiss molecular field theory of ferromagnetism (Weiss, 1907). In the modern parlance of cluster variation methods (CVM), Bragg–Williams theory is a point cluster approximation (de Fontaine, 1973). The quasichemical approach of Bethe, emphasizing pairs of atom is a mean field theory in which pairs are immersed in a mean field in contrast to the Bragg–Williams formulation wherein single atomic species are effectively immersed in the background of the mean field derived from an "average" environment.

The Bragg–Williams theory introduces an LRO parameter based on occupancy of the appropriate sublattices, A atoms on α sublattice sites, B atoms on β sublattice sites ("right" sites) and B atoms on α sites, A atoms on β sites ("wrong" sites), and so on. We first will examine the equiatomic AB alloy undergoing the A2(bcc) → B2(sc) ordering transition. See **Figure 21**d and e. The degree of LRO is formulated quantitatively most generally as

$$\eta = \frac{(r_\alpha - X_A)}{Y_\beta} = \frac{(r_\beta - X_B)}{Y_\alpha} \tag{38}$$

where r_α is the fraction of α-sites occupied by A atoms ("right" atoms) and r_β is the fraction of β-sites occupied by B atoms ("right" atoms); Y_α is the fraction of α-sites and Y_β is the fraction of β-sites in the ordered superstructure, respectively. X_A and X_B are the atomic fractions of A and B in the alloy. This expression for η is applicable to stoichiometric and nonstoichiometric compositions

and has a maximum value of unity in the perfectly ordered stoichiometric alloy. Clearly for non-stoichiometric compositions the maximum possible value is less than one. Using this description the order parameter varies from $\eta = 0$ in the disordered state (random solid solution) to $\eta = 1$ in the perfectly ordered state and most importantly the intensities of the "superlattice reflections" in diffraction patterns are generally found to vary as η^2 for both stoichiometric and nonstoichiometric compositions.

As mentioned earlier, the Bragg–Williams ordering energy or interchange energy is assumed to be related to the work done, W, in interchanging A and B atoms in the ordered structure from "right" sites to "wrong" sites among the sublattice sites characterizing the superlattice or superstructure. In this theory the interchange energy is assumed to be linearly related to the degree of order in the emerging superlattice as $W = \eta W_0$ where W_0 is the interchange energy when the alloy exhibits a state of perfect order ($\eta = 1$). An expression for the equilibrium degree of order η as a function of temperature was developed in terms of a simple kinetic equation describing the atomic transfer between sublattice sites (atomic transfer from "right" sites to "wrong" sites and the reverse); the forward and back reaction rates were set equal at equilibrium. The ratio of the rate constants (equilibrium constant) was set equal to a Boltzmann-like term $\exp\left(-\frac{W}{k_B T}\right)$, where $W = \eta W_0$ and k_B is the familiar Boltzmann constant in accord with basic chemical thermodynamics. When the solution energetics are written in terms of AA, BB and AB nearest-neighbor bond energies (E_{AA}, E_{BB} and E_{AB}) the interchange energy term W_0 is readily shown to be equal to $W_0 = -z(2E_{AB} - E_{AA} - E_{BB})$ where z is the nearest-neighbor coordination. When $2E_{AB} < E_{AA} + E_{BB}$ unlike pairs are favored, that is, the system tends to show ordering. This Bragg–Williams formulation gives the variation of η with temperature as

$$\ln\left(\frac{1-\eta}{1+\eta}\right) = -\frac{W_0 \eta}{2k_B T} \tag{39}$$

or,

$$\eta = \tanh\left(\frac{W_0 \eta}{4k_B T}\right) \tag{40}$$

which can be solved numerically. See Figure 22.

The results for the $A2 \rightarrow B2$ disorder–order show a continuous change in the degree of order from $\eta = 1$ at low temperatures to $\eta = 0$ at the critical temperature T_C, which can be shown to be given by $T_C = \frac{W_0}{4k_B}$. There is no latent heat associated with the phase transition and thermodynamic analysis reveals a finite discontinuity in the specific heat or heat capacity (C_v or C_P) at the critical temperature T_C as depicted in Figure 23.

This behavior shows all the earmarks of an Ehrenfest transition of Second Order (Ehrenfest, 1933). The Bragg–Williams theory does describe, at least qualitatively, the general behavior of systems such as CuZn (β-brass); however, the experimental results in terms of the behavior of the specific heat in the vicinity of the critical temperature are more complex. The neglect of local correlations (SRO) is clearly a major shortcoming of this zeroth approximation wherein SRO is found to persist even above T_C. See Figure 24. Indeed, a complete solution to this singularity has not yet been achieved. See Pippard (1966).

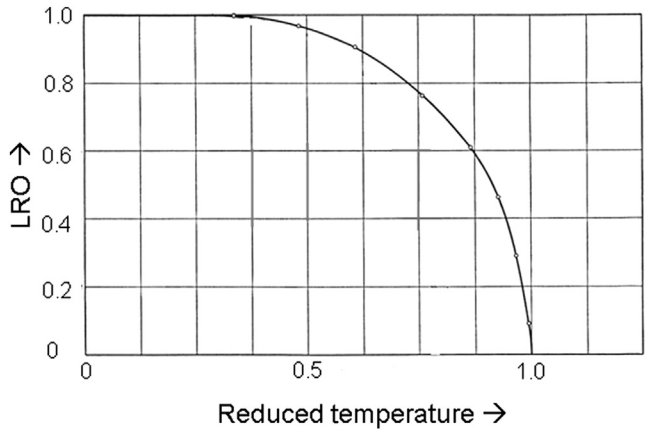

Figure 22 The order parameter vs. temperature plot for a Bragg–Williams second-order transition. Note the infinite slope as T approaches T_C. After Nix and Shockley (1938).

If the solution thermodynamics are formulated in terms of pairwise interaction energies for the A–B binary alloy assuming random mixing on the sublattices, the free energy of mixing of the ordering alloy can be written as

$$F_M = E_M - TS_M = NzV\left\{c(1-c) + \frac{\eta^2}{4}\right\} - k_B T \ln \omega \tag{41}$$

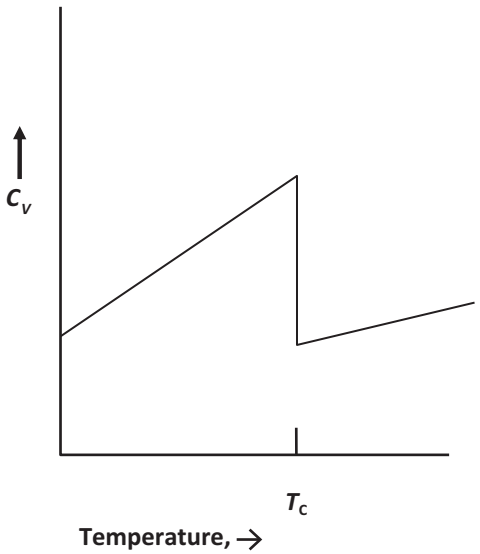

Figure 23 Plot of heat capacity vs. temperature for a Bragg–Williams second-order transition. Note the finite discontinuity at the critical temperature.

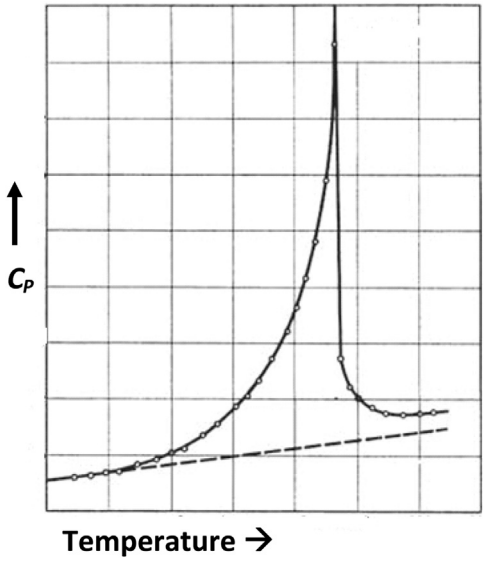

Figure 24 Variation of C_P vs. temperature plot for CuZn. Notice that the shape looks like the Greek letter *lamda*. This curve is different than that predicted by the Bragg–Williams treatment. After Nix and Shockley (1938).

where N is the total number of atoms in the alloy, $z = z_1 = 8$ is the coordination number of the first nearest-neighbor shell for the B2 structure, c is atomic fraction of B atoms,

$$V = \frac{1}{2}\left(2E^1_{\mathrm{AB}} - E^1_{\mathrm{AA}} - E^1_{\mathrm{BB}}\right),$$

where the superscripts refer specifically to first or nearest-neighbor (n–n) interactions (later we will generalize the Bragg–Williams model to include 2nd n–n interactions), and $k_{\mathrm{B}}\ln\,\omega$ is the configurational entropy term (the vibrational entropy contribution is neglected). The ω term is the number of possible arrangements or microstates corresponding to thermodynamically equivalent macrostates or distributions of A and B atoms on the sites of the sublattices (thermodynamic probability). The configurational entropy derived assuming random mixing on the sublattices can be written as

$$\mathrm{S}_M = k_{\mathrm{B}}\,\ln\,\omega = k_{\mathrm{B}}\,\ln\,\frac{\left(\frac{\mathrm{N}}{2}\right)!\left(\frac{\mathrm{N}}{2}\right)!}{\left(N^{\alpha}_A\right)!\left(N^{\alpha}_B\right)!\left(N^{\beta}_A\right)!\left(N^{\beta}_B\right)!} \tag{42}$$

where N^{α}_{A} and N^{α}_{B} are the number of A and B atoms on the α sites and N^{β}_{A} and N^{β}_{B} are the number of A and B atoms on the β sites, respectively. Using the usual Stirling's approximation, and counting the number of AA, BB and AB bonds in terms of the concentration c and the sublattice occupancies, the free energy of mixing can be written as a function of c and η as follows:

$$\begin{aligned} F_M(c,\eta) = Nz_1V\left\{c(1-c) + \frac{\eta^2}{4}\right\} + \frac{Nk_{\mathrm{B}}T}{2}\left\{\left(1-\mathrm{c}+\frac{\eta}{2}\right)\ln\left(1-\mathrm{c}+\frac{\eta}{2}\right) + \left(c-\frac{\eta}{2}\right)\ln\left(c-\frac{\eta}{2}\right)\right. \\ \left. + \left(1-c-\frac{\eta}{2}\right)\ln\left(1-c-\frac{\eta}{2}\right) + \left(c+\frac{\eta}{2}\right)\ln\left(c+\frac{\eta}{2}\right)\right\} \end{aligned} \tag{43}$$

the first term being the heat of mixing $H_m = Nz_1V\,c\,(1-c)$ associated with forming a disordered solid solution of A and B atoms statistically occupying the sites of a bcc solid solution and $V<0$ for the ordering system. Taking $\frac{\partial F_M}{\partial \eta}=0$ and $\frac{\partial^2 F_M}{\partial^2 \eta}=0$ yields $\eta = \tan h\left(-\frac{4V\eta}{k_BT}\right)$ and $T_C = -\frac{4V}{k_B}$, consistent with the classic Bragg–Williams results outlined earlier.

The Bragg–Williams approach or zeroth approximation of the quasichemical models can readily be extended to the case of A1(fcc) → A_3B ($L1_2$, sc) ordering where

$$F_M = Nz_1V\left\{c(1-c)+\frac{\eta^2}{16}\right\} - k_BT\ln\omega\ldots \tag{44}$$

with $S_M = k_B \ln \frac{\left(\frac{3N}{4}\right)!\left(\frac{N}{4}\right)!}{(N_A^\alpha)!(N_B^\alpha)!}$ with the α and β sublattices for the A_3B superstructure shown in Figure 21b. The expanded entropy term becomes

$$S_M = -\frac{Nk_B}{4}\left\{3\left(c-\frac{\eta}{4}\right)\ln\left(c-\frac{\eta}{4}\right)+3\left(1-c+\frac{\eta}{4}\right)\ln\left(1-c+\frac{\eta}{4}\right)+\left(c+\frac{3\eta}{4}\right)\ln\left(c+\frac{3\eta}{4}\right)\right.$$
$$\left.+\left(1-c-\frac{3\eta}{4}\right)\ln\left(1-c-\frac{3\eta}{4}\right)\right\} \tag{45}$$

Taking $\frac{\partial F_M}{\partial \eta}=0$ yields the equilibrium value of the order parameter η for the A_3B composition as a function of temperature given by the transcendental equation as follows:

$$\ln\left(\frac{(1+3\eta)(3+\eta)}{3(1-\eta)^2}\right) = -\frac{2z_1V\eta}{3k_BT} \tag{46}$$

For $F_M = F_M(\eta,T)$ there exists a critical temperature T_C such that $F_M(\eta^*,T_C) = F_M(0,T_C)$ with $\frac{\partial F_M(\eta*,T_C)}{\partial \eta} = \frac{\partial F_M(0,T_C)}{\partial \eta} = 0$. At the critical temperature T_C, one finds by successive approximation, $\eta^* = 0.463$ and the critical temperature approximately given by $T_C = -\frac{0.137z_1V}{k_B}$. The variation of η with temperature is depicted in Figure 25 and clearly displays a markedly different behavior than the A2 → B2 transition. At the critical temperature T_C the order parameter η undergoes a discontinuous change from $\eta=\eta^*$ to $\eta=0$ and represents an equilibrium between an ordered phase ($\eta=\eta^*$) and a disordered phase ($\eta=0$) with an associated latent heat ΔH_t given approximately by 0.78 T_C cal^{-1} mol^{-1} (Nix and Shockley, 1938). These thermodynamic features indicate a first-order transition according to the Ehrenfest classification.

The Bragg–Williams approximation does predict a first-order transition for the A1 → A_3B ($L1_2$) ordering in agreement with experiment, but the quantitative limitations are strikingly evident when one compares the value of $\eta^* = 0.463$ with the generally observed values of 0.7–0.8. Higher level theoretical approximations, for example cluster methods, predict values nearer 0.9. Furthermore, the more rigorous theoretical treatments predict lower critical temperatures by as much 50% (Christian, 2002).

As demonstrated earlier, the Bragg–Williams model captures essential features of AB and A_3B ordering (the B2 and $L1_2$ superstructures being crystallographic derivatives of bcc and fcc parent phases, respectively) showing the occurrence of two-phase equilibrium between a disordered phase

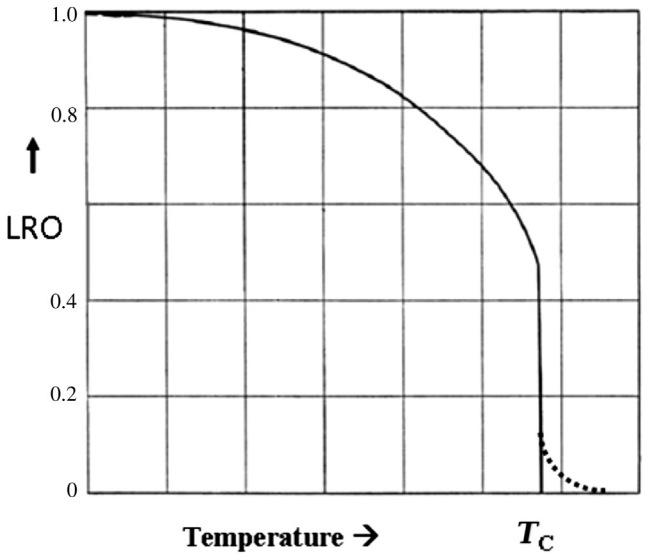

Figure 25 The Bragg–Williams LRO parameter vs. temperature plot for the fcc to $L1_2$ transition. The discontinuity at the critical temperature signals that this is a first-order (Ehrenfest) transition. After Nix and Shockley (1938).

($\eta = 0$) and an imperfectly ordered phase ($0 < \eta < 0$) at $T = T_C$ for the $L1_2$ ordering but no such two-phase equilibrium for the B2 ordering occurs which shows a continuous transition from $\eta = 1$ to $\eta = 0$ at T_C. The phase transitions are identified as first-order and second order according to the well-known Ehrenfest criteria. The free energies of the phases formulated earlier included a composition dependence although in the thermodynamic analysis we emphasized the stoichiometric compositions. Computational thermodynamic analysis using the general expressions for the free energies F_m (c, η, T) allows one to generate a temperature (T) versus composition (C) phase diagram and the ordering transitions are mapped into a conventional binary phase diagram in **Figure 26**. In the late 1930s Nix and Shockley (1938) compiled an extensive review of the subject including various early theoretical approaches.

8.2.4.1 First and Second Nearest–Neighbor Interactions

The energetics of binary substitutional metallic solid solutions based on pairwise interaction energies or A–A, B–B and A–B bonds within a zeroth approximation quasichemical approach can be readily extended to include both first nearest-neighbor (1st nn) and second nearest-neighbor (2nd nn) interactions by distinguishing two so-called interchange energies:

$$V = \frac{1}{2}\left(2E^1_{AB} - E^1_{AA} - E^1_{BB}\right)$$
$$U = \frac{1}{2}\left(2E^2_{AB} - E^2_{AA} - E^2_{BB}\right) \tag{47}$$

where E^i_{AA}, E^i_{BB} and E^i_{AB} refer to the ith nearest-neighbor interaction energies—all taken to be negative reflecting the "strength" of the A–A, B–B and A–B bonds, respectively. In the usual approaches

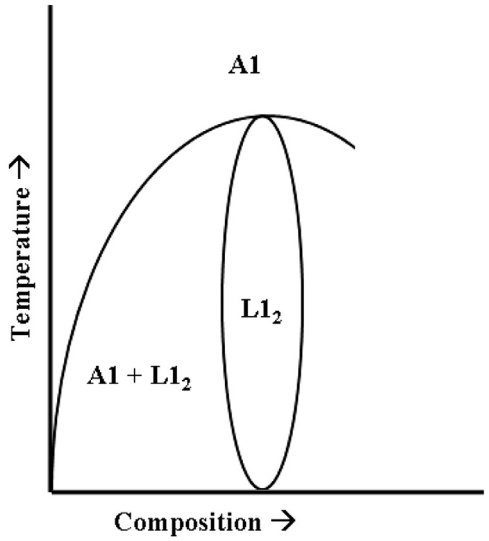

Figure 26 The Bragg–Williams phase diagram for A1(fcc) and $L1_2$ phases. Note the two-phase region (A1 + $L1_2$) between the ordered $L1_2$ phase and the disordered fcc phase, since this transition is first order.

incorporating only 1st nn interactions, $V < 0$ favors unlike A–B bonds and the system is classified as having a tendency for *ordering*. For $V > 0$, like A–A and B–B pairs are favored within the solid solution and the system has a tendency for *clustering* and *phase separation*. The heat or enthalpy of mixing can be written as $\Delta H_m = NzC(1-c)V$ for a bcc or fcc assembly of N atoms where $(1-c)$ and c are the atomic fractions of the species A and B, respectively; z is the 1st nn coordination of the structure. Clearly, $\Delta H_m < 0$ indicates a tendency for ordering and $\Delta H_m > 0$ is indicative of a clustering system. Importantly, in the 1st nn approximation ordering and clustering effects are essentially mutually exclusive—the system either tends to order (SRO or LRO) or shows clustering and a tendency to phase separate. However, extending this pairwise interaction model to include 2nd nn interactions, the model becomes richer in terms of possible behaviors since the 1st nn and 2nd nn (and higher) interactions may be of opposite sign. Ordering and phase separation are no longer mutually exclusive behaviors and the association of a miscibility gap within an ordering system emerges and this interplay of ordering and clustering tendencies can markedly influence the thermodynamic stability of a solution with respect to ordering and phase separation. Spinodal decomposition can actually be involved in the formation of ordered precipitates during the decomposition of supersaturated solid solutions (see e.g. Soffa and Laughlin, 1982, 1988, 1989).

Following the straightforward approach of Ino (1978) in the case of A2 → B2 ordering, the free energy of mixing is written as a function of the composition c and order parameter η as follows:

$$F_M(c,\eta) = Nc(1-c)[z_1V + z_2U] + \frac{N\eta^2}{4}[z_1V - z_2U] + \text{entropy terms} \tag{48}$$

wherein we have included the 2nd nn intereaction energies with $z_1 = 8$ and $z_2 = 6$ referring to coordination of the 1st nn and 2nd nn shells for the A2 → B2 ordering; η is the usual Bragg–Williams (LRO)

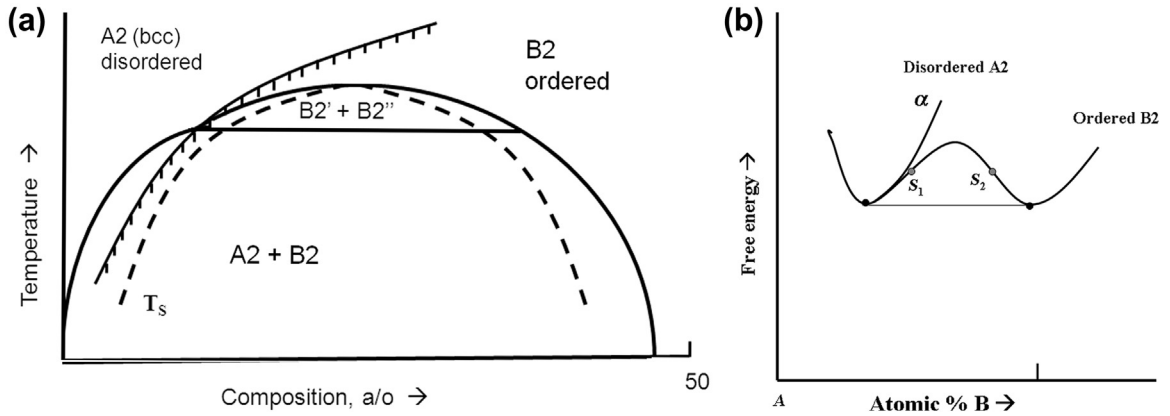

Figure 27 (a) Interplay of ordering and phase separation in an A2/B2 ordering system showing phase separation of the partially ordered B2 phase and associated spinodal locus. (b) Free energy–composition curves showing ordering and phase separation at low temperatures.

order parameter which in the case of the A2 → B2 transition in a stoichiometric A–B alloy can be written simply as

$$\eta = \frac{R - W}{R + W} \tag{49}$$

with R being the total number of "right"atoms and W the total number of "wrong" atoms occupying the conventional α and β sublattices of the B2 superlattice denoted previously. The entropic terms in this generalized Bragg–Williams model are the same as those in Eqn (40) assuming random mixing on the sublattices.

This free energy functional can lead to a phase diagram configuration shown schematically in Figure 27 for the case $U \approx \frac{|V|}{3}$ with $V < 0$ and $U > 0$. In this situation a miscibility gap appears in the system below the order→disorder line of critical points along with an associated chemical spinodal locus $\left(\frac{\partial^2 F_M}{\partial c^2} = 0\right)$. An alloy of composition $c \approx 0.25$ cooled from the α (A1; disordered bcc) single-phase field will order upon crossing the A2 → B2 critical temperature giving rise to an imperfectly ordered B2 superlattice and as the temperature is further decreased the alloy will phase separate into two imperfectly ordered B2 phases—B2′ + B2″—of different compositions. At still lower temperatures one phase will become disordered and the other will increase in composition and degree of order resulting in an equilibrium two-phase mixture of solute-depleted α (A1; disordered bcc) + solute-enriched B2 (ordered; sc). An associated free energy–composition diagram is depicted in Figure 27b showing the solution energetics and instabilities deriving from the expanded model which includes higher order interactions.

The generalized Bragg–Williams model including 1st and 2nd nn interactions can be extended to A1(fcc) → $L1_2$(A_3B; sc) ordering systems discussed earlier. (The reader is reminded that A2 → B2 ordering is generally a second-order/higher order transition whereas A1 → $L1_2$ is first order according to the Ehrenfest classification.) The free energy of mixing of the fcc-based solid solution relative to the pure components A and B can be written as

$$F_M(c, \eta) = Nc(1 - c)[12V + 6U] + \frac{N\eta^2}{16}[12V - 18U] + \text{entropic terms} \tag{50}$$

and again the entropic terms assuming random mixing on the conventional sublattices α_1, α_2, α_3 (the three designated α sublattices are crystallographically equivalent) and β are identical to those formulated previously. For $\frac{U}{|V|} \approx 0.4$ with $V < 0$ and $U > 0$ one finds a phase diagram configuration and stability loci depicted in Figure 28a. This description of the phase boundaries and stability limits includes a locus T_i^- which represents instability with respect to ordering and a chemical spinodal (T_S) locus instability with respect to phase separation contingent on prior ordering (condition spinodal instability). Figure 28a and b shows a summary of these results in graphical form including a free energy–composition diagram. This will be discussed, in detail, in a subsequent section on precipitation of ordered phases within supersaturated solid solutions. What is clear is that in both cases (the A2 → B2 and the A1 → $L1_2$ ordering systems) the inclusion of 1st and 2nd nn interactions leads to a substantially more

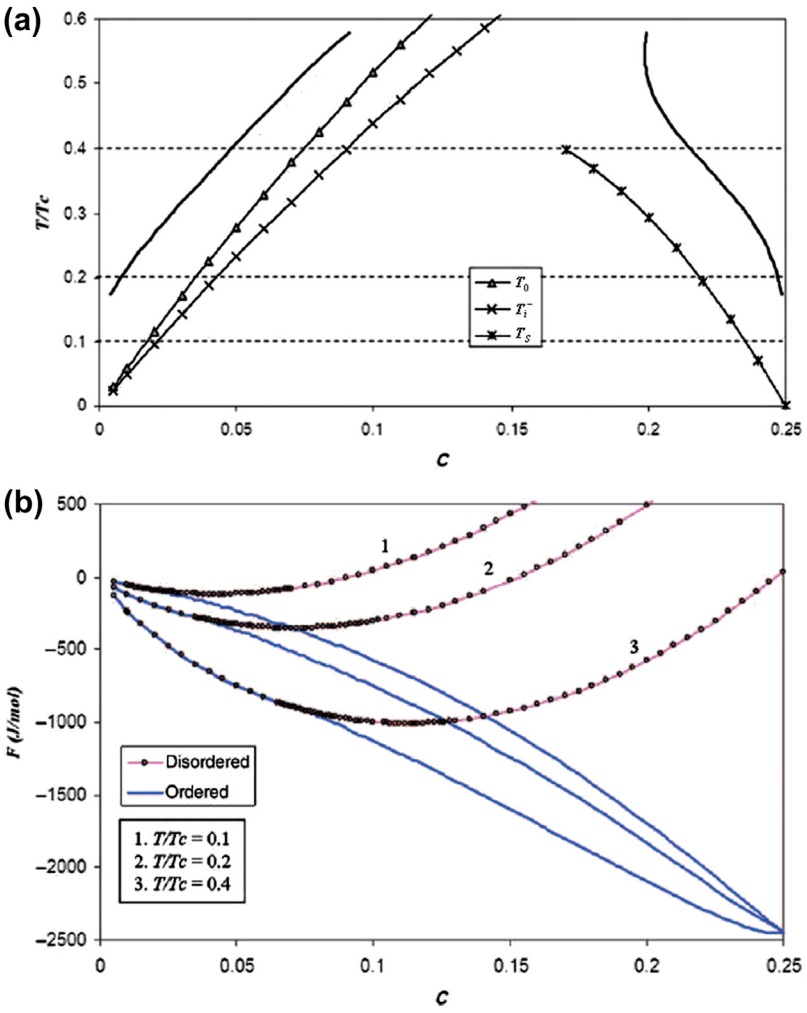

Figure 28 (a) The phase boundaries and instability loci and (b) the free energy vs. composition curves at three temperatures for $\frac{U}{|V|} \approx 0.4$ for the $L1_2$ ordering. After Soffa et al. (2010).

complex solution behavior which can allow for varied diffusional paths involving ordering and clustering in the transformation of the system as it approaches equilibrium (Soffa et al., 2010).

8.2.4.2 The Ground State of Binary Alloys with $V < 0$

Following Richards and Cahn (1971) we can write the enthalpy of mixing of an A–B alloy up to second neighbors as

$$\Delta H_M = NV\left[Z_{AB}^{(1)} + Z_{AB}^{(2)}\frac{U}{V}\right] \tag{51}$$

where U and V are defined above, Z_{AB}^{i} is the number of ith neighbor A-B bonds per atom and N is the total number of atoms in the alloy. The values of Z_{AB}^{i} can be easily calculated by considering the number of A-B bonds in the unit cell and dividing by the number of atoms in the unit cell. At 0 K (the ground state) the structure which minimizes ΔH_M is the equilibrium structure. Thus if $V < 0$, the equilibrium state is the one which maximizes the expression $\left[Z_{AB}^{(1)} + Z_{AB}^{(2)}\frac{U}{V}\right]$, whereas for $V > 0$ the state which minimizes it is the equilibrium state.

If both V and U are positive, the expression $\Delta H_M = NV\left[Z_{AB}^{(1)} + Z_{AB}^{(2)}\frac{U}{V}\right]$ is minimized for both $Z_{AB}^{(1)}$ and $Z_{AB}^{(2)}$ equal to zero, that is no opposite first or second neighbors. At 0 K the equilibrium state of A–B alloys would be composed of a pure A phase and a pure B phase with fractions determined by the lever rule. Any other configuration would have a larger (more positive) enthalpy of mixing and therefore not be in a state of stable equilibrium.

8.2.4.2.1 BCC Ground States

Let us look at the two ordered phases of 50% B based on the bcc structure (B2 and B32) shown in Figure 29a and b.

It can be seen that for the B2 structure, $Z_{AB}^{(1)} = 4$ and $Z_{AB}^{(2)} = 0$, whereas for the B32 structure $Z_{AB}^{(1)} = 2$ and $Z_{AB}^{(2)} = 3$. Thus, if we compare the two expressions that are to be maximized to determine the stable state:

$$\text{for B2}: \left[4 + 0\frac{U}{V}\right]$$

$$\text{for B32}: \left[2 + 3\frac{U}{V}\right]$$

it is seen that the expression for B32 is larger than that for B2 when $\frac{U}{V} > \frac{2}{3}$. That is, B32 is the stable ordered phase when $\frac{U}{V} > \frac{2}{3}$: otherwise B2 is the stable phase. This implies that second neighbors are of importance in the B32 structure.

One other case could be compared with these two ordered phases, namely a completely disordered 50% B alloy. For this case the average $Z_{AB}^{(1)} = 2$ and $Z_{AB}^{(2)} = 1.5$. For $\frac{U}{V} > 0$ B32 has the lower enthalpy of mixing and therefore is more stable. But for $\frac{U}{V} < \frac{2}{3}$ B2 is the stable phase. Thus, if $V < 0$, the homogeneously disordered phase is never the one with the lowest enthalpy of mixing. Note that for the case of negative $\frac{U}{V}$ the use of first and second neighbor interaction energies shows that a configurationally disordered phase is not stable at 0 K in agreement with the third law of thermodynamics.

At 25% B for $\frac{U}{V} > 0$ the phase with the $D0_3$ structure is the stable one since all of the B atoms have opposite first and second neighbors, which is favored when both U and $V < 0$. Between the composition 0% B and 25% B, a two-phase mixture of pure A and fully ordered stoichiometric

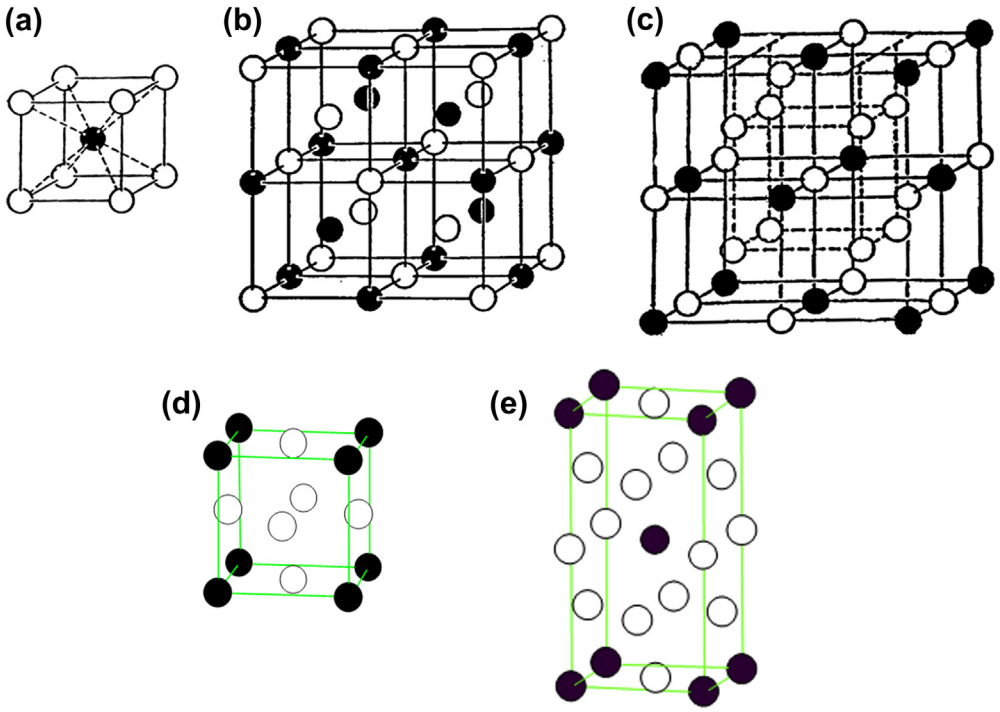

Figure 29 (a) The B2 (CsCl) structure. (b) The B32 (NaTl) structure. (c) The $D0_3$ (BiF_3) structure. (d) The $L1_2$ (fcc derivative) structure. (e) The $D0_{22}$ (fcc derivative) structure.

$D0_3$ has the lowest enthalpy of mixing and is therefore the stable configuration. Between the composition 0% B and 25% B, a homogeneously ordered $D0_3$ phase (order parameter less than unity) may have the same configurational enthalpy of mixing (it is degenerate with the two-phase mixture) but since it has configurational entropy, it is not a stable phase at 0 K according to the third law of thermodynamics.

A diagram showing the stable phases for bcc derivative ordered structures is shown in Figure 30a.

8.2.4.2.2 FCC Ground States

Figure 29d and e displays two possible ordered phases that have derivative structures of the FCC (A1) structure, namely the $L1_2$ (Cu_3Au) and $D0_{22}$ (Ti_3Al) structures. It can be seen that for the $L1_2$ structure, $Z_{AB}^{(1)} = 3$ and $Z_{AB}^{(2)} = 0$, whereas for the structure $D0_{22}$, $Z_{AB}^{(1)} = 3$ and $Z_{AB}^{(2)} = 0.5$. Thus, if we compare the two expressions that are to be maximized to determine the stable state:

$$\text{for } L1_2: \left[3 + 0\frac{U}{V}\right]$$

$$\text{for } D0_{22}: \left[3 + 0.5\frac{U}{V}\right]$$

it is seen that the expression for $D0_{22}$ is larger than that for $L1_2$ when $\frac{U}{V} > 0$. That is, $D0_{22}$ is the more stable ordered phase whenever there is a tendency for next near neighbors to prefer to be opposite.

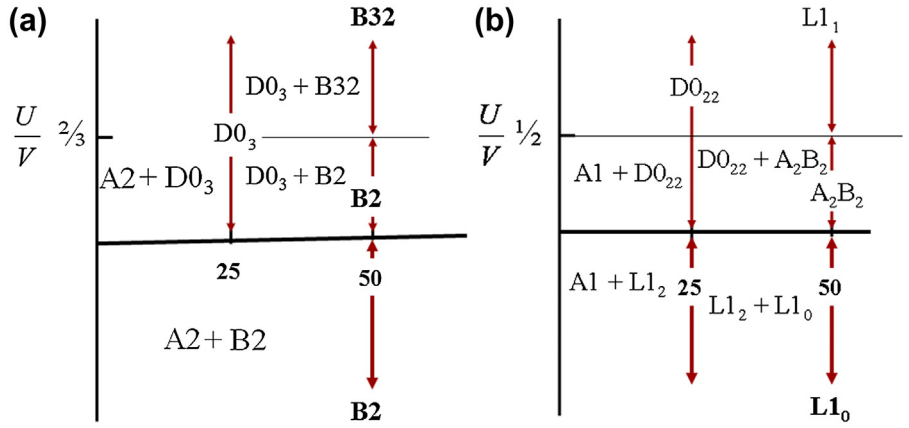

Figure 30 (a) A partial ground state diagram for bcc derivative ordered phases. (b) A partial ground state diagram for fcc derivative ordered phases.

Other cases of FCC derivative structures could be explored. For example the AB alloy (50% each) has three possible ordered phases: $L1_0$, $L1_1$ and the so-called A_2B_2 structure (space group $I\frac{4_1}{a}md$). By similar reasoning as shown above it can be shown that for $\frac{U}{V} < 0$ $L1_0$ is the ground state phase: for $0 < \frac{U}{V} < \frac{1}{2}$ the A_2B_2 structure is the ground state and for $\frac{U}{V} > \frac{1}{2}$ $L1_1$ is the ground state structure. A partial ground state phase diagram for FCC derivative structures is shown in Figure 30b.

More complete ground state diagrams for BCC and FCC can be found in Richards and Cahn (1971). An HCP ground state diagram is found in Singh and Lele (1991).

8.2.4.3 k-Space Solution Energetics

Let us now briefly introduce an extension of the familiar Bragg–Williams quasichemical treatment employed earlier using the language of Khachaturyan's static concentration wave (SCW) formalism (Khachaturyan, 1978, 1983) which has been employed extensively by Khachaturyan and others.

In this "k-space energetics" the site occupancies and interchange energies are formulated in k-space (reciprocal space) through the use of Fourier analysis and the discrete Fourier transform. In this approach the site occupation probability $n(\mathbf{r})$ is given by

$$n(\mathbf{r}) = c + \sum Q(\mathbf{k}) \exp(ik \cdot r) \tag{52}$$

where $Q(\mathbf{k})$ is the amplitude of the Fourier component with wave vector $\mathbf{k}$ and c is the average composition; $\mathbf{r} = x\mathbf{a_1} + y\mathbf{a_2} + z\mathbf{a_3}$ is a vector in real space locating the atomic positions (x,y,z) within the conventional unit cell. Here the atomic arrangement is viewed as a superposition of concentration waves with wave vectors $\mathbf{k}$ and amplitude $Q(\mathbf{k})$ localized in the first Brillouin zone. Furthermore, the interchange energies are represented by a Fourier transform $V(k)$ as follows:

$$V(k) = \sum V(r) \exp(ik \cdot r) \tag{53}$$

where the summation is over the 1st and 2nd nn shells. For the case of fcc-based $L1_2$ ordering the superstructure can be generated by the emergence of a set of concentration waves $\{k_0\}$ comprising a so-called "star" of the structure (dictated by symmetry) and written as

$$k_0 = 2\pi\left(a_1^* + a_2^* + a_3^*\right)$$

and the occupation probability written as

$$n(r) = c + \sum(\gamma\eta)\exp(ik_0 \cdot r)$$

where γ is a constant depending on the crystal structure and equal to $^1/_4$ for the $L1_2$ superstructure and η is the order parameter. Thus, for the evolution of the $L1_2$ superstructure:

$$n(r) = c + \frac{\eta}{4}\sum \exp\left(2\pi\frac{x}{a}\right) + \exp\left(2\pi\frac{y}{a}\right) + \exp\left(2\pi\frac{z}{a}\right) \tag{54}$$

resulting from the growth of three symmetrically related concentration waves along [100], [010] and [001], respectively. The Fourier transforms of the interchange parameter for 1st and 2nd nn interactions yield

$$V(k_0) = -4V + 6U \tag{55}$$

$$V(0) = 12V + 6U \tag{56}$$

where V and U are the 1st and 2nd nn interchange parameters defined above; the term $V(0)$ for $k = 0$ (Brillouin zone center) is associated with the disordered reference solid solution. In this formalism the free energy functional for the fcc solid solution is written as

$$F_m(c,\eta) = Nc(1-c)V(0) - \frac{3}{16}N\eta^2 V(k_0) + \text{entropic terms} \tag{57}$$

wherein the entropic terms are identical to those derived above assuming random mixing on the sublattices of the superstructure.

8.2.4.4 k-Space Solution Energetics/$L1_o$

The k-space formulation of fcc-based solution energetics and stability analysis has been extended to the A1 → $L1_o$ ordering transition by Cheong and Laughlin (1994) and Soffa et al. (2011) employing the generalized Bragg–Williams approach (1st nn and 2nd nn interactions) including an elastic relaxation term in the free energy. The free energy of mixing of an A–B binary solution is written as

$$F_m(c,\eta) = Nc(1-c)[12V + 6U] + \frac{N\eta^2}{4}[4V - 6U] + \text{entropic terms} \tag{58}$$

where the entropic terms are given by

$$S_m = -\frac{Nk_B}{2}\left\{\left[(1-c)+\frac{\eta}{2}\right]\ln\left[(1-c)+\frac{\eta}{2}\right] + \left[c-\frac{\eta}{2}\right]\ln\left[c-\frac{\eta}{2}\right] + \left[c+\frac{\eta}{2}\right]\ln\left[c+\frac{\eta}{2}\right] + \left[(1-c)-\frac{\eta}{2}\right]\ln\left[(1-c)-\frac{\eta}{2}\right]\right\} \tag{59}$$

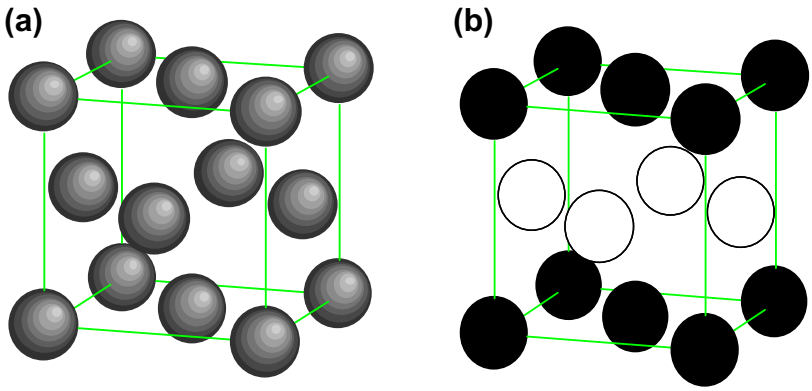

Figure 31 (a) FCC unit cell and (b) the $L1_0$ unit cell based on the FCC unit cell.

assuming random mixing on the $L1_o$ sublattice sites within a conventional fcc unit cell. See **Figure 31**. These can be then be transposed to the k-space representation as follows:

$$F_m(c,\eta) = Nc(1-c)[V(0)] - \frac{N\eta^2}{4}V(k_0) + \text{entropic terms} \tag{60}$$

where $k_0 = 2\pi a_3^*$ and $V(0) = 12V + 6U$ and $V(k_0) = -4V + 6U$. This model based on a rigid cubic lattice will lead to a second-order/higher order A1 $\rightarrow$ $L1_0$ transition similar to the result arrived at in the classic work of Nix and Shockley (1938). Guggenheim in 1952 using a quasichemical approach and a tetrahedron approximation was able to capture the first-order character of the A1 $\rightarrow$ $L1_2$ transition within this precursor of the modern CVM. Interestingly, Larikov et al. (1975) asserted that the phase change is first order if changes in lattice dimensions are incorporated into the free energy functional within a modified Bragg–Williams model. If an elastic energy term deriving from the elastic relaxation stemming from the cubic to tetragonal transformation strain is grafted on to the free energy expression in Eqn (60) in the form $E_{\text{ELASTIC}} = -Ne^4\eta^4$ where e is an elastic strain coupling term which is a function of the transformation strain and elastic constants, the ordering transition becomes first order. (See Cheong and Laughlin, 1994).

8.2.5 Landau Theory of Phase Transformations

In the late 1930s, Landau (1937) proposed that all second order transitions (including the ferromagnetic to paramagnetic transition in iron) and many first order phase transitions such as atomic ordering in alloys can be characterized by one or more so-called generalized order parameters (η). The order parameter describes salient properties of an assembly of constituent particles, that is electrons, atoms, ions, spins, and changes systematically as a critical temperature T_c (at constant pressure), for example, is approached. The order parameter describes the evolution of the system in terms of measurable physical parameters and has an equilibrium value for a given set of relevant thermodynamic variables (T, P, E, H, …). The behavior of the order parameter in the vicinity of the critical point serves as a useful basis for classifying the nature of the phase transition/transformation. The order parameter η can be formulated to describe the

(1) magnetization of a ferromagnet
(2) polarization of a dielectric

(3) occupancy of sublattices in an alloy superstructure
(4) fraction of superconducting electrons in a metal and
(5) atomic displacements associated with structural phase changes

When normalized, $\eta = 0$ at high temperatures in the disordered state and becomes finite in the ordered state at low temperatures with $\eta \to 1$ as $T \to 0$.

The essential hypothesis of the Landau theory is that the free energy difference between the ordered ($\eta > 0$) and disordered states ($\eta = 0$), $G(\eta)$ can be expanded in a power series in the order parameter in the neighborhood of the critical point, that is, the free energy is assumed to be an analytic function of η in the vicinity of $\eta = 0$. Landau recognized that this may not be rigorously true but suggested that this would not affect the general character of the transformation arising in the model. Ginzburg, Levanyuk and Sobyanin (1987) quantified the region in which the expansion is not valid and showed that when long-range fields (electric, magnetic, strain) and interactions are involved, the region in which the Landau theory fails is small, of the order of a degree or two. Furthermore, it should be mentioned that Landau's phenomenological theory is essentially a "mean field" theory and basically a generalization of the Weiss molecular field theory approximation to ferromagnetism (Weiss, 1907).

Landau wrote the free energy difference

$$G(\eta) = G(\eta \neq 0) - G(\eta = 0)$$

between states of finite order parameter (ordered states) and states $\eta = 0$ (disordered states) as

$$G(\eta) = A\eta^2 + B\eta^3 + C\eta^4 + D\eta^5 + E\eta^6 + \ldots \tag{61}$$

where the coefficients $A,B,C, \ldots$ are generally functions of temperature (T) and pressure (P), that is, $A(T,P)$, $B(T,P)$, $C(T,P)$. At constant pressure, A can be taken as a linear function of temperature given by

$$A = a(T - T_0) \tag{62}$$

with B, C, essentially constants, in the first approximation. Importantly, the coefficient $A = a(T - T_0)$ is such that the parameter a is a positive constant for the case where the high-temperature phase is the high-symmetry phase. In general, symmetry considerations play an important role in analyses based on the Landau theory. The coefficient A clearly represents the curvature of the $G(\eta)$ versus η plot at $\eta = 0$ and changes sign at $T = T_0$. Furthermore, T_0 will be identified as an instability temperature wherein the high-temperature phase at $\eta = 0$ becomes thermodynamically unstable with respect to a low-temperature ordered phase.

When truncating the expansion beyond fourth order, namely,

$$G(\eta) = A\eta^2 + B\eta^3 + C\eta^4 \tag{63}$$

there are two broad classes of interest, namely, where $B = 0$ and $B \neq 0$. (Note: for $B = 0$ there are also two cases of interest, $C > 0$ and $C < 0$; however, for $C < 0$ we must include a sixth order term to keep the free energy positive at large values of the order parameter.)

For the case $B = 0$, $G(\eta)$ is an even function of η, that is

$$G(\eta) = G(-\eta) \tag{64}$$

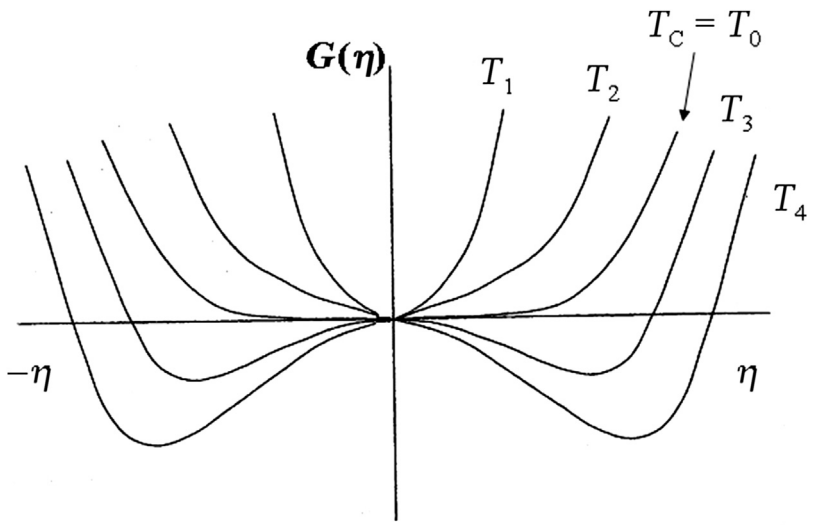

Figure 32 Gibbs free energy for the case of the Landau expansion with A and $C \neq 0$. At T_C the disordered phase becomes unstable. $T_1 > T_2 > T_C = T_0 > T_3 > T_4$. This represents a higher order transition.

and $A = a(T - T_0)$ changes sign at $T = T_0$. The behavior of $G(\eta)$ as a function of temperature and the variation of the order parameter with temperature are shown in Figure 32.

This is the signature of a SECOND-ORDER transition in the Landau theory. The equilibrium order parameter varies continuously from zero to a finite value on cooling through the transition or critical temperature $T = T_C = T_0$. (Note that the physical states of the system for $+\eta$ and $-\eta$ are essentially identical.) At equilibrium, for $T < T_C$, taking $\frac{\partial G}{\partial \eta} \equiv G_\eta = 0$ yields the following equation:

$$\eta = \left(\left(\frac{a}{2C}\right)(T_C - T)\right)^{\frac{1}{2}} \tag{65}$$

and inserting $\eta = 1$ at $T = 0$ K gives $\left(\frac{a}{2C}\right) = \frac{1}{T_C}$, leading to the well-known result

$$\eta = \left(\frac{(T_C - T)}{T_C}\right)^{\frac{1}{2}} = \left(1 - \frac{T}{T_C}\right)^{\frac{1}{2}} \tag{66}$$

which is identical to the result deriving from mean field approaches with a so-called critical exponent of $^1/_2$. This SECOND-ORDER or continuous transition is virtually identical to the behavior predicted by Ehrenfest (1933). In this case, $T = T_C = T_0 = T_i^-$, the critical temperature T_C can be identified with the parameter T_0 which is an instability temperature T_i^- for the disordered phase on cooling. Below $T_C = T_i^-$ small fluctuations about the disordered state ($\eta = 0$) experience no intrinsic thermodynamic restoring force and the free energy is monotonically decreasing to equilibrium ordered states $+\eta^*$ and $-\eta^*$ with the magnitude of η^* increasing continuously as T is decreased below T_C. At T_C, $G_\eta = 0$ and $G_{\eta\eta} = 0$ at $\eta = 0$, that is, just above or at $T = T_C$ finite fluctuations away from the disordered state ($\eta = 0$) lead to small changes in the free energy of the system and tend to appear profusely throughout

the system because of the flattening of the $G(\eta)$ versus η curve near $\eta = 0$, virtually as premonitory signaling of the phase transition. Just below the critical temperature T_C, minima appear in the free energy at small values of η and the free energy decreases monotonically to these equilibrium values.

This model describes the salient features of a second-order phase transition and the behavior of relevant thermodynamic properties of the system in a straightforward manner.

The difference in Gibbs free energy between the ordered state and disordered state, G_O is found by substituting the equilibrium value of η in 2.65 into 2.63 (with $B = 0$). One obtains

$$G_O = -\frac{a(T_C - T)^2}{2T_C} \tag{67}$$

The entropy S of the system varies continuously through the transition and the entropy change can be found from $S_O = -\frac{\partial G_O}{\partial T}$ as

$$S_O = -a\frac{(T_C - T)}{T_C} \tag{68}$$

The heat capacity relative to the disordered state at constant pressure is thus

$$\Delta C_P^O = T\left(\frac{\partial S_O}{\partial T}\right) = \frac{aT}{T_C}. \tag{69}$$

which produces a finite discontinuity in the heat capacity at $T = T_C$ equal to the coefficient a. See Figure 22.

Finally, the enthalpy difference H_O is equal to $= G_O + TS_O$:

$$H_O = \frac{a}{2}\frac{\left(T^2 - T_C^2\right)}{T_C} \tag{70}$$

This equation shows an absence of a latent heat of transformation at T_C. However, the slope of the variation of the order parameter η with temperature as $\eta \to 1$ at $T = 0$ K is negative in this mean field model, which is at variance with the predicted slope of zero according to the requirements of the Third Law of Thermodynamics.

The SECOND-ORDER transition behavior predicted earlier occurs very rarely in real materials. However, there is one important case that shows the earmarks of a textbook second-order transition, namely, the normal → superconducting transition in zero field (Stanley, 1971). Most phase transitions/transformations occurring in nature are FIRST ORDER according to Ehrenfest's thermodynamic classification and will be discussed subsequently, in detail, but there are important transitions in materials which are not FIRST ORDER or SECOND ORDER. For example, the magnetic transition in iron (Fe) at its Curie temperature (1041 K)—paramagnetic→ferromagnetic transition—is at least third order (Pippard, 1966). The specific heat of many ferromagnets in the vicinity of the Curie temperature (T_C) exhibits singular behavior quite different than predicted for a second-order transition as discussed earlier. Similarly, a number of ordering transitions and superlattice formation in alloys which are clearly not first-order transitions show similar behaviors, for example the A2 → B2 ordering in Cu–Zn alloys (β-brass). See Figure 24. Indeed, the classic Weiss molecular approach to the magnetic transition in iron (Fe) and the Bragg–Williams approach to superlattice formation are mean field theories and predict second-order behavior. The complexities of the behavior near the critical temperature for these

transitions which are neither first or second order are lumped into a category called HIGHER ORDER or λ-TRANSITIONS (the latter description based on the shape of the specific heat near T_C, see **Figure 24**) circumventing the need to differentiate discontinuities in third, fourth, and so on, derivatives of the free energy functional. The complex behavior mentioned earlier derives from short-range ordering effects, correlations and fluctuations near the critical point and remains a challenge in modern statistical physics.

If in the Landau expansion the series is again truncated beyond fourth order, but we take $B < 0$ and $C > 0$ with $A = a(T - T_0)$ as above, we reveal another type of behavior of major importance—a FIRST-ORDER transition. In this case, A remains finite at $T = T_C$ and two minima appear at $\eta = 0$ and $\eta = \eta^*$, respectively. This situation represents two-phase equilibrium at T_C between a disordered phase ($\eta = 0$) and an ordered phase ($\eta = \eta^*$). This behavior is indicative of a FIRST-ORDER transition characterized by a discontinuous change in the entropy (S) and enthalpy (H) at the transition temperature T_C associated with a latent heat ΔH_t and $\Delta S_t = \Delta H_t / T_C$. For $T < T_C$, a minimum in the free energy develops with increasing order parameter as the temperature is decreased. A single-phase ordered state becomes the thermodynamically preferred state of the system with the order parameter continuously increasing toward unity after the discontinuous jump at $T = T_C$. See **Figure 33**.

Note also that the free energy functional $G(\eta)$ is no longer an even function of η, that is, $G(\eta) \neq G(-\eta)$ for this case, that is, it is an odd function of η.

This thermodynamic analysis has implications regarding the possible mechanisms of the ordering transformation. Here we see in this FIRST-ORDER case that at the higher temperature regime $T \leq T_C$ there is local maximum between the equilibrium ordered state $\eta = \eta^*$ and the disordered state $\eta = 0$ including $T = T_C$. This represents an intrinsic thermodynamic restoring force within the disordered state with respect to small fluctuations away from the disordered state $\eta = 0$; that is, relatively small fluctuations tend to be damped or decay, thus to trigger the transformation, a relatively large fluctuation away from the initial state is required which releases free energy and allows the system to seek the lower free energy equilibrium ordered state. This is not the nucleation barrier Δg^*, per se to form the ordered

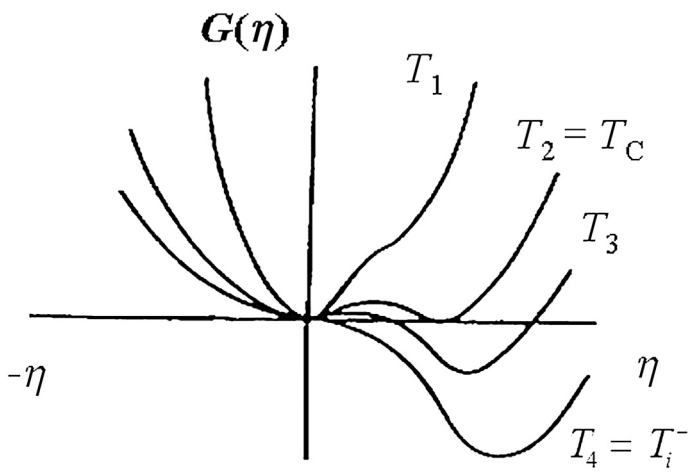

Figure 33 Gibbs free energy for the case of the Landau expansion with A, B and $C \neq 0$. At $T_2 = T_C$ the disordered phase has the same free energy as an ordered phase. At T_3 an ordered phase is stable. At T_0, if the disordered phase is retained it becomes unstable with respect to ordering. This represents a first-order transition. Here, $T_1 > T_2 = T_C > T_3 > T_i^-$.

state but a thermodynamic condition which imposes a requirement that the ordered state can only be achieved by large fluctuations away from $\eta = 0$—a nucleation event. At a temperature $T = T_0 = T_i^- < T_C$, the local maximum disappears and the free energy $G(\eta)$ versus η curve is monotonically decreasing away from $\eta = 0$ rendering the disordered state thermodynamically unstable with respect to the equilibrium ordered state $\eta = \eta^*$. It can be shown that

$$T_C - T_i^- = \frac{B^2}{4aC} \tag{71}$$

for this case.

This thermodynamic instability appearing when the system is displaced far from equilibrium suggests that the kinetic behavior will mimic the second-order/higher order transition whereby it is possible that ordering will occur continuously or homogeneously throughout the undercooled system without the initial partitioning of the system into transformed and untransformed regions, as is the case for nucleation and growth processes. In the special case of atomic ordering and superlattice formation in alloys this involves uniformly occurring preferential atomic jumping into sites which locally increase the order parameter.

Another case of interest involves the symmetrical FIRST-ORDER behavior wherein $A = a(T - T_0)$, $B = 0$, $C < 0$, $D = 0$ and $E > 0$; that is, the $G(\eta)$ functional is symmetric about $\eta = 0$ with two phases in thermodynamic equilibrium at $T = T_C$ and $T_0 = T_i < T_C$. See **Figure 34**.

As above, only the quadric term is given a temperature dependence and $C < 0$ and $E > 0$ are taken as constants. The sixth order term insures the proper thermodynamic behavior at low temperatures yielding real solutions for the order parameter. This specific behavior would apply to the A1(fcc) → $L1_0$ superlattice formation in equiatomic AB alloys (Cheong and Laughlin, 1994).

The Landau approach is increasingly entering the metallurgical phase transformation literature and providing valuable insight in various contexts. For example, it was argued for a number of years that the well-known BCC → ω-phase transformation in Zr-base and Ti-base alloys might be second/higher order. However, since the atomic displacement (which is the order parameter in this case) characterizing the transformation produces different structures for $\eta+$ versus $\eta-$ (atomic displacements in opposite directions), the free energy functional $G(\eta)$ is an odd function and therefore the transition is first order (de Fontaine, 1973). In the materials field, in general, the Landau theory has been a particularly valuable tool in the area of ferroelectric behavior and in analyzing certain displacive transformations (International Tables for Crystallography, 2006). Finally, as mentioned earlier, symmetry considerations and restrictions emerge quite naturally in the Landau theory and one important result is that if the transformation is second order or continuous, the symmetry group of the low-temperature phase must be a subgroup (lower symmetry) of the group of the high-temperature phase.

8.2.6 Surface Energy and Capillarity Effects

A wide variety of effects related to surface or interfacial (free) energy and interface curvature play a central role in phase transformations and microstructural development. These effects include most prominently the nucleation and growth of phases, coarsening and the shape and distribution of phases in polyphase materials. The term capillarity refers to a composite of phenomena related to the energetics and kinetic behavior of surfaces and interfaces and their role in fundamental processes governing the evolution of material structure during processing and heat treatment. (The term surface is sometimes used to refer strictly to the boundary between a condensed phase and a vapor phase, whereas the

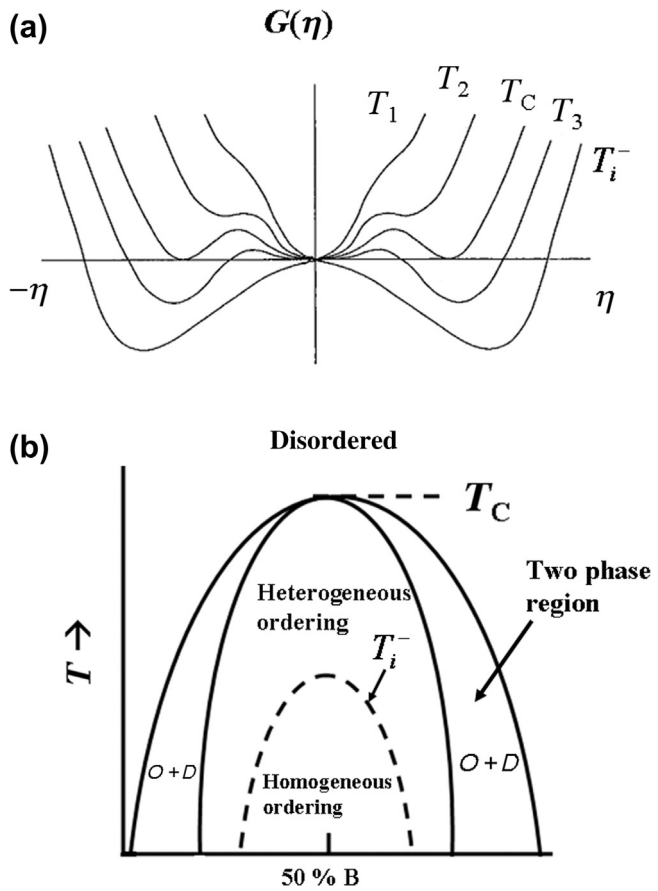

Figure 34 (a) Gibbs free energy for the case of the Landau expansion with A, C and $E \neq 0$, but $C < 0$. At T_C the disordered phase is in equilibrium with an ordered phase ($|\eta| \leq 1$). The disordered phase becomes unstable with respect to ordering at T less than or equal to T_i^-. This is the case of a symmetrical first-order transition. In the figure $T_1 > T_2 > T_C > T_3 > T_i^-$. (b) Schematic of the phase diagram that corresponds to the free energy curves of the 50%B plot in 34a. Note the region of homogeneous/spinodal ordering below T_i^-.

term interface is considered more general, referring to the region of contact between any two phases as well as grain boundaries within a single-phase polycrystalline solid. However, these terms are more often than not used synonymously in the literature and textbooks.)

Surface energy and interfacial effects are of paramount importance when the surface area-to-volume ratio of a phase is relatively large and/or when the interface has a large curvature. Generally, the effects of surface energy and curvature derive from the fact that the atomic environments of the atoms at an interface are different than those residing in the bulk phase. As a result, the energy of the surface atoms can be quite different than those located in the bulk and, indeed, the energy to add an atom to a surface or boundary location is generally higher than adding an atom to the bulk; this is essentially the origin of surface or interfacial energy as an *excess thermodynamic quantity* and is often described in terms of unsaturated/dangling bonds or perturbed electronic charge density.

When discussing the energetics and properties of interfaces three terms arise which must be carefully distinguished and understood. The *surface (free) energy* (σ) is the quantity associated with the reversible work required to create a unit area of new surface under prescribed thermodynamic constraints. If the area of an existing surface is increased by an increment dA, σdA is the surface work expended as the surface is extended without changing the nature or intrinsic structure of the surface. The *surface tension* (γ) and *surface stress* (f_{ij}) relate to forces acting within an interface resisting stretching the surface layer and which determine the forces against which work must be expended in extending the surface; the surface tension and surface stress essentially act as restoring forces resisting stretching the surface or interface. Importantly, the surface stress (f_{ij}) generally is a second rank tensor quantity describing the plane stress state of the surface or interface and the surface tension (γ) can be viewed as the average of the surface stresses in two mutually perpendicular directions within the surface. The surface stress at any point in a surface is the force acting across a line which passes through this point in the limit as the line length goes to zero. The surface (free) energy (σ) is a scalar quantity which has the same fundamental units as the surface stress and surface tension (J m^{-2}/N m^{-1}/ergs cm^{-2}/dyne cm^{-1}) and for liquids (which are isotropic) $\sigma = \gamma$, that is, the surface free energy and the surface tension of liquids are identical in the absence of adsorption or desorption effects. An important feature of the liquid state is that atoms have sufficient mobility to rearrange themselves during the extension of the surface maintaining a constant surface structure which is not necessarily the case for a crystalline solid. Furthermore, for crystalline solids, which are generally anisotropic, σ varies with orientation and the equilibrium shape of a crystal is found to be nonspherical, as discussed more fully subsequently. In the following brief review of the thermodynamics of interfaces we will emphasize the role of the specific interfacial free energy σ associated with a surface, internal interface or interphase interface and will neglect any adsorption/desorption effects.

Let us now briefly elucidate the relationship between surface (free) energy σ and the surface stress f (f_{ij}) in a more fundamental thermodynamic approach. The presence of a surface or interface of area A in a system contributes an excess Gibbs free energy $G^s = \sigma A$. If we now extend the surface at constant T and P by an amount dA, there can be two contributions to the surface work required as follows:

$$\mathrm{d}G^S = \mathrm{d}(\sigma A) = \sigma \mathrm{d}A + A\mathrm{d}\sigma \tag{72}$$

where the term σ dA is simply the increase in free energy due to the new interfacial area created maintaining a constant interface structure or constant σ in the process, whereas the second term, Adσ, allows that an existing surface may be strained or distorted thereby modifying σ. We can use this result to define the surface stress f as

$$\begin{aligned} dG^S &= f dA = \sigma dA + A d\sigma = \sigma dA + A\frac{d\sigma}{dA}dA \\ f &= \sigma + A\frac{d\sigma}{dA} \end{aligned} \tag{73}$$

or, more rigorously,

$$f_{ij} = \sigma\delta_{ij} + \frac{\partial\sigma}{\partial\varepsilon_{ij}} \tag{74}$$

wherein $\mathrm{d}A = A\delta_{ij}d\varepsilon_{ij}$ and $d\varepsilon_{ij}$ is a surface elastic strain tensor (assuming the modification of σ derives from elastic distortion of the surface structure). For a crystal surface with threefold or higher rotational symmetry the normal stresses within the surface are equal and no shear stresses act within the surface.

This follow from Hermann's theorem, which states that "…if an r rank tensor has an N fold symmetry axis and $r < N$, then this tensor also has a symmetry axis of infinite order along N." (Hermann, 1934; Sirotin and Shaskolskaya, 1982). Thus the property is isotropic in the plane perpendicular to N.

Therefore, when the surface stress is isotropic it can be taken as a scalar quantity wherein

$$f - \sigma = \frac{\mathrm{d}\sigma}{\mathrm{d}e} \tag{75}$$

and $e = \dfrac{\mathrm{d}A}{A}$ is an elastic strain within the surface. Only when $\dfrac{\mathrm{d}\sigma}{\mathrm{d}e} = 0$ does the surface (free) energy σ equal the surface stress f (Howe, 1997; Trivedi, 1999).

The most straightforward thermodynamic definition of σ can be written as

$$\sigma = \left(\frac{\mathrm{d}W}{\mathrm{d}A}\right)_{T,P,n_i} = \left(\frac{\mathrm{d}W}{\mathrm{d}A}\right)_{T,V,n_i} \tag{76}$$

where $\mathrm{d}W$ is the reversible surface work required to increase the surface area(A) of a surface or interface by an amount $\mathrm{d}A$ at constant T,P or T,V in a thermodynamic system at constant composition (n_i). From the fundamental relationships for reversible changes in the Gibbs (G) and Helmholtz (F) free energies:

$$\mathrm{d}G = -S\mathrm{d}T + V\mathrm{d}P + \sigma\mathrm{d}A + \sum_i \mu_i \mathrm{d}n_i \tag{77}$$

and

$$\mathrm{d}F = -S\mathrm{d}T - P\mathrm{d}V + \sigma\mathrm{d}A + \sum_i \mu_i \mathrm{d}n_i \tag{78}$$

we can also write

$$\sigma = \left(\frac{\partial G}{\partial A}\right)_{T,P,n_i} = \left(\frac{\partial F}{\partial A}\right)_{T,V,n_i} \tag{79}$$

where σ is viewed as a specific interfacial free energy associated with an excess free energy stemming from the presence of surfaces or interfaces. Sometimes when dealing with processes unfolding at constant T,V and μ_i (such as nucleation) the surface (free) energy can be defined as

$$\sigma = \left(\frac{\mathrm{d}W}{\mathrm{d}A}\right)_{T,V,\mu_i} \tag{80}$$

which will be discussed subsequently. Finally, in a crystalline solid, σ can be highly anisotropic varying markedly with the crystallographic direction of the normal to the crystal plane in question. This anisotropy is readily illustrated using the well-known polar plot shown in **Figure 35**. The polar plot can be used to establish the equilibrium shape of a crystal through the Gibbs–Wulff construction as discussed later in this section.

Let us now consider a closed thermodynamic system (constant composition) at equilibrium composed of two phases α and β at constant T, V and uniform chemical potentials μ_i; the β phase is in the form of a small sphere of radius r embedded in the α phase and the α–β interface is characterized by a specific surface or interfacial free energy σ (assumed to be isotropic). See **Figure 36**. If a small virtual

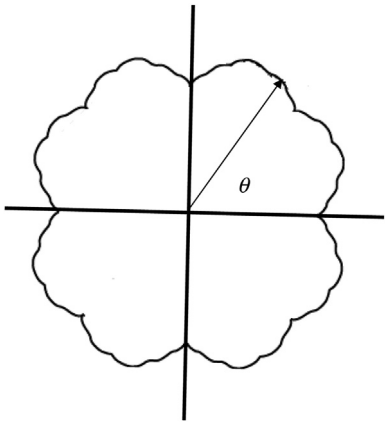

Figure 35 Schematic polar plot of a crystal with a fourfold axis of symmetry perpendicular to the plane of the diagram. After Christian (2002).

reversible displacement of the interface occurs expanding normal to itself into the α phase, the change in Helmholtz free energy is given by:

$$\mathrm{d}F = -S\mathrm{d}T - P^{\alpha}\mathrm{d}V^{\alpha} - P^{\beta}\mathrm{d}V^{\beta} + \sigma\mathrm{d}A + \sum_i \mu_i \mathrm{d}n_i \tag{81}$$

where $\sigma \mathrm{d}A$ is the reversible surface work expended in the operation. Under isothermal ($\mathrm{d}T = 0$) and isochoric ($\mathrm{d}V = \mathrm{d}V^{\alpha} + \mathrm{d}V^{\beta} = 0$) conditions, at constant composition ($\mathrm{d}n_i^{\alpha} = -\mathrm{d}n_i^{\beta}$) and uniform chemical potential of all species $\mu_i^{\alpha} = \mu_i^{\beta}$ at equilibrium $\mathrm{d}F = 0$ and it follows that

$$P^{\beta} - P^{\alpha} = \sigma \frac{\mathrm{d}A}{\mathrm{d}V^{\beta}} \tag{82}$$

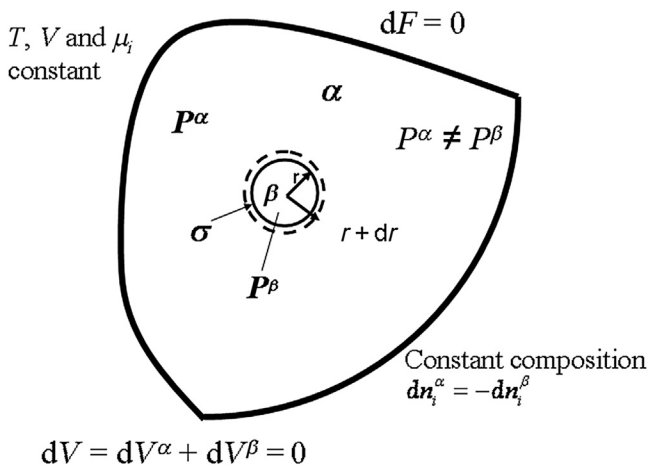

Figure 36 Small spherical β phase particle of radius r in equilibrium with the matrix α. A thermodynamic analysis of the α/β equilibrium shows that $P^{\beta} - P^{\alpha} = \frac{2\sigma}{r}$ where σ is the interfacial free energy.

Since for a spherical surface $\frac{dA}{dV^{\beta}} = \frac{2}{r}$ we find that

$$P^{\beta} - P^{\alpha} = \frac{2\sigma}{r} \tag{83}$$

that is, under equilibrium conditions there is a pressure difference across the α–β interface with $P^{\beta} > P^{\alpha}$. This is the famous Laplace equation which can be generalized for an arbitrary interface wherein locally

$$P^{\beta} - P^{\alpha} = \sigma \frac{dA}{dV^{\beta}} = \sigma\left(\frac{1}{r_1} + \frac{1}{r_2}\right) \tag{84}$$

where r_1 and r_2 are the local principal radii of curvature at a point defined within two orthogonal planes intersecting the surface at that point. See **Figure 37**. This is a fundamental result of the thermodynamics of capillarity theory.

The Laplace equation can be used to derive the important Gibbs–Thomson relation using the thermodynamic relation $d\mu_T = VdP$. Consider the α phase in the preceding discussion to be the vapor phase in equilibrium with a condensed phase (solid or liquid) β for a single-component system.

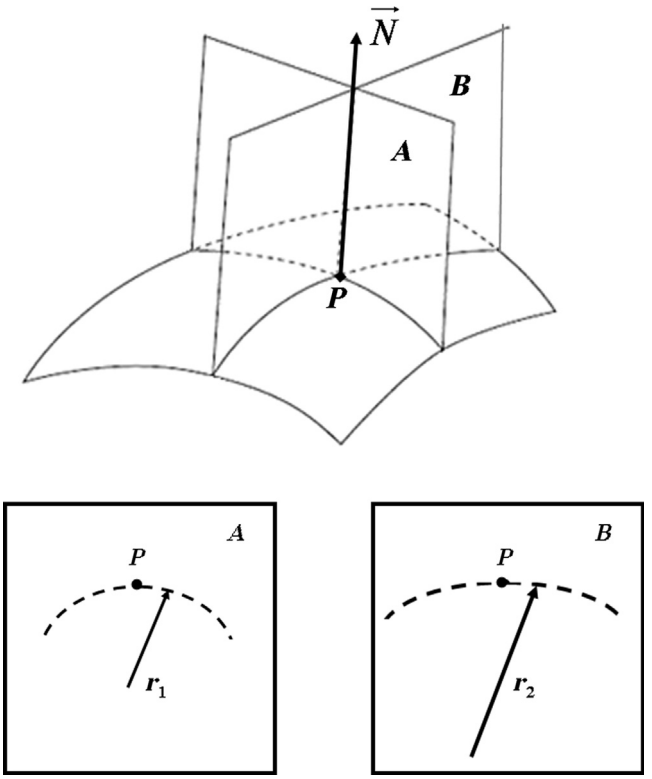

Figure 37 Principal radii of curvature of a surface element defined in two orthogonal planes *A* and *B* passing through the point *P* with local normal $\vec{N}$.

The change in chemical potential of the β phase as a result of the pressure change at constant temperature within the sphere compared with P_0, the equilibrium vapor pressure in equilibrium with β across a flat or plane interface is

$$\mu^{\beta}\left(T, P^{\beta}\right) - \mu^{\beta}(T, P_0) = \int_{P_0}^{P^{\beta}} V^{\beta} \mathrm{d}P \tag{85}$$

where V^{β} is the molar volume of the β phase and $P^{\beta} = P^{\beta}(r)$ according to the Laplace equation. To maintain thermodynamic equilibrium the vapor pressure will change from P_0 to $\mathrm{P}^{\alpha}(r) = P(r)$. Using the approximation $\int_{P_0}^{P^{\beta}} V^{\beta} \mathrm{d}P \approx V^{\beta} \Delta P$ with $\Delta P = \mathrm{P}^{\beta} - P_0 \sim \mathrm{P}^{\beta} - P$ since $(P^{\beta} - P) >> (P - P_0)$, we can now derive the vapor pressure $P^{\alpha}(r) = P(r) = P$ in equilibrium with the small particle or droplet as a function of the size (r) of the β phase. Since $\mu^{\beta}\ (T, P^{\beta}) - \mu^{\beta}\ (T, P_0) = \mu^{\alpha}(T, P) - \mu^{\alpha}(T, P_0)$ it follows that

$$\mu^{\alpha}(T, P) - \mu^{\alpha}(T, P_0) = RT \ln \frac{P(r)}{P_0} = \frac{2\sigma V^{\beta}}{r} \tag{86}$$

after inserting $(P^{\beta} - P_0) \sim (P^{\beta} - P) = \dfrac{2\sigma}{r}$ from the Laplace equation. This is a version of the Gibbs–Thomson equation which derives from the influence of the capillarity pressure $(P^{\beta} - P^{\alpha})$ across the curved interface.

Importantly, if we are dealing with solutions of condensed phases (solid or liquid), the change in chemical potential of a species i within the β phase resulting from interface curvature can be viewed to first order as a change in free energy $\Delta P \overline{V_i}$ where $\overline{V_i}$ is the partial molar volume of the component i in solution and ΔP is the capillarity pressure as above. Thus, the change in chemical potential of i in solution in the condensed β phase beneath the curved interface can be written as

$$\mu_i^{\beta}(r) = \mu_i^{\beta}(\infty) + \frac{2\sigma \overline{V_i}}{r} \tag{87}$$

where $\mu_i^{\beta}(\infty)$ is the chemical potential i beneath a planar interface $(r = \infty)$ and $\mu_i^{\beta}(r)$ is the chemical potential of i within the small spherical β phase of radius r. This is just another version of the Gibbs–Thomson equation. When the two phases α and β are in equilibrium separated by a planar interface $\mu_i^{\beta}(r) = \mu_i^{\alpha/\beta(\infty)}$ whereas with β in the form of a small spherical particle $\mu_i^{\beta}(r) = \mu_i^{\alpha/\beta(r)}$ where $\mu_i^{\alpha/\beta(\infty)}$ and $\mu_i^{\alpha/\beta(r)}$ are the chemical potentials of i in the α phase in equilibrium with the β phase across a planar interface and a curved interface, respectively. (Note that when $r >> 2\sigma \overline{V_i}$ capillarity effects are unimportant and bulk thermodynamics prevails.)

Let us look at the influence of capillarity effects on the liquid → solid transformation in a single-component system, for example the melting of a pure metal at ambient pressure. The thermodynamics of the transition can be represented graphically in a G vs. T (molar free energy versus temperature) plot shown in Figure 38. The melting temperature T_{m} of the bulk solid phase is the intersection of the free energy curves for the bulk solid and liquid phases where $G^L = G^S$ (molar free energies of the bulk liquid and solid phases, respectively). Now consider an equilibrium between

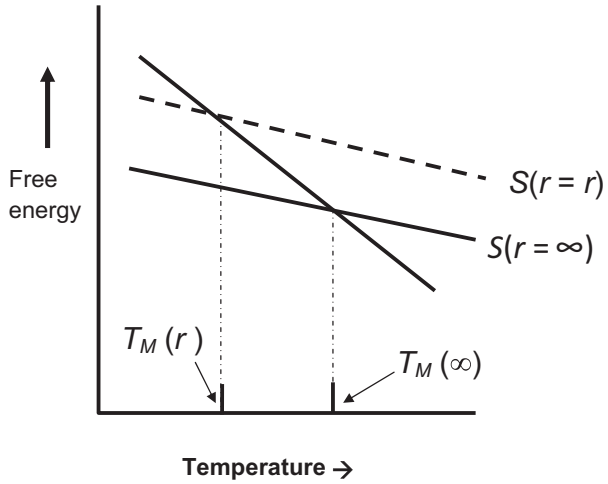

Figure 38 Schematic of free energy vs. temperature curve for the liquid phase and a large solid particle and a small solid particle (dotted line, showing that T_M is lowered).

a small spherical crystallite of radius r with the bulk liquid phase. The molar free energy (chemical potential) of the solid is now altered by capillarity and is a function of size given by $G^S(r) = G^S(\infty) + \frac{2\sigma_{S-L}V^S}{r}$ where the notation (∞) refers to the bulk solid. Clearly this Gibbs–Thomson effect modifies the equilibrium between liquid and solid raising the curve for the solid phase and a melting temperature $T'_m(r)$ defined by $G^S(r) = G^L = G^L(\infty)$ is established effectively lowering the melting point of the small crystallite compared with that of the bulk solid. This lowering of the melting point of the small crystallite contains the seeds of a Gibbsian capillarity-based nucleation theory. Indeed, the small crystallite is in unstable equilibrium with the bulk liquid having an equal probability of growing or melting at the temperature $T_M(r)$ and size r. This concept will be explored more fully in Section 8.4 of this chapter on nucleation.

Let us consider a two-phase mixture in the simple binary phase diagram shown in Figure 39 and the corresponding free energy vs. composition (X) diagram at a temperature T_A. The common tangent construction depicted in Figure 39b establishes the equality of the chemical potentials of the components A and B in the conjugate α and β phases in thermodynamic equilibrium. We consider that the dispersed phase (β) is essentially a nearly stoichiometric compound phase existing over a very restricted composition range (as indicated in the phase diagram) about the composition A_aB_b; the α matrix phase is a solid solution with appreciable solid solubility of B in A. Again the notation (∞) will be used to denote bulk phases or equilibrium in the absence of capillarity effects. We assume that the overall composition of the alloy X_0 is in the two phase field and that the β phase essentially has a composition of X_0^β which remains unchanged when capillarity pressure effects are present at small particle sizes. The dispersed β phase in the α matrix is assumed to be in the form of small spherical particles on the submicron/nanoscale and are of uniform size with radius r; the α–β interface is characterized by an interfacial (free energy) $\sigma_{\alpha\beta}$ (isotropic). In Figure 40 the common tangent construction shows the change in the composition of the α matrix in equilibrium with the β phase from

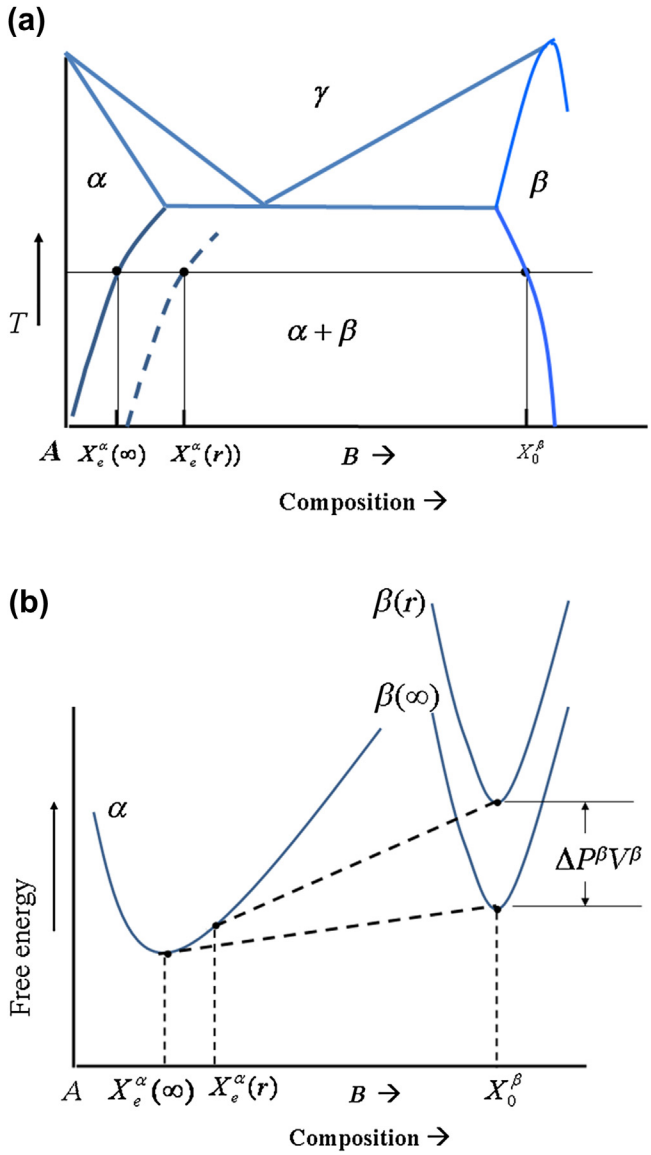

Figure 39 (a) Binary *A–B* phase diagram showing equilibrium between a precipitate phase β (A_aB_b) in a form of small particles and a matrix phase α. This schematic shows the change in solvus for small particles vs. equilibrium between bulk phases α and β. (b) Free energy composition curves for the α/β equilibrium in Figure 39a showing the effect of capillarity on the solid solubility.

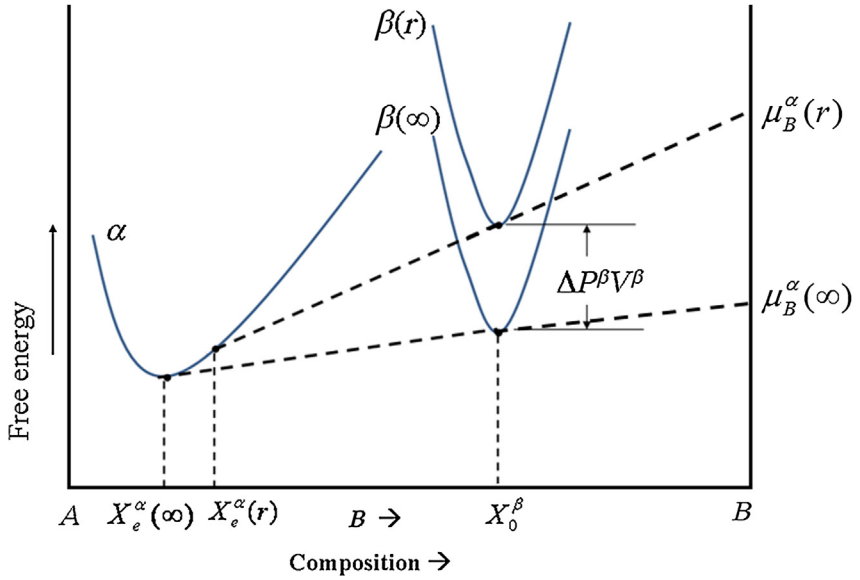

Figure 40 Influence of capillarity on the equilibrium between two phases α (matrix) and β (precipitate) for the general case wherein the capillarity effects change the equilibrium composition of the matrix and precipitate phases.

$X_e^\alpha(\infty)$ to $X_e^\alpha(r)$ as a result of the change in pressure within the β phase resulting from the small particle size. From construction, this change in solid solubility with particle size can be approximated as follows:

$$\frac{\Delta P^\beta V^\beta}{\left[X_0^\beta - X_e^\alpha(\infty)\right]} = \frac{RT \ln\left[\dfrac{X_e^\alpha(r)}{X_e^\alpha(\infty)}\right]}{\left[1 - X_e^\alpha(\infty)\right]} \tag{88}$$

and since $\Delta P^\beta V^\beta = \dfrac{2\sigma_{\alpha\beta}}{r}$

$$RT \ln\left[\frac{X_e^\alpha(r)}{X_e^\alpha(\infty)}\right] = \left(\frac{2\sigma_{\alpha\beta}}{r}\right) \frac{\left[1 - X_e^\alpha(\infty)\right]}{\left[X_0^\beta - X_e^\alpha(\infty)\right]} \tag{89}$$

where V^β is the molar volume of the β phase. This Gibbs–Thomson equation is an excellent approximation assuming $[(X_e^\alpha(r) - X_e^\alpha(\infty))]$ is small and that the relevant activity coefficients do not change significantly over this composition range. This Gibbs–Thomson effect essentially defines a new size-dependent solvus as depicted in Figure 39a. The two-phase equilibrium can be generalized to the case where the β phase is a solution phase and this is depicted in Figure 40; now the composition of the dispersed phase in equilibrium with the α matrix can change when the capillarity pressure shifts the free energy–composition curve and a new common tangent is established. This can be worked out analytically as well when the change in chemical potential of the β phase associated with this change in composition is properly taken into account in addition to the change in pressure within the small particles.

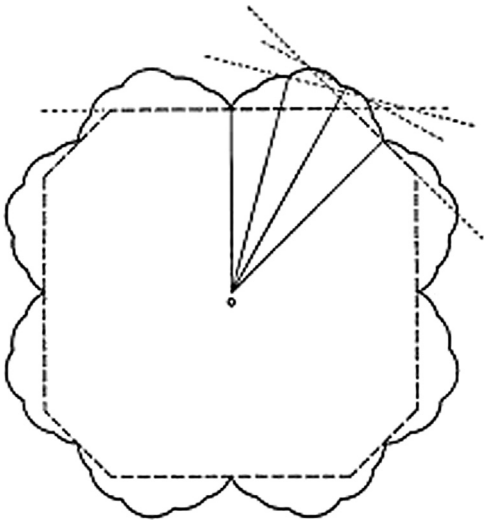

Figure 41 Wulff construction using the surface free energy polar plot. The inner envelope of the perpendiculars to the vectors drawn to each point on the plot gives rise to the equilibrium shape of the crystal. After Christian (2002).

In our preceding discussion we have briefly mentioned that the surface (free) energy σ of a crystalline solid can be highly anisotropic, that is, the energy of the $\{111\}$ faces can have a very different energy than the $\{100\}$ or $\{110\}$ faces in a cubic crystal. This is illustrated in the $\sigma(\mathbf{n})$ versus $\mathbf{n}$ plot where $\mathbf{n}$ is the normal to a crystallographic plane in the material and the distance from the origin in this polar plot (the magnitude of $\mathbf{n}$) is proportional to the value surface energy characterizing the particular plane; this so-called Gibbs–Wulff construction has the property that a radius vector $\mathbf{n}$ locates a point on the locus generated and the tangent plane normal to the radius vector at that point is an image of the crystal plane—the Wulff plane. Thus, one generates an envelope of Wulff planes as a function of $\mathbf{n}$ and the *inner envelope* can be shown to form a figure which minimizes the surface energy $\int \sigma dA$ and defines the equilibrium shape of the crystal. See Figure 41. Depending on the nature of the Wulff plot the crystal can be bounded by continuously curved regions or extended flat regions. In general, cusps in the $\sigma(\mathbf{n})$—plot result in finite flat regions.

The equilibrium shape can be used to formulate a generalized Gibbs–Thomson equation based on the construction shown in Figure 42. It is found that the parameter $\sigma(\mathbf{n})/\lambda(\mathbf{n})$ is an invariant of the equilibrium shape where $\lambda(\mathbf{n})$ is the normal distance defined in the two-dimensional representation. This condition insures that the capillarity pressure difference across all surface elements of the equilibrium shape is the same and thus the chemical potential is invariant along the surfaces and faces defining the equilibrium shape of the crystal (Johnson, 1965).

The anisotropy of the surface energy of a crystal can be understood structurally in terms of "broken bonds" associated with so-called terrace, ledge and kink densities for a general orientation as depicted in Figure 43. Certain atomic configurations will minimize the surface free energy for an arbitrary orientation and distorting these surface structures during stretching contributes to the relationship between surface stress and surface energy discussed earlier. Furthermore, the orientation dependence of $\sigma = \sigma(\boldsymbol{\theta})$ where $\boldsymbol{\theta}$ is an orientation parameter can lead to a significant torque acting on a surface tending to rotate the surface plane to a new orientation of lower energy. As a consequence of the orientation dependence of σ nominally flat surfaces can break up into two or more prominent areas of low-index planes called

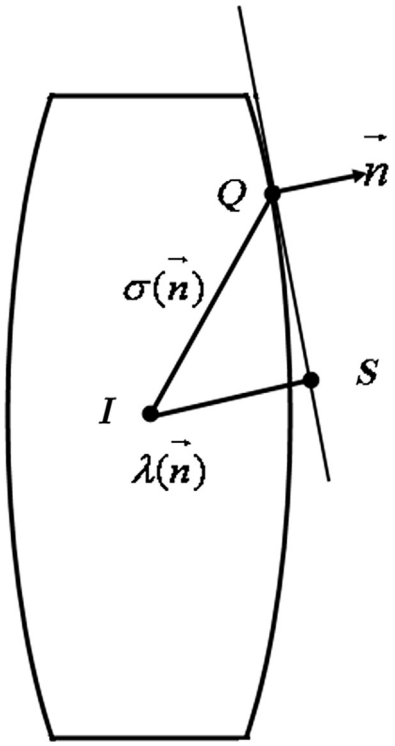

Figure 42 Schematic of generalized Gibbs–Thomson relation defining the vectors **n** and λ (**n**) with respect to the plane S. The parameter σ(**n**)/λ(n) is a constant along the locus defining the equilibrium shape. After Johnson (1965).

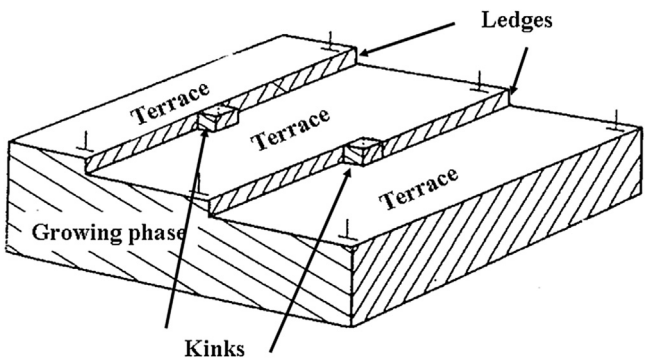

Figure 43 Terrace–Ledge–Kink (TLK) representation of a typical crystal interface.

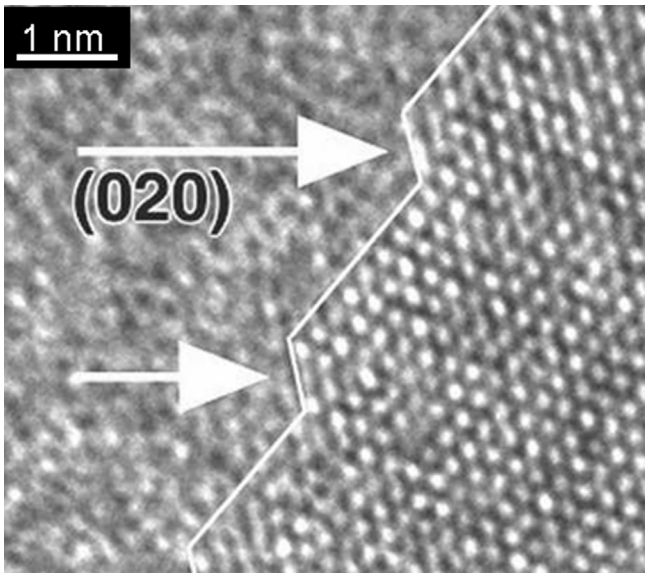

Figure 44 HREM image of facets between a product and parent phase. After Yanar et al. (2002).

Table 1 Typical surface energies in materials (metallic)

Liquid–solid	100–2000 erg cm^{-2} = mJ m^{-2}
Vapor–solid	500–3000 erg cm^{-2} = mJ m^{-2}
Solid–solid	
Coherent	10–200 erg cm^{-2} = mJ m^{-2}
Semicoherent	200–400 erg cm^{-2} = mJ m^{-2}
Incoherent	400–1000 erg cm^{-2} = mJ m^{-2}
Grain boundary	400–600 erg cm^{-2} = mJ m^{-2}

facets which can markedly lower the overall surface energy even though the surface area is increased. This occurs readily at higher temperatures where atomic transport is rapid. See **Figure 44**. This behavior is described most clearly using the so-called inverse σ-plot ($1/\gamma$ plot; Meijering, 1963b).

Table 1 shows a compilation of typical surface energies for various types of interfaces relevant to our discourse on phase transformations in subsequent sections. Note that solid–liquid interfacial energies (σ_{S-L}) are typically in the range 100–2000 erg cm^{-2} whereas solid–solid interphase interfacial or surface energies ($\sigma_{\alpha\beta}$) can range from 10 to 1000 erg cm^{-2} depending on the degree of coherency or crystallographic matching.

In describing the thermodynamics of interphase interfaces Gibbs (1875, ff) pointed out that the density, energy, entropy, and so on, of the individual phases in contact are not likely to be uniform up to the plane of contact resulting in a sharp discontinuity of thermodynamic properties. Cahn and Hilliard (1958, 1959) in their generalized treatment of the thermodynamics of inhomogeneous systems formulated a thermodynamic treatment of a diffuse interface characterized by a transition layer as shown in **Figure 45** in contrast to the so-called sharp interface. The composition and free energy in the interfacial region are considered to be continuous functions through transition region. The free

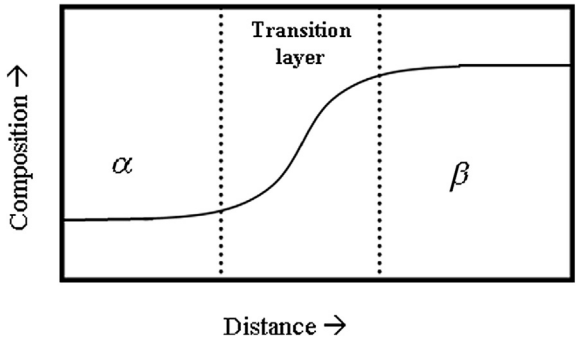

Figure 45 Schematic of composition vs. distance plot through an interphase interface showing the transition layer.

energy of the two-phase system incorporating the energetics of the transition layer can be written as

$$G = An_V \int_{-\infty}^{+\infty} \left\{ g(C) + \kappa \left(\frac{\mathrm{d}C}{\mathrm{d}x} \right)^2 \right\} \mathrm{d}x \tag{90}$$

where n_V is the number of atoms/molecules per unit volume and $g(C)$ is the free energy per atom/molecule of a homogeneous solution of composition C; the second term $\kappa \left(\frac{\mathrm{d}C}{\mathrm{d}x} \right)^2$ associated with the local gradient in composition is called the gradient energy with the gradient energy coefficient κ assumed to be a constant. (This term derives from a truncated Taylor expansion of the free energy functional.) The surface free energy per unit area is calculated by subtracting from this expression the free energy of the inhomogeneous system the free energy that it would have if the phases actually were homogeneous up to a fiducial sharp interface. This leads to an expression for the surface free energy σ (per unit area) given by

$$\sigma = n_V \int_{-\infty}^{+\infty} \left\{ \Delta g(C) + \kappa \left(\frac{\mathrm{d}C}{\mathrm{d}x} \right)^2 \right\} \mathrm{d}x \tag{91}$$

where $\Delta g(C) = g(C) - [(1 - C)\mu_A^e + C\mu_B^e]$ with μ_A^e and μ_B^e being the equilibrium chemical potentials of species A and B in the two phases. Clearly the $\Delta g(C)$ term is an excess free energy stemming from the species being at nonequilibrium compositions with respect to the bulk phases in crossing the interfacial region. This interfacial free energy functional is a minimum when $\Delta g(C) = \kappa \left(\frac{\mathrm{d}C}{\mathrm{d}x} \right)^2$ which produces a sigmoidal composition profile through the interface. The interfacial free energy with a change in the variable of integration can alternatively be written as

$$\sigma = 2n_V \int_{C_\alpha}^{C_\beta} [\kappa \Delta g(C)]^{\frac{1}{2}} \mathrm{d}C \tag{92}$$

For further details of this continuum description of a coherent interface the reader is directed to the seminal papers of Cahn and Hilliard cited earlier and to the text of Howe (1997). Importantly, this approach to interphase interfaces is central to our modern understanding of spinodal decomposition

which will be treated, in detail, in subsequent sections. It also has proven very useful in the modeling of microstructural evolution using the phase field approach.

8.3 Rate Processes in Solids

8.3.1 Basic Concepts

During the latter part of the nineteenth century a number of scientists became interested in the fundamental phenomena governing the rate of chemical reactions. This was a time when thermodynamics and the kinetic theory of gases were reaching maturity along with a developing statistical mechanics and the emergence of physical chemistry as a scientific and academic discipline. The Dutch chemist van't Hoff in 1884 presented a treatise on reaction rates (Etudes de dynamique chimique). He asserted that a wide variety of chemical reactions showed a temperature dependence described by an exponential function with the rate $\propto \exp\left(-\frac{T_R}{T}\right)$ where T_R is a constant characteristic of the reaction over a broad temperature range and T is the absolute temperature. In the 1880s Svante Arrhenius on an academic travel grant from the Swedish Academy of Sciences for a time associated with van't Hoff in Amsterdam and in 1889 offered an interpretation of the exponential dependence of reaction rates on temperature by introducing the concept of activation energy as fundamental to understanding the rate at which a reaction proceeds. The basic idea is that the rate of a reaction is not governed by the thermodynamic difference between reactants and products but by an intermediate state of higher (free) energy than both reactants and products which constitutes a barrier—activation barrier—that must be overcome when the reactant and product species encounter each other through gaseous collisions or within solutions. It should be pointed out that during his scientific sojourn Arrhenius studied with Ludwig Boltzmann in Austria and indeed the "Boltzmann distribution" and Boltzmann factor indicated that in collisions the number of atomic or molecular events which are likely to achieve some threshold energy to allow reaction should be proportional to $\exp\left(-\frac{E_A}{RT}\right)$ where E_A is related to the T_R parameter in van't Hoff's exponential expression.

During the twentieth century an Arrhenius equation of the type rate $= A \exp\left(-\frac{Q}{RT}\right)$ has been found to apply to a plethora of rate processes from chemical reactions to diffusion in solids. The rate of chemical reactions is often formulated as rate $= k_R C_A^{\alpha} C_B^{\beta}$ where k_R is called a specific rate constant and C_A^{α} and C_B^{β} are concentrations of the reactants and α and β are characteristic exponents; the rate constant generally obeys an Arrhenius relation. In chemical reactions the activated state or "activated complex" is seen as a critical configuration or distortion of the participating species on a potential surface in a hyperspace and the reaction proceeds along a "reaction coordinate" from reactants to products over a saddle point on the potential surface. In modern theoretical statistical mechanical treatments of the fundamental process the "activated complex" is considered to be a valid thermodynamic state that is in quasi-equilibrium with the reactant state and the reaction rate is controlled by the concentration of activated complexes and the rate at which this extraordinary state at the top of the activation barrier can decompose to the product state. This theoretical superstructure and its various formulations is often referred to as Absolute Reaction Rate Theory as is comprehensively reviewed in the classic treatise by Glasstone et al. (1941). A rigorous extension of this formalism particularly applicable to atomic migration in solids is that due to Vineyard (1957).

The activated state for an elementary diffusional jump from one site to another is viewed as an intermediate state at the top of the (free energy) barrier separating lattice sites and the thermally activated

jumps can be seen in terms of Absolute Reaction Rate Theory by considering an assembly of harmonic oscillators where at any time in the system an equilibrium number of these oscillators is at the top of the barrier and this species crosses through the activated state with a certain frequency $\frac{1}{\tau}$ where τ is the mean time it takes for the migrating species to pass through a region of spatial extent δ where the potential energy $V(x)$ is assumed to be constant and equal to E_A. In general, the potential energy of the oscillator in the well is described in the harmonic approximation as $V(x) = E_0 + {}^1/_2\ Kx^2$. Staying with the basic tenets of Absolute Reaction Rate Theory, the probability that a given oscillator will at any instant of time be at the top of the activation barrier can be written as a ratio of partition functions (the ratio of the number of oscillators in the "activated state" compared with the number of harmonic oscillators vibrating about their equilibrium positions within the potential well or "reactants"). The ratio of partition functions essentially relates to an equilibrium constant for the equilibrium between the atoms in normal vibrational states and the extraordinary species in the activated state. The ratio of partition functions can be written as

$$\frac{Z_A^*}{Z_A} = \frac{\int_{X^*-\delta}^{X^*+\delta} \exp\left(-\frac{V(x)}{k_B T}\right) dx}{\int_{-\infty}^{+\infty} \exp\left(-\frac{V(x)}{k_B T}\right) dx} = \frac{\delta \exp\left(-\frac{E_M}{k_B T}\right)}{\sqrt{\frac{2\pi k_B T}{K}} \exp\left(-\frac{E_0}{k_B T}\right)} = \delta \sqrt{\frac{K}{2\pi k_B T}} \exp\left(-\frac{E_M - E_0}{k_B T}\right) \tag{93}$$

where X^* is the coordinate locating the activated state along the reaction coordinate. This ratio of partition functions also can be interpreted as the ratio of the time spent at the top of the barrier τ^* compared with the time in a normal state τ' which is approximately the total time under consideration ($\tau' >> \tau^*$). From classical statistical mechanics the time for the activated species to pass through the activated state is given by $\frac{\delta}{v^*} = \frac{\delta}{\sqrt{\frac{k_B T}{2\pi m^*}}}$ (v^* is the average velocity along the jump direction and m^* is the mass of the migrating species). Therefore, we can write that the average number of crossings per unit time or the average jump frequency of the migrating species as follows:

$$\omega = \frac{\tau*}{\left(\frac{\delta}{v^*}\right)} \text{ times } \frac{1}{\tau'} = \frac{\sqrt{\frac{k_B T}{2\pi m^*}}}{\delta} \text{ times } \frac{\tau*}{\tau'} = \frac{\sqrt{\frac{k_B T}{2\pi m^*}}}{\delta} \delta \sqrt{\frac{K}{2\pi k_B T}} \exp\left(-\frac{E_M - E_0}{k_B T}\right)$$

$$= \frac{1}{2\pi} \sqrt{\frac{K}{m*}} \exp\left(-\frac{E_M - E_0}{k_B T}\right)$$

$$\omega = \nu \exp\left(-\frac{\Delta E}{k_B T}\right) \tag{94}$$

where ν is the vibrational frequency (Einstein frequency $\approx 10^{12}$–$10^{14}\ s^{-1}$) and $\Delta E = E_M - E_0$ is the height of the activation barrier separating equilibrium sites. This is the rate at which diffusing atoms in a crystal jump into adjacent vacant sites based on this elementary version of the statistical mechanics of thermally activated atomic jumping based on a treatment by Girifalco (1971). See **Figure 46**. (If the

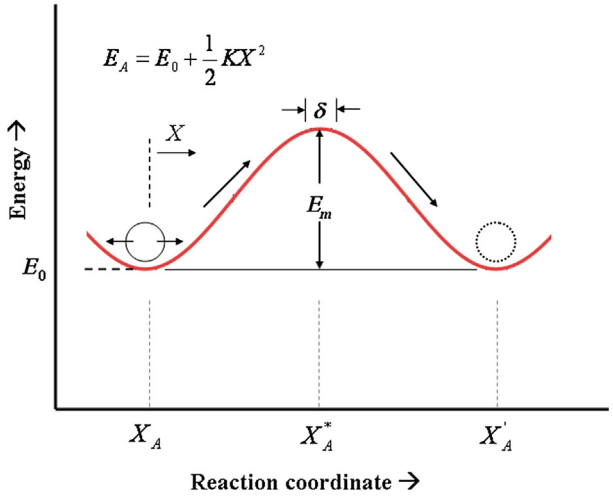

Figure 46 Schematic diagram showing the energetics of an elementary thermally activated atomic jump from X_A to X_A'. The migrating atom must overcome the activation barrier, E_m through thermal fluctuation. In this simple analysis the migrating atom is viewed as a simple harmonic oscillator within the equilibrium energy well having energy equal to E_A. The activated state is assumed to exist over a region δ at the top of the barrier.

atom is migrating through a periodically varying *free* energy field then the jump rate can be written as $\omega = \nu \exp\left(-\frac{\Delta g_m}{k_B T}\right)$ where Δg_m is a free energy barrier for migration: see Figures 47 and 48).

Let us briefly return to the essential features of the classic Eyring formulation of reaction rate theory which was more specifically directed at chemical reaction rates such as $A \leftrightarrows A^* \rightarrow B$. The rate of reaction was described explicitly in terms of the concentration of "activated complexes" and the frequency with which this species A^* decomposes along the reaction coordinate to produce the product state B. The reactant state is assumed to be in equilibrium with the activated state as mentioned earlier. The concentration of activated species is proportional to $\exp\left(-\frac{\Delta G^*}{k_B T}\right)$ where ΔG^* is considered a standard free energy of formation of the activated complex associated with an equilibrium constant

$$\frac{C_A^*}{C_A} = K^* = \exp\left(-\frac{\Delta G^*}{k_B T}\right) \tag{95}$$

where C_A^* and C_A are the equilibrium concentrations of A^* and A per unit volume. Writing the equilibrium constant as a ratio of molecular partition functions per unit volume including translational, vibrational, rotational, and so on, degrees of freedom and again assuming that the activated state exists over a distance δ along the reaction coordinate the specific rate constant for a simple first-order reaction $\left(-\frac{dC_A}{dt} = k_R C_A\right)$ is $K^* C_A$ times $\frac{\sqrt{\frac{k_B T}{2\pi m^*}}}{\delta}$; this last term represents the frequency with which A^* passes through the activated state and decomposes to produce the products similar to the treatment earlier. If

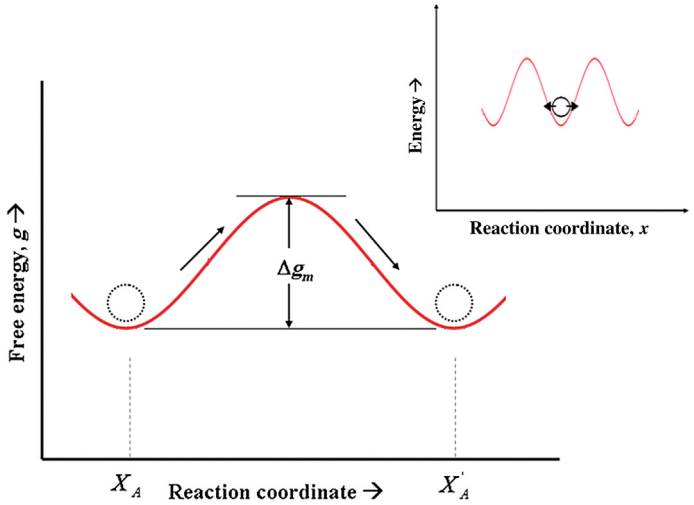

Figure 47 Elementary thermally activated jump viewed as a migration over free energy barriers Δg_m.

one factors out the translational degree of freedom along the reaction coordinate from the total partition function of the activated complex writing $Z_{A^*} = \sqrt{\frac{2\pi m^* k_B T}{h^2}}$ times Z'_{A^*}, then the expression for the rate constant becomes $k_R = \frac{k_B T}{h} \exp\left(-\frac{(\Delta G^*)'}{k_B T}\right)$ where $\Delta G^{*'}$ is the standard free energy of formation of an activated species which has no translational degree of freedom along the reaction

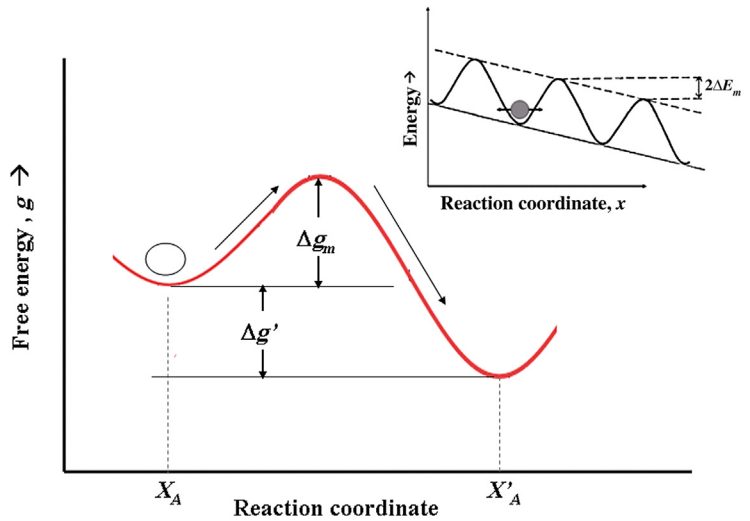

Figure 48 Thermally activated atomic migration under the influence of a driving force $\Delta g'$ which biases the jumps since the activation barrier is not the same for jumps from left to right compared with right to left.

coordinate corresponding to decomposition of the state; $\frac{k_B T}{h}$ is essentially a universal frequency $\approx 10^{12}$ to 10^{14} s^{-1} governing the rate process; the rate constant for the reaction can also be written as

$$k_R = \frac{k_B T}{h} \exp\left(\frac{(\Delta S^*)'}{k_B}\right) \exp\left(-\frac{(\Delta H^*)'}{k_B T}\right)$$

separating out the entropic and enthalpic components of the activation free energy. Clearly the rate process is expected to show an Arrhenius behavior as a function of temperature (the pre-exponential term $\frac{k_B T}{h}$ shows a weak temperature dependence compared with

$$\exp\left(-\frac{(\Delta H^*)'}{k_B T}\right)$$

agreeing with the virtually universal experimental result

$$k_R = A \exp\left(-\frac{Q}{k_B T}\right)$$

Returning to thermally activated atomic jumping during diffusion in solids, let us look at the so-called Wert–Zener modification. In applying reaction rate theory to their studies of solid-state diffusion Wert and Zener (1950) were theoretically uncomfortable with the idea of not conserving the number of degrees of freedom in passing from the reactant state to an activated state and thus suggested factoring out a vibrational degree of freedom from the partition function of an atom in a normal site, namely $\frac{k_B T}{h\nu}$ leading to a modified expression

$$k_R = \nu \exp\left(-\frac{(\Delta G^*)''}{k_B T}\right)$$

where $\Delta G^{*''}$ can be interpreted as the work done in taking the migrating atom from its normal state in an atomic site to the activated state constraining it to vibrate normal to the reaction path.

The Arrhenius concept of an activated state of higher (free) energy separating an initial state from a final state is universally applied to a wide range of thermally activated processes from chemical reactions, nucleation and growth, diffusion, coarsening, plastic deformation, and so on, and the Arrhenius plot—applied to rate constants, diffusivities, growth rates, and so on—generally involves plotting the natural log of a rate parameter versus $\frac{1}{T}$ with the slope equal to $-\frac{Q_{exp}}{R}$ and generally one attempts to relate the magnitude of this experimental activation energy Q_{exp} to elementary processes controlling the rate phenomenon in question.

8.3.2 Diffusion Kinetics

Diffusion is the flow of matter from one region to another in a material system generally driven by a concentration gradient. However, a more rigorous description of diffusional processes identifies the "driving force" as a gradient in the chemical potential of the migrating species. This is obvious from the fact that two phases of vastly differing compositions can coexist in thermodynamic equilibrium but the chemical potentials of the components are uniform throughout the phase mixture and no diffusive

flow occurs within the compositionally inhomogeneous system. Also, during an allotropic transformation a more stable phase grows into the less stable phase often mediated by short-range diffusional jumps across an advancing interface at constant composition and the net atomic flux to the more stable phase derives from the local gradient in chemical potential.

Adolf Fick in the middle of the nineteenth century formulated a set of differential equations—Fick's First and Second laws—describing chemical diffusion analogous to Fourier's earlier treatment of heat flow. Fick's laws of chemical diffusion relate the flow of matter explicitly to the concentration gradient and are written as

$$J_x = -D\frac{\partial c}{\partial x} \qquad (1-\text{Dimensional}) \tag{96}$$

and

$$\overrightarrow{J} = -D\nabla c \qquad (3-\text{Dimensional}) \tag{97}$$

and

$$\frac{\partial c}{\partial t} = \frac{\partial\left(D\frac{\partial c}{\partial x}\right)}{\partial x} = D\frac{\partial^2 c}{\partial x^2} \qquad (D \text{ constant and } c = c(x,t))$$

and

$$\frac{\partial c}{\partial t} = -\text{div}\,\overrightarrow{J} = D\nabla^2 c \qquad (D \text{ constant and } c = c(x,y,z,t)) \tag{98}$$

where D is a phenomenological parameter (like the thermal conductivity in Fourier's equations) called the *diffusion coefficient* or *diffusivity*; J_x and $\mathbf{J}$ (J_x, J_y, J_z) are the fluxes (atoms $\text{cm}^{-2}\ \text{s}^{-1}$ or mol $\text{cm}^{-2}\ \text{s}^{-1}$) or mass flow rates across a unit cross-sectional area in a local concentration gradient. Importantly, employing the local concentration gradient as the driving force for mass flow within a phase is acceptable operationally if the absence of a concentration gradient leads to a uniformity of the chemical potentials and chemical equilibrium; therefore, in many diffusion problems Fick's laws are invoked. Fick's First law relates the concentration gradient to the local concentration gradient and the solution of Fick's Second law (the diffusion equation) gives the time evolution of the concentration $c(x,y,z,t)$ for various initial and boundary conditions.

When describing diffusion fluxes in a material system it is important to define the frame of reference or coordinate system (which might be moving relative to a fixed reference frame or laboratory frame) in which the diffusion fluxes are prescribed. In the conventional diffusion couple setup between two pure metals A and B which interdiffuse across an initial weld interface between the two metal blocks the concentration profile evolves typically as shown in Figure 49. If the diffusion fluxes of A and B are described in terms of a coordinate system fixed relative to the ends of the couple—a laboratory frame—the intermixing can be analyzed in a mathematically convenient manner employing a single diffusion coefficient D_{AB}—the interdiffusion coefficient—wherein the fluxes are written as

$$J_A = -D_{AB}\frac{\partial c_A}{\partial x} \text{ and } J_B = -D_{AB}\frac{\partial c_B}{\partial x} \tag{99}$$

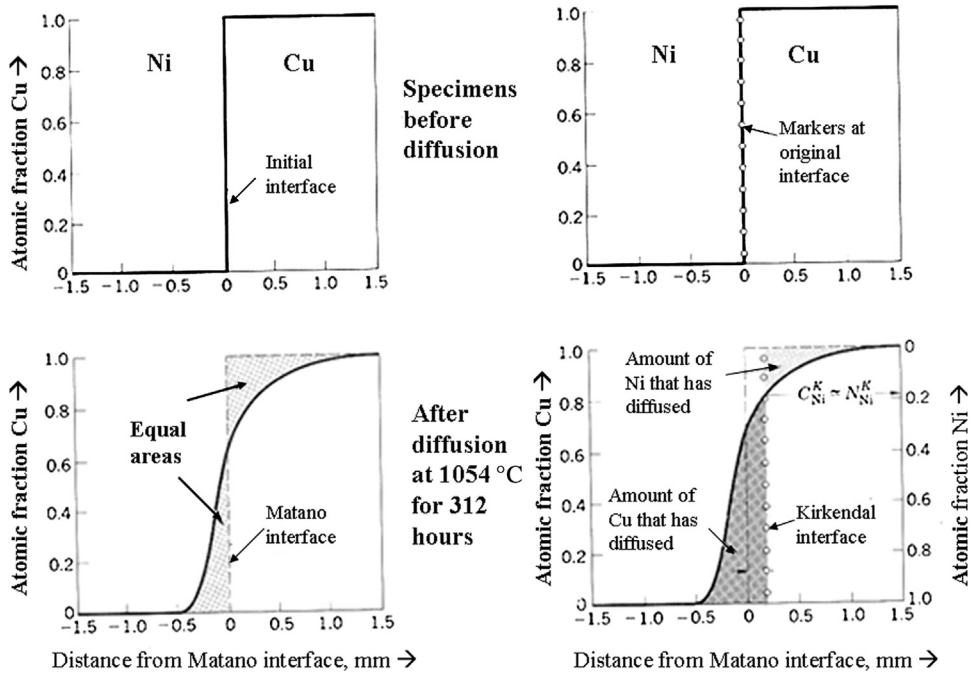

Figure 49 Schematic of interdiffusion between two metals A and B showing the Matano and Kirkendall interfaces wherein the intrinsic diffusivities are unequal ($D_B > D_A$). The Matano interface corresponds to the initial weld interface and the Kirkendall interface is the plane of the markers which initially were located at the weld interface but moved as a result of the unequal diffusive flows of the A and B atoms. After Guy and Hren (1974).

and in this frame $J_A + J_B = 0$ or $J_A = -J_B$. In this description the initial weld interface is the so-called *Matano interface* across which equal numbers of A atoms have crossed from left to right as B atoms from right to left. However, the classic Kirkendall–Smigelskas effect dealing with interdiffusion in substitutional metallic solid solutions indicated that the atomic migration occurs via a vacancy mechanism and that the A and B atoms do not diffuse down their local concentration gradients at the same rate, that is, the interdiffusion process actually involves two diffusion coefficients D_A and D_B called the intrinsic diffusivities or diffusion coefficients of A and B, respectively. The intrinsic diffusivities relate the diffusional fluxes of A and B to their local concentration gradients in a frame of reference fixed on a lattice plane in the diffusion-affected zone, that is,

$$J'_A = -D_A \frac{\partial c_A}{\partial x} \quad \text{and} \quad J'_B = -D_B \frac{\partial c_B}{\partial x} \tag{100}$$

where $J'_A \neq J'_B$.

The unequal rates of migration of A and B lead to a net flux of vacancies across the initial weld interface and causes the destruction of lattice planes on one side and the creation of lattice planes on the other side as evidenced by the marker movement in the Kirkendall–Smigelskas experiment (1947). There is effectively a bulk flow or convective motion in the diffusion-affected zone and lattice planes are essentially moving with this motion relative to the ends of the diffusion couple. (The bulk flow is

basically a plastic regression in the solid involving dislocation climb.) In the elegant Darken analysis of the interdiffusion process it is clear that in the laboratory frame the fluxes J_A and J_B are composed of two components:

$$J_A = J'_A + c_A V_m = -D_A \frac{\partial c_A}{\partial x} + c_A V_m \tag{101}$$

and

$$J_B = J'_B + c_B V_m = -D_B \frac{\partial c_B}{\partial x} + c_B V_m \tag{102}$$

where the first term on the right is a purely diffusive flow down the local concentration gradient and the second term is a bulk flow giving rise to an apparent flux in the laboratory frame where $J_A + J_B = 0$; V_m is the local velocity of the alloy medium relative to the laboratory frame and revealed by the velocity of markers in the diffusion-affected zone. The interdiffusion coefficient and the intrinsic diffusivities can be shown to be related at any composition as follows:

$$D_{AB} = X_B D_A + X_A D_B \tag{103}$$

where X_A and X_B are the atomic fractions of A and B with D_A and D_B the intrinsic diffusivities as defined earlier. Note that these diffusion coefficients are generally a function of composition although the assumption $D_{AB} =$ constant is widely used successfully in a wide variety of practical problems.

The use of the interdiffusion coefficient incorporates the bulk flow into the diffusion fluxes and allows us to describe the intermixing and time evolution of the concentration versus distance profile without concerning ourselves with sorting out these effects (bulk flow versus diffusive flow across the reference plane and $D_A \neq D_B$). If one wants to calculate the time to homogenize an alloy casting or dissolve a second phase during solution treatment of an age hardening alloy one can just use the interdiffusion coefficient at the temperature of interest and solve Fick's Second law.

The simplest expression relating the local chemical potential gradient to the rate of flow/flux of a diffusing species i for one-dimensional flow along the x-axis can be written as

$$J_i = -L_i \frac{\partial \mu_i}{\partial x} \tag{104}$$

where L_i is a phenomenological coefficient and $\frac{\partial \mu_i}{\partial x}$ is the chemical potential gradient of i along the x-axis. We can also write the diffusion flux in terms of a local diffusion velocity of the migrating species V_i along the x-axis and a mobility M_i as

$$J_i = c_i V_i = -M_i c_i \frac{\partial \mu_i}{\partial x} \tag{105}$$

where M_i is the velocity per unit "driving force" (the gradient in chemical potential) and equal to $\frac{L_i}{C_i}$. This flux is a purely diffusive flow of the migrating species down its local chemical potential gradient. We now relate the diffusion flux to the concentration gradient according to Fick's First law

$$J'_i = -D_i \frac{\partial c_i}{\partial x}$$

where D_i is clearly an intrinsic diffusion coefficient or intrinsic diffusivity. Writing

$$J_i = -M_i c_i \frac{\partial \mu_i}{\partial c_i}\frac{\partial c_i}{\partial x} \tag{106}$$

and recalling that $\mu_i = \text{constant} + RT \ln a_i$ and $a_i = \gamma_i c_i$ we arrive at the relation

$$D_i = M_i RT\left(1 + \frac{\partial \ln \gamma_i}{\partial \ln c_i}\right) = M_i RT\left(1 + \frac{\partial \ln \gamma_i}{\partial \ln X_i}\right) \tag{107}$$

wherein the term $\left(1 + \frac{\partial \ln \gamma_i}{\partial \ln X_i}\right)$ is called the "thermodynamic factor" which relates the solution thermodynamics to aspects of the atomic migration.

We shall elucidate the role of the thermodynamic factor by reviewing the relationship between atomic jumps from one lattice site to another and between lattice planes in a concentration gradient. If c_1 and c_2 are the concentrations (atoms cm^{-3}) of the diffusing species on adjacent planes 1 and 2 ($c_1 > c_2$) normal to the concentration gradient and of spacing α, the number of atoms of the diffusing species per unit area of these planes is $n_1 = \alpha c_1$ and $n_2 = \alpha c_2$, respectively. If these atoms are jumping randomly from site to site with a frequency $\Gamma\ \text{s}^{-1}$ wherein one-sixth of their jumps are down or up the concentration gradient, on an atomic level there will be a net flux (atoms $\text{cm}^{-2}\ \text{s}^{-1}$) down the concentration gradient given by $\frac{1}{6}\alpha\Gamma(c_1 - c_2)$. The local concentration gradient is essentially $-\dfrac{(c_1 - c_2)}{\alpha}$ and thus the flux can be related to the concentration gradient as follows:

$$J = \frac{1}{6}\Gamma\alpha^2(c_1 - c_2) = -\frac{1}{6}\Gamma\alpha^2\frac{dc}{dx} \tag{108}$$

which is Fick's First law if the intrinsic diffusivity is taken to be $D = \frac{1}{6}\Gamma\alpha^2$. This is an important result relating a macroscopic phenomenological parameter—D in Fick's First law—to the underlying atomistics of the diffusion process, namely an atomic jump frequency Γ and an elementary jump distance α. If the jumps are restricted to nearest-neighbor sites, $\alpha = \dfrac{\sqrt{2}}{2}a_0$ and $\alpha = \dfrac{\sqrt{3}}{2}a_0$ for FCC and BCC lattices, respectively, where a_0 is the lattice parameter of the conventional cubic unit cell. If the atomic jumps are mediated by exchange with an adjacent vacancy–vacancy mechanism—as is the case of diffusion in substitutional metallic solid solutions (and self-diffusion in pure metals), the above expression must be modified to include what is called a "correlation factor" f that accounts for the fact that when the vacancy mechanism is operative the atomic jumps are not completely random since after executing an elementary atomic jump the diffusing species statistically is most likely to jump back into the vacant site from whence it came. Thus, we write

$$D = \frac{f}{6}\Gamma\alpha^2$$

where $f = 0.78$ and 0.72 for FCC and BCC lattices, respectively.

Using radioactive tracers one can monitor the atomic migration of the tracer into a pure metal or into a homogeneous alloy in the absence of a concentration gradient, that is, one can analyze the tracer diffusion process and measure self-diffusion coefficients or tracer diffusivities ($D^*_{\text{M}}, D^*_{\text{A}}, D^*_{\text{B}}$) that describe the nearly random (but including correlation effects) jumping of the tracer species in a pure metal or alloy. Let us return to the migration of A and B in a binary alloy in a concentration gradient and recall that the simple analysis presented earlier for diffusion in the concentration gradient was based on random

jumping and flow down the gradient is essentially a statistical flow from plane 1 to plane 2 because there are more atoms on plane 1 than on plane 2 (there is no bias to their individual jumps up or down the gradient). Therefore, the variation of the free energy of the diffusing atom from site to site looks like that shown in Figure 47. The activation barrier for jumps from left to right is the same as that for jumps from right to left leading to random jumping. However, if the diffusing atom "sees" a free energy profile like that in Figure 48 because of the effects of different atomic environments, for example, the jumps will be biased producing what effectively amounts to a drift velocity along the concentration gradient. The diffusive flow in the concentration gradient can essentially be considered to be composed of two components, namely, a statistical flow and flow deriving from a "driving force" which produces a drift velocity.

Let us return to the incorporation of the thermodynamic factor into the expression for the intrinsic diffusivities that is

$$D_i = M_i RT\left(1 + \frac{\partial \ln \gamma_i}{\partial \ln X_i}\right).$$

First we note that for dilute solutions ($\gamma_i = \gamma_i^{\circ} = \text{constant}$) and ideal solutions ($\gamma_i = 1$) this becomes $D_i = M_i RT$ which is the famous Nernst–Einstein equation.

Assuming that $M_i = M_i^*$, we write $D_i^* = M_i^* RT = M_i RT$ where D_i^* is a tracer diffusivity. We then write

$$D_i = D_i^*\left(1 + \frac{\partial \ln \gamma_i}{\partial \ln X_i}\right)$$

relating the intrinsic diffusivity to the corresponding tracer diffusivity at a given concentration. Thus, the diffusion flux in a concentration gradient in a binary alloy can be separated into a statistical flow and a drift term (nonrandom jumping) in the concentration gradient as follows:

$$J_i = -D_i^* \frac{\partial c_i}{\partial x} + c_i V_m^D \tag{109}$$

with the drift velocity $V_m^D = -M_i \dfrac{\partial \mu_i'}{\partial x}$ and $\mu_i' = RT \ln \gamma_i$ which is the nonideal contribution to the chemical potential of the diffusing species i.

At this point in our review we remind the reader that like the thermal conductivity the diffusivities and mobilities are tensor properties of a crystalline solid (Second Rank polar matter tensors). Thus, for diffusion the fluxes along the x-, y- and z-axes of a species should be written in terms of the components of the second rank polar tensor D_{ij} as follows:

$$\begin{aligned} J_1 &= -D_{11}\frac{\partial c}{\partial x_1} - D_{12}\frac{\partial c}{\partial x_2} - D_{13}\frac{\partial c}{\partial x_3} \\ J_2 &= -D_{21}\frac{\partial c}{\partial x_1} - D_{22}\frac{\partial c}{\partial x_2} - D_{23}\frac{\partial c}{\partial x_3} \\ J_3 &= -D_{31}\frac{\partial c}{\partial x_1} - D_{32}\frac{\partial c}{\partial x_2} - D_{33}\frac{\partial c}{\partial x_3} \end{aligned} \tag{110}$$

where the notation $x \to 1$, $y \to 2$ and $z \to 3$ is used to relabel the coordinate axes; J_1, J_2 and J_3 are diffusion fluxes along the $1(x)$, $2(y)$ and $3(z)$ axes, respectively. In this generalized description of diffusion in an anisotropic crystal we see that composition gradients along orthogonal axes can, in principle, induce flows along the 1, 2 and 3 coordinate axes. Thus, the net flux vector $\mathbf{J}(J_1, J_2, J_3)$ is not necessarily parallel to the vector ∇c, i.e. $\left(\dfrac{\partial c}{\partial x_1}, \dfrac{\partial c}{\partial x_2}, \dfrac{\partial c}{\partial x_3}\right)$. However, if the second rank tensor is referred

to the so-called principal axes the diffusivity tensor D_{ij} takes the following diagonal form

$$D_{ij} = \begin{pmatrix} D_{11} & 0 & 0 \\ 0 & D_{22} & 0 \\ 0 & 0 & D_{33} \end{pmatrix} \tag{111}$$

wherein gradients along the principal axes always lead to flows parallel to these axes; however, if the gradient ∇c is along a direction which is not a principal axis the net flux vector $\mathbf{J}(J_1, J_2, J_3)$ is not parallel to ∇c in the general anisotropic case. The nature of the diffusivity tensor is strongly dependent on crystal symmetry and embodied in Neumann's Principle: *The symmetry elements of any physical property of a crystal must include the symmetry elements of the point group of the crystal.* The symmetry of cubic crystals requires that $D_{11} = D_{22} = D_{33} = D$ rendering cubic crystals isotropic with respect to diffusion: in fact, cubic crystals are isotropic with respect to all physical properties which are second rank tensorial properties of the material including the thermal conductivity. For tetragonal and hexagonal crystals $D_{11} = D_{22} \neq D_{33}$ and for the orthorhombic case $D_{11} \neq D_{22} \neq D_{33}$. The principal axes for cubic, tetragonal and orthorhombic crystals are along the conventional orthogonal crystal axes of these systems. For hexagonal crystals the *c*-axis is a principal axis and orthogonal directions within the basal plane are principal axes.

Let us now revisit the relationship of thermally activated atomic jumps of individual atoms and macroscopic diffusion behavior. As pointed out earlier virtually all diffusion coefficients empirically exhibit a temperature dependence of the Arrhenius form

$$D = D_0 \exp\left(-\frac{Q}{RT}\right)$$

where Q is called the experimental activation energy for diffusion which is typically $\approx$ 45–65 kcal mol^{-1} for diffusion in substitutional metallic solid solutions and self-diffusion in pure metals; the pre-exponential D_0 is generally $\approx$ 0.1–1.0 cm^2 s^{-1}. The activation energy for interstitial diffusion, for example C in α-Fe and γ-Fe is $\approx$ 20–30 kcal mol^{-1}. We derived a relationship between the diffusivity (D as in Fick's laws) of a migrating species and atomistic parameters through the basic equation

$$D = \frac{f}{6}\Gamma\alpha^2 \tag{112}$$

where Γ and α are the average jump frequency and the elementary jump distance, respectively. The correlation factor, f, is unity for diffusion of interstitial solutes jumping among the atomic sites of a dilute interstitial solid solution and less than one for diffusion of a substitutional solute in solid solution migrating via a vacancy mechanism as discussed earlier. The average jump frequency can be addressed using an elementary interpretation of thermally activated jumping as follows: the diffusing atom is vibrating about its equilibrium position within a potential well with some frequency $\nu \approx 10^{13}$ s^{-1} and the probability that on any oscillation against the barrier separating atomic sites the atom will be energetic enough to move over the barrier and jump to an adjacent site (if the site is available to accommodate the migrating species) is from elementary statistical thermodynamics $\exp\left(-\frac{\Delta g_m}{k_B T}\right)$ where Δg_m is the height of the (free) energy barrier or the (free) energy of activation for the elementary diffusional jump. (The subscript m explicitly identifies this as an activation free energy for *atomic migration*.) See **Figure 47**. For diffusion occurring via a vacancy mechanism the probability that the site is vacant is $\exp\left(-\frac{\Delta g_V}{k_B T}\right)$ where Δg_v is the (free) energy of formation of a vacant site $\approx$ 1 eV in

a metallic system. If there are z equivalent sites surrounding the migrating atom the average jump frequency will be $\nu z \exp\left(-\frac{\Delta g_m + \Delta g_V}{k_B T}\right)$ with $z = 12$ (fcc) and $z = 8$ (bcc) for nearest-neighbor jumps. For interstitial diffusion, for example C and N in Fe, the probability that an adjacent interstitial site is vacant is essentially one so that the jump frequency is given by $\nu z \exp\left(-\frac{\Delta g_m}{k_B T}\right)$. Thus, the diffusivity of a species controlled by thermally activated jumps mediated by a vacancy mechanism can be written as

$$D = \frac{f\alpha^2 \nu z}{6} \exp\left(-\frac{\Delta g_m + \Delta g_V}{k_B T}\right) \tag{113}$$

and for interstitial diffusion

$$D = \frac{\alpha^2 \nu z}{6} \exp\left(-\frac{\Delta g_m}{k_B T}\right) \tag{114}$$

and are often written as

$$D = \frac{f\alpha^2 \nu z}{6} \exp\left(-\frac{\Delta g_m + \Delta g_V}{k_B T}\right) = \frac{f\alpha^2 \nu z}{6} \exp\left(\frac{\Delta S_m + \Delta S_V}{R}\right) \exp\left(-\frac{\Delta H_m + \Delta H_V}{RT}\right)$$

and

$$D = \frac{\alpha^2 \nu z}{6} \exp\left(-\frac{\Delta g_m}{k_B T}\right) = \frac{\alpha^2 \nu z}{6} \exp\left(\frac{\Delta S_m}{R}\right) \exp\left(-\frac{\Delta H_m}{RT}\right) \tag{115}$$

respectively. Clearly, these expressions for the diffusivity are of the Arrhenius form $D = D_0 \exp\left(-\frac{Q}{RT}\right)$ and from a plot of ln D vs. $\frac{1}{T}$ the slope $-\frac{Q}{R}$ is $\left(-\frac{\Delta H_m + \Delta H_V}{R}\right)$ or $\left(-\frac{\Delta H_m}{R}\right)$, respectively.

The intercept of the plot ln D_0 is related to the preexponential parameters. The experimental activation energy Q is a composite term when a vacancy mechanism is operative composed of the enthalpic part of the free energy of activation for migration ΔH_m and the enthalpic contribution to the free energy of formation of vacant sites. In the case of interstitial diffusion Q is related directly to the enthalpic contribution to the free energy of activation for an elementary thermally activated jump from one interstitial site to another adjacent site.

Various aspects of atomic migration and thermally activated atomic jumping are often related to the basic tenets of what is called random walk theory (Shewmon, 1963). The root mean squared distance a migrating atom will travel from its initial position in time t after $n = \Gamma t$ jumps is shown to be $R = n^{1/2}\alpha$ and thus can be related to the diffusivity as $R = (6Dt)^{1/2}$ from our discussion earlier. If the diffusion is isotropic then $R^2 = X^2 + Y^2 + Z^2$ and for an arbitrary set of axes is such that $R^2 = 3X^2$ since all directions X, Y and Z are equivalent and thus the root mean squared travel distance along a particular direction is $X = \sqrt{2Dt}$. This relation is useful for "back of the envelope" estimates of diffusion distances in a particular context, for example approximately how thick is a carburized layer after a case-hardening treatment of steel ball bearings for some time t.

The discussion of mass transport to this point has focused on what we call bulk or lattice diffusion involving atomic jumps among the normal lattice sites or interstitial sites of the crystalline solid.

However, we know that most metallic (and ceramic) solids are polycrystalline and contain lattice defects such as dislocations. Atomic migration along grain boundaries and dislocations can occur much more rapidly than within the bulk crystal lattice with an activation energy of the order of one-half that for lattice diffusion. However, although diffusion is more rapid along these short-circuit paths the fraction of atoms associated with grain boundaries and dislocations is small of order 10^{-6} to 10^{-8} depending on the grain size and dislocation density. The contribution of short-circuit paths to overall mass transport depends on the ratio $\frac{D_{gb}f}{D_L}$ or $\frac{D_P f}{D_L}$ where D_L is the ordinary lattice or bulk diffusivity and D_{gb} and D_P are the diffusivities characterizing the grain boundary and dislocation "pipe" high-diffusivity paths; f is the fraction of atomic sites associated with the short-circuit paths. When these ratios approach 1 the short-circuit paths start to make a significant contribution to the overall diffusive flow and the apparent or effective diffusion coefficient is enhanced compared with that deriving from bulk diffusion alone. This occurs for grain boundary diffusion below about two-thirds the melting point $\frac{2}{3}T_M$ and for dislocations below about one-half the melting point $\frac{1}{2}T_M$, that is, short paths become more important at lower temperatures.

Numerous practical problems involving diffusion require a solution to the diffusion equation (Fick's Second law) for various initial and boundary conditions and a number of solutions relevant to materials problems are discussed in texts such as Shewmon (1963), Glicksman (2000), Wilkinson (2000) and Kirkaldy and Young (1987). It should be pointed out that useful solutions to the diffusion equation can often be extracted from books on heat flow such as Carslaw and Jaeger (1946) since the heat flow equation and its solutions can be converted to solutions to diffusion problems through a change in variables.

8.3.3.1 Johnson–Mehl–Avrami–Kolmogorov (JMAK) Kinetics

In the previous sections the kinetic mechanisms involved in the change of phase have been reviewed. In this section a general phenomenological approach to the kinetics of phase change is discussed. The following discussion is based on a series of papers published between 1937 and 1942 (Kolmogorov, 1937; Avrami, 1938, 1940, 1941; Johnson and Mehl, 1939). For a recent commentary see Barmak (2010) and Hillert (2011).

It is important to be able to understand and delineate how fast a transformation occurs, and to be able to display this on a simple plot of fraction transformed, X, versus time, t. A typical plot of the volume fraction transformed, X versus time, t for a first-order phase transformation is shown in **Figure 50**.

It can be seen that such transformations start off slowly, increase in rate and then slow down as the transformation nears completion. From the figure it can be seen that the equation for this curve should display the conditions

$$X = 0 \text{ at } t = 0$$

$$X = 1 \text{ at } t = \infty$$

$$\frac{dX}{dt} = 0 \text{ at } t = 0$$

$$\frac{dX}{dt} = 0 \text{ at } t = \infty$$

An equation which satisfies these conditions is

$$x = 1 - \exp(-(kt)^n) \tag{116}$$

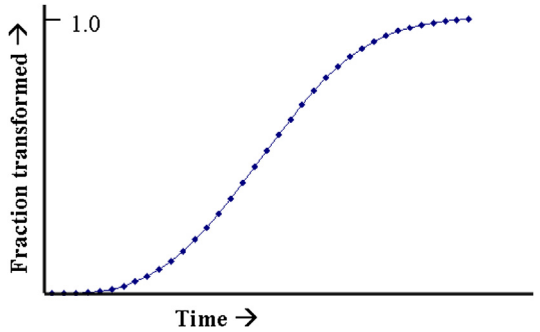

Figure 50 Typical volume fraction transformed, X, vs. time for a first-order phase transformation at a given temperature.

(Note: some authors place the temperature-dependent constant k outside of the parenthesis in the above equation. We prefer to keep it within so that it always has the units of inverse time, regardless of the value of the exponent, n.)

If sufficient data are available, the two constants k and n can be determined from a plot of $\ln \ln \frac{1}{(1-X)}$ *vs.* $\ln t$. The slope of the plot will be equal to n and the intercept will be $n \ln k$. These values can then be used to determine the fraction transformed at any time at the temperature in question. The effect of temperature comes into play via the temperature-dependent $k(T)$.

At a given temperature, the maximum rate of transformation occurs at the point of inflection of the curve, that is, when the second derivative of X with respect to time is equal to zero. The value of $X_{\max}$ in terms of the value of n is determined as follows:

$$X = 1 - \exp(-(kt)^n)$$

$$\frac{dX}{dt} = nk(kt)^{n-1}(1-X)$$

$$\frac{d^2X}{dt^2} = (n-1)nk^2(kt)^{n-2}(1-X) + nk(kt)^{n-1}\left(-\frac{dX}{dt}\right)$$

$$set = 0 \text{ and solve :}$$

$$(n-1)nk^2(kt)^{n-2}(1-X) = nk(kt)^{n-1}(1-X)nk(kt)^{n-1}$$

$$(kt)^n = \frac{n-1}{n} \text{ or } X_{\max} = 1 - \exp\left(-\frac{n-1}{n}\right)$$

Thus, if the inflection point can be determined, the value of n can be found. This is a second way to obtain the value of n for a given transformation. This can only be utilized if there is sufficient data to obtain the point of inflection of the X vs. t plot.

8.3.3.2 Initial Slopes of X vs. Time Curves

From the derivative of Eqn (116) we obtain

$$\frac{dX}{dt} = nk(kt)^{n-1}(1-X) \tag{117}$$

The following can be seen to obtain

(1) $n > 1 \left(\frac{dX}{dt}\right)_{t=0} = 0$

(2) $n = 1 \left(\frac{dX}{dt}\right)_{t=0} = \text{constant} = nk^n = k$

(3) $0 < n < 1 \left(\frac{dX}{dt}\right)_{t=0} = \infty$

(4) $n < 0$ (not physical)

It can be seen that the expression 116 also allows for initially rapid transformations, if n is less than or equal to 1.

8.3.3.3 Models for Predicting Values of n and k

From the above equations we have

$$\begin{aligned} X &= 1 - \exp[-(kt)^n] \\ \frac{dX}{dt} &= \exp[-(kt)^n] nk(kt)^{n-1} \\ \frac{dX}{dt} &= (1 - X) nk^n t^{n-1} \end{aligned} \tag{118}$$

For short times, by expanding the exponential in the first expression and dropping higher order terms we obtain

$$\begin{aligned} X &= (kt)^n \\ \frac{dX}{dt} &= nk^n t^{n-1} \end{aligned} \tag{119}$$

The difference between equations 118 and 119 is the factor $(1 - X)$, which is the fraction of the sample that is untransformed. This term has been called the "impingement factor" and it takes into account the fact that the volume fraction available to transform decreases with time.

We have

$$\left(\frac{dX}{dt}\right)_{\text{corrected for impingement}} = (1 - X)\left(\frac{dX}{dt}\right)_{\text{not corrected for impingement}} \tag{120}$$

The fraction not corrected for impingement is called the extended volume fraction, X_x.

Note, by rearranging Eqn (120) and integrating, the following is obtained:

$$\frac{dX}{(1 - X)} = dX_X$$

$$-\ln(1 - X) = X_x$$

$$(1 - X) = \exp(-X_X)$$

$$X = 1 - \exp(-X_X) \tag{121}$$

Thus if the transformation rate can be modeled in terms of the extended volume fraction transformed (that is, not taking into account impingement) we can obtain the actual transformation fraction transformed by Eqn (121).

8.3.3.4 Modeling the Nucleation Process

The rate of nucleation, I, is the number of transformation centers, N, coming into existence per unit time per unit volume of untransformed phase. Thus

$$I = \frac{1}{(1-X)}\frac{dN}{dt}$$

Avrami (1939) has written

$$\frac{dN}{N} = -\nu_1 dt$$

$$N = N_0 \exp(-\nu_1 t)$$

where N is the number of possible nuclei sites remaining and N_0 is total number of possible nuclei sites. (Note that the rate of change of the remaining sites is equal to but opposite in sign to the rate of change of sites where nucleation has occurred.)

The number of possible sites for nucleation decreases with time. Thus, using the above assumption of Avrami, we obtain for the rate of nucleation

$$\frac{dN}{dt} = N_0\nu_1 \exp(-\nu_1 t)$$

$$I = \left(\frac{1}{1-X}\right) N_0\nu_1 \exp(-\nu_1 t)$$

Two extreme cases may be considered:

(1) ν_1 is very *large*:

$\frac{dN}{dt} = 0$: all nucleation has occurred at $t = 0$.

(2) ν_1 is very *small*:

$\frac{dN}{dt} \approx N_0\nu_1 =$ constant nucleation rate.

8.3.3.5 Modeling the Growth Process

The growth rate, G, of a linear dimension r of the new phase is defined as

$$G = \frac{dr}{dt}$$

There are two cases of interest for solid-state diffusional transformations, those whose rate of growth is constant

(1) $G =$ constant,

thus $r \propto t$ (linear)

(2) $G \propto t^{-1/2}$,

hence $r \propto t^{1/2}$ (parabolic).

8.3.3.6 Modeling the Volume Fraction Transformed

We will look at four special cases for the prediction of the values of k and n.

Case 1a	$I = 0$	$G =$ constant
Case 1b	$I = 0$	$G =$ parabolic
Case 2a	$I =$ constant	$G =$ constant
Case 2b	$I =$ constant	$G =$ parabolic

Case 1a

(1) All nucleation at $t = 0$
(2) Particles grow as spheres
(3) $G = \frac{dr}{dt} =$ constant.

Thus: $X_X = N\frac{4}{3}\pi G^3 t^3$ and $X = 1 - \exp\left(-\frac{4\pi}{3}NG^3t^3\right)$

For this case we obtain $n = 3$ and $k = \left(\frac{4\pi N}{3}\right)^{\frac{1}{3}} G$

Case 1b

(1) All nucleation at $t = 0$
(2) Particles grow as spheres
(3) $G = k_r t^{-1/2}$

Thus $dr = k_r t^{-1/2} dt$

$r - r_0 = 2k_r t^{1/2}$

$r \approx 2k_r t^{1/2}$.

Now $X_X = \frac{32}{3}\ \pi k_r^3\ Nt^{3/2}$

$X = 1 - \exp\left(-\frac{32\pi}{3}k_r^3 N t^{3/2}\right)$

For this case we obtain $n = 3/2$ and $k = \left(\frac{32\pi}{3}N\right)^{\frac{2}{3}} k_r^2$

Case 2a (The original Johnson–Mehl Equation)

Assumptions:

(1) I and G not functions of x, t
(2) Random nucleation in untransformed regions
(3) Particles grow as sphere

At time t, the volume of a spherical particle that formed at $\tau(0 < \tau < t)$ is

$$\text{Vol} = \frac{4}{3}\pi G^3(t-\tau)^3$$

$$\text{Thus } X_X = \int_{\tau=0}^{\tau=t} \frac{4}{3}\pi G^3(t-\tau)^3 I d\tau = \frac{\pi}{3} G^3 I t^4$$

$$\text{and } X = 1 - \exp\left(-\frac{\pi}{3} l G^3 t^4\right)$$

$$\text{For this case } n = 4 \text{ and } k = \left(\frac{\pi I G^3}{3}\right)^{\frac{1}{4}}$$

Case 2b

Same assumptions as 2a, but the growth is parabolic in time.

$$G = k_r t^{-1/2}$$

$$\text{Vol} = \frac{4}{3}\pi k_r^3 (t-\tau)^{3/2}$$

$$X_X = \int_{t=0}^{\tau=t} \frac{4}{3}\pi k_r^3 (t-t)^{3/2} I \mathrm{d}t = \frac{4}{3}\frac{2}{5}(\pi k_r^3 I) t^{5/2}$$

$$X = 1 - \exp\left(-\frac{8\pi}{15} k_r^3 l t^{5/2}\right)$$

$$\text{For this case } n = 5/2 \text{ and } k = \left(\frac{8\pi k_r^3 I}{15}\right)^{\frac{2}{5}}$$

From these cases it can be seen that the time exponent n for the growth of the new phase shaped as spheres is made up of two terms, p and q.

$p = 0$	If all nucleation occurs at $t = 0$
$p = 1$	If nucleation occurs with time
$q = 3$	If growth is linear
$q = 3/2$	If growth is parabolic

Thus, n can be $\frac{3}{2}, 3, \frac{5}{2}$ or 4 for the nucleation and growth of spheres.

Other values of n can be obtained. For example, if the nucleation rate is a function of time, n can be greater than 4.

If the new phase is not spherical in shape, other values of n can be found. For example, suppose the particle grows linearly as a plate in two dimensions but the third-dimension parabolic. Then, q is determined to be 5/2. The value of n could be 5/2 or 7/2, or greater, depending on the nucleation conditions.

It can be seen that the same value of n could be determined for cases with very different nucleation, growth or shapes of the new phase. It is always wise to supplement these kinetic studies with actual metallographic observations of the shape of the new phase.

Other complications can also arise. For example the diffusion fields of the growing particles could overlap, causing a slowing down of the kinetics. This is called soft impingement and the values of n and k will no longer be constant for a given temperature.

8.4 Classical Nucleation

Nucleation is basically a fluctuation phenomenon within an undercooled or supersaturated phase that produces regions of a new phase (or combination of phases) that can grow spontaneously dissipating

the excess free energy and changing the phase constitution of the material system. The rate of this basic process during phase transformations occurring in materials systems often determines the microstructural scale of the transformation products and thus can ultimately influence the structure–properties relationships in engineering materials. The emergence of the new phase generally occurs at distinct sites within the parent phase and the number of these transformation centers or nuclei appearing in a unit volume per unit time essentially defines a nucleation rate. If the nuclei appear at random sites within the parent phase, the nucleation process is termed *homogeneous*. The formation of the new phase may be catalyzed by the presence of singularities in the system such as container walls or lattice defects and occurs preferentially at these special sites; this nonrandom appearance of the new phase or phases is called *heterogeneous* nucleation. The rate of heterogeneous nucleation is clearly limited by the density of these special sites.

Let us look briefly at the elementary thermodynamics of fluctuation behavior in an isolated system. Writing the combination of the First and Second Laws of Thermodynamics as

$$\Delta E = T\Delta S + W \tag{122}$$

where T is the temperature, W is the work done on or within the system and ΔS is the entropy change associated with some process occurring within the system; ΔE is the associated change in internal energy of the system. If an appreciable fluctuation occurs locally within the isolated system, $\Delta E = 0$, one finds

$$\Delta S = -\frac{W}{T} \tag{123}$$

Recalling that ΔS can be written according to elementary statistical thermodynamics as

$$\Delta S = k_{\mathrm{B}} \ln\left(\frac{P_2}{P_1}\right) \tag{124}$$

where P_2 is the thermodynamic probability of the fluctuated state and P_1 is the thermodynamic probability of the initial metastable state. We see that the less probable fluctuated state entails $\Delta S < 0$ and a local heterophase fluctuation occurs with a probability related to $\exp\left(-\frac{W}{k_{\mathrm{B}}T}\right)$, where W is essentially the work that must be expended, in principle, to create the fluctuation or perturbation. Such thermal fluctuations are associated with the initiation of phase transformations in a metastable parent phase and in the case of a nucleation event the thermodynamic driving force for the phase change can contribute to the work of formation of the fluctuation or nucleus of the new phase. We therefore expect that the rate of nucleation will be proportional to a term $\exp\left(-\frac{W}{k_{\mathrm{B}}T}\right)$, where W is the work required to assemble a critical nucleus as discussed subsequently.

The foundations of what metallurgists and materials scientists, physicists, and chemists call classical nucleation theory (CNT) were essentially laid by Gibbs (1875, ff) in the late nineteenth century. He clearly showed that the initiation of a phase transformation in an undercooled or supersaturated metastable phase produced by crossing a phase boundary in the relevant phase diagram, generally encounters a "nucleation barrier" inhibiting formation of the thermodynamically preferred phase or phases. This kinetic barrier or inhibition arises because the embryos of the new thermodynamically more stable phase(s) involve the formation of small regions separated by an interphase interface requiring an expenditure of (free) energy or work in their creation. This surface (free) energy or work presents a primary barrier to the formation of the new phase; however,

in the case of solid–solid phase transformations, the appearance of embryos/nuclei of the new phase may be accompanied by local misfit stresses/strains within the parent and emerging phase as a result of a difference in molar volume between phases or due to crystallographic mismatch. The associated elastic energy contributes to the work involved in the formation of the heterophase fluctuations which trigger the transformation of the system. In the language of the chemist the nucleation barrier is an activation barrier that controls the rate of the reaction or rate of formation of the "seeds" of the more stable phase.

Based on the seminal ideas of Gibbs, Volmer and Weber (1926), Farkas (1927) and Becker and Doering (1935) in the 1920s and 1930s formulated the approach of CNT primarily addressing the formation of nuclei in supersaturated vapor phases. This VWBD theory embodied the capillarity thermodynamics of Gibbs and was later modified and refined by Becker (1938), Turnbull and Fisher (1949), Russell (1970) and Aaronson et al. (2010) and applied to nucleation in condensed phases. In spite of the uncomfortable assumptions of the classical theory regarding extrapolation of bulk thermodynamic properties to the small embryos/nuclei and assumptions regarding the nature of the interphase interfaces between the parent and emerging phase, CNT has provided a useful semi-quantitative basis for systematizing the transformation behavior in a wide variety of material systems, and, importantly, for understanding the development of microstructure during the thermomechanical processing of engineering materials.

8.4.1 Basic Tenets of CNT

8.4.1.1 Fundamentals: Homogeneous Nucleation

In the first approximation to calculating the rate of nucleation we follow the quasi-equilibrium approach of Volmer and Weber (1926) which writes the nucleation rate as the product of the equilibrium concentration of critical nuclei times the rate at which single atoms/molecules (monomers) can join the nuclei rendering them supercritical and capable of spontaneous growth as transformation centers of the new phase. Any back flux of supercritical nuclei is neglected. We address the equilibrium distribution of embryos of various sizes up to the critical size using the usual Gibbs free energy approximation to describe the energetics of their formation which is not rigorous when the compressibility of the phases cannot be ignored. For condensed phases this is a useful approximation and the error entailed is quite small.

Whether in a vapor phase or condensed phase it is assumed that the embryos/nuclei of the incipient phase form through a series of bimolecular reactions of the form

$$\begin{aligned}
&\alpha_n + \alpha_1 \rightarrow \alpha_{n+1} \\
&\cdots \\
&\cdots \\
&\cdots \\
&\alpha^*_{n-1} + \alpha_1 \rightarrow \alpha^*_n. \\
&\alpha^*_n + \alpha_1 \rightarrow \alpha^*_{n+1}
\end{aligned}$$

where the α_n is a cluster or embryo containing n atoms/molecules (monomers) and α^*_n is a cluster of critical size; the last step is considered to be irreversible and governs the effective nucleation rate. The other bimolecular reactions are in metastable equilibrium and these equilibria determine the

distribution of embryos of a given size at any time in the system. The irreversible crossing of clusters of critical size to the supercritical state is assumed to not perturb the metastable equilibrium distribution. This quasi-equilibrium approach to the nucleation problem is fundamentally similar to the so-called Absolute Reaction Rate Theory (Glasstone et al., 1941) applied to the description of the rate of chemical reactions with the critical nucleus (cluster of critical size α_n^*) playing the role of the so-called "activated complex" or "transition state".

The overall reaction for cluster formation can be considered to be

$$n\alpha_1 = \alpha_n$$

and is assumed to be amenable to a treatment based on standard equilibrium chemical thermodynamics in terms of an equilibrium constant and the van't Hoff isotherm yielding an expression for the equilibrium concentration of embryos of various sizes n given by

$$\frac{N_n}{N_0} = \exp\left(-\frac{\Delta G_n}{k_B T}\right) \tag{125}$$

where N_n is the equilibrium number of embryos containing n monomers, N_0 is the number of unassociated atoms or molecules (essentially equal to the number of atoms or molecules in the system) and ΔG_n is a standard free energy of formation of embryos of size n. The number of clusters of critical size or critical nuclei at any time is then

$$\frac{N_{n^*}}{N_0} = \exp\left(-\frac{\Delta G_n^*}{k_B T}\right) = \exp\left(-\frac{\Delta G^*}{k_B T}\right) \tag{126}$$

(It should be noted that the critical nuclei are in unstable thermodynamic equilibrium with the supersaturated or undercooled parent phase.) See **Figure 51a**. The undercooled parent phase is characterized by an equilibrium distribution of embryos and nuclei at any time and the nucleation rate is simply governed by the concentration of critical nuclei C^* (number per unit volume) and the rate (ω^*) at which single atoms/molecules (monomers) can join these clusters of critical size taking them over the nucleation barrier and into the realm of spontaneous growth to form regions of the new more stable phase, that is, $I_v = C^*\omega^*$, where I_v is a widely used nomenclature designating the rate of homogeneous nucleation as the number of nuclei crossing the barrier per unit volume per unit time. In the case of condensation from a vapor phase ω^* can be estimated from the kinetic theory of gases. In condensed systems (liquid → solid and solid → solid transformations), the ω^* term involves a thermally activated diffusional jump from the parent phase to the critical nucleus and will be discussed in detail subsequently. See **Figure 51**.

Let us now look at the free energy of formation of embryos/nuclei using the conventional approach where the Gibbs free energy is used to estimate the work of formation of the critical nucleus. It is assumed that the transformation ($\alpha \rightarrow \beta$) is occurring at constant composition in a condensed phase and that bulk thermodynamic properties of the parent and product phases can be extrapolated to the small length scales involved in the nucleation process including the relevant surface energies and, furthermore, the interface between the parent and incipient phases is assumed to be sharp. The free energy of formation of a cluster containing n atoms/molecules, ΔG_n, written as a sum of a volume term and surface term, neglecting any strain energy accompanying the transformation as follows:

$$\Delta G_n = nv(\Delta G_v) + n^{\frac{2}{3}}\Sigma a_i \sigma_i \tag{127}$$

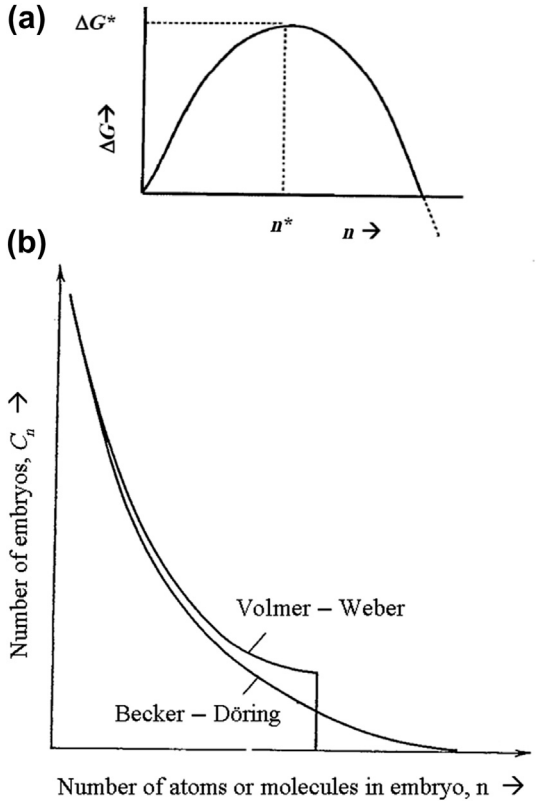

Figure 51 (a) Free energy of formation of clusters/embryos as a function of n, the number of atoms/molecules in the cluster. The cluster n^* is the cluster of critical size and the free energy of formation is ΔG^*. (b) The number of embryos as a function of cluster size n, according to Volmer–Weber and Becker–Doring approaches. After Reed-Hill (1972).

where v is the atomic/molecular volume, ΔG_V is the free energy released per unit volume of the phase change $\alpha \rightarrow \beta$, effectively the thermodynamic "driving force" for the transformation, and $n^{\frac{2}{3}} \sum a_i \sigma_i$ is the surface energy associated with the cluster/matrix interface expressed as a summation over facets i, where a_i is a geometric parameter, with units of area. Henceforth, this is written as simply as $\Sigma a\sigma$ following the notation of Turnbull (1956). Assuming that the embryos and nuclei develop with an optimized shape, one finds that ΔG_n as a function of size n, goes through a maximum at $n = n^*$. See Figure 51a. These critical values are given by

$$n^* = -\left(\frac{2(\Sigma a\sigma)}{3v\Delta G_V}\right)^3 \tag{128}$$

and

$$\Delta G_{n^*} = \Delta G^* = \frac{4(\Sigma a\sigma)^3}{27(v\Delta G_V)^2} \tag{129}$$

The activation barrier ΔG^* is the minimum work required through thermal fluctuations to create a heterophase fluctuation that can spontaneously decrease its free energy by growth to macroscopic

dimensions. The cluster containing n^* monomers is the critical nucleus and is in unstable equilibrium with the undercooled parent phase; the critical nucleus has equal probability of growing or shrinking to subcritical size whereas embryos with $n < n^*$ are more likely to shrink in size. For a spherical nucleus r^*, the following well-known textbook equations result

$$\Delta G^* = \frac{16\pi\sigma^3}{3\Delta G_V^2} = \frac{4\pi(r^*)^2\sigma}{3} \tag{130}$$

and

$$r^* = -\frac{2\sigma}{\Delta G_V} \tag{131}$$

where σ is the isotropic surface energy of the α–β interface. We see that in this simple formulation of the nucleation barrier that the work to create the critical nucleus through thermal fluctuations is one-third the actual work expended in forming the α–β interface, the other two-thirds is supplied by the thermodynamic driving force.

If elastic strains accompany the appearance of the new phase (solid–solid transformation) the associated strain energy must be considered in the energetics of cluster/embryo formation. Assuming that the strain energy scales with the volume of the cluster and is independent of shape, in the first approximation, it is straight forward to write a modified expression for the standard free energy of formation of a cluster containing n atoms/molecules as

$$\Delta G_n = n\nu(\Delta G_V + \Delta G_S) + n^{\frac{2}{3}}\Sigma a\sigma \tag{132}$$

where ΔG_S is the attendant strain energy per unit volume of the cluster. Again the free energy of formation passes through a maximum at ΔG^* and n^* given by

$$\Delta G^* = \frac{4(\Sigma a\sigma)^3}{27\nu^2(\Delta G_V + \Delta G_S)^2} \tag{133}$$

and

$$n^* = -\left(\frac{2(\Sigma a\sigma)}{3\nu(\Delta G_V + \Delta G_S)}\right)^3 \tag{134}$$

Since ΔG_V is negative and ΔG_S is positive, the strain energy reduces the effective driving force and can suppress transformation. Generally, strain energy will increase the undercooling or supersaturation required for nucleation of the new phase. The strain energy only affects the equilibrium shape of the critical nucleus when it becomes a significant fraction of the driving force, that is, a critical level of strain energy is required to markedly influence the nucleus shape.

If the surface and strain energies are functions of the shape and strain, the ΔG^* appears at a saddle point in a hyperspace $\Delta G_n = f(n, s, \varepsilon)$ where s is a shape parameter or set of shape parameters and ε is a set of strains in the matrix and nucleus and n is the number of monomers in the nucleus as before. The size and shape of the nucleus optimize the surface and strain energies at the saddle point n^*, s^*, ε^*. In crystalline solids the energetics of nucleation are complicated further by the fact that various orientation relationships between the parent and product phases can be established and various types of interfaces

(coherent, semicoherent, and incoherent) and elastic misfits can develop as discussed previously (see **Figure 43**). In **Figure 52** a coherent quasi-spherical precipitate is depicted showing attendant coherency strains.

Numerous investigators have approached the estimation of the strain energy attendant to nucleation in solid–solid transformations. We first mention the classic work of Nabarro (1940) which is strictly applicable to an incoherent nucleus where the strain energy introduced into the parent phase by an incompressible nucleus in the shape of a prolate or oblate spheroid is calculated. The results have been presented in numerous textbook treatments and treatises over the years (e.g. Christian, 2002) showing a maximum for a sphere and minimum for a disc and an intermediate level for a rod-like geometry. However, it is generally agreed today that incoherent nucleation is likely to be strain free if the diffusion of vacancies is possible and therefore these well-known results are not actually applicable to diffusional nucleation in solids (Russell, 1970).

Eshelby (1957) considered the formation of coherent nuclei of one cubic phase within another where the strain associated with the transformation is a uniform expansion or contraction, the nucleus and matrix are assumed to be elastically isotropic and have the same elastic constants. The strain energy per unit volume of the nucleus, E_S, is found to be given by

$$E_S = \frac{E\left(\varepsilon_{11}^T\right)^2}{(1-\nu)} \tag{135}$$

where $3\varepsilon_{11}^T = \Delta V/V$, the fractional volume misfit; E and ν are the Young's modulus and Poisson's ratio related to the shear modulus $G = \dfrac{E}{2(1+\nu)}$ in the isotropic approximation. The transformation strain ε_{11}^T is defined as $\varepsilon_{11}^T = \delta = \dfrac{a_m^0 - a_p^0}{a_m^0}$, the so-called disregistry or stress-free linear transformation strain, with a_m^0 and a_p^0 being the lattice parameters of the (unconstrained) matrix (m) and precipitate (p)

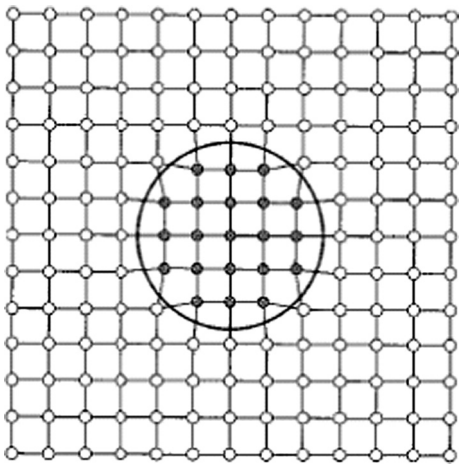

Figure 52 Coherent nucleus/embryo with attendant coherency strain.

phases, the term precipitate being used to generically refer to the nucleus/embryo of the new phase. This strain energy per unit volume of the nucleus/embryo is independent of shape. For volume misfits of a few to several percent the strain energy can reach values which are a significant fraction of the thermodynamic driving force (10–100 erg/cm^3).

Eshelby also considered the case of a rigid incompressible matrix and a nucleus with finite elastic constants (assuming elastic isotropy) and showed that the strain energy per unit volume of the nucleus is about three times that for the case of equal stiffnesses and given by

$$E_S = \frac{3E_P\delta^2}{2(1-2\nu_P)} \tag{136}$$

and for an incompressible nucleus the result is

$$E_S = \frac{3E_M\delta^2}{(1+\nu_M)} \tag{137}$$

which is approximately 1.5 times that for equal stiffnesses of the matrix and nucleus. If the transformation has associated shear strain, the Eshelby analysis assuming elastic isotropy and equal elastic stiffness of the matrix and nucleus predicts a level of elastic shear strain energy per unit volume of the precipitate which is a function of particle shape:

$$E_S = \frac{E\left(\varepsilon_{13}^T\right)^2}{(1+\nu)}\frac{\pi(2-\nu)}{4(1-\nu)}\frac{c}{r} \tag{138}$$

where ε_{13}^T is a shear component of transformation strain tensor of an oblate spheroid lying in the $x_1 - x_2$ plane and c/r the shape parameter of the oblate spheroid of major axis r and minor axis c (c being along x_3 normal to the plane $x_1 - x_2$). The strain energy now becomes a function of the particle shape described by c/r even in the isotropic approximation and equal elastic stiffness. This result generally favors a plate-like morphology but at the expense of surface energy indicating a nucleus shape which optimizes the surface energy and strain energy expenditures in the free energy of formation. Finally, Aaronson et al. (2010) report on the volume strain energy for coherent nuclei/precipitates with differing but finite elastic constants and considered the role of elastic anisotropy. For "soft" particles discs are favored; for "hard" particles spheres are the energetically favorable morphology. When the problem of anisotropy is addressed, clearly the orientation relationship becomes a new variable. It is found that generally if any anisotropy exists the strain energy is shape dependent.

Before formulating the supposedly more rigorous steady-state theory (Becker-Doering, 1935) description of the nucleation problem let us derive an expression for the rate of homogeneous nucleation based on the quasi-equilibrium approach developed earlier. Recall that the nucleation rate is considered to be given by the product of the concentration of critical nuclei times the rate at which this activated state can cross over the barrier, that is, the rate at which atoms/molecules (monomers) can attach themselves to the nuclei taking them into the regime of spontaneous growth accompanied by a progressive decrease in the free energy of the cluster or heterophase fluctuation. In condensed phases this latter step of atomic attachment will generally involve a thermally activated diffusional jump across the interface from parent phase to the nucleus and the rate, $\omega^{*'}$ expected to be controlled the number of monomers in the vicinity of the matrix–nucleus interface times an Arrhenius-type term $\exp\left(-\frac{q_m}{k_B T}\right)$

where q_m is an activation energy for the diffusional jump or atomic migration. Thus, the nucleation rate can be expressed as

$$I_V = \omega^* C^* = K_{\text{homo}} \exp\left(-\frac{(\Delta G^* + q_m)}{k_B T} \right) \tag{139}$$

where the ω^* term is the rate of atomic jumping across the interface and C^* is the concentration of critical nuclei in unstable thermodynamic equilibrium with the parent phase. The result is typically

$$I_V = (10^{30} \text{ to } 10^{40}) \exp\left(-\frac{(\Delta G^* + q_m)}{k_B T} \right) \tag{140}$$

and a sensible nucleation rate is expected for $\Delta G^* = (60\text{–}70)\ k_B T$ in most material systems. An important feature of this result is that the onset of nucleation is so sharp that the nucleation rate can be expected to vary over as much as five or six orders of magnitude in a temperature range of only a few degrees, that is, there is virtually a critical undercooling or supersaturation required to initiate nucleation (see **Figure 53**). This precipitous rise or burst slows down and passes through a maximum and eventually decays exponentially to zero at 0 K. This drop-off stems from the limited atomic mobility at low temperatures (the $\exp\left(-\frac{q_m}{k_B T}\right)$ term).

The steady-state theory of nucleation developed by Becker and Doering (1935) and others (e.g. Zeldovich, 1943) attempts to formulate the nucleation problem more fundamentally as a kinetic process defining the nucleation rate as a steady-state current through the embryo size distribution or along the n axis of the ΔG_n versus n-plot employed earlier. In this treatment where the nucleation rate is essentially a steady-state current or diffusion flux in "n-space" account is taken that embryo/clusters which actually exceed the critical nucleus size described earlier may decompose back to the subcritical regime and furthermore takes into account that the effective concentration of clusters in the vicinity of the top of the barrier is perturbed from the metastable equilibrium value. See **Figure 51**. The current through the size distribution is written as a difference equation:

$$j = \beta(n)C(n) - \alpha(n+1)C(n+1) \tag{141}$$

where $\beta(n)$ is the rate at which monomers are absorbed by embryos of size n and $\alpha(n+1)$ is the rate of decomposition of embryos of size $n+1$; $C(n)$ nd $C(n+1)$ are the steady-state concentrations of

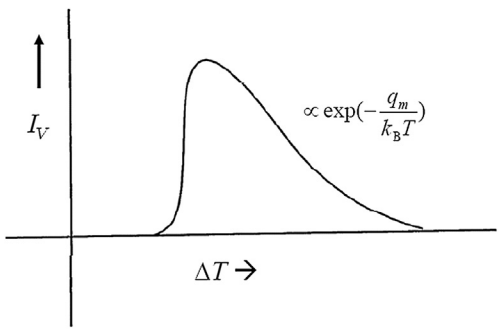

Figure 53 Predicted variation of the rate of homogeneous nucleation as a function of undercooling.

embryos of sizes n and $n+1$, respectively (C_n^0 and C_{n+1}^0 are then taken as the equilibrium concentrations). See Figure 51b. Solving for the steady-state flux yields the following result:

$$J = Z\beta^* C_{n^*}^0 = Z\omega^* C^* = Z\omega^* N \exp\left(-\frac{\Delta G^*}{k_B T}\right) \tag{142}$$

wherein Z is called the Zeldovich nonequilibrium factor, $\beta^* = \omega^*$ is the rate at which single atoms/molecules (monomers) can join the critical nucleus, $C_{n^*}^0 = C^*$ is the equilibrium concentration of clusters of size $n = n^*$ (critical nuclei), N and ΔG^* have their usual meaning previously defined earlier. The Zeldovich factor is shown to be related to the curvature of the ΔG_n versus n curve at $n = n^*$. It should be pointed out that $Z \approx 10^{-1}$ to 10^{-2} for most systems of interest, thus, the nonequilibrium factor reduces the predicted nucleation rate by a factor of about 100 and given that the preexponential for condensed systems is $\approx 10^{30}$ to 10^{40} this correction is not likely to be resolved experimentally. However, the theory indicates that a time-dependent nucleation rate should be observed given by

$$J(t) = Z\omega^* N \exp\left(-\frac{\Delta G^*}{k_B T}\right)\exp\left(-\frac{\tau}{t}\right) \tag{143}$$

where τ is essentially an incubation time characterizing the approach to steady-state nucleation and approximately given by $\tau \approx \frac{1}{\omega^* Z}$. See Figure 54.

8.4.1.2 Heterogeneous Nucleation

It must be emphasized again that in the vast majority of phase transformations occurring in metallurgical (materials) systems involving nucleation and growth of new phases, homogenous nucleation is extremely rare and heterogeneous or catalyzed nucleation generally dominates the phase change at significantly reduced undercoolings or supersaturations compared with those required to induce homogeneous nucleation. It is extremely difficult to isolate systems whether undercooled melts, supersaturated vapors or solid solutions from the influence of catalyzing singularities such as container/mold walls, impurity particles or lattice defects. Some ingenious experimental approaches such as the classic small droplets experiments used in the study of solidification (Vonnegut, 1948; Turnbull and Fischer, 1949) have been designed to isolate the influence of nucleation catalysts. Large undercoolings compared with those observed for the freezing of bulk melts were observed but the validity of the results and interpretation of

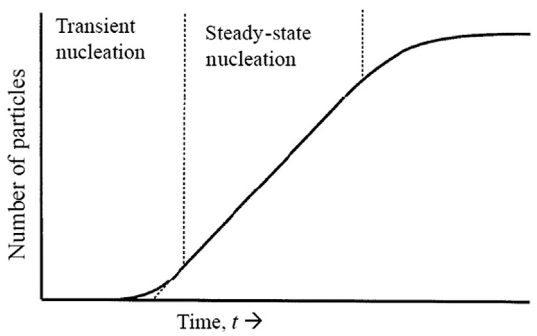

Figure 54 Number of particles nucleated as a function of time, showing an interval of steady-state nucleation.

these famous experiments has been called into question as to whether the realm of homogeneous nucleation was actually observed (Kelton and Greer, 2010). However, the Gibbsian capillarity-based CNT outlined earlier for homogeneous nucleation provides a framework for constructing an analysis of the energetics and kinetics of heterogeneous nucleation. (It should be mentioned that Gibbs also addressed the energetics of heterogeneous nucleation compared with homogeneous nucleation.)

Heterogeneous nucleation preferentially at "special sites" occurs because the interaction of the embryos/nucleus with the singularity, for example mold wall during freezing, reduces the free energy barrier ΔG^*, allowing the formation of the new phase at substantially reduced undercoolings. Nucleation of the solid phase during the freezing of undercooled melts is known to take place on impurity particles and container walls and preferential nucleation in solid–solid transformations is well established to occur at grain boundaries and dislocations (Christian, 2002). Generally, catalyzing the nucleation process on a planar singularity or surface essentially depends on a net reduction of surface energy required to form a nucleus (in the absence of significant strain energy effects).

Following a simple surface energy/capillarity approach, the free energy of formation of an embryo/nucleus of a β phase on a surface/substrate(s) within an undercooled α phase can be written as

$$\Delta G_s = A_{\beta s} W_s + A_{\alpha\beta}\sigma_{\alpha\beta} + V^{\beta}\Delta G_V \tag{144}$$

where $A_{\beta s}$ is the area of the β–s interface created, $A_{\alpha\beta}$ is the area of the α–β interface created and V^{β} is the volume of the spherical cap (see **Figure 55**); $\sigma_{\alpha\beta}$ is the isotropic surface energy of the α–β interface and ΔG_v has its usual meaning, that is, the free energy released per unit volume of the β phase formed. The parameter $W_s = \sigma_{\beta s} - \sigma_{\alpha s}$ is the free energy change accompanying the replacement of a unit area of the α–s interface with a unit area of β–s interface with surface energies $\sigma_{\alpha s}$ and $\sigma_{\beta s}$, respectively. There are three relevant interfacial free energies or surface energies $\sigma_{\alpha\beta}$, $\sigma_{\alpha s}$ and $\sigma_{\beta s}$ and can be related by $\sigma_{\alpha\beta}\cos\ \theta + \sigma_{\beta S} = \sigma_{\alpha S}$ assuming an incompressible substrate and mechanical equilibrium at the junction of the σ, β and s phases, where θ is called the contact angle from surface chemistry describing the "wetting" of the substrate by the β phase. Also, the contact angle can be written in terms of W_s as $\cos\theta = -\dfrac{W_s}{\sigma_{\alpha\beta}}$. For a spherical cap of radius r, $A_{\beta s} = \pi r^2 \sin^2\theta$, $A_{\alpha\beta} = 2\pi r^2(1-\cos\theta)$ and $V^{\beta} = \dfrac{\pi r^3(2 - 3\cos\theta - \cos^3\theta)}{3}$. Inserting these relations into Eqn (144) and setting $\dfrac{\partial \Delta G_s}{\partial r} = 0$, the nucleation barrier is found to be

$$\Delta G_s^* = \frac{16\pi\sigma_{\alpha\beta}^3 f(\theta)}{3\Delta G_V^2} \tag{145}$$

where

$$f(\theta) = \frac{\left(2 - 3\cos\theta + \cos^3\theta\right)}{4} \tag{146}$$

whereby $f(\theta)$ reduces the nucleation barrier for $\theta < \pi$; that is, the "wetting" of the substrate surface by the β phase catalyzes the nucleation process. Also, it is found that

$$r^* = -\frac{2\sigma_{\alpha\beta}}{\Delta G_V} \tag{147}$$

and therefore the critical radius (of curvature) is identical to that for homogeneous nucleation but the volume is decreased. Indeed, an interesting result of this analysis is that ΔG_s^* is proportional to the

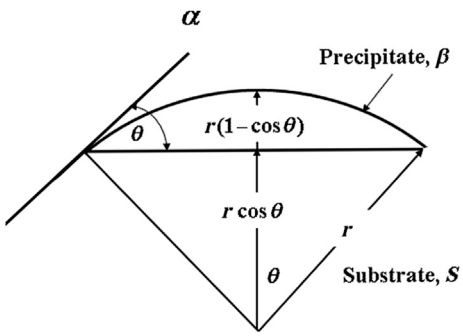

Figure 55 A schematic of a spherical cap embryo showing the relevant geometric parameters.

volume of the critical nucleus V^*, and it can be shown that for $\theta = \pi/2$ the nucleation barrier ΔG_s^* is reduced to exactly one-half that for homogeneous nucleation. Also, note that $\Delta G_s^* \to 0$ as $\theta \to 0$, that is, the nucleation barrier vanishes in the case of "perfect wetting".

The treatment earlier can readily be used to address the heterogeneous nucleation of new phases on grain boundaries in solid–solid transformations (Christian, 2002). It is well established experimentally that grain boundaries (surfaces, edges and corners) act as favorable sites for nucleation in metallic and ceramic materials in conjunction with polymorphic transformations, massive transformations, precipitation and eutectoid decomposition. A straightforward extension of the foregoing analysis is the case of an incoherent allotriomorph forming on a grain boundary surface in the shape of a doubly spherical lens (see Figure 56b). The energetics of formation of an embryo/nucleus on the boundary surface can be formulated as

$$\Delta G_s(B) = V^\beta \Delta G_\gamma + A_{\alpha\beta}\sigma_{\alpha\beta} - A_{\alpha\alpha}\sigma_{\alpha\alpha} \tag{148}$$

where V^β is the volume of the β embryo/nucleus, $A_{\alpha\beta}$ is the area of the α–β interface created and $A_{\alpha\alpha}$ is the area of the grain boundary removed and ΔGv is the free energy released per unit volume accompanying the $\alpha \to \beta$ transformation as above. The geometric terms for this shape are given by

$$V^\beta = \frac{2\pi r^3\left(2 - 3\cos\theta - \cos^3\theta\right)}{3} \tag{149}$$

$$A_{\alpha\alpha} = \pi r^2 \sin^2\theta \tag{150}$$

$$A_{\alpha\beta} = 4\pi r^2(1 - \cos\theta) \tag{151}$$

where r is the radius of curvature of the spherical cap and θ is the contact angle characterizing the interaction of the embryo/nucleus with the planar grain boundary surface. Clearly, in this case, $2\cos\theta = \dfrac{\sigma_{\alpha\alpha}}{\sigma_{\alpha\beta}}$, where $\sigma_{\alpha\alpha}$ is the grain boundary energy and $\sigma_{\alpha\beta}$ is the interfacial free energy associated with the new α–β interface. Setting $\dfrac{\partial \Delta G_S}{\partial r} = 0$, as earlier, one finds that

$$\frac{\Delta G_S^*(B)}{\Delta G_H^*} = \frac{2 - 3\cos\theta + \cos^3\theta}{2} \tag{152}$$

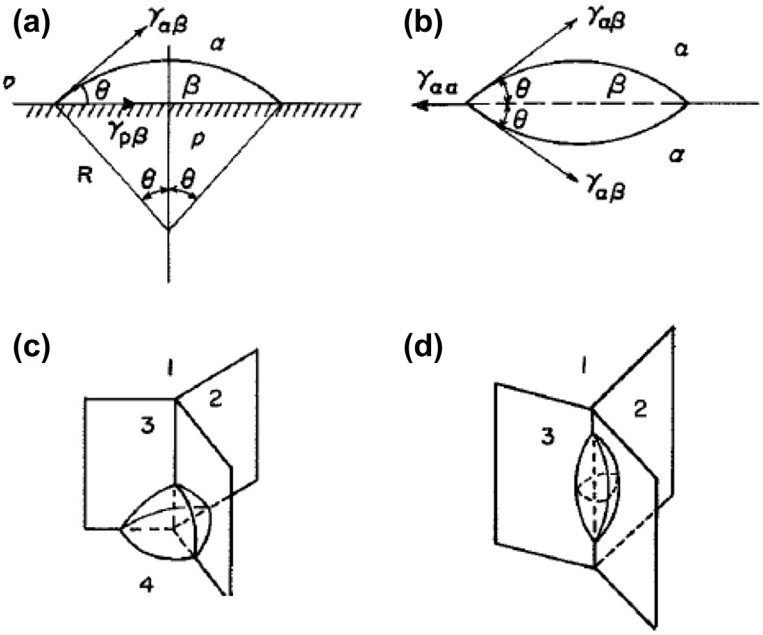

Figure 56 Nucleus/embryo geometries for nucleation at grain boundary faces, corners and edges. After Jena and Chaturvedi (1992).

where $\Delta G_S^*(B)$ is the reversible work to create the grain boundary nucleus on the boundary surface and $\Delta G_H^* = \dfrac{16\pi\sigma_{\alpha\beta}^3}{3\Delta G_V^2}$ is the nucleation barrier for homogeneous nucleation of β within the undercooled α phase. The catalytic potency of the grain boundary surface increases as the ratio $\sigma_{\alpha\alpha}/\sigma_{\alpha\beta}$ increases and the nucleation barrier vanishes as $\sigma_{\alpha\alpha} \rightarrow 2\ \sigma_{\alpha\beta}$ or as $\theta \rightarrow 0$.

Given the well-known topology of polycrystalline aggregates we know that special grain boundary sites are located at the intersection of grain boundaries such as three-grain junctions (edges) and four-grain junctions (corners) and a similar analysis can be carried out for these more complex embryo/nucleus shapes (see **Figure 56**c and d). The results indicate a greater reduction in ΔG_s^* for the grain boundary edge and corner sites, that is, $\Delta G_s^*(\mathrm{C}) < \Delta G_s^*(\mathrm{E}) < \Delta G_s^*(\mathrm{B}) < \Delta G_H^*$ as shown in **Figure 57**; $\Delta G_s^*(\mathrm{C})$, $\Delta G_s^*(\mathrm{E})$ and $\Delta G_s^*(\mathrm{B})$ refer to the nucleation barriers at the corner (C), edge (E) and planar (B) boundary sites, respectively. It should be mentioned that $\Delta G_s^* \rightarrow 0$ at different values of $\dfrac{\sigma_{\alpha\alpha}}{\sigma_{\alpha\beta}}$ for the corner and edge sites, namely, $\Delta G_s^*(\mathrm{C}) \rightarrow 0$ as $\sigma_{\alpha\alpha}/\sigma_{\alpha\beta} \rightarrow \frac{2\sqrt{2}}{\sqrt{3}}$ and $\Delta G_s^*(\mathrm{E}) \rightarrow 0$ as $\dfrac{\sigma_{\alpha\alpha}}{\sigma_{\alpha\beta}} \rightarrow \sqrt{3}$. Importantly, heterogeneous nucleation at grain boundary sites can markedly reduce the nucleation barrier for the formation of the new more stable phase allowing transformation to be initiated at substantially reduced undercoolings or supersaturations; however, the contribution of these sites to an overall nucleation rate is always limited by the density of these sites in the parent phase, as mentioned earlier. The density of the various sites (surfaces/faces (B),

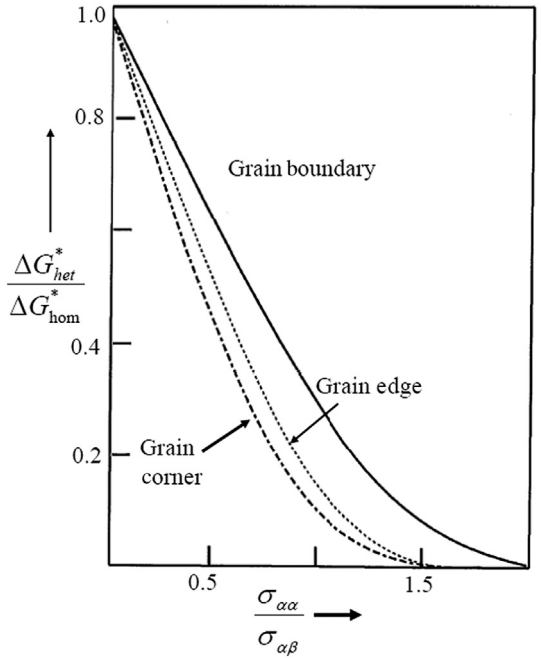

Figure 57 Nucleation barriers for heterogeneous nucleation on grain boundary sites compared with homogeneous nucleation. After Cahn (1956).

edges (E), corners (C)) is expected to scale as $\frac{\delta}{d}$, $\left(\frac{\delta}{d}\right)^2$ and $\left(\frac{\delta}{d}\right)^3$, respectively, where δ is the grain boundary thickness and d is the average grain diameter $\left(\frac{\delta}{d} \approx 10^{-5} - 10^{-6}\right)$. Cahn (1956) has analyzed this aspect of the problem, in detail, and shows that corner and edge sites become important with respect to the overall nucleation rate primarily at very small undercoolings and when $\frac{\sigma_{\alpha\alpha}}{\sigma_{\alpha\beta}}$ is relatively small. See Figure 57.

Other factors can influence the energetics of nucleation at grain boundaries such as the possibility of grain boundary nuclei establishing a low-energy coherent or semicoherent interface and an orientation relationship with one of the grains and an incoherent interface with respect to an adjoining grain with subsequent grow governed primarily by migration of the more mobile incoherent interphase interfaces. Also, facets can create low-energy regions along an interphase interface at special orientations (see Figure 58a and b).

Many investigators dating back to the 1940s suggested that dislocations might be expected to catalyze nucleation of phases in solid-state transformations. Cahn (1957) presented the first quantitative treatment of heterogeneous nucleation at dislocations addressing the energetic of nucleation of incoherent nuclei. Gomez-Ramirez and Pound (1973) also subsequently analyzed the case of incoherent nuclei, whereas Larche' (1979), Lyobov and Solov'yev (1965) and Dollins (1970) considered the case of coherent nuclei. In the first approximation, Cahn assumed that an incoherent nucleus/embryo of cylindrical shape of radius r, forming along a straight dislocation, effectively removes the strain energy

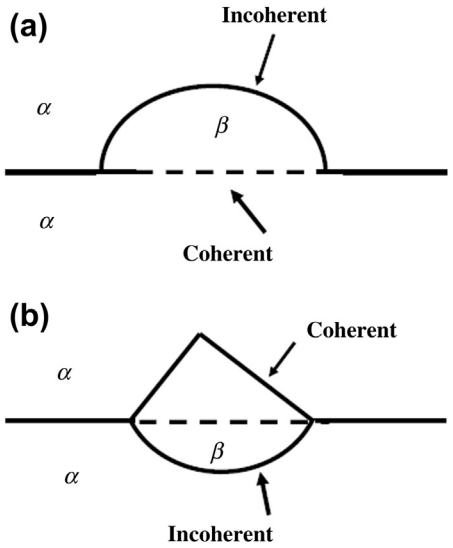

Figure 58 Grain boundary nuclei showing an interplay between coherent (semicoherent) and incoherent segments of the interphase interface.

of the dislocation over a unit length. The free energy of formation of the embryo per unit length is written as

$$\Delta G(r) = \pi r^2 \Delta G_V - A \ln r + 2\pi r\sigma + \text{constant} \tag{153}$$

where A is taken as $\dfrac{\mu b^2}{4\pi(1-\nu)}$ for an edge and $\dfrac{\mu b^2}{4\pi}$ for a screw dislocation; μ is the shear modulus and b is the Burgers vector with all other parameters having their usual meanings.

Taking $\dfrac{\partial \Delta G(r)}{\partial r} = 0$, it is found that, in general, $\Delta G(r)$ passes through a minimum at small r and then a maximum at intermediate values of r as a function of r. See Figure 59. A parameter $\alpha_D = -\frac{2A\Delta G_V}{\pi\sigma^2}$ emerges as an important variable governing the behavior. For $\alpha_D > 1$ the driving force/strain energy term dominates the surface energy term and there is no barrier to nucleation on the dislocation and spontaneous growth of the new phase occurs along and out from the line defect. If $\alpha_D < 1$, a subcritical metastable cylinder along the line defect is predicted to form along the dislocation (Cottrell atmosphere) at small r and a nucleation barrier appears at larger $r = r^*$ as shown in Figure 59. Cahn then addressed the optimum shape of a nucleus and calculated the free energy barrier to form a nucleus on the dislocation compared with that for homogeneous nucleation. See Figure 59b and 60. Given that the total number of dislocation sites essentially scales as $\approx N^{1/3}\rho$ where N is the total number of atomic sites in the system and ρ is the dislocation density, heterogeneous nucleation at dislocations is expected to become important when $\alpha_D \approx 0.5$ for $\rho \approx 10^8$–10^{10} cm^{-2}. Clearly, α_D reflects the catalytic potency of dislocations to induce heterogeneous nucleation in this treatment. Gomez-Rameriz and Pound (1973) attempted to investigate the dislocation strain field effects in more detail assuming that the nucleation barrier is relatively insensitive to the nucleus shape. In both cases, dislocations are predicted to lower the barrier for incoherent nucleation of the new phase. The works of

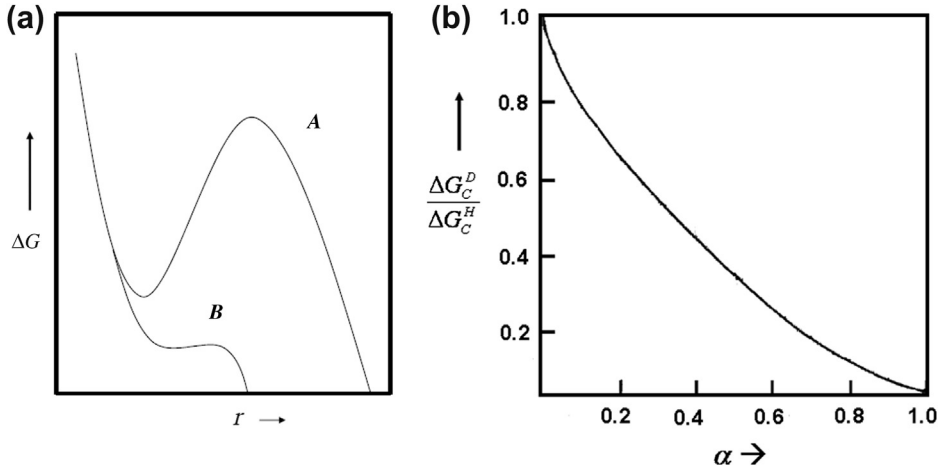

Figure 59 (a) Free energy of formation of a nucleus on a dislocation for $\alpha_D < 1$ and $\alpha_D > 1$ (after Cahn, 1957). (b) The nucleation barrier to form a nucleus on a dislocation as a function of α_D compared with the barrier for homogeneous nucleation of a spherical precipitate. After Cahn (1957).

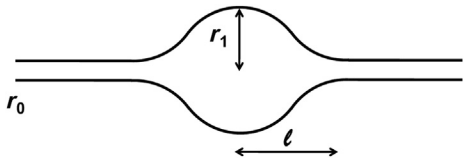

Figure 60 A schematic representation of a nucleus forming along a dislocation line. After Cahn (1957).

Lyubov and Solovyov (1965), Rollins (1970) and Larche′ (1979) on the nucleation of coherent precipitates suggest that the elastic interaction of the nuclei and dislocation strain fields significantly relieves the usual strain energy term in the nucleation energetics. The nuclei form preferentially in the compressive or expansive regions of the dislocation strain field, that is, in regions that relieve the largest proportion of the dilatational transformation strains (edge). However, elastic analysis indicates that nucleation can be suppressed near dislocations if the nucleus has a small misfit strain and if the new phase has a much higher shear modulus than that of the matrix. The analysis of Larche′ of the coherent nucleation problem suggests that for an edge dislocation the interaction of a misfitting spherical nucleus/embryo with the elastic field of the dislocation can be folded into a correction to the effective interfacial free energy term $\sigma_{\alpha\beta}$ wherein the usual expression for $\sigma_{\alpha\beta}$ is replaced by $\sigma_{\alpha\beta} - \frac{\mu b^2(1+\nu)\varepsilon^T}{9\pi(1-\nu)}$ where ε^T is the stress-free transformation strain. This correction can be very significant ($\approx$30–40%) in systems with a large $e^T \approx 0.05$. These analyses for incoherent and coherent nuclei indicate a significant catalytic potency of dislocations on the nucleation process of similar magnitude relative to that of homogeneous nucleation, in general.

From this discussion of heterogeneous nucleation in solid–solid transformations it must be emphasized again that the impact of catalyzed nucleation at singularites in the system with respect to the

Table 2 Nucleation site densities (after Nicholson, 1970)

	Grain boundary		*Grain edge*		*Dislocation density*		*Vacancy* N_V
Defect density	Grain size, 5×10^{-4} m	Grain size, 5×10^{-6} m	Grain size, 5×10^{-4} m	Grain size, 5×10^{-6} m	$10^7/cm^2$	$10^{10}/cm^2$	10^{-6}
$\frac{N_S^{het}}{N_S^{hom}}$	10^{-6}	10^{-4}	10^{-13}	10^{-9}	10^{-8}	10^{-5}	10^{-6}

overall nucleation rate and transformation behavior is always limited by the density of these special sites. Table 2 after Nicholson (1970) tabulates the typical density of sites relative to that for homogeneous nucleation. Under circumstances where there is an actual competition between heterogeneous and homogeneous nucleation, the rate of heterogeneous compared with that for homogeneous nucleation will scale to a good approximation as ratio of available sites times $\exp\left(\frac{\Delta G^*_{\mathrm{HET}} - \Delta G^*_{\mathrm{HOMO}}}{k_B T}\right)$ where $\Delta G^*_{\mathrm{HET}} < \Delta G^*_{\mathrm{HOMO}}$ and the ratio of sites $N_{\mathrm{HET}}/N_{\mathrm{HOMO}} << 1$. This analysis clearly indicates that heterogeneous nucleation will be most significant at small undercoolings or supersaturations. These conclusions are in excellent agreement with a plethora of experimental results.

Stowell (2002) has subjected the classical (capillarity) theory of nucleation to a critical analysis incorporating some ideas of Kashchiev (2000) in the evaluation and reevaluation of the data of LeGoues and Aaronson (1984) and Kirkwood (1970) from studies of well-known precipitation systems. He found reasonable agreement with the form of the equations of the capillarity model when noise associated with heterogeneous nucleation during some heat treatments was sorted out. A number of investigators (Kampmann and Kahlweit, 1970; Wagner and Kampmann, 1991) have called attention to competitive coarsening during the early stages of nucleation and growth and this will be discussed in the section on precipitation. Kelton and Greer (2010) in their recent book focused on nucleation in condensed systems present an extraordinary overview of nucleation applied to a broad range of topics from materials to biology; however, the treatment of nucleation in Christian's treatise on transformations [2002] remains the most rigorous treatment of the subject.

We close this section on CNT by pointing out that a treatment of nucleation behavior can be developed wherein the ad hoc assumptions of a sharp interface between the parent and emerging phases as well as a uniform composition within the effective nuclei are relaxed. This nonclassical formulation sometimes referred to as Cahn–Hilliard (1958 and 1959) nucleation will be addressed in the precipitation section as well.

8.5 Diffusional Growth of Phases

8.5.1 Parent and Product Phases Have the Same Composition

After *nucleation* of a more stable phase within a metastable phase the nuclei moving over the nucleation barrier generally enter the stage wherein their *growth* leads to a continuous decrease in the free energy of the system. The first case we address is where the growing phase has the same composition as the parent phase. This analysis is relevant to allotropic/polymorphic and massive transformation in the solid state. The migration of the interphase interface is assumed to be essentially

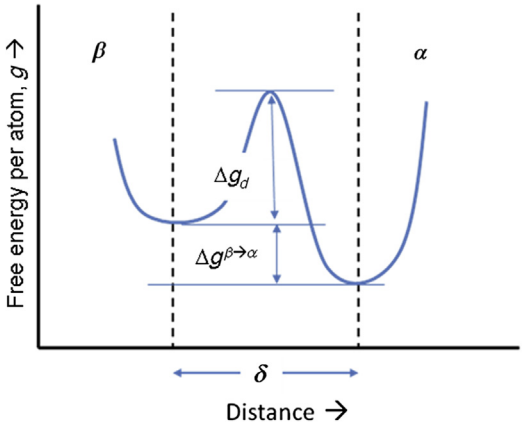

Figure 61 Variation of the free energy per atom, g, in the vicinity of the α/β interface during the transformation $\beta \rightarrow \alpha$; $\Delta g^{\beta \rightarrow \alpha}$ is the thermodynamic driving force and Δg_d is the free energy of activation for an elementary diffusional jump of an atom from β to α at the interface. The effective thickness of the interface is δ.

isotropic and controlled by thermally activated atomic jumps across the interface involving continuous, nearly random jumping of individual atoms or atomic attachment mediated by a ledge mechanism. We begin by describing essentially random atomic detachment and attachment at the interface between two phases α and β where α is the more stable growing phase. The interphase boundary is assumed to be disordered or incoherent and strain energy effects are assumed negligible. In the vicinity of the α–β interface the atoms see a free energy profile like that shown in Figure 61. The atoms are jumping from β to α and from α to β but the energetics of these elementary atomic processes give rise to a net transfer of atoms from β to α leading to growth of the α phase and the consumption of the β phase.

Let us assume that the effective number of atoms per unit area N_S at the boundary is the same at both sides of the interface, that is, $N_S^{\alpha} = N_S^{\beta} = N_S$ and the vibrational frequency (attempt frequency) of these atoms is taken to be $\nu \approx 10^{12}\ \mathrm{s}^{-1}$. From elementary rate theory we expect the rate of jumping of atoms from the β phase to the α phase to be described essentially by

$$\frac{\mathrm{d}N^{\beta \rightarrow \alpha}}{\mathrm{d}t} = N_S \nu \exp\left(-\frac{\Delta g_d}{k_B T}\right) \tag{154}$$

wherein the atoms at the interface "attack" the activation barrier $\Delta g_d \nu$ times per second and the probability that an atom will have enough (free) energy to surmount the barrier on any attempt is $\exp\left(-\frac{\Delta g_d}{k_B T}\right)$. Similarly, we write for the jumping of atoms from α to β

$$\frac{\mathrm{d}N^{\beta \rightarrow \alpha}}{\mathrm{d}t} = N_S \nu \exp\left(-\frac{\Delta g_d + \Delta g^{\beta \rightarrow \alpha}}{k_B T}\right) \tag{155}$$

where Δg_d is the free energy barrier controlling thermally activated jumps from β to α : the effective barrier for reverse jumping $\alpha \rightarrow \beta$ is larger by $\Delta g^{\beta \rightarrow \alpha}$, the thermodynamic "driving force" (per atom) for

the $\alpha \rightarrow \beta$ transformation. The net flux of atoms (atoms $cm^{-2}\ s^{-1}$) across the interface is given by the difference in these jump rates and can be written as

$$\frac{dN}{dt} = \frac{dN^{\alpha\rightarrow\beta}}{dt} - \frac{dN^{\beta\rightarrow\alpha}}{dt} = N_S\nu \exp\left(-\frac{\Delta g_d}{k_B T}\right)\left(1 - \exp\left(-\frac{\Delta g^{\beta\rightarrow\alpha}}{k_B T}\right)\right) \tag{156}$$

This net flux can be converted to a linear growth rate or interface velocity since a net transfer of N_S atoms across a unit area of interface advances the interface by a distance δ, the thickness of the interfacial region; thus, we can write the velocity of the interface (cm s^{-1}) as

$$V = \delta\nu \exp\left(-\frac{\Delta g_d}{k_B T}\right)\left(1 - \exp\left(-\frac{\Delta g^{\beta\rightarrow\alpha}}{k_B T}\right)\right) \tag{157}$$

The velocity of the interface or growth rate of the more stable low temperature phase α into the undercooled high-temperature β phase generally will vary directly as the difference in free energy as a function of undercooling below the equilibrium transformation temperature $T_t = T_{\alpha\beta}$. See **Figure 62**. At temperatures where $k_B T >> \Delta g^{\beta\rightarrow\alpha}$ taking $\left(1 - \exp\left(-\frac{\Delta g^{\beta\rightarrow\alpha}}{k_B T}\right)\right.$ after expanding in a Taylor series gives a velocity $V \approx \delta\nu \frac{\Delta g^{\beta\rightarrow\alpha}}{k_B T} \exp\left(-\frac{\Delta g_d}{k_B T}\right)$ essentially proportional to the thermodynamic driving force. Recall that $\frac{\Delta g^{\beta\rightarrow\alpha}}{k_B T}$ is proportional to ΔT at small undercoolings. At low temperatures $k_B T << \Delta g^{\beta\rightarrow\alpha}$, the $\exp\left(-\frac{\Delta g^{\beta\rightarrow\alpha}}{k_B T}\right)$ term is small and the velocity $V \approx \delta\nu \exp\left(-\frac{\Delta g_d}{k_B T}\right)$, that is, the rate of growth is limited by the atomic mobility at low temperatures decreasing exponentially as $T \rightarrow 0$ K. See **Figure 63**. This description appears to apply very well to the temperature dependence of the growth rate of the transformation α-Sn (white) $\rightarrow$ β-Sn (gray) below $T_{\alpha\beta} \approx 286$ K (13 °C). See **Figure 64**a and b. Note that for the reverse transformation β-Sn (gray) $\rightarrow$ α-Sn (white) the growth rate is monotonically increasing with temperature since the atomic mobility is increasing continuously as the transformation temperature is raised.

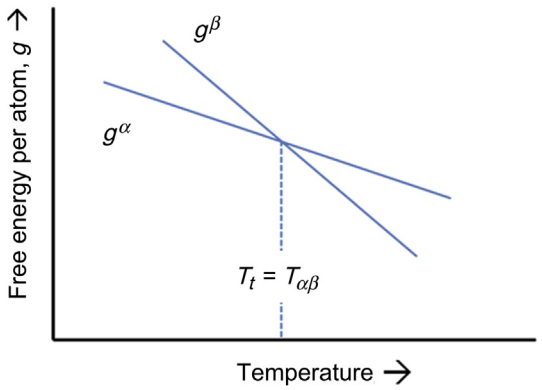

Figure 62 The free energy per atom of the α and β phases as a function of temperature; $T_t = T_{\alpha\beta}$ is the equilibrium transition temperature for the allotropic/polymorphic phase change.

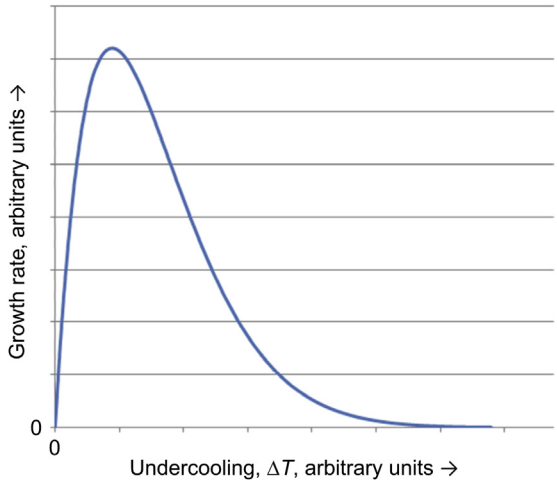

Figure 63 The growth velocity of the α/β interface as a function of ΔT ($\Delta T = T_{\alpha\beta} - T$), predicted by Eqn (156). Note that the velocity varies approximately linearly with ΔT for small ΔT and decreases exponentially at large ΔT and low temperatures.

This description of the growth rate for a compositionally invariant transformation is often referred to in the literature as the Burke–Turnbull analysis (see Burke and Turnbull, 1952) which can be extended to include the case wherein the atomic attachment and detachment processes involve ledges moving within the interphase interface. See Figure 65. A modified Burke–Turnbull equation is often invoked where the velocity of the interface is written as follows:

$$V = \frac{h}{\lambda}\delta v \exp\left(-\frac{\Delta g_d}{k_B T}\right)\left(1 - \frac{\Delta g^{\beta\to\alpha}}{k_B T}\right) \tag{158}$$

with h being the average ledge height and λ the average ledge spacing. This modified version has been applied to the massive transformation occurring in several systems as discussed subsequently.

8.5.2 Parent and Product Phases Having Different Compositions

Let us consider diffusional growth of a spherical precipitate phase β within a supersaturated solid solution α of average composition C_0. See Figure 66. We assume that during the early and intermediate stages (times) of growth the matrix composition far from the growing particle remains C_0 and a solute-depleted region exists primarily in the near vicinity of the particle. See Figure 66. In our initial approximation we assume that growth is diffusion-controlled and that local equilibrium exists at the α–β interface, that is, the composition of α is $C_\alpha^\beta = C_\alpha^\beta(\infty) = C_\alpha^E$ which is in thermodynamic equilibrium with the β phase of composition $C_\beta^\alpha = C_\beta^\alpha(\infty) = C_\beta^E$ given by the phase diagram. If one employs a so-called quasi-steady-state solution to the diffusion field (this assumes that the concentration profile in the matrix changes very slowly with time), the solution to Fick's second law is approximately

$$C(\rho) = \frac{A}{\rho} + B \tag{159}$$

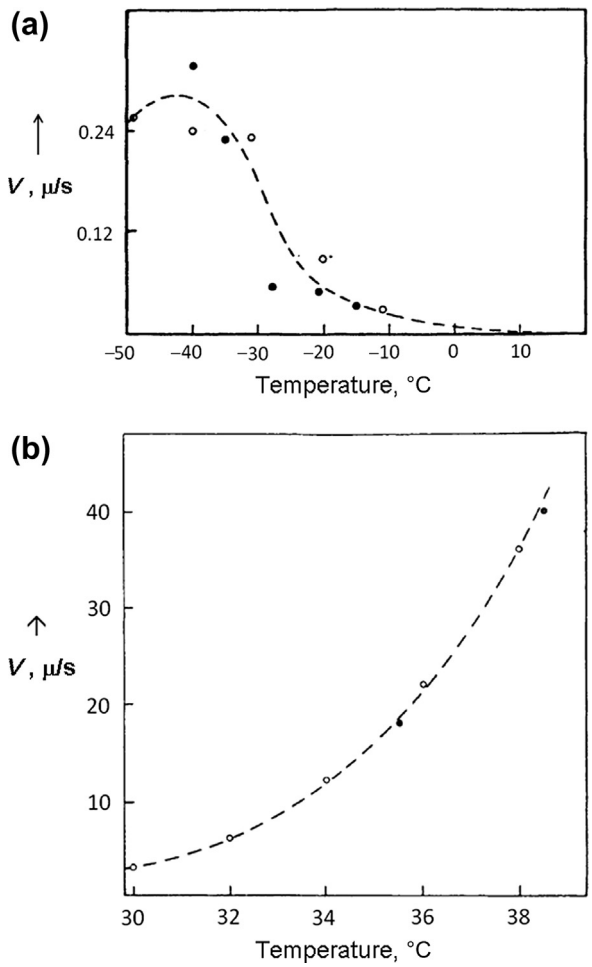

Figure 64 Experimental results for the α to β and the β to α transformations in Sn, showing the variation of the growth rate V as a function of undercooling (a) and superheating (b). After Burgers and Groen (1957).

where ρ is the distance from the center of the particle; the instantaneous radius of the particle is taken to be $\rho = R$. Since at $\rho >> R$ the composition is taken to be C_0 and at the interface $\rho = R$ the composition is fixed at C_α^E the constants A and B can readily be determined and the solution for the concentration profile in the matrix is given by

$$C(\rho) = C_0 - \frac{R}{\rho}\left(C_0 - C_\alpha^E\right) \tag{160}$$

and the concentration gradient at the advancing interface is given by

$$\left(\frac{\partial C(\rho)}{\partial \rho}\right)_{\rho=R} = \frac{\left(C_0 - C_\alpha^E\right)}{R} \tag{161}$$

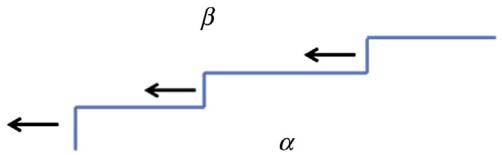

Figure 65 Schematic of the operation of a ledge growth mechanism wherein atomic attachment occurs at the ledge risers.

Applying a mass balance to the advancing α–β spherical interface requires that

$$\left(C_\beta^E - C_\alpha^E\right)\frac{dV}{dt} = 4\pi R^2\left(\frac{D\left(C_0 - C_\alpha^E\right)}{R}\right) \tag{162}$$

where $\frac{dV}{dt} = 4\pi R^2\frac{dR}{dt}$ and D is an appropriate diffusion coefficient (note: the concentrations C are given as atoms cm^{-3} or mol cm^{-3}). Here the growth rate is completely determined by the atomic flux arriving at the interphase interface via diffusive flow down the concentration gradient in the matrix. The growth rate is given by

$$\frac{dR}{dt} = \frac{D}{R}\frac{\left(C_0 - C_\alpha^E\right)}{\left(C_\beta^E - C_\alpha^E\right)} \tag{163}$$

and integration from $t = 0$ to $t = t$ yields

$$R^2(t) - R^2(0) = 2Dt\frac{\left(C_0 - C_\alpha^E\right)}{\left(C_\beta^E - C_\alpha^E\right)} \tag{164}$$

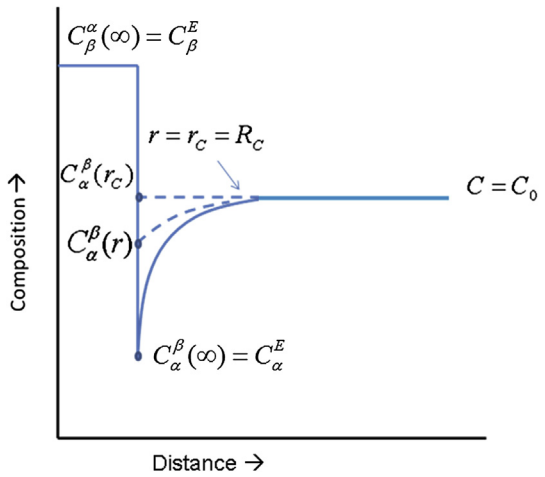

Figure 66 Composition profiles in the vicinity of a growing spherical β precipitate within a matrix of initial composition C_0. The solid line represents the diffusion field in the absence of interface curvature or capillarity effects. The dashed curves show the effects of capillarity on the concentration profiles.

for the time evolution of the particle radius during diffusion-controlled growth with $R(0)$ being the particle radius at the onset of the growth process. Assuming $R(t) >> R(0)$, the radius $R(t)$ increases as $t^{\frac{1}{2}}$ and the volume of the particle V_P varies as $t^{\frac{3}{2}}$. Ham (1959) showed that provided the shape of a nonspherical particle (defined by the eccentricity for prolate and oblate spheroids) remains constant during diffusional growth, the volume will increase as $t^{\frac{3}{2}}$ since each dimension will grow as $t^{\frac{1}{2}}$. It should be pointed out that if the growing particle is small enough where capillarity effects come into play, the concentration profile is changed since the matrix concentration in local equilibrium with the small particle of radius r will be enhanced approximately to

$$C_\alpha(r) = C_\alpha^E\left(1 + \frac{2\sigma V_m^\beta}{rRT}\right) \tag{165}$$

where σ is the interfacial free energy or surface energy of the α–β interface and V_m^β is the molar volume of the β phase. We have used the simplifying approximation that the atomic fraction $X_\beta^E \approx 1$ and that $\exp\left(\frac{2\sigma V_m^\beta}{rRT}\right)$ can be approximated $\left(1 + \frac{2\sigma V_m^\beta}{rRT}\right)$. The instantaneous growth rate $\frac{dR}{dt}$ is modified to

$$\frac{dR}{dt} = \frac{D}{R}\frac{\left(C_0 - C_\alpha^E\right)}{\left(C_\beta^E - C_\alpha^E\right)}\left(1 - \frac{R_C}{R}\right) \tag{166}$$

where at $R = R_C$, the equilibrium concentration C_α^β at the interface reaches C_0 and $\frac{dR}{dt} \to 0$ according to Eqn (166). Note in this limit the particle is in thermodynamic equilibrium with the supersaturated matrix. See **Figure 66**.

Note: The reader is reminded that the capillarity correction for the α–β equilibrium is more rigorously given by

$$X_\alpha^\beta(r) = X_\alpha^\beta(\infty)\exp\left(\frac{2\sigma V_m^\beta\left(1 - X_\alpha^\beta(\infty)\right)}{rRT\left(X_\beta^\alpha - X_\alpha^\beta(\infty)\right)}\right) \tag{167}$$

where $X_\alpha^\beta(r)$ is the matrix composition (atomic fraction) or composition of the α phase in equilibrium with a spherical β precipitate of composition $X_\beta^\alpha = X_\beta^\alpha(\infty) = X_\beta^E$ (assumed to be constant) and $X_\alpha^\beta(\infty)$ is the composition of the α phase in equilibrium with β across a flat interface $r = \infty$. Clearly as $X_\beta^E \to 1$ the usual approximations obtain.

Let us consider the case where a steady-state obtains at the interface during diffusional growth as a concentration C_I is established at the interface such that an interfacial reaction governed by a rate equation $K_I(C_\beta - C_I)$ where K_I is a rate constant describing the rate at which atoms can join the growing phase at the interface is equal to the rate at which atoms arrive at the matrix–precipitate interface by diffusion down a modified concentration gradient in the matrix. If the interfacial reaction is very sluggish ($K_I << D$) the interface concentration C_I approaches C_0 and when C_I reaches C_0 the reaction is said to be *interface controlled* and the depleted region in the vicinity of the growing particle virtually vanishes. At intermediate steady-state values $C_\alpha^E < C_I < C_0$ growth is said to governed by *mixed control*. Note that in the limiting case $C_I \to C_0$ the rate of growth becomes a constant value and $R \propto t$. See **Figure 67**.

Another case of interest is where a precipitate phase nucleates copiously along the grain boundaries of a parent phase forming chunks or semicontinuous slabs which grow out into the

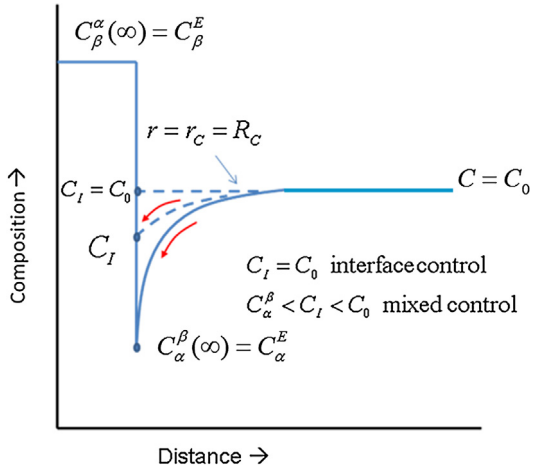

Figure 67 Composition profiles in the vicinity of a growing spherical β precipitate when an interfacial reaction leads to mixed and interface controlled growth.

matrix behind a virtually planar reaction front or interphase interface. These grain boundary chunks are often referred to as grain boundary allotriomorphs. See Figure 68. A classic example of this situation is the formation of proeutectoid ferrite in steels (Fe–C–X alloys). Upon cooling a plain carbon steel containing about the 0.4 wt.% C from the austenite phase field, the ferrite (bcc) proeutectoid phase ($\sim$0.02 wt.% C) nucleates primarily at the austenite grain boundaries exhibiting two morphologies, namely "chunky" allotriomorphs and sharp, blade-like growths emanating from the grain boundary regions into the parent austenite referred to as Widmanstatten "sideplates". See Figure 68. Importantly, the grain boundary ferrite nuclei generally establish an orientation relationship, for example the Kurdjumov–Sachs relationship wherein the closest packed planes and directions of the two phases are parallel with one of the adjoining grains and subsequent growth occurs primarily into the other grain where no bicrystallographic relationship exists. The migrating ferrite–austenite interface is essentially a disordered incoherent phase boundary. We will focus our attention first on the ferrite slabs (α) which grow into the parent austenite (γ) via diffusion of carbon in front of an advancing planar interphase interface into the austenite. See Figure 69. In the first approximation we again assume that the carbon concentration at large distances (much larger than the ferrite allotriomorph thickness) remains $C_0 \approx 0.4$ wt. % in our analysis and that local equilibrium prevails at the ferrite–austenite interface, that is, C^α and C^γ are the equilibrium compositions of ferrite and austenite given by the Fe–C phase diagram at the transformation temperature. The carbon concentration in the austenite in the vicinity of the growing ferrite normal to the reaction front can be assumed to be adequately described by an error function solution to Fick's second law based on the boundary conditions in spite of the moving interface. The carbon distribution in the austenite can be written as

$$C = C_0 - (C_0 + C^\gamma)\left[\left(1 - erf\left(\frac{z-r}{2\sqrt{Dt}}\right)\right)\right] \tag{168}$$

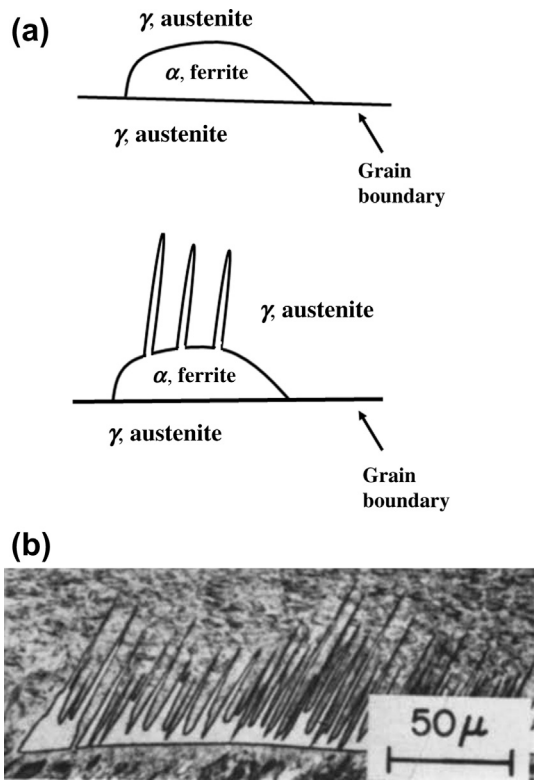

Figure 68 (a) Schematics of ferrite morphologies showing the allotriomorphs and sideplates typical in Fe–C–X alloys. (b) micrographs displaying morphologies of the allotriomorphs and sideplates typical in Fe–C–X alloys. After Shewmon (1963).

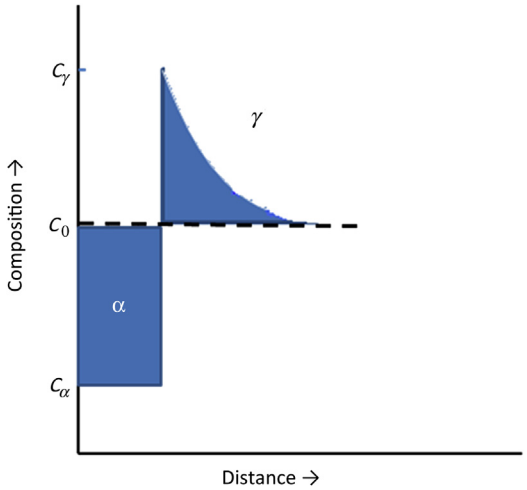

Figure 69 Carbon concentration profile in the parent austenite in front of a growing ferrite slab.

where the variable z is taken as the distance from the grain boundary and $z = r$ is the location of the advancing ferrite–austenite interphase interface. At the interface $\left(\frac{\partial C}{\partial z}\right)_{z=r} = \frac{C_0 - C^\gamma}{\sqrt{\pi D t}}$, and we can formulate a planar growth rate $\frac{dr}{dt}$ as above, equating the flux of carbon rejected into the austenite to the flux of carbon down the concentration gradient into the austenite as follows:

$$\frac{dr}{dt} = \left(\frac{D}{\pi t}\right)^{\frac{1}{2}} \frac{C^\gamma - C_0}{C^\gamma - C^\alpha} \tag{169}$$

and integrating show that the thickness of the ferrite slab follows a rate law $r \propto t^{\frac{1}{2}}$.

Let us now briefly address the appearance of the striking ferrite morphology called Widmanstatten sideplates wherein blades or spikes of the α phase shoot out into the parent austenite. The first approximation to understanding this morphological transformation is to use the simple analysis applied to the formation of dendrites during the freezing of an alloy. The advance of the solid–liquid interface generally involves the rejection or enhancement of solute as the solid forms from the liquid and a concentration gradient develops in the liquid phase in front of the interface. If a thermal fluctuation produces a small bump on an otherwise planar solid–liquid interface the isoconcentration lines in the liquid will be compressed leading to an enhanced diffusion of solute to or away from the interface allowing a spike of solid to grow out rapidly ahead of the generally plane front. This "point effect of diffusion" leads to a breakdown of the planar interface and amounts to an interfacial instability leading to dendritic growth. See **Figure 70**. The growth of such spikes in the solid state can be analyzed using a modified version of the approaches employed earlier for the case of ferrite sideplates assuming that the sideplates emerge from interfacial instability at the ferrite–austenite interface resulting from the point effect of diffusion of carbon within the parent austenite. The emergence of a blade-like protuberance at the interface will change the local equilibrium concentration of carbon and the effective concentration gradient at the blade edge or tip because of capillarity. The gradient at the edge with an effective radius of curvature ρ can be approximated by

$$\left(\frac{\partial C}{\partial r}\right)_{\text{edge}} = \frac{C^\gamma - C_0}{k\rho}\left(1 - \frac{\rho_C}{\rho}\right) \tag{170}$$

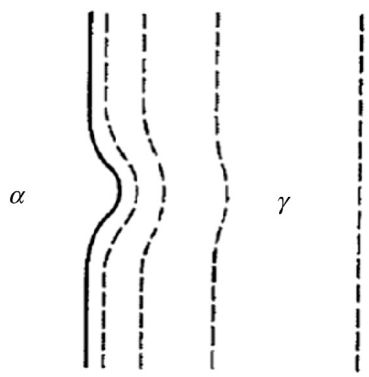

Figure 70 Compression of the isoconcentration lines in the austenite resulting from a local protuberance developing at the interface through fluctuations. After Shewmon (1963).

and the edge velocity written as

$$V_{\text{edge}} = D\frac{C^{\gamma} - C_0}{k\rho(C^{\gamma} - C^{\alpha})}\left(1 - \frac{\rho_C}{\rho}\right) \tag{171}$$

where, as above, ρ_C defines a critical curvature that renders the ferrite in local equilibrium with the supersaturated austenite of composition C_0 and $V \to 0$; k is a constant of order unity. The growth velocity of the edge or tip controlled by the diffusion of carbon in the austenite under the influence of the point effect of diffusion is a maximum for $\rho = 2\rho_C$. This expression for the growth rate of the blade or sideplate is the well-known Zener–Hillert equation (Zener 1946 and Hillert, 1957). A more detailed and rigorous treatment of the problem has been formulated by Trivedi (1970, 1975).

In the case of Widmanstatten sideplates considerations of crystallography and interface structure as well as mechanism must be folded into a rigorous treatment. A number of investigators using various approximations have addressed these issues.

The analyses of precipitate growth discussed earlier did not address the case where the diffusion fields of the growing particles impinge or where the growth of many particles simultaneously leads to a decrease in the average composition of the matrix well away from the depleted shells surrounding the growing particles during the latter stages. The treatments earlier were developed pedagogically to show how a fundamental approach to precipitate growth requires an interplay of thermodynamics and diffusion kinetics with capillarity or surface curvature often entering the problem as a major factor when describing microstructural evolution on a fine scale. One approach to the impingement problem modifies the growth rate of a spherical particle as follows:

$$\frac{\mathrm{d}R}{\mathrm{d}t} = \frac{D}{R}\left(\frac{C_0 - C_{\alpha}^{E}}{C_{\beta}^{E} - C_{\alpha}^{E}}\right)(1 - Y) \tag{172}$$

where Y is the fraction of the second phase precipitated at time t and given by

$$Y = \frac{C_m(t) - C_{\alpha}^{E}}{C_0 - C_{\alpha}^{E}} \tag{173}$$

with $C_m(t)$ being the average concentration throughout the matrix at time t. If $(1 - Y)$ is known as a function of time t the rate equation can be integrated as above (Wert and Zener, 1950).

8.5.3 Cellular Phase Separation: Eutectoid Decomposition and Discontinuous Precipitation

Cellular phase separation refers to phase reactions wherein a single phase decomposes into two phases via a mechanism involving the concomitant formation of the new phases behind a reaction front. The formation of the new phases generally produces a characteristic morphology, for example, lamellar phase mixtures, common in eutectoid (and eutectic) decomposition as well as in precipitation systems. The phase reactions can be described as

$$\gamma \to \alpha + \mathrm{Fe_3C}(\text{eutectoid decomposition})$$

$$\alpha_0 \to \alpha_{\text{eq}} + \beta(\text{discontinuous precipitation})$$

noting in the case of discontinuous precipitation the product phase α_{eq} has the same crystal structure as the parent phase, α_0. The two-phase duplex microconstituent resulting from the cellular reaction can

exhibit various morphologies, for example, lamellar, rod like, depending on the specificities of the surface energies and nucleation and growth behavior of the two phases comprising the two-phase mixtures. These resultant structures are examples of self-organization of the phases forming the microconstituents.

8.5.3.1 Eutectoid Decomposition

Let us now consider a classic metallurgical problem in microstructural evolution involving the diffusional growth of technological significance relating to the efforts in the mid-twentieth century to establish a sound scientific understanding of practical issues in the heat treatment of steels such as hardenability (Zackay and Aaronson, 1962). The eutectoid reaction in Fe–C–X alloys involves the decomposition of austenite into two phases α (ferrite) and Fe_3C (cementite) below the eutectoid reaction isotherm ($\sim$723 °C). See the Fe–C binary diagram in Figure 71. Between approximately 723 °C and 550 °C the eutectoid decomposition $\gamma \rightarrow \alpha + Fe_3C$ occurs in a manner which produces a self-organized duplex structure composed of alternating lamellae of the α and Fe_3C phases called pearlite after early descriptions by optical metallographers. See Figure 72. The blades of the phases apparently conjugate along low-energy $\alpha - Fe_3C$ interphase interfaces and the characteristic spacing of

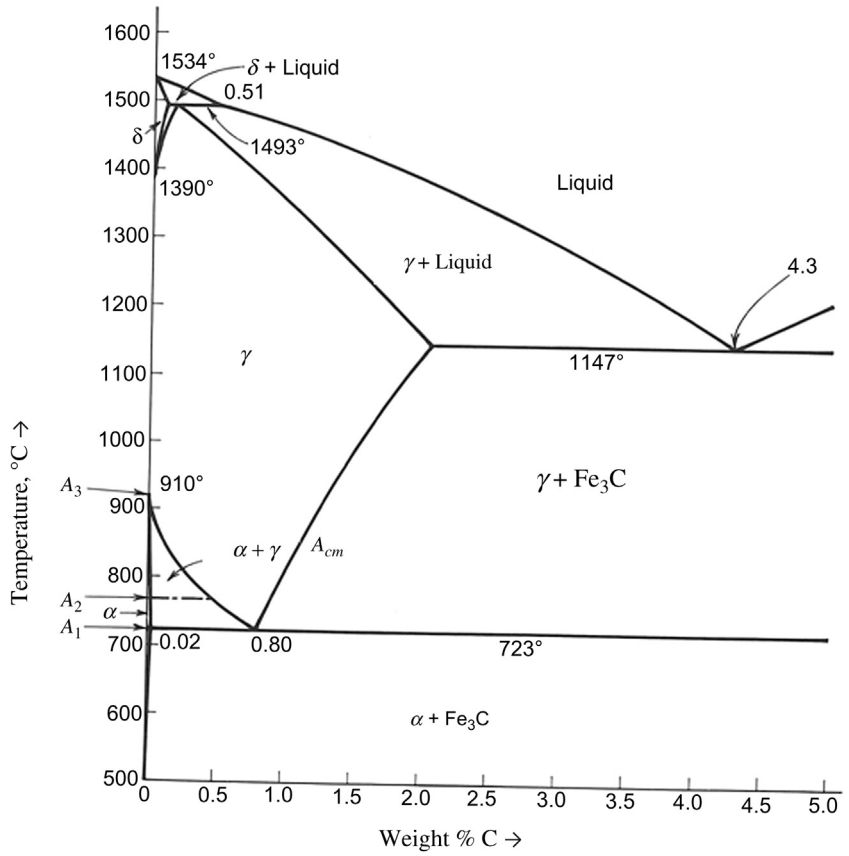

Figure 71 Binary metastable Fe–Fe_3C phase diagram. After Shewmon (1963).

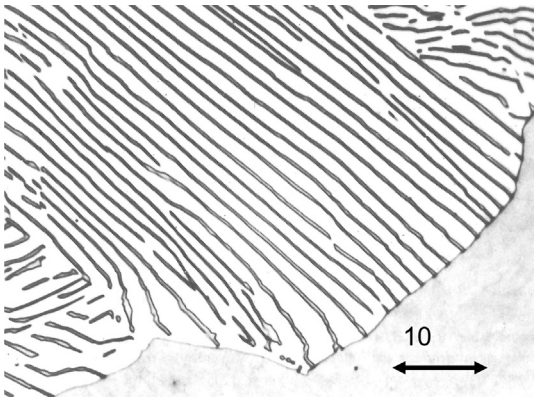

Figure 72 Microstructure of pearlite which has grown into an austenite (γ) grain. After Shewmon (1963).

the lamellar microconstituent is found to vary systematically with the transformation temperature. At temperatures between 550 and 650 °C the interlamellar spacing is much smaller than the spacing observed when the transformation occurs just below the eutectoid temperature. We also find that the growth rate of the lamellar colonies increases rapidly with the degree of undercooling below the equilibrium eutectoid temperature.

Let us try to develop a systematics to understand the salient features of this well-known solid-state transformation based on a fundamental thermodynamic framework and basic diffusion kinetics. Our approach will not be the most rigorous but will again emphasize pedagogy and principles governing the phenomena and which are generally applicable to understanding the microstructural evolution in conjunction with phase transformations.

The lamellar pearlite colonies emerge at the grain boundaries of the parent austenite phase and grow behind a reaction front as shown in **Figure 72**. As the two-phase aggregates grow a partitioning of carbon occurs between a solute-depleted ferrite (α) phase and a solute-enriched cementite (Fe_3C) phase via diffusional processes. The diffusional redistribution of carbon can occur within the austenite just ahead of the reaction front, within the austenite–pearlite boundary or even locally within the ferrite.

We will first approach the problem assuming that volume diffusion within the parent austenite in the near vicinity of the reaction front on a length scale of the order of S controls the edgewise growth.

Before developing the diffusional kinetics governing the cooperative growth of the $\alpha + Fe_3C$ duplex microconstituent let us briefly address the thermodynamics of the austenite $\rightarrow$ pearlite reaction and the observation that the lamellar aggregates exhibit a constant spacing S during isothermal growth wherein S becomes smaller as the undercooling ΔT below the eutectoid temperature increases, that is, the pearlite becomes finer at lower transformation temperatures. We begin our analysis by noting that the lamellar aggregates produced by the eutectoid reaction $\gamma \rightarrow \alpha + Fe_3C$ store free energy within the transformation product stemming from the creation of α-Fe_3C interfaces in the two-phase duplex microconstituent. The net free energy change accompanying the formation of pearlite must include this surface energy expenditure. Thus, the net free energy released per unit volume of austenite transformed, ΔG_V, is written as

$$\Delta G_V(S) = \Delta G_V(\infty) + \frac{2\sigma_{\alpha-Fe_3C}}{S} \tag{174}$$

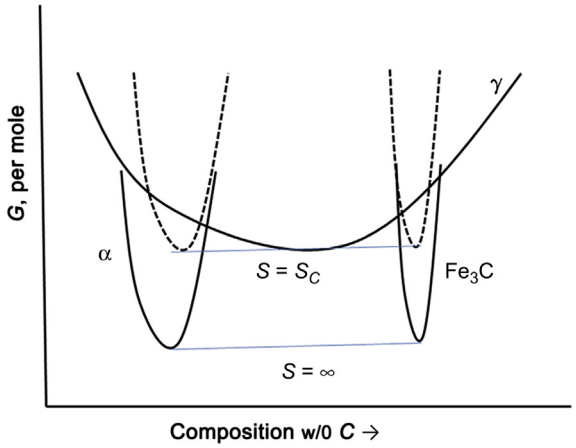

Figure 73 Schematic free energy–composition diagrams for the α, γ and Fe_3C phases showing the influence of capillarity on the phase equilibrium; at a critical spacing of the pearlite $S = S_C$ the two-phase microconstituent pearlite is in thermodynamic equilibrium with the parent austenite phase. $S = \infty$ refers to a spacing of the pearlite where capillarity or interface curvature effects are negligible.

where $\Delta G_V(\infty)$ is the bulk free energy change per unit volume or for a spacing so large that the interfacial free energy associated with the $\alpha - Fe_3C$ interfaces is negligible and the second term $\frac{2\sigma_{\alpha-Fe_3C}}{S}$ is the interfacial free energy stored per unit volume when forming the lamellae of finite spacing S. Since the thermodynamic driving force $\Delta G_V(\infty)$ is < 0 below the eutectoid temperature and $\frac{2\sigma_{\alpha-Fe_3C}}{S} > 0$, there is a critical spacing $S = S_C$ such that $\Delta G_V(S_C) = 0$, that is, the austenite (γ) is in equilibrium with the pearlite $(\alpha + Fe_3C)$ phase mixture. See Figure 73.

Note: The shape of the ferrite and cementite tips at the advancing interface are dictated by the surface (free) energies and these curvatures give rise to significant capillarity effects raising the free energy curves of these phases and changing the local equilibrium concentrations along the interface depending on the spacing S. The critical spacing is given by

$$S_C = -\frac{2\sigma_{\alpha-Fe_3C}}{\Delta G_V(\infty)} \tag{175}$$

This result will be used to formulate an approximate capillarity correction of the form $1 - \frac{S_C}{S}$ as shown in the following discussion.

Let us now derive a first approximation to an expression for the growth rate or velocity of the pearlite cells into the austenite assuming that the cooperative growth is controlled by (volume) diffusion in the near vicinity of the reaction front as mentioned earlier. As a ferrite blade moves into the austenite with a velocity V, a lateral flux of carbon must accompany this advance given by $V(C_\gamma^\alpha - C_\alpha^\gamma)_I$ where C_γ^α is the concentration of carbon in the austenite (γ) in local equilibrium with the ferrite (α) and C_α^γ is the concentration of carbon at the ferrite tip in local equilibrium with γ. (The subscript I refers to local equilibrium at the interface.) The carbon in the austenite diffuses down

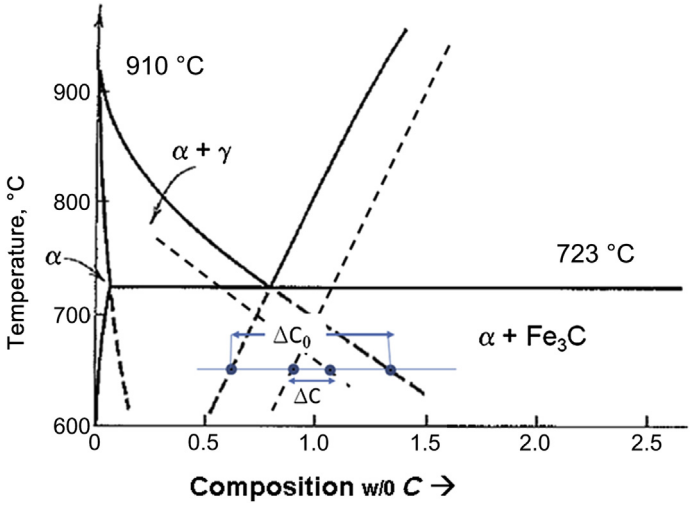

Figure 74 Portion of the Fe–C phase diagram showing shift of phase boundaries resulting from capillarity or interface curvature effects which modify the effective concentration gradient relevant to the diffusional austentite → pearlite reaction. ΔC_0 refers to local equilibria in the absence of capillarity effects whereas ΔC is the "corrected" concentration gradient.

a gradient in the austenite which goes as $\frac{\Delta C}{S}$ where $\Delta C = (C_\gamma^\alpha - C_\gamma^{Fe_3C}) = (C_\gamma^\alpha(\infty) - C_\gamma^{Fe_3C}(\infty))\left(1 - \frac{S_C}{S}\right)$ often written as

$$\Delta C = \Delta C_0\left(1 - \frac{S_C}{S}\right) \text{where } \Delta C_0 = \left(C_\gamma^\alpha(\infty) - C_\gamma^{Fe_3C}(\infty)\right)$$

so ΔC_0 refers to bulk phases and the $\Delta C_0\left(1 - \frac{S_C}{S}\right)$ is the capillarity correction for interface curvature of the ferrite and cementite lamellae. See Figures 73 and 74. Equating these fluxes one arrives at an expression for the growth velocity as follows:

$$V = \frac{D_C^\gamma\left(C_\gamma^\alpha - C_\gamma^{Fe_3C}\right)}{\left(C_\gamma^\alpha - C_\alpha^\gamma\right)_I \eta S} = \frac{D_C^\gamma \Delta C_0\left(1 - \frac{S_C}{S}\right)}{\left(C_\gamma^\alpha - C_\alpha^\gamma\right)_I \eta S} \tag{176}$$

where D_C^γ is the diffusivity of carbon in γ and η is a geometric parameter of order unity. However, we do not have a solution in closed form because as shown earlier the system can utilize any spacing $S < S_C$ at a given undercooling ΔT below the eutectoid reaction isotherm. What spacing does the system select? Some variational principle must be invoked. Let us suppose we assume that S is the spacing that maximizes the growth rate $V(S)$. Setting $\frac{dV(S)}{dt} = 0$, we find that $V = V_{MAX}$ when $S = 2S_C$; the growth rate then becomes

$$V = V_{\max} = \frac{D_C^\gamma \Delta C_0}{\left(C_\gamma^\alpha - C_\alpha^\gamma\right)_I 4\eta S_C} \tag{177}$$

and since $\Delta C_0 \sim \Delta T$ and $S_C \sim \Delta T^{-1}$ the growth rate might be expected to vary as $V \sim D_C^{\gamma} (\Delta T)^2$. This predicted dependence of V on ΔT or temperature appears to describe the growth rate of pearlite in a variety of steels. Also, the observed pearlite spacing apparently obeys the relation $S_C \sim \Delta T^{-1}$ as predicted earlier. Eutectoids with a pearlitic-like or lamellar morphology occur in alloy systems with substitutional solute elements but the growth velocities generally vary as $D(\Delta T)^3$ because the solute redistribution does not occur by volume diffusion in the parent phase but is controlled by boundary diffusion within the interface between the growing cells and the parent phase. This results from the fact that in the case of boundary diffusion control the effective cross-section area through which the diffusion flux passes is reduced by a factor of the order of $\frac{\delta}{S}$ giving a growth velocity $V \sim \frac{D_B \Delta C_0 \delta}{S_c^2}$ where D_B is a boundary diffusivity and δ is the thickness of the boundary region.

8.5.3.2 Discontinuous Precipitation

Discontinuous precipitation is essentially a mode of precipitation similar to the austenite–pearlite reaction described earlier in that it is a form of cellular phase separation involving heterogeneous nucleation of a phase along the grain boundaries of an alloy and the formation of colonies of a two-phase mixture exhibiting a characteristic morphology which grow through a cooperative codeposition of phases behind a migrating high-angle grain boundary. See Figure 75. However, the phase reactions involved are somewhat different most generally we could have

Type 1:	$\alpha_0 \rightarrow \alpha_{eq} + \beta$
Type 2:	$\alpha' + \beta' \rightarrow \alpha_{eq} + \beta$
Type 3:	$\alpha' + \delta' \rightarrow \alpha_{eq} + \beta$

where in the first case α_0 is an initial supersaturated solid solution and α_{eq} is a solute-depleted α phase (same crystal structure) which is in equilibrium with the β precipitate. In the second case, $\alpha' + \beta'$ is a metastable (often coherent) two-phase mixture which initially has formed throughout the matrix by a uniform continuous precipitation from supersaturated solid solution and then subsequently consumed by the more stable two-phase mixture $\alpha_{eq} + \beta$ through the growth of the cellular colonies. Here the coherent metastable β' phase has the same structure as the equilibrium β phase and thus this reaction can be considered essentially a coarsening reaction driven by a reduction of surface free energy and strain energy. The third case involves continuous precipitation of a coherent metastable δ' phase which has a different crystal structure than the equilibrium β phase.

Figure 76 shows proposed mechanisms for the genesis of the self-assembled colonies each of which have been observed to operate in various systems. Cellular or discontinuous precipitation is ubiquitous in precipitation systems often leading to a degradation of engineering properties.

Once assembled the cells grow by boundary diffusion control and the growth rate generally varies as $\frac{D_B \delta}{S^2}$ where D_B is a grain boundary diffusivity, S is the spacing of the lamellar morphology and δ is an effective boundary thickness. The thermodynamic driving force for the cellular reaction is the chemical free energy often augmented by coherency strain energy ($\alpha' + \beta' \rightarrow \alpha_{eq} + \beta$) but always reduced by the interfacial free energy stored in the interphase interfaces incorporated in the cellular morphology. In thermomechanically processed alloys the stored energy of cold work in the matrix or phase mixture being consumed by the colonies can provide additional driving force for the migrating grain boundaries similar to recrystallization of a cold-worked alloy. It is interesting to note that cellular or discontinuous

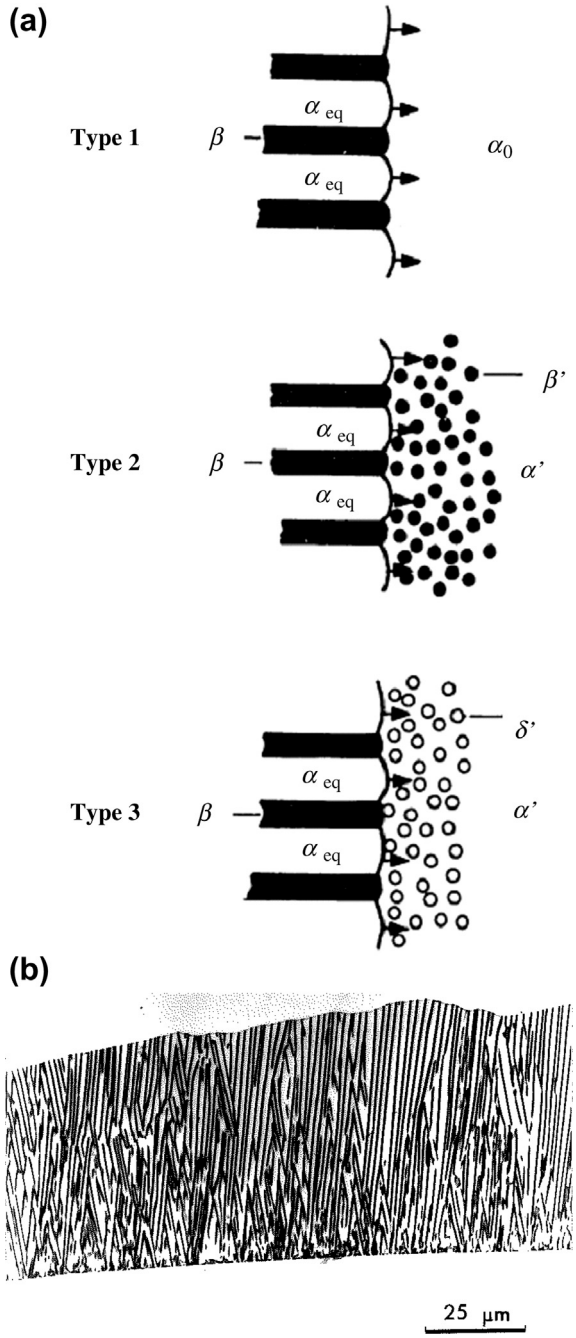

Figure 75 (a) Schematic showing various grain boundary discontinuous reactions. After (Williams and Butler, 1981).

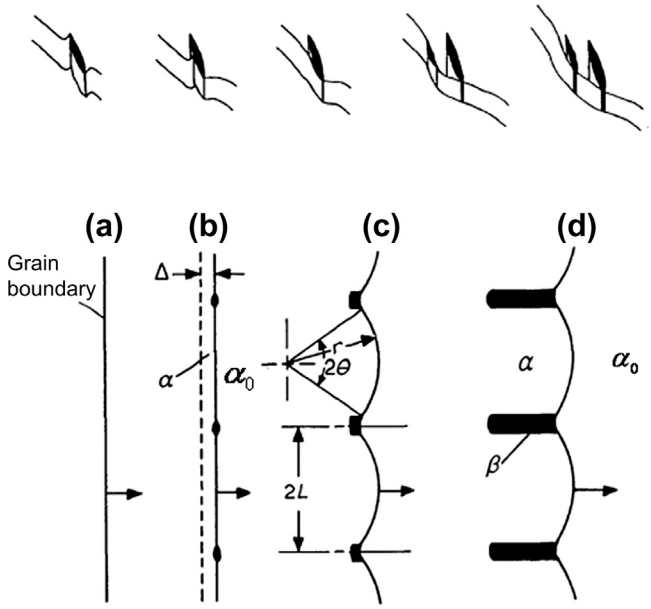

Figure 76 Schematics showing possible mechanisms involved in the genesis of cellular/discontinuous precipitation. After Williams and Butler (1981), Fournelle and Clarke (1972) and Turnbull and Tu (1970).

precipitation in age hardening alloys was often referred to as a "recrystallization reaction" because the microstructural changes involved the sweeping of the structure by migrating high-angle grain boundaries as occurs in recrystallization. It is important to mention that the lamellar products of discontinuous or cellular precipitation show a characteristic spacing at a given degree of supersaturation or driving force determined by similar thermodynamic and kinetic factors discussed in eutectoid decomposition and the edgewise growth of pearlite (Gust, 1979; Williams and Butler, 1981; Manna et al., 2001).

8.5.4 Growth of Widmanstatten Morphologies

A classic precipitate growth morphology is that of Widmanstatten platelets which were first discovered by Count Alyois von Widmanstatten in his early nineteenth century studies of meteorites (Barrett and Massalski, 1966). See **Figure 77**. The Widmanstatten patterns in meteorites were coarse enough to be viewed by the naked eye and derived from precipitation of α (bcc) platelets within a γ (fcc) matrix in essentially Fe–Ni alloys under conditions of extraordinarily slow cooling rates ($\sim 1\,^{\circ}\text{C}$ per 10^6 years) during their journey through space. The α platelets form parallel to the {111} planes of the γ matrix matching the {111} *habit planes* of the matrix and the {110} planes of the α precipitates across the broad faces of the Widmanstatten plates. Similar microstructures have been revealed on the microscopic scale in numerous alloy systems wherein matching of planes and directions of the matrix and precipitate phases across the habit plane occurs. In the case of the Cu–Si alloy shown in **Figure 78** the precipitation occurs along the {111} planes of an fcc matrix which are parallel to the (0001) of the basal planes of the hexagonal platelet precipitates with the close-packed directions in the conjugate phases parallel across the interface plane as well. The phases remain fully coherent across the broad faces until the very late stages of aging when the misfit strains eventually lead to a loss of coherency.

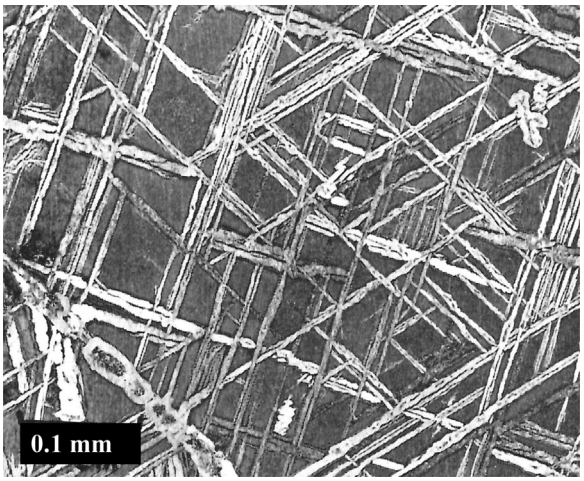

Figure 77 Widmanstatten precipitates in an Fe–Ni meteorite showing platelets of α(bcc) forming along the {111} planes of the γ(fcc) phase. After Finniston (1971).

This striking plate-like morphology appears to be primarily the result of a growth anisotropy directly related the structure of the interphase interfaces bounding the precipitate phase. However, there still persists some controversy as to the degree to which thermodynamic factors are folded into the formation and propagation of these low-energy interfaces. The broad faces of the Widmanstatten plates are virtually always coherent or semicoherent whereas the sides are generally disordered or incoherent. This difference in interfacial structure markedly influences the effective mobility of the interfaces during diffusional growth. The broad faces are structurally inhibited and almost certainly grow normal to themselves (plate thickening) via a ledge mechanism (see **Figure 41**) where atoms are added to the disordered risers of the ledges leading to lateral motion of the ledges within the interphase boundary. The sides are relatively

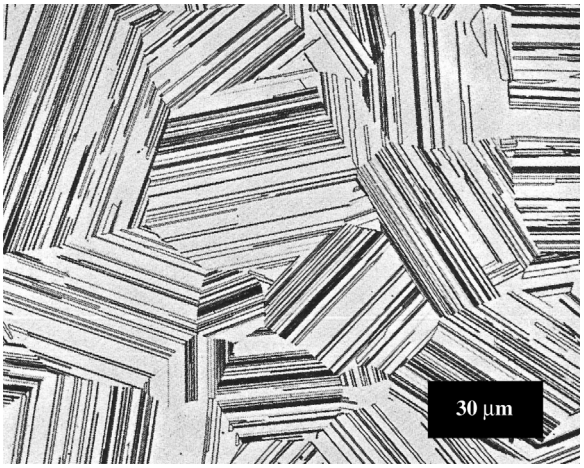

Figure 78 Widmanstatten platelets of a hexagonal phase precipitated along the {111} matrix (fcc) planes in a Cu–Si alloy. After Barrett and Massalski (1966).

much more mobile compared with the coherent/semicoherent faces of the platelets and in principle can grow (lengthen) at a rate controlled by volume diffusion whereas the thickening will depend on the supply and migration of the ledges within the interface (Aaronson et al., 2010).

8.5.5 Coarsening (Ostwald Ripening) of a Two-Phase Mixture in a Binary Alloy

8.5.5.1 Particle Coarsening in a Matrix

We now address a very important aspect of microstructural behavior from both a scientific and technological point of view. Consider the formation of a fine dispersion of second-phase particles (β) distributed uniformly within a matrix (α) resulting from nucleation and growth within an initially supersaturated solid solution during heat treatment. In the latter stages of this precipitation process the supersaturation of the matrix is substantially reduced because the growth of the precipitates drains solute from the surrounding phase wherein the matrix composition approaches $C_\alpha^\beta(\infty)$, the composition of the parent matrix in thermodynamic equilibrium with the β precipitates. The precipitates generally have nucleated at different times and grown to produce a range of particle sizes about some mean radius $\bar{r}$. Because of this size distribution even after the supersaturation has virtually vanished and no new particles appear there are local chemical potential and concentration gradients in the system associated with the particles because of the variation of solid solubility with particle size (Gibbs–Thomson or capillarity effects). See **Figure 79**. The concentration of solute in the matrix in local equilibrium in the near vicinity of a particle differs from particle to particle and importantly differs from the concentration in equilibrium with the mean particle size. The larger particles in the distribution tend to grow and the smaller tend to shrink with time as solute flows by diffusion in the matrix leading to an increase in the average particle size. The overall thermodynamic driving force for this microstructural change is the decrease in the total interfacial (free) energy per unit volume associated with the α–β interphase interfaces mediated by capillarity effects. This process is called (particle) *coarsening* or sometimes referred to as *Ostwald ripening*.

The classic approach to describing this diffusion-controlled coarsening of a two-phase mixture was carried out by Greenwood (1956) and later extended to include particle size distribution effects by Lifshitz and Slyozov (1961) and Wagner (1961). In the literature the theory is often called the L–S–W theory of particle coarsening, but should explicitly include Greenwood's seminal contribution and thus appropriately be referred to as the G–L–S–W theory (Balluffi et al., 2005). Greenwood's versions (1956, 1978) are somewhat simpler treatments of the kinetic analysis and will be substantially followed here for heuristic and pedagogical reasons. The approach is essentially what is referred to as a "mean field" solution to the diffusion problem wherein the growing or shrinking particles do not "see" the other particles except through a change in the average solute concentration remote from any

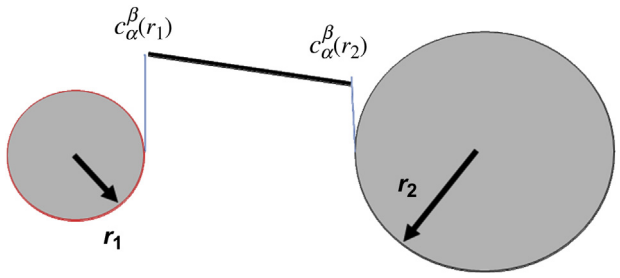

Figure 79 Schematic drawing showing concentration gradient between two particles of different sizes, $r_2 > r_1$, leading to a flow of solute from the vicinity of r_1 to r_2.

individual particle, that is, a particle in question is immersed in a mean or average environment which is perturbed only locally in the near vicinity of a particle (Gibbs–Thomson effect). This approximation essentially monitors the behavior of a particle effectively at zero volume fraction.

We start our discussion by assuming the volume fraction of the second-phase particles β is constant, that is

$$\sum_{i=1}^{i=N_p} V_i = \text{constant} \tag{178}$$

and

$$\sum_{i=1}^{i=N_p} \frac{\mathrm{d}V_i}{\mathrm{d}t} = \sum_{i=1}^{i=N_p} 4\pi r_i^2 \frac{\mathrm{d}r_i}{\mathrm{d}t} = 0 \tag{179}$$

where N_P is the number of particles at time t and V_i and r_i are the volume and radius of the ith particle, respectively.

The concentration of solute in the α matrix in local equilibrium with the ith particle of radius r_i is given by the familiar Gibbs–Thomson expression:

$$C_\alpha^\beta(r_i) = C_\alpha^\beta(\infty)\left(1 + \frac{2\sigma_{\alpha\beta}V^\beta}{r_i RT}\right) \tag{180}$$

assuming dilute or ideal solution behavior for the solute in α. We also are assuming that in this first approximation that the precipitate phase β is essentially pure B in an A–B binary solid solution; this simplification will be modified later in the formulation. If the concentration remote from the particle is taken to be $C^\wedge$ we can use the quasi-steady-state solution to describe the instantaneous rate of growth (or shrinkage) of the ith particle as follows:

$$\frac{\mathrm{d}r_i}{\mathrm{d}t} = \frac{D}{r_i}\left(\frac{\left[C^\wedge - C_\alpha^\beta(r_i)\right]}{\left[C_\beta^\alpha(\infty) - C_\alpha^\beta(r_i)\right]}\right) \tag{181}$$

where $C_\beta^\alpha(\infty) - C_\alpha^\beta(r_i)$ can be written as $C_\beta^\alpha(\infty) - C_\alpha^\beta(\infty)$ by replacing $C_\alpha^\beta(r_i)$ by $C_\alpha^\beta(\infty)$ in the difference compared with $C_\beta^\alpha(\infty)$. A bit of algebra shows that $C^\wedge = \overline{C}$, the mean concentration in the matrix or the concentration in equilibrium with the average particle size r. Noting also that in this approximation $[C_\beta^\alpha(\infty) - C_\alpha^\beta(\infty)] \approx \frac{1}{V^\beta}$ since $[C_\beta^\alpha(\infty) >> C_\alpha^\beta(\infty)$ when the β phase approaches pure B. Thus, we can write

$$\frac{\mathrm{d}r_i}{\mathrm{d}t} = \frac{2D}{r_i}\left[C_\alpha^\beta(\infty)\frac{\sigma_{\alpha\beta}\left(V^\beta\right)^2}{RT}\right]\left[\frac{1}{\overline{r}} - \frac{1}{r_i}\right] \tag{182}$$

for the growth rate of a particle relative to the average particle size and find that $\frac{\mathrm{d}r_i}{\mathrm{d}t} > 0$ for $r_i > \overline{r}$ and $\frac{\mathrm{d}r_i}{\mathrm{d}t} < 0$ for $r_i < \overline{r}$, that is, particles with radii greater than the average particle radius increase in size while particles with radii smaller than the average tend to shrink. The "big" particles are growing at the expense of the "smaller" ones even leading to the disappearance of some of

the smaller members of the ensemble. It is useful to focus on the fastest growing particles for some radius $r_i = r_m$. Setting $\frac{d}{dr_i}\left(\frac{dr_i}{dt}\right) = 0$ one finds that $r_m = 2\bar{r}$ leading to the expression:

$$\frac{dr_m}{dt} = \frac{2D}{r_m^2}\frac{C_\alpha^\beta(\infty)\sigma_{\alpha\beta}\left(V^\beta\right)^2}{RT} \tag{183}$$

for the growth rate of the fastest growing particle size. Integrating and inserting the relationship $r_m = 2\bar{r}$ we arrive at a kinetic law for the time evolution of the average particle size during diffusion-controlled coarsening given by

$$\bar{r}^3(t) - \bar{r}^3(0) = \frac{3}{4}DC_\alpha^\beta(\infty)\frac{\sigma_{\alpha\beta}\left(V^\beta\right)^2}{RT}t = K_1 t \tag{184}$$

where $\bar{r}(0)$ is the average particle size at the onset of the coarsening process. If $\bar{r}(t) >> \bar{r}(0)$ this is often written as $\bar{r}(t) \approx K' t^{\frac{1}{3}}$. The exact solution emanating from the Lifshitz and Slyozov (1961) theory when more rigorous attention is given to the nature of the behavior of the size distribution gives a modified K_1 as $K_1 = \frac{8}{9}D\left(\frac{C_\alpha^\beta(\infty)\sigma_{\alpha\beta}(V^\beta)^2}{RT}\right)$.

Coarsening is fundamentally a process rooted in capillarity effects expressed in the Gibbs–Thomson equation. However, most precipitates are not terminal solid solutions and the variation of solid solubility with particle size should be corrected for the precipitate composition, as mentioned earlier in the discussion of particle growth, that is, for intermediate phase precipitates, for example A_3B, the capillarity term that should be used in the treatment is that of Eqn (167) which includes a composition term which is essentially 4 for Al_3Li and 3 for Al_2Cu precipitate phases. Another consideration is that of nonspherical shapes and anisotropy of the interfacial or surface free energy σ. As discussed earlier a generalized Gibbs–Thomson equation can be formulated for the nonspherical equilibrium shapes wherein a parameter $\frac{\sigma_i}{\lambda_i}$ is invariant around the particle; σ_i is the surface energy of the ith surface element on the particle interface and λ_i is the distance of this element from the center of the precipitate projected along the normal to the surface element. The result is that the chemical potential is constant around the surface of the particle and thus the solubility is constant about the equilibrium shape.

Let us briefly return to the diffusion-controlled coarsening rate equations 181 and 182 and insert the general capillarity term mentioned earlier (Eqn (167)). Furthermore, we will forego the approximation $[C_\beta^\alpha(\infty) - C_\beta^\alpha(\infty)] \approx 1/V^\beta$ for the more general case where the dispersed phase is not a terminal solid solution or pure B but an intermediate composition A_aB_b. Eqn (183) then becomes

$$\frac{dr_m}{dt} = \left(\frac{2DX_\alpha^\beta(\infty)}{r_m^2}\right)\left(\frac{\sigma_{\alpha\beta}V^\beta}{RT}\right)\left(\frac{1 - X_\alpha^\beta(\infty)}{\left(X_\beta^\alpha(\infty) - X_\alpha^\beta(\infty)\right)^2}\right) \tag{185}$$

wherein we have assumed $[X_\beta^\alpha(\infty) - X_\alpha^\beta(r_i)] \approx [X_\beta^\alpha(\infty) - X_\alpha^\beta(\infty)]$ as discussed earlier. Also, again we find $r_m = 2\bar{r}$ and, thus, integrating as before gives

$$\bar{r}^3(t) - (\bar{r}(0))^3 = K_2 t$$

where $K_2 = \left(\frac{3DX_\alpha^\beta(\infty)}{4}\right)\left(\frac{\sigma_{\alpha\beta}V^\beta}{RT}\right)\left(\frac{1 - X_\alpha^\beta(\infty)}{(X_\beta^\alpha(\infty) - X_\alpha^\beta(\infty))^2}\right)$

Interjecting the LSW refinements, K_2 becomes

$$K_2 = \left(\frac{8DX_\alpha^\beta(\infty)}{9}\right)\left(\frac{\sigma_{\alpha\beta}V^\beta}{RT}\right)\left(\frac{1 - X_\alpha^\beta(\infty)}{\left(X_\beta^\alpha(\infty) - X_\alpha^\beta(\infty)\right)^2}\right)$$

This more rigorous capillarity correction was used by Novotny and Ardell (2001) in their analysis of coarsening in binary Al–Sc alloys.

As stated earlier, the classic GLSW theory is essentially a mean field theory virtually for zero volume fraction of second-phase particles. However, as pointed out back in the 1960s and 1970s by Asimow (1963) and Ardell (1972) the volume fraction of second phase is expected to become important at volume fractions where the distances between precipitates is of the order of the mean particle size altering the effective diffusion fields controlling the coarsening process. As a first approximation Ardell suggested that the basic result $r^3(t) - r^3(0) = Kt$ derived earlier in the GLSW approximation be multiplied by a factor $K'(f_V)$ which is a function of the volume fraction f_V which ranges from 1 ($f_V = 0$) to about 10 ($f_V = 0.25$) increasing the coarsening rate significantly. He also pointed out that the steady-state particle size distribution for bulk diffusion-controlled coarsening was expected to be markedly different than that predicted by the GLSW theory. However, the experimental results seem quite complicated and system specific wherein composition changes and changes in coherency strains may play a role. It is important to point out that in spite of the simplifications of the original treatment a kinetic law of the form $r^3(t) - r^3(0) = Kt$ seems to hold for the coarsening or ripening of two-phase microstructures across a wide variety of systems (Ardell, 1987).

In this discussion we did not delve into grain boundary diffusion-controlled coarsening of precipitates or coarsening of precipitates associated with dislocation arrays involving pipe diffusion as a rate-controlling process (Martin et al., 1997).

8.5.5.2 Discontinuous Coarsening

In the coarsening reactions discussed earlier, particles of a single phase distributed in a solid solution matrix increase their average size with time. Another type of coarsening occurs in eutectoid and cellular type microstructures as shown in **Figure 80**. Here both phases increase their size (and therefore spacing) discontinuously. Here the word discontinuous is used because the coarsening is not uniform in space but occurs at an advancing reaction front or interface driven by a reduction in surface energy of the lamellar two-phase mixture. This parallels the use of the term in Section 8.1.4 for discontinuous transformations. In the case shown in **Figure 80** the two phases are incoherent with each other (they need not be). Another point of interest is that the diffusion process for this coarsening is along the boundaries separating the coarsened region from the uncoarsened region, as opposed to the matrix diffusion in the particle coarsening reactions.

8.5.5.3 The Effect of Strain on Coarsening

So far we have considered only the role of surface energy on the coarsening of precipitates. Another important thermodynamic energy to consider is the elastic energy due to misfit between the crystal lattices of the particles and the matrix. Such energy depends on the shape, habit, configuration and volume of the precipitates (Khachaturyan et al., 1988).

The elastic energy of an isolated particle in a matrix plays a role in determining the shape of the particle. Indeed shape changes occur as the particle size increases to take into account the elastic

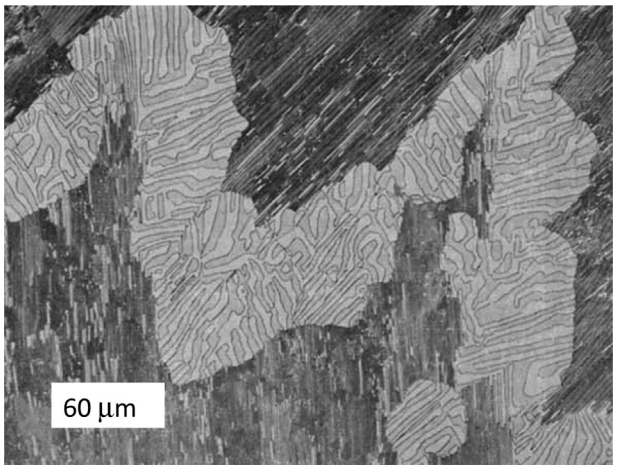

Figure 80 Co–Si alloy displaying discontinuous coarsening of a cellular microstucture. After Livingston and Cahn (1975).

anisotropies of the matrix and precipitate. For example a precipitate with isotropic surface energy still may have a cuboidal shape to lower its elastic energy.

Another consideration is the role of the interaction between the stress fields of the precipitates, commonly called an interaction energy. Ardell and Nicholson (1966) have shown that such interaction energy can cause precipitates to align along elastically soft directions of the matrix. Khachaturyan and Airapetya (1974) also showed that a large enough precipitate can decompose into smaller ones and align themselves along elastically soft directions of the matrix. This was later observed experimentally by Miyazaki et al. (1982) and Doi et al. (1984) for cuboidal precipitates of γ' in an Ni alloy. See **Figure 81**.

In such cases, the increase in surface area (and hence surface energy) is off set by the decrease in total elastic energy because of the negative elastic interaction term. Such a process produces smaller precipitates and has been termed "inverse coarsening".

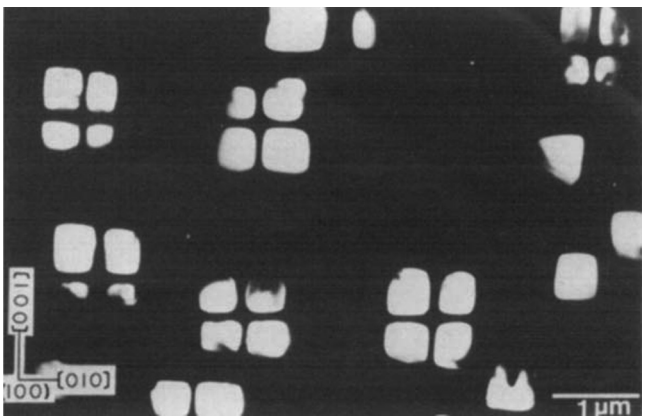

Figure 81 Elastic effects during coarsening leading to particle splitting. After Doi (1994)

8.6 Precipitation from Solid Solution

Precipitation from solid solution produces a phase mixture from the decomposition of an initial supersaturated phase resulting in a matrix phase whose crystal structure is similar to that of the parent phase, but of different composition and usually different lattice parameter(s), as well as an essentially dispersed phase (precipitate) that may differ in crystal structure, composition and/or degree of order. The physical, mechanical and chemical properties of the resultant two-phase alloy can vary markedly with the size, shape (morphology) and distribution of the precipitate phase within the matrix and this solid-state reaction provides the basis for one of the most powerful and versatile means available to the physical metallurgist and materials engineer for tailoring the properties of high-strength alloys through heat treatment and thermomechanical processing called *age hardening* or *precipitation hardening*. Precipitation effects can influence magnetic and superconducting properties as well as mechanical strength. Sometimes precipitation can cause unwanted effects in alloy applications and must be accounted for and controlled.

Precipitation from supersaturated solid solution as a phase transformation is ubiquitous in metallic and ceramic systems and in Figure 82 we show various phase diagram configurations which can give rise to precipitation reactions in the solid state. Precipitation phenomena embody a range of fundamental processes central to understanding the role of transformation behavior in controlling microstructural development during processing and heat treatment, namely *nucleation*, *growth*, and *coarsening*

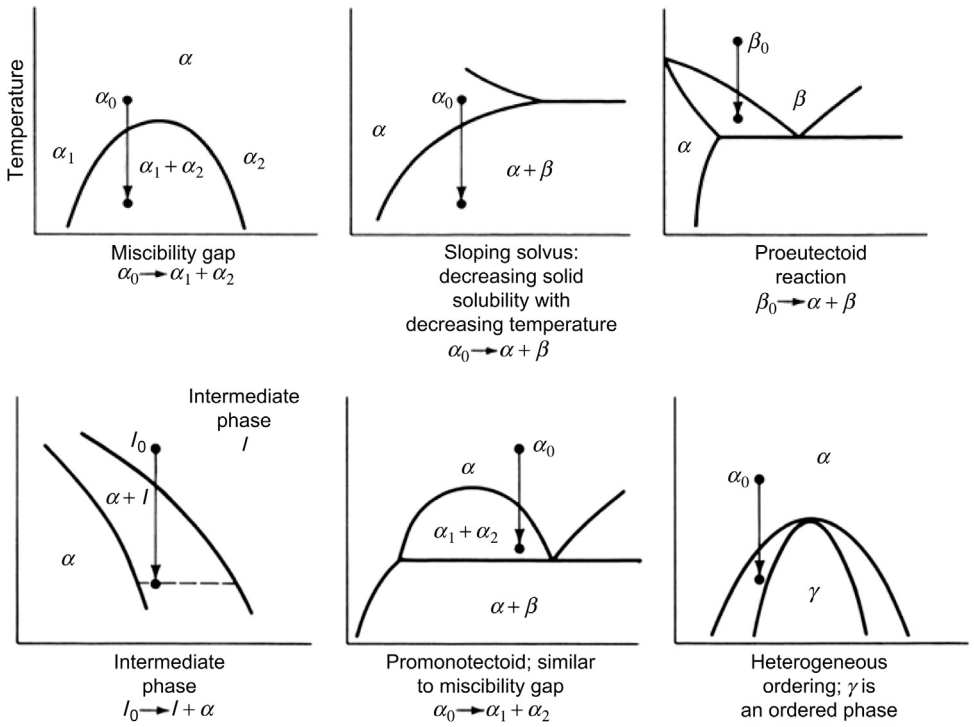

Figure 82 Equilibrium phase diagram configurations illustrating various conditions for precipitation of a second phase in a binary alloy. After Soffa (1985).

and competition among them. Furthermore, this solid-state transformation involves some of the most challenging fundamental issues at the forefront of thermodynamics and statistical mechanics such as nonequilibrium, irreversibility, the theory of rate processes, fluctuation behavior and self-organization in material systems.

8.6.1 Historical Background

During the first decade of the twentieth century A. Wilm in Germany wondered whether the emerging aluminum alloys could be strengthened employing methods used in other alloys, such as the quench hardening approach that was so successful with steels, or what is now called substitutional solution hardening, employed in Cu alloys. Both of these methods of strengthening had been used dating back to antiquity. The as-quenched aluminum alloys, however, were found to be soft much to Wilm's surprise. Furthermore, often the fastest cooling rates appeared to be softer yet. Fortunately following a set of Saturday morning "failures", he reexamined the disappointing results on Monday of the next week and found that the hardness and tensile properties had increased markedly while the specimens sat for 2 days at room temperature. They had "aged" over the weekend and these somewhat misguided experiments led to the discovery of age hardening. (Fortuitously, trace elements in the alloy micro-chemistry, e.g. Mg rendered these alloys "naturally aging", that is, unknown to Wilm at the time significant precipitation occurred at room temperature within the supersaturated alloys produced by quenching.) Wilm then more systematically explored the aging response in alloys containing ~4 wt.% Cu plus about 0.5 wt. % Mg along with traces of Mn, Fe and Si and patented his findings in 1906. His first archival publication was not contributed until 1911 (Wilm, 1911). This genre of alloy was christened DURALUMIN and was the primary structural material for the famous Zeppelins that were flying about between 1910 and 1920. The strengthening from the aging behavior increased the yield strength of the alloys by a factor of 2 or more compared with the as-quenched condition.

However, full exploitation of this phenomenon and extension to other alloys lay dormant for a decade until 1919 when Merica et al. (1921) in the United States identified the fundamental basis for the aging response; they recognized that this was the result of decreasing solid solubility with temperature resulting in precipitation from supersaturated solid solution of a second phase during the aging process at ambient (naturally aging) or moderately elevated temperature in a two-phase field. Quenching from a single-phase field at high temperature produces the supersaturated state, for example excess Cu dissolved in Al and the aging allows the nonequilibrium state to relax toward equilibrium (stable or metastable) dictated by the relevant solvus line in the phase diagram. Archer and Jeffries (1925) put forth a slip interference theory or "keying effect" as the mechanism for the enhanced mechanical strength wherein they hypothesized that the increased resistance to plastic flow derived from submicroscopic particles of a second phase which inhibit the elementary slip process of glide along crystallographic planes.

The association of this strengthening mechanism with decreasing solid solubility with decreasing temperature and the formation of fine-scale "pre-precipitates" or precipitate phases during aging by Merica et al., (1921) was the major breakthrough since following this revelation numerous age hardening alloys were developed not restricted to DURALUMIN-type aluminum alloys including copper-base and nickel-base alloys. Here we have an excellent example of a modest fundamental understanding of a phenomenon providing the foundation for the development of a new alloy technology beyond the specific context of the seminal discovery. Today *age hardening* or *precipitation hardening* is indeed one of the most effective approaches to designing high-strength alloys for a plethora of applications in modern technology.

The details of the nanoscale phenomena often involved in the precipitation process were not elucidated until the advent of sophisticated X-ray diffraction methods in the 1930s (Guinier 1938b; Preston 1938c) and ultimately through direct observation with the emergence of transmission electron microscopy in the 1950s and 1960s (Nicholson and Nutting, 1958; Nicholson et al., 1959). It was found that the precipitation process in the original DURALUMIN-type alloys generally exhibited a complex multistage decomposition of the supersaturated solid solution before the formation of the equilibrium phase indicated by the phase diagram, for example $CuAl_2$ (θ) in the binary Al–Cu system involving the appearance of nanoscale copper-rich "zones". Mehl and Jetter (1940) called these early-stage zones or precipitates Guinier–Preston (G.P.) zones after the early X-ray investigators in France and Great Britain (Guinier 1938a, 1938b; Preston 1938a, 1938b, 1938c.). Most importantly, it is now recognized that effective age hardening in most alloy systems generally derives from the formation of fine-scale metastable phases (sometimes referred to as "transition precipitates") before the appearance of the stable equilibrium precipitate phase; the formation of the equilibrium phase often leads to a degradation of properties developed with the metastable precipitates. A quantitative approach to correlating the precipitation microstructures with mechanical properties had to wait for the resolution of the nature of these ultrafine scale dispersions of second-phase particles and the development of a mature dislocation theory of plastic flow. Most notable is the theory of the yield strength due to Orowan (1948). Approaches to a quantitative description of the flow stress of particle hardening up to 1960 are summarized in the review by Kelly and Nicholson (1963) including the early work of Mott and Nabarro (1940). Books by Martin (1998) and Nembach (1996) provide excellent overviews of progress in the field. We shall not treat this topic in any depth in this chapter.

8.6.2 Nucleation and Spinodal Decomposition

In this section we focus on the initial stages of formation of a second phase through homogeneous decomposition within a supersaturated solid solution. Fundamental to understanding the breakdown of a supersaturated solid solution produced by quenching from a single-phase region into a two-phase field is the concept of the isothermal free energy–composition diagram and its relation to the phase diagram as discussed earlier. We will first consider precipitation within a miscibility gap such as depicted in **Figure 12**a. The associated free energy–composition curve is generally depicted showing a characteristic double well with a region of negative curvature in between the local minima delineated by the so-called chemical spinodal points $\dfrac{\partial^2 G}{\partial X^2} = 0$. The common tangent construction establishes the compositions of the equilibrium phases $X_e^{\alpha_1}$ and $X_e^{\alpha_2}$, respectively. Between the two inflection points (spinodal points) the free energy curve has a negative curvature and supersaturated states lying in this region are intrinsically unstable with respect to diffusional processes (recall the chord construction and that the effective diffusion coefficient $D \propto \frac{\partial^2 G}{\partial X^2}$, as discussed in an earlier section) and will tend to spontaneously phase separate. Supersaturated states lying on the curve where the curvature (point S in **Figure 12**) is positive are metastable and require a relatively large fluctuation in composition locally to initiate the precipitation reaction (nucleation). Gibbs recognized the possibility of these different kinetic paths leading to the breakdown of the supersaturated state and the formation of the two-phase mixture indicated by the phase diagram through the phase reaction $\alpha_0 \rightarrow \alpha_1 + \alpha_2$, where α_0 is the initial supersaturated solution and α_1 and α_2 are the equilibrium conjugate phases in the two-phase field, respectively. According to Gibbs, decomposition of the supersaturated state can be triggered by large localized fluctuations in composition which can grow spontaneously by diffusion down the concentration gradient which develops in the vicinity of these "critical nuclei" or by the continuous growth of

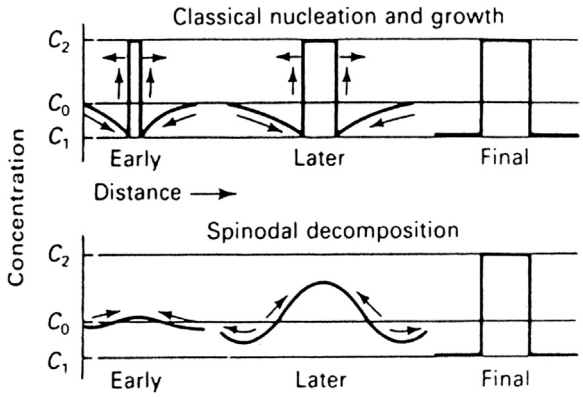

Figure 83 Classical nucleation and growth contrasted with spinodal decomposition as alternative modes of diffusional transformation leading to the formation of a second phase. After Soffa and Laughlin (1985).

initially low-amplitude composition fluctuations which are more spatially extended and exhibit rather diffuse incipient interphase interfaces during the early stages of phase separation gradually evolving into a distinct two-phase mixture. See Figure 83. Clearly the latter case involves "up-hill diffusion" or an effective negative diffusion coefficient. The first alternative refers to essentially **classical** nucleation of the new phase and the latter describes that which in the modern lexicon is called spinodal decomposition. The overall rate of these processes depends on the rate of atomic migration and the diffusion distances involved (undercooling). It is important to point out that the "spinodal line" depicted in Figure 12a is not a phase boundary but a demarcation indicating a difference in thermodynamic stability of supersaturated states and essentially a limit of metastability (Figure 84).

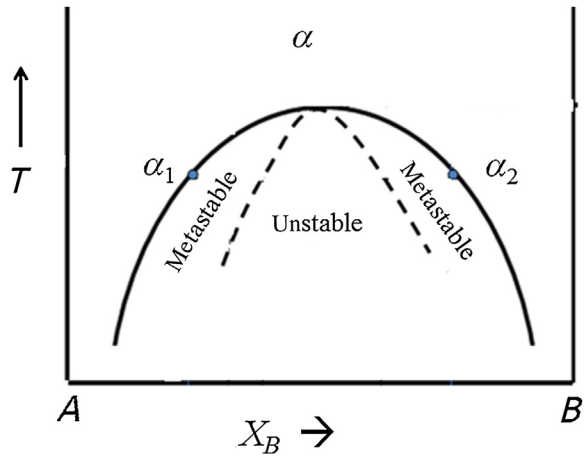

Figure 84 Schematic delineating metastable and unstable supersaturated states within a simple miscibility gap.

It is generally well established that at low to moderate undercoolings or supersaturations CNT as formulated earlier is an effective operational description of the system behavior and can be applied semiquantitatively depending on available data. The rate of homogeneous nucleation is expected to vary as $\frac{4\pi(r^*)^2}{a^4} DN_0 \exp\left(-\frac{\Delta G^*}{k_B T}\right)$ for a spherical nucleus, where a is an atomic dimension $\sim$0.2–0.4 nm and the other terms as defined previously. The nucleation barrier ΔG^* is composed of the surface energy and strain energy terms and varies roughly as $\Delta G^* = \frac{A\sigma^3}{(\Delta T)^2 T}$ where ΔT is the undercooling below the relevant solvus and is a measure of the degree of supersaturation (driving force); A is essentially a constant and σ and T have their usual meanings. If one defines the start of the nucleation and growth precipitation reaction by a parameter τ that is the time to observe 1% transformation (generally controlled by the nucleation rate), then one can generate a locus in a classic TTT (time–temperature–transformation) diagram for 1% transformation yielding a well-known *C*-curve in the TTT transformation map. See Figure 85. The parameter $\frac{1}{\tau}$ essentially is a measure of the rate of reaction (nucleation rate) and scales as $\exp\left(-\frac{Q_D}{k_B T}\right)\exp\left(-\frac{A\sigma^3}{(\Delta T)^2 T}\right)$ Q_D is the activation energy for the thermally activated diffusional jumps from the parent phase to the critical nucleus. This approximate description shows the central role of the nature of the interphase interface and the associated interfacial free energy σ of a precipitate phase in determining the rate of formation of the phase during isothermal aging. Clearly coherent phases with low σ

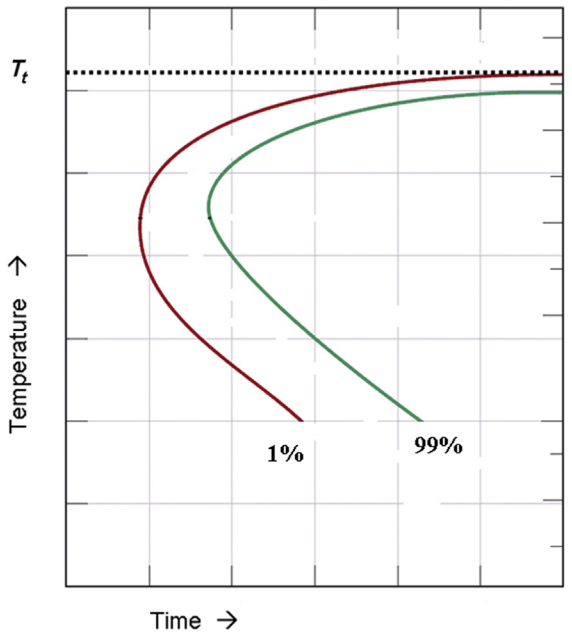

Figure 85 Typical Time—Temperature—Transformation (TTT) diagram exhibited by diffusional phase transformations. The start of transformation is labeled 1% and the finish 99%.

($\sim$50–200 erg cm^{-2}) are favored over incoherent phases with significantly higher σ ($\sim$400–1000 erg cm^{-2}) if the attendant strain energy for coherent nucleation is not prohibitive. This will be a major consideration when considering more complex phase diagrams and phases (stable or metastable) which do not have the same crystal structure as we find with the simple miscibility gap. Importantly, the equation for the initial nucleation rate shows the fundamental basis for the ubiquitous *C*-curve kinetics; at small undercoolings the nucleation barrier is high because the "driving force" is low and at large undercoolings the kinetics are sluggish because of restricted atomic mobility (high value of the activation energy for diffusional jumps in substitutional solid solutions).

Let us now consider a supersaturated state which lies within the "spinodal region" $\left(\frac{\partial^2 G}{\partial X^2} < 0\right)$. As mentioned earlier, the unstable solution tends to spontaneously unmix or phase separate without the requirement of a distinct nucleation step but through the amplification of initially extended low-amplitude fluctuations and this spinodal reaction involving diffusional clustering allows for a continuous evolution of the equilibrium $\alpha_1 + \alpha_2$ phase mixture. See **Figure 83**. The essential features of the spinodal process can be understood by considering this diffusional unmixing as the inverse of the homogenization of a nonuniform solid solution exhibiting a sinusoidal (or cosinusoidal) variation in composition with distance. In metastable solutions these small deviations from the average concentration, C_0, will generally decay according to $\Delta C = C(\gamma, t) - C_0 = \Delta C_0 \exp\left(-\frac{t}{\tau}\right)$, where $\Delta C_0(\gamma) = A_0 \sin\frac{\pi\gamma}{\lambda}$ describes the initial composition fluctuation as a function of distance γ and wavelength λ. The relaxation time of decay $\tau \approx \frac{\lambda^2}{D}$ where D is an appropriate diffusion coefficient and in a binary system is related to the curvature of the free energy–composition diagram $\frac{\partial^2 G}{\partial X^2}$ as mentioned in preceding discussions. In a metastable solution D is positive and the fluctuation decays exponentially toward the state of uniform composition (homogenization). However, if the solution is unstable, D is negative, and "uphill" diffusion occurs, that is diffusive flow of solute up the concentration gradient, and the amplitude of the concentration fluctuation grows with time, that is, $\Delta C = \Delta C_0 \exp\left(-\frac{t}{\tau}\right)$ becomes $\Delta C = \Delta C_0 \exp(R(\beta)t)$ where $R(\beta)$ is an amplification factor and a function of the wave number $\beta = \frac{2\pi}{\lambda}$. (This treatment of the behavior of a simple sinusoidal concentration wave in a heterogeneous solution is more general than it appears since through Fourier analysis an arbitrary composition heterogeneity can be considered as a superposition of Fourier components of various amplitudes and wavelengths and independently subject to a stability analysis.) This simple treatment captures important aspects of the spinodal process; however, the behavior of concentration fluctuations in an unstable solution requires that rigorous attention be paid to the energetics of the inhomogeities or concentration waves. We will find that long wavelength components will tend to grow sluggishly but short wavelength components are suppressed by a so-called gradient energy or incipient interfacial/surface free energy associated with the diffuse interfaces which evolve during the continuous unmixing process. We will address this important issue in the following overview of the modern theory of spinodal decomposition.

Becker (1937) and Dehlinger (1937, 1939) apprehended in the 1930s that the spinodal points on the free energy–composition curve of a binary system delineated a regime of supersaturated states wherein the diffusion coefficient in Fick's laws was negative and anticipated some unique behavior. Later Borelius (1937) attempted to develop a theory of localized fluctuation behavior contrasting behavior inside and outside the spinodal region, but never captured the essence of the problem. The core of the modern theory emerged when Hillert (a former student of Borelius) using a one-dimensional discrete lattice model based on regular solution energetics analyzed the behavior of composition fluctuations using

a modified diffusion equation (Hillert, 1956, 1961). In his analysis a term related to composition differences between adjacent planes arises in describing the chemical potential gradient governing the diffusion flux across the discrete lattice. This term in the thermodynamics of an inhomogeneous binary solution is equivalent to the gradient energy referred to above. Hillert's formulation produced a nonlinear diffusion equation which he solved numerically showing selective growth of certain wavelengths of the composition fluctuations or modulations. The result clearly indicated a spontaneous periodic clustering or phase separation without the occurrence of a classical nucleation event. Initially low-amplitude extended composition fluctuations on a certain length scale were found to be amplified through "uphill" diffusion leading to continuous phase separation now universally known as spinodal decomposition. Here in Hillert's doctoral thesis at MIT submitted in 1956 a numerical solution to the diffusion equation reveals the essential behavior of unstable solutions exhibiting Gibbs' alternative to classical nucleation (fluctuations of the second kind) as a mode of breakdown of the supersaturated solution and continuous phase separation resulting in quasi-periodic concentration waves evolving toward the formation of the equilibrium phase mixture. This model also provided a fundamental basis for the observations of Bradley (1940) and analyses of Daniel and Lipson (1943) in the 1940s of periodic precipitation in the "sideband alloys" such as Cu–Ni–Fe alloys. The X-ray results were in accord with periodic modulation of the composition along the ⟨100⟩ directions of the decomposing cubic parent phase with a wavelength of 100 Å, the same order predicted by Hillert. In addition, Hillert showed that outside the spinodal region a nucleation barrier appears, in addition to discussing G. P. zone formation, diffuse interfaces as well as continuous ordering. This revolutionary thesis work was belatedly published in 1961 (Hillert et al., 1961) but its impact preceded the formal publication in an archival journal (see Cahn, 2006 for this evaluation of the impact of the paper which he says greatly influenced his work). Cahn and Hilliard at the General Electric research Laboratory were impressed and intrigued by Hillert's work and began to work on this topic and addressed some of the fundamental issues embodied in it. This team of outstanding thermodynamicists with excellent mathematical facility first focused on the proper thermodynamic description of the diffuse interfaces as well as the general thermodynamic description of a compositionally inhomogeneous system. The work was followed by a treatment of the nucleation problem outside the spinodal but relaxing the ad hoc assumptions of CNT regarding the nature of the interphase interface separating the nucleus and parent phase and the composition profile of the nucleus (Cahn and Hillard, 1958, 1959). They showed that indeed the work to form the critical nucleus vanishes at the spinodal as well (Cahn and Hillard, 1958, 1959). This Cahn–Hilliard or nonclassical nucleation will be discussed in more detail subsequently after discussing Cahn's theory of the spinodal process.

The Cahn theory of spinodal decomposition[1] is based on a stability analysis of concentration waves (Fourier components) in an inhomogeneous system and a solution of a generalized or modified diffusion equation in a three-dimensional continuum wherein the gradient energy is incorporated explicitly using a Ginzburg-Landau (1950) approximation. Using the Cahn–Hilliard (Cahn and Hillard, 1958, 1959) result to describe the thermodynamics of a nonuniform solution (a solution exhibiting concentration fluctuations about the mean concentration) one writes the total free energy of the system as

$$G = \int \left[g(c) + \kappa (\nabla c)^2 \right] \mathrm{d}V \tag{186}$$

where the first term under the integral is the local free energy density $g(c)$ (the local free energy per unit volume of a homogeneous region of composition c) and the second term $\kappa(\nabla c)^2$ is the excess free

[1] van der Waals (1908) first used the term spinodal (Cahn 1968) and Cahn coined the term spinodal decomposition (Cahn, 1961).

energy per unit volume due to the local concentration gradient ∇c or *gradient energy* (κ is called the gradient energy coefficient). Consider a one-dimensional composition wave along the y-axis of a rectangular block of uniform cross-sectional area A' and length L ($V = A'L$) of wavelength λ described by

$$c(y) - c_0 = A\cos(\beta y) \tag{187}$$

where c_0 is the mean concentration, A is the amplitude of the modulation and $\beta = \dfrac{2\pi}{\lambda}$ is the wave number as above. Expanding the free energy density about the average composition gives

$$g(c) = g(c_0) + (c - c_0)\left(\frac{\partial g}{\partial c}\right)_{c=c_0} + \frac{1}{2}(c - c_0)^2\left(\frac{\partial^2 g}{\partial c^2}\right)_{c=c_0} + \text{higher order terms} \tag{188}$$

yielding to second order the following expression for the free energy difference between the inhomogeneous solution and an initial homogeneous solution

$$\frac{\Delta G}{V} = \frac{A^2}{4}\left(\frac{\partial^2 g}{\partial c^2} + 2\kappa\beta^2\right) \tag{189}$$

which indicates that if the second derivative is positive the fluctuated or inhomogeneous state is a higher free energy state and will tend to decay back toward the state of uniform composition (κ is assumed to be positive giving rise to an incipient surface energy). However, if the second derivative $\dfrac{\partial^2 g}{\partial c^2}$ is negative (inside the spinodal region) periodic fluctuations with wavelengths greater than λ_c or $\dfrac{2\pi}{\beta_C}$ given by

$$\lambda_C = \left[-\frac{8\pi^2\kappa}{\dfrac{\partial^2 g}{\partial c^2}}\right]^{\frac{1}{2}} \tag{190}$$

lead to a decrease in free energy and tend to grow spontaneously; the supersaturated state is unstable with respect to such composition fluctuations. Clearly the effect of the gradient energy is to prohibit decomposition on too fine a scale in spite of the kinetic advantage the short wavelength fluctuations have in terms of shorter diffusion distances.

The stability analysis discussed earlier must be amended if the molar volume of the solution varies with composition and coherency strains develop between adjacent regions of different composition in the inhomogeneous system. For an isotropic system this misfit strain energy (per unit volume) associated with the concentration wave can be approximated by the expression

$$E_S = \frac{A^2\eta^2 E}{2(1-\nu)} \tag{191}$$

where η is the linear expansion per unit composition change, E is Young's modulus and ν is Poisson's ratio. For a crystalline solid (cubic) η can be taken to be $\dfrac{d\ln(a)}{\mathrm{d}c}$ where a is the lattice parameter. The excess free energy of the inhomogeneous solution with a quasi-sinusoidal composition modulation is then written as

$$\frac{\Delta G}{V} = \frac{A^2}{4}\left(\frac{\partial^2 g}{\partial c^2} + 2\kappa\beta^2 + \frac{2\eta^2 E}{1-\nu}\right) \tag{192}$$

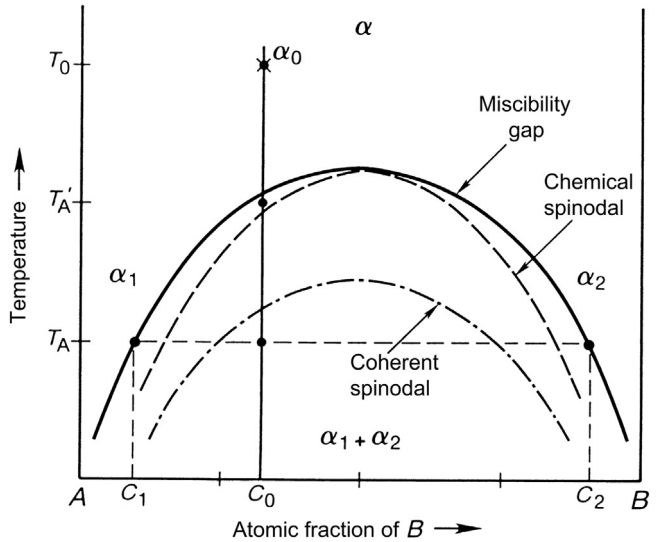

Figure 86 Schematic showing miscibility gap in the solid state and associated spinodal lines (chemical and coherent). After Soffa and Laughlin (1985).

which essentially defines a new stability criterion or a new spinodal region delineated by a locus called the *coherent spinodal* lying beneath the conventional *chemical spinodal*. See Figure 86. The strain energy has the effect of stabilizing the solution with respect to extended fluctuations of all wavelengths. The limit of stability is now given by

$$\left(\frac{\partial^2 g}{\partial c^2} + \frac{2\eta^2 E}{1-\nu}\right) = 0 \tag{193}$$

resulting from the influence of coherency strain energy on the energetics of the inhomogeneous solution which can totally suppress the spinodal process in some systems.

Crystalline solids can be highly anisotropic in terms of their elastic properties including cubic crystals. This introduces a new and important consideration with respect to the behavior of the concentration waves which tend to evolve during decomposition of the unstable supersaturated state. As a result of elastic anisotropy the elastic energy attendant to the formation of concentration waves differs depending on the crystallographic direction along which the composition modulation occurs and this will be shown to impact the nature of the resultant microstructures stemming from the spinodal process.

A cubic crystal generally has three independent elastic constants C_{11}, C_{12} and C_{44} whereas in the isotropic case $2\ C_{44} - C_{11} + C_{12} = 0$, thus in an isotropic material there are only two independent elastic constants. In the case of a cubic crystal the strain energy term takes the form $2\eta^2 Y$ where

$$Y[100] = \frac{(C_{11} + 2C_{12})(C_{11} - C_{12})}{C_{11}} \quad \text{and} \quad Y[111] = \frac{6C_{44}(C_{11} + 2C_{12})}{4C_{44} + C_{11} + 2C_{12}}$$

for concentration waves along $\langle 100 \rangle$ and $\langle 111 \rangle$ directions, respectively. The elasticity parameter Y is a minimum for modulations along $\langle 100 \rangle$ when $2C_{44} - C_{11} + C_{12} > 0$ and a minimum for modulations

along $\langle 111 \rangle$ when $2C_{44} - C_{11} + C_{12} < 0$. Thus, concentration waves will tend to develop preferentially along these directions cannibalizing the other Fourier components in the spectrum characterizing the initial composition inhomogeneity depending on the elastic anisotropy of the system (Cahn, 1961, 1962a, 1968 and Hillard, 1970).

Spinodal decomposition involves the selective amplification of concentration waves during the early stages of decomposition. We now focus our attention on the essential kinetic features of this process as a diffusional growth process occurring within the unstable system which represents the inverse of the homogenization problem involving "uphill diffusion" (flow against the concentration gradient; however, the diffusive flow is always down the chemical potential gradient). For diffusion in the binary system in one dimension along a γ-axis the fluxes (moles $\mathrm{cm}^{-2}\ \mathrm{s}^{-1}$) of the components A and B can be related to the local gradients of chemical potential of these species as follows: the driving

$$J'_A = -C_A M_A \left(\frac{\partial \mu_A}{\partial \gamma}\right) = -(1-X)\rho_m M_A \left(\frac{\partial \mu_A}{\partial \gamma}\right) \tag{194a}$$

$$J'_B = -C_B M_B \left(\frac{\partial \mu_B}{\partial \gamma}\right) = -X\rho_m M_B \left(\frac{\partial \mu_B}{\partial \gamma}\right) \tag{194b}$$

where C_A and C_B are the local concentrations (mol cm^{-3}), $(1-X)$ and X are the corresponding atomic fractions, ρ_m the molar volume of the solution assumed to be constant; M_A and M_B are the mobilities of the diffusing species (diffusion velocities per unit driving force) with $\frac{\partial \mu_A}{\partial \gamma}$ and $\frac{\partial \mu_B}{\partial \gamma}$ the gradients in chemical potential (the driving forces for diffusion). These fluxes J'_A and J'_B are purely diffusive flows down the local chemical potential gradients of A and B, respectively, measured with respect to the lattice frame (a coordinate system fixed on a lattice plane) that moves with the bulk or convective flow as observed through a local marker movement with respect to a laboratory or Matano frame (Kirkendall effect). With respect to the Matano frame the fluxes are written as

$$J_A = J'_A + C_A \mathrm{V_m} \quad \text{and} \quad J_B = J'_B + C_B v_m \tag{195}$$

where v_m is a local marker velocity and noting that $J_A + J_B = 0$ in this frame. Eliminating v_m between the flux equations one can write the flux J_B as follows:

$$J_B = -\rho_m M \frac{\partial(\mu_B - \mu_A)}{\partial \gamma} \tag{196}$$

where $(\mu_B - \mu_A)$ is sometimes referred to as the *diffusion potential* for the interdiffusion and $M = X\ (1-X)[(1-X)\ M_B + X\ M_A]$ is essentially an interdiffusion mobility. We recall from solution thermodynamics that $(\mu_B - \mu_A) = \frac{\partial G}{\partial X} \equiv G'$ and $G'' \equiv \frac{\partial^2 G}{\partial X^2}$ wherein the chemical potentials and molar free energy G will now include the gradient and elastic strain energies as described earlier.

The phenomenological description of the diffusion instability can now be formulated in terms of a modified Fick's laws writing the flux (First law) as

$$J_B = -M\left(G'' + 2\eta^2 Y\right)\frac{\partial C_B}{\partial \gamma} + 2M\kappa \frac{\partial^3 C_B}{\partial \gamma^3} \tag{197}$$

and the continuity equation (Fick's Second law) as

$$\frac{\partial C_B}{\partial t} = +M\left(G'' + 2\eta^2\gamma\right)\frac{\partial^2 C_B}{\partial \gamma^2} - 2M\kappa\frac{\partial^4 C_B}{\partial \gamma^4} \tag{198}$$

and for a cosinusoidal composition fluctuation $C_B - C_0 = A\cos(\beta\gamma)$ this diffusion equation admits an analytical solution $C_B(\gamma,t)$ as similar to that previously obtained with the simple approach. The new solution for the time evolution of the initially cosinusoidal fluctuation is

$$A(\beta, t) = A(\beta, 0)\exp(R(\beta)t) \tag{199}$$

where the amplification factor $R(\beta)$ is a function of the wavelength $\left(\beta = \frac{2\pi}{\lambda}\right)$ and given by

$$R(\beta) = -M\beta^2\left[G'' + 2\eta^2 Y + 2\beta^2\kappa\right] \tag{200}$$

as shown in Figure 87. The $A(\beta,0) = A_0$ is the initial amplitude of the fluctuation (Fourier component) in question. The maximum value of the amplification factor occurs at $\beta_{\max} = \frac{\beta_C}{\sqrt{2}}$ where $\beta_C^2 = -\frac{(G'' + 2\eta^2 Y)}{2\kappa}$ recalling that only wavelengths greater than $\lambda_C = \frac{2\pi}{\beta_C}$ will be amplified and lead to a decrease in free energy; the supersaturated state is unstable with respect to such composition fluctuations while the shorter wavelength fluctuations will tend to be damped or decay as discussed earlier. Fourier components at and in the near vicinity of $\beta_{\max}$ will be the dominant concentration waves and essentially determine the scale of the microstructure during the early stages of decomposition and this length scale varies as $\left(\frac{\kappa}{(\Delta T)}\right)^{\frac{1}{2}}$ where $\Delta T = T_s - T$, in which T_S is the spinodal temperature and T is the aging temperature or temperature of the spinodal process.

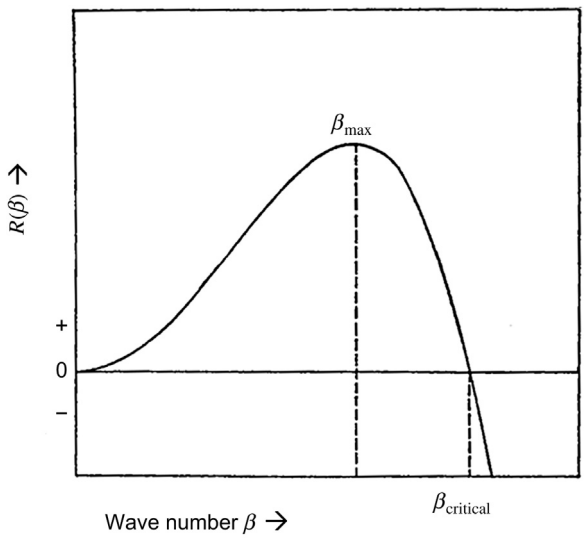

Figure 87 Variation of the amplification factor $R(\beta)$ with wave number, $\beta = \frac{2\pi}{\lambda}$ showing a maximum at $\beta = \beta_{\max}$ and crossover at β_{critical} where short wavelength fluctuations are suppressed.

The impact of Cahn's phenomenological or continuum theory based on an analytical solution of a modified diffusion equation was a major development in the theory of phase transformations bringing the spinodal concept and spinodal decomposition into the main stream of thinking about transformation behavior in metallic and nonmetallic systems. A new mode of phase separation distinct from classical nucleation based on a quantitative theory—albeit rigorously applicable to the early stages of decomposition—was recognized and the phenomenon began to be recognized to be relevant to a plethora of alloy systems of technological significance such as ferritic stainless steels (Fisher et al., 1953; Williams and Paxton, 1957; Imai et al., 1966; DeNys and Gielen, 1971; Vintaykin et al., 1966, 1970), Alnicos (Voss, 1969) and other permanent magnet alloys (Rossiter and Houghton, 1984) and numerous age hardening alloys (Ditchek and Swartz, 1979). Interestingly, Cahn's theory strongly impacted glass scientists almost immediately clarifying the structure and properties of phase-separated glasses, a phenomenon which is ubiquitous in glass technology. A new ingredient of major importance was introduced into the spinodal theory by Cahn, that being the elastic energy associated with the concentration waves and the influence of elastic anisotropy. Here we have a fundamental basis for the occurrence of modulated structures developing along certain crystallographic directions, for example $\langle 100 \rangle$, in numerous cubic systems as well as unidirectional modulations in decomposing TiO_2–SnO_2 tetragonal solid solutions (Stubican and Schultz, 1970). Thomas and coworkers (1970 and 1971) published the first comprehensive transmission electron microscopy (TEM) studies of the classic Cu–Ni–Fe sideband alloys revealing the emergence of modulated structures along the $\langle 100 \rangle$ matrix directions and the development of crystallographically aligned quasi-periodic two-phase mixtures. See **Figure 88**. The mechanism of decomposition was found to be homogeneous throughout the grains and uniform up to the grain boundaries as shown in **Figure 89**. The satellite reflections or sidebands and the emergence of a periodic and aligned microstructure were revealed prominently in the electron diffraction analysis of the spinodally decomposing alloys as displayed in **Figure 90**. It is important to note that Ardell and Nicholson (1966) in the mid-1960s pointed out in their studies of Ni–Al alloys that periodic microstructures mimicking the latter stages of spinodal decomposition could result from elastic interaction of coherent precipitates during stress-affected growth and coarsening of an initially random array of nucleated particles.

The Fe–Cr binary system exhibits a miscibility gap at low temperature giving rise to the formation of two bcc phases, one Fe rich and the other Cr rich and this miscibility gap including its metastable extension at elevated temperatures is significant in a number of technological contexts including ferritic stainless steels and tailored permanent magnet alloys based on the Fe–Cr–Co ternary system as cited earlier. Because of the similar atomic sizes these Fe–Cr spinodally decomposing alloys exhibit an isotropic spinodal morphology composed of interconnected veins of Cr-rich and Cr-depleted regions resulting from the amplification of concentration waves in three dimensions exhibiting no directionality because the elastic or misfit energy is small. The isotopic, sponge-like spinodal morphology is shown in **Figure 91** (Such a microstructure is expected in phase-separated glasses and indeed is found experimentally. In the glasses the absence of elastic anisotropy produces the isotropic behavior whereas in the metallic Fe–Cr–X metallic systems it is the small misfit.) This isotropic morphology in phase-separated Fe–Cr and Fe–Cr–Co was revealed by field-ion microscopy in the 1980s including atom probe studies of the time evolution of the concentration waves (Brenner et al., 1982, 1984). These early atom probe results showed the amplitude of the waves progressively increasing toward their equilibrium values indicated by the phase diagram. Later in the 1990s Miller et al. (1995) and Hyde et al. (1995b, 1995c) at Oxford in a series of papers carried out an impressive quantitative analysis of the system employing new atom probe techniques such as PoSAP and extensive computer simulations. **Figures 92** and **93** show reconstructions of the emerging microstructures stemming from the spinodal

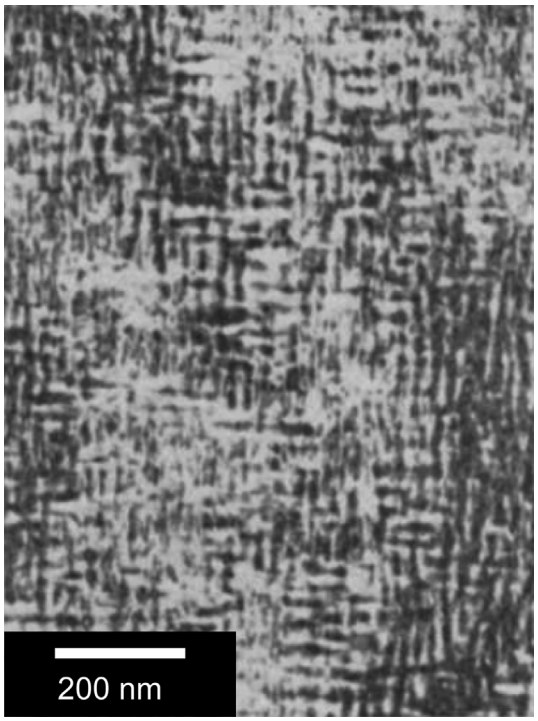

Figure 88 Spinodal microstructure revealed by TEM in an aged CuNiFe alloy showing a periodic, crystallographically aligned two-phase mixture; the foil normal is approximately [001], and the particles of the second phase are aligned along the [100] and [010] matrix directions. After Butler and Thomas (1970).

reaction. Danoix and Auger (2000) have reviewed atom probe studies of the Fe–Cr system directly applicable to stainless steel technology. It should be noted that the ternary Cu–Ni–Cr system exhibits a ternary miscibility gap and behavior very similar to the Cu–Ni–Fe system. See **Figure 94**. Importantly, atom probe analysis of the phase separation process in the Cu–Ni–Cr alloys revealed a similar progressive change of extended composition fluctuations toward the equilibrium compositions of the resultant phases consistent with the concept of spinodal decomposition versus classical nucleation and growth (Abe and Soffa, 1991). Small-angle X-ray and neutron scattering have also been employed to effectively monitor the development of composition modulations during spinodal decomposition showing the selective growth and decay of Fourier components across the β spectrum. The early stages for which Cahn's theory is rigorously applicable are found to be difficult to access experimentally and most results show an early coarsening of the dominant wavelength of the emerging microstructure.

Classical nucleation and spinodal decomposition represent extremes in a decomposition spectrum within a miscibility gap characterized by a gradual change from metastability to instability. The Cahn–Hilliard nonclassical nucleation theory (Cahn and Hillliard, 1958) essentially provides the critical linkage for understanding the progressive change in the nature of the decomposition process as the supersaturation or undercooling of the parent phase is increased. Let us look briefly at this generalized nucleation theory. Cahn and Hilliard used their analysis of inhomogeneous systems and diffuse interfaces (Cahn and Hillliard, 1958) to reexamine the nucleation problem. They allowed the

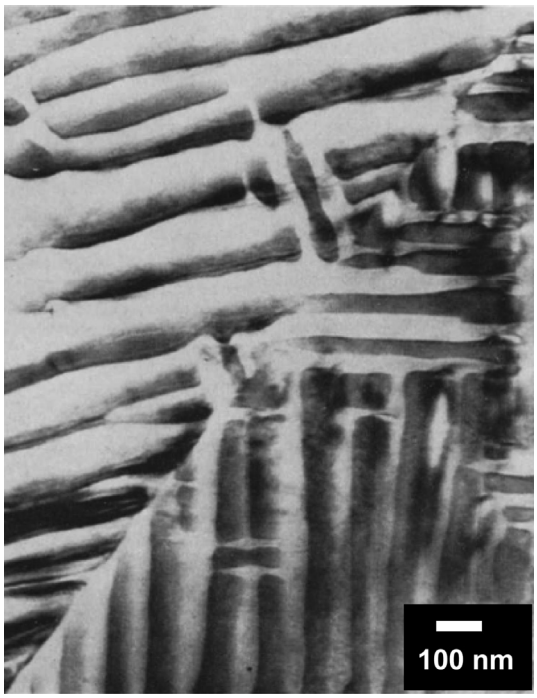

Figure 89 TEM micrograph of the decomposed CuNiFe alloy showing the phase separation being homogeneous up to the grain boundaries of the parent phase. After Butler and Thomas (1970).

composition profile of potential nuclei to vary and considered the interface between the parent and emerging phases to be generally diffuse rather than sharp as assumed in CNT. See **Figure 45**. At low supersaturations the critical nuclei look very much like classical nuclei but as the supersaturation increases the work to form the critical nucleus decreases continuously to zero at the spinodal. However, the effective radius or spatial extent of the critical fluctuation rapidly increases at high supersaturations approaching infinity in the vicinity of the spinodal. Furthermore, the interface becomes progressively more diffuse and the concentration difference between the center of the nucleus and the supersaturated solution decreases toward zero as well. What are we to make of this apparent singular behavior or discontinuity from the "nucleation side" to the "spinodal side?" As pointed out by Cahn (1962b), there is no discontinuity. As the supersaturation is increased toward the spinodal the critical nucleus or fluctuation becomes more diffuse and progressively exhibits characteristics very different from the "classical nucleus". The amplitude of the critical fluctuations begins to deviate significantly from the equilibrium composition of the precipitating phase and the interface between the incipient precipitate and parent phases becomes markedly extended. Furthermore, the "nucleation barrier" rapidly decreases approaching k_BT and a range of finite-amplitude fluctuations against which the system is unstable becomes part of the spectrum of frequently occurring fluctuations and a well-defined critical nucleus loses its meaning. A variety of fluctuations of varying spatial extent and amplitude readily leads to decomposition of the supersaturated state. The system no longer follows an optimum path toward equilibrium. The transition regime is expected to extend into the "spinodal side" or inside the spinodal since true spinodal instabilities with their characteristic long wavelengths (large diffusion distances)

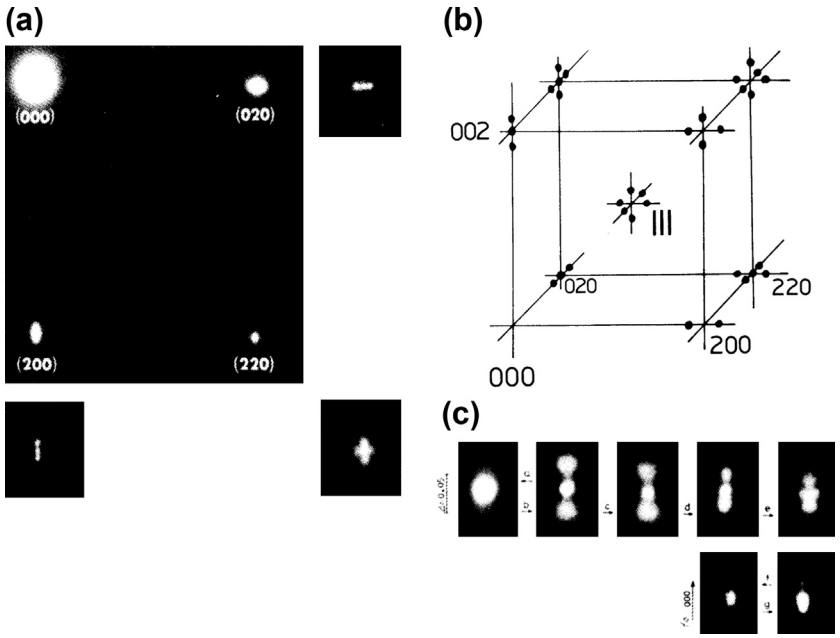

Figure 90 (a) An [001] electron diffraction pattern of a spinodally decomposed Cu–Ti alloy showing satellite configurations, consistent with periodic strain modulations along the [100] and [010] matrix directions. (b) Schematic of the positions of the satellites in reciprocal space. (c) Enlarged images of (200) reflections showing details of the satellites. After Hakkarainen (1971) and Soffa and Laughlin (1982).

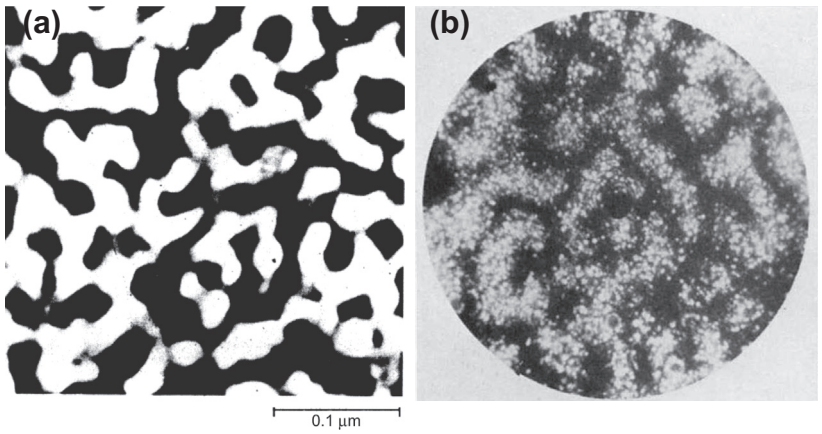

Figure 91 (a). TEM image of an isotropic spinodal morphology developed in an Fe–Cr–Co alloy (Zeltzer). (b) Field ion micrograph image of an isotropic spinodal morphology in an Fe–Cr–Co alloy. After Soffa et al. and Brenner et al. (1984).

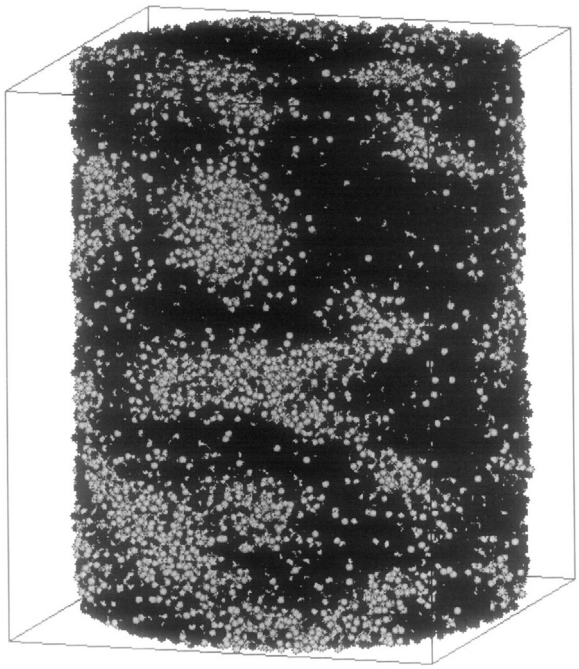

Figure 92 An atomic reconstruction of a spinodally decomposed Fe–Cr alloy aged at 773 K. The lighter spheres represent Fe atoms and the darker spheres Cr atoms. After Miller et al. (1995).

will be slow to evolve whereas finite-amplitude fluctuations with smaller spatial extent will develop more rapidly. Thus, the transition from metastability to instability is characterized by a hybrid process and the reaction path does not necessarily minimize the free energy of formation of the critical fluctuations but maximizes the rate of decomposition. A comprehensive pedagogical review article which this section closely followed is found in Hilliard (1970).

8.6.3 Spinodal Decomposition and Ordering

Clustering and ordering effects and instabilities during the decomposition of supersaturated solid solutions were essentially considered mutually exclusive behaviors until the 1960s and 1970s based on textbook treatments of these phenomena which discussed the energetics and stability of binary alloys in terms of first nearest-neighbor pairwise interactions within a zeroth approximation quasichemical theory or the classic Bragg–Williams description of ordering. In particular, spinodal decomposition and ordering tendencies were thought to be incompatible or unrelated behaviors in precipitation systems. However, it is now well established that an interplay of clustering and ordering tendencies can occur synergistically during the precipitation of ordered phases and influence the morphology and resultant microstructural scale. As early as 1963 Israel and Fine (1963) suggested that such behavior was involved in the formation of the metastable Ni_3Ti phase in the Ni–Ti system. Gentry and Fine (1972) in later studies of precipitation of Ni_3Al in Ni–Al alloys suggested that Cahn–Hilliard nucleation or spinodal decomposition was involved in the formation of the ordered phase. Corey et al. (1973) in their

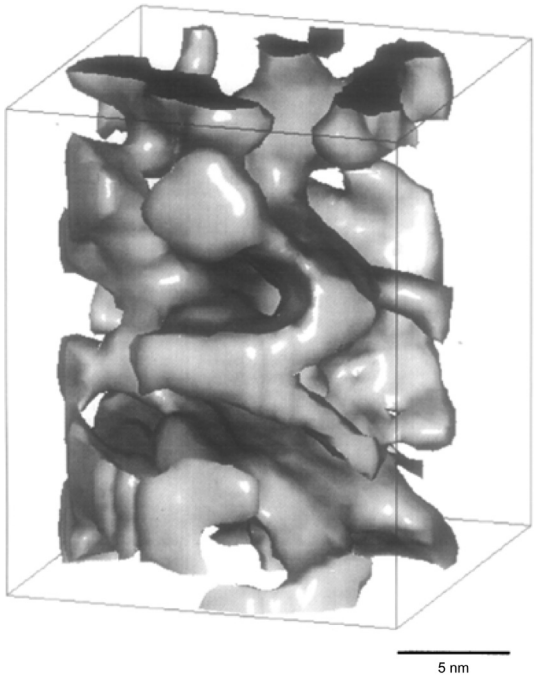

Figure 93 Isosurface reconstruction from PoSAP (position sensitive atom probe) analysis showing morphology of Cr-enriched regions in a spinodally decomposed Fe–Cr alloy aged at 773 K. After Miller et al. (1995).

contemporaneous work in the early 1970s on nonstoichiometric Ni_3Al-base alloys also concluded that these alloys undergo a two-step decomposition process consisting of an ordering transition followed by phase separation by spinodal decomposition. These authors also presented an attempt to rationalize the synergistics of the two-step process in terms of simple free energy–composition diagrams (graphical thermodynamics) relevant to the phase separation and ordering.

A thermodynamically sound basis for concomitant and synergistic ordering and phase separation behavior started to emerge in 1976 with the works of Allen and Cahn (1976), Ino (1978) and Kokorin and Chuistov (1976). Allen and Cahn (1976) addressed the mechanisms of phase transformations in the Fe–Al system revealed by electron microscopy (TEM) in association with a tricritical point which can occur when a line of critical points or a locus of higher order transitions ends uniquely on a miscibility gap. See **Figure 95**. The line of critical points represents the α (disordered; bcc; A2) $\rightarrow$ B2 disorder–order transition which is a higher order transition. Using free energy–composition curves associated with the phase diagram in the vicinity of the tricritical point they introduce explicitly the concept of spinodal phase separation contingent on prior ordering—the conditional spinodal reaction—and contrast a limit of metastability with a spinodal line. The limit of metastability is where the curvature of the free energy–composition curve changes sign (plus to minus) discontinuously on passing from a disordered state to an ordered state and is coincident with the extrapolated line of critical points associated with the A2 $\rightarrow$ B2 ordering in this case. Within this graphical thermodynamic scheme a disordered A2 phase which is metastable with respect phase separation can be rendered unstable upon continuously ordering and spinodally phase separate finally resulting in a disordered α phase and

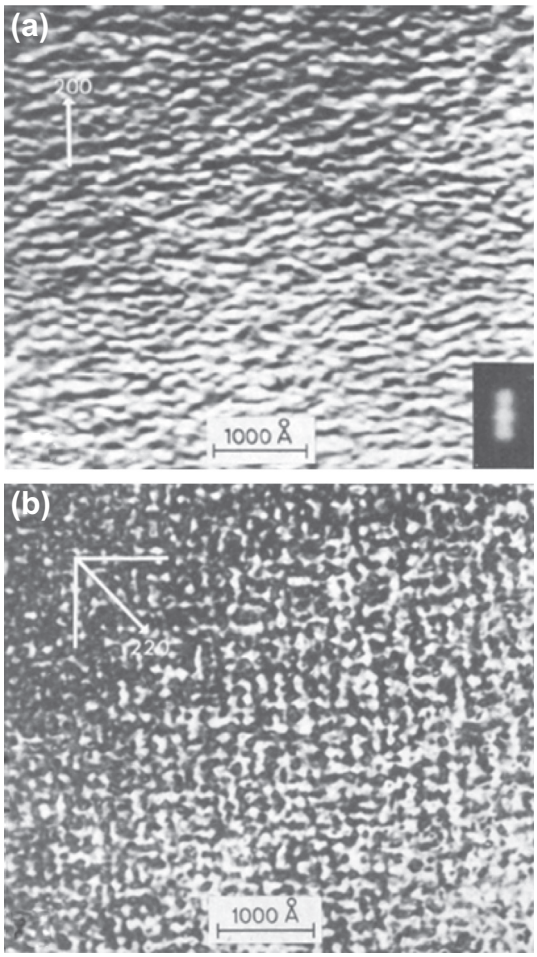

Figure 94 TEMs of Cu-31.6 Ni-1.7 Cr alloy aged at 650 °C for 1 h revealing matrix strain contrast striations along traces of the {1 0 0} matrix planes under different imaging conditions; the average wavelength of the modulated structure is about 170A. (a) Foil normal near (0 0 1); $g = [20\,0]$; insert shows satellite flanking matrix reflection. (b) Foil normal near (001); $g = [2\,2\,0]$; interpenetrating modulations revealed indicative of triaxially modulated structure (Chou et al., 1978).

an ordered nonstoichiometric B2 phase. They also suggested that the continuous ordering of the initial disordered parent phase is expected to occur much more rapidly than any competing nucleation and growth mechanism. Ino (1978) using a straightforward quasichemical model but including first and second nearest-neighbor pairwise interactions of opposite sign was able to predict a similar behavior associated with the A2 → B2 ordering. The interplay between phase separation and ordering stemmed from writing the interchange energies as $V = \frac{1}{2}[2E^1_{AB} - E^1_{AA} - E^1_{BB}]$ and $U = \frac{1}{2}[2E^2_{AB} - E^2_{AA} - E^2_{BB}]$ for first and second nearest-neighbor interactions, respectively, and assuming random mixing on the α and β sublattices of the B2 structure. This is sometimes referred to as a generalized Bragg–Williams model. Kubo and Wayman (1980) later also described miscibility gaps intersecting the A2 → B2 transition in CuZn alloys. Kokorin and Chuistov (1976) addressed the possibility of spinodal decomposition in

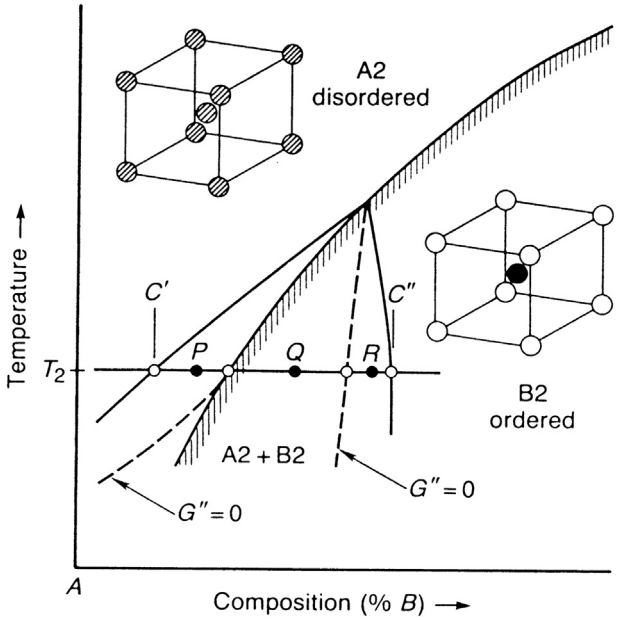

Figure 95 Region in the vicinity of a tricritical point showing the emergence of a spinodal line associated with the disordered solid solution at low temperatures ($G'' = 0$). Alloys quenched to points *P*, *Q* and *R* exhibit different regions of thermodynamic stability with respect to clustering and ordering. After Laughlin and Soffa (1988).

conjunction with the formation of an ordered A_3B ($L1_2$) phase within a supersaturated binary fcc solid solution emphasizing the dependence of the free energy of the system on the composition and order parameter at a given temperature as well as incorporating second nearest-neighbor interactions in a generalized Bragg–Williams model. The A1(fcc) → $L1_2$ ordering transformation is first order under equilibrium conditions. Khachaturyan et al. (1988) addressed the problem as well using a generalized Bragg–Williams model and SCW formalism to elucidate phase equilibria and precipitation of the $A_3B(L1_2$ phase) in Al–Li alloys. They described the possibility of spinodal decomposition of homogeneously ordered Al–Li solid solutions into a disordered phase and ordered phase mixture as reported experimentally by Radmilovic et al. (1989) in their TEM studies of the Al–Li system, similar to the discussion of Datta and Soffa (1973, 1976) in their studies of age hardening Cu–Ti alloys. Khachaturyan et al. (1988) defined a congruent ordering process whereby a disordered single-phase state transforms without composition change via nucleation and growth of ordered regions within a metastable solid solution (heterogeneous ordering).

Soffa and Laughlin (1989) extended this analysis to include a detailed graphical thermodynamic analysis of the interplay of the clustering and ordering tendencies in conjunction with a thermodynamically first-order disorder → order transformation in a precipitation system. Soffa et al. (2010, 2011) subsequently used the generalized Bragg–Williams approach in a computational thermodynamic analysis to generate free energy–composition diagrams emphasizing the role of second nearest-neighbor interactions on thermodynamic stability and the synergistics of ordering and spinodal decomposition. This graphical thermodynamics of Soffa and Laughlin (1989) represents a convolution of the usual free energy–composition diagram with the Landau graphical representation of ordering

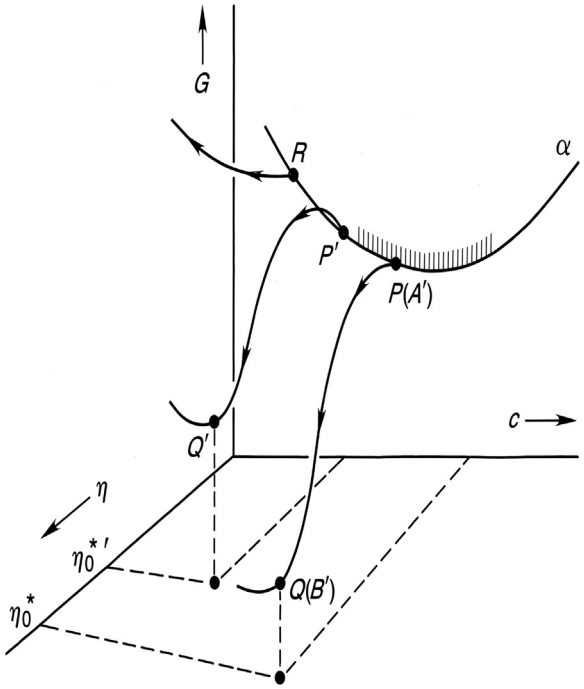

Figure 96 Schematic representation of G–c–η space showing different regions of stability and instability at points R, P' and P. A disordered alloy at R is stable with respect to atomic ordering, an alloy at P' is metastable with respect to ordering and one at P is unstable with respect to atomic ordering. The hatching along the free energy composition curve denotes thermodynamic instability with respect to ordering. After Soffa and Laughlin (1989).

transformations as shown in Figure 96. Ordering instabilities (T_i^-) and spinodal regions (T_S) can be delineated and an interesting array of reaction paths predicted in agreement with experimental evidence. Figure 97 shows an alloy of composition C_0 quenched to temperature T_3 which might be expected to continuously order (below T_i^-) and then spinodally decompose (below T_S) producing an ordered precipitate within a disordered matrix. The continuous phase separation or spinodal reaction is contingent on the prior ordering and will be discussed subsequently.

8.6.4 Precipitation Sequences: Modes; Coherency and Metastable Phases

Let us now return to the classic Al–Cu age hardening system and examine, in detail, the reaction path during aging of supersaturated Al–Cu solid solutions giving rise to the strengthening which derives from the precipitation reaction. Alloys nominally containing 2–4 wt.% Cu (1.0–1.7 at.% Cu) when solution treated and quenched from the single-phase region ($\sim$500 °C) and subsequently aged at $\sim$100 °C undergo a multistage decomposition characterized by the formation of a series of metastable precipitate phases before the formation of the equilibrium precipitate $CuAl_2$ (θ). The reaction sequence can be summarized as: $\alpha_0 \rightarrow \alpha''' + \text{G.P. I zones} \rightarrow \alpha'' + \text{G.P. II zones } (\theta'') \rightarrow \alpha' + \theta' \rightarrow \alpha_{eq} + CuAl_2\ (\theta)$ where α_0 is the initial supersaturated FCC solid solution. It is useful to represent the multistage reaction path in this manner because the sets of phases ($\alpha'' + \text{G.P. II zones } (\theta'')$, etc.) represent

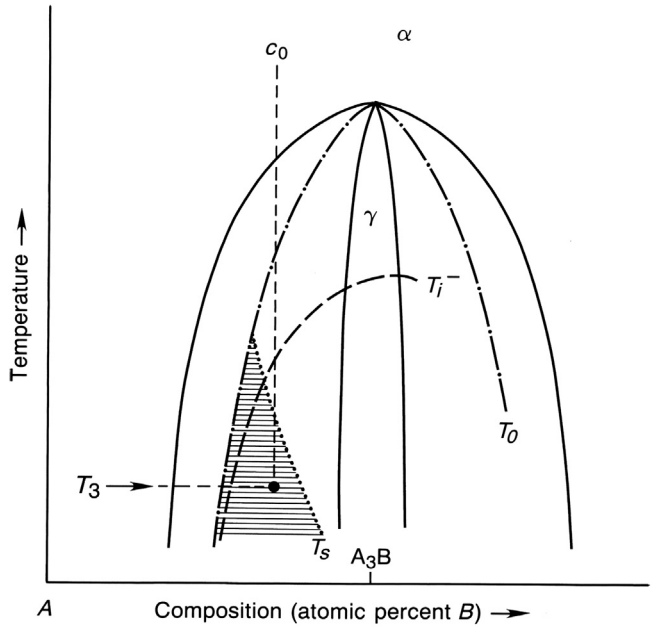

Figure 97 Phase diagram configuration associated with A_3B ordering (A1 → $L1_2$; first-order transition) showing ordering instability locus and spinodal regime (shaded) along with T_0 the temperature below which an ordered solution is thermodynamically favored (lower free energy) with respect to a disordered phase.

metastable two-phase equilibria which precede the formation of the stable $\alpha_{eq} + CuAl_2$ (θ) equilibrium phase mixture. The structure and morphology of these different phases are shown in Figure 98. The basic question to be addressed is: What fundamental principles underlie this multistage approach to stable equilibrium involving the appearance of a sequence of metastable precipitates? The rate of approach to equilibrium from the initial supersaturated state is controlled by the activation barriers along the reaction path generally associated with thermally activated processes involved in the construction of a new phase or phases which lower the free energy of the constituent assembly such as nucleation and atomic migration. The metastable transition precipitates during the early stages of decomposition of the supersaturated state are generally crystallographically similar to the matrix allowing the formation of low-energy coherent (semicoherent) interphase interfaces during the nucleation process. As discussed earlier, CNT shows that the nucleation barrier ΔG^* is proportional to $\frac{\sigma_{M-P}^3}{(\Delta G_V + \Delta G_S)^2}$ where σ_{M-P} is the interfacial free energy of the matrix–precipitate interphase interface, ΔG_v is the thermodynamic driving force per unit volume (the free energy released per unit volume of the new phase formed) and ΔG_s is the strain energy per unit volume attendant to the formation of the new phase (coherency strain energy), as defined earlier. Since the nucleation rate of a phase varies exponentially as $\exp\left(-\frac{\Delta G^*}{k_B T}\right)$ the nucleation of a coherent transition phase with $\sigma_{M-P} \sim 30$ erg/cm^2 will occur more easily compared with the equilibrium phase with $\sigma_{M-P} \sim 400 - 1000$ erg/cm^2 despite having a lower driving force and some associated strain energy expenditure, in general. The different stages can be depicted in a free energy–composition diagram and common tangent constructions can

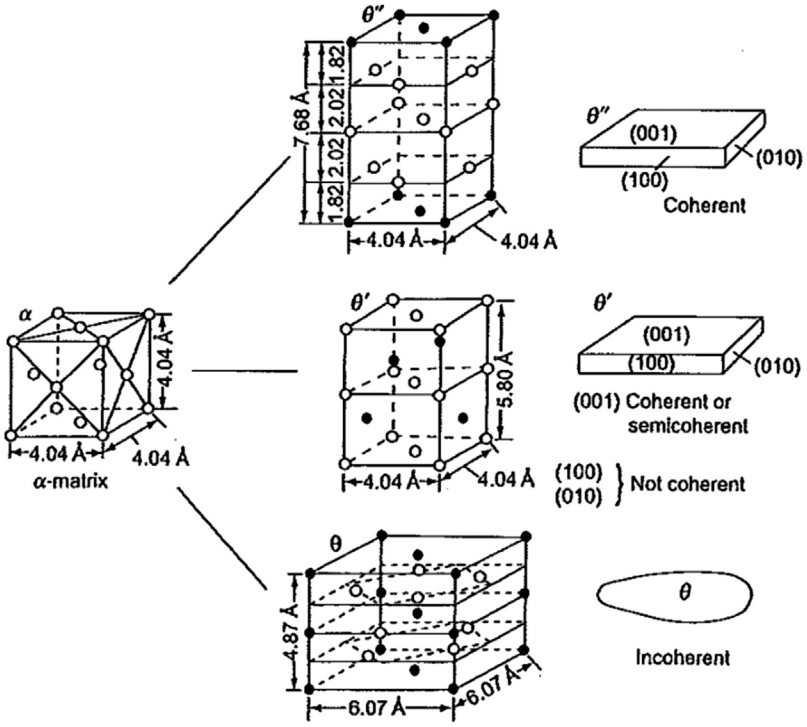

Figure 98 Schematic showing the structures of precipitate phases occurring in Al–Cu age hardening alloys including the morphologies and nature of their interphase interfaces. After Smallman (1963).

be employed at different temperatures to map out the loci of metastable solvi of precipitate phases. See Figure 99. Also, *C*-curves marking the start of precipitation for the different competing phases can be established with respect to the metastable solvi as discussed earlier and depicted in Figure 100. It should be mentioned that the thermodynamic validity of these metastable solvi, for example G.P. I solvus, can be categorically established by a *reversion* experiment wherein if the metastable two-phase mixture is rapidly reheated above the G.P. I solvus a temporary softening is often observed resulting from the re-solution of the G.P. I zones followed by further hardening on continued aging with the appearance of the θ'' phase. In the free energy–composition schemes depicted in Figure 99, G.P. I zones could form by spinodal decomposition at sufficiently high supersaturations. Indeed, Rioja and Laughlin (1977) have studied the early stages of G.P. I zone formation in aged Al-4 Wt.% Cu alloys using electron microscopy and diffraction. The observation of diffuse satellite reflections and the apparent formation of a modulated microstructure (the development of concentration waves along the $\langle 100 \rangle$ directions of the decomposing matrix) supports the notion of a spinodal mechanism. These conclusions have been supported by the small-angle X-ray scattering results reported by Kaskyap and Koppad (2011). The well-known plate-like G.P. I zones along the $\{100\}$ matrix planes emerge during the later stages of the spinodal process and coarsening of the modulated structure under the influence of the strain energy. It is interesting to note that the heat of mixing of Al–Cu alloys in the solid state appears to be negative over most of the composition range except for perhaps an anomalous behavior

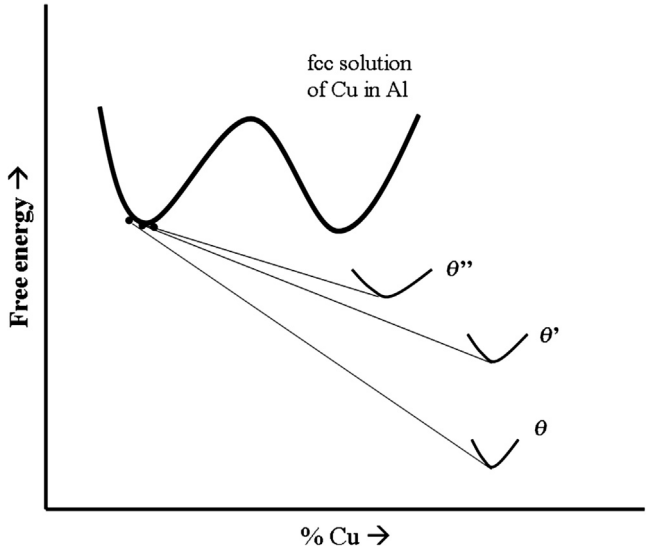

Figure 99 Hypothetical free energy–composition curves for the precipitate phases in Al–Cu alloys. After Fine (1964) and Hardy and Heal (1954).

near the Al-rich side of the alloy (Hardy and Heal, 1954; Meijering, 1952). However, even if the heat of mixing is negative over the entire composition range, an inflected G vs. X curve and a metastable miscibility gap can result if the heat of mixing curve is sufficiently inflected (Meijering, 1952); thus, a positive heat of solution or mixing *is not a prerequisite* for the occurrence of spinodal phase separation

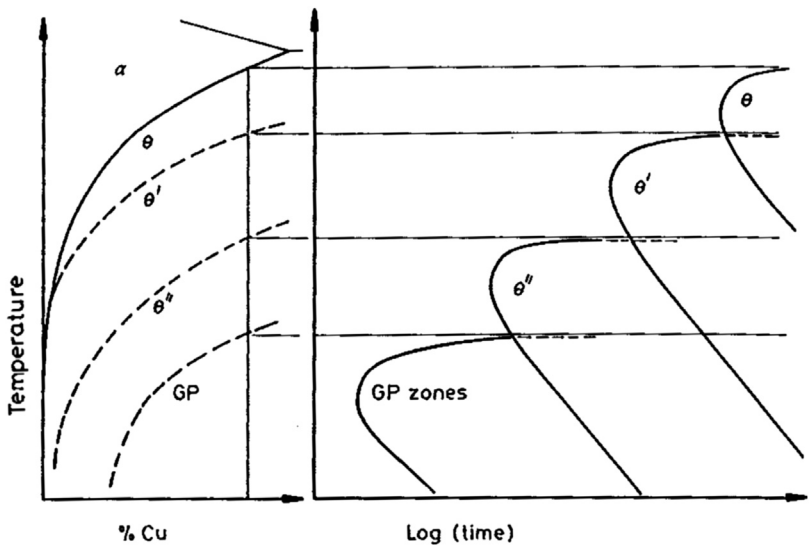

Figure 100 Portion of a schematic Al–Cu phase diagram depicting stable and metastable solvi as well as TTT curves (precipitation start) for the various precipitation reactions. After Smallman (1963).

in the system. Furthermore, it should be pointed out that the subsequent phases following G.P. I zone formation are, in fact, atomically ordered phases, namely, G.P. II (θ''), θ' and θ.

Clearly, there must be some synergistics between the formation of the n-th and (n+1)-th phases in the precipitate sequence. The copious formation of a coherent intragranular phase through homogeneous nucleation or spinodal decomposition creates a high density of interphase interfaces which can serve as effective nucleation sites for subsequent phase formation. Also, in some cases the next phase in a precipitation sequence may form through continuous transformation of the previous phase which may be the situation in the G.P. I zones → G.P. II zones (ordering) transition. The formation of the equilibrium precipitates are generally relegated to heterogeneous nucleation at high-angle grain boundaries after long aging times. It should be pointed out that the formation of a more stable phase in any precipitation sequence will lead to the dissolution of the less stable phase because of chemical potential/composition gradients which develop since the concentration in local equilibrium with the more stable phase is less than that in equilibrium with the less stable phase.

The Ni–Ti system is generally of the same genre as that of the Ni–Al alloys and both are of great importance in the metallurgy of modern superalloys with Ti along with Al playing a primary role in the formation of the Ni_3 (Al, Ti) γ' phase. The γ' phase exhibits the $L1_2$ superstructure in Ni–Al and Ni–Ti alloys and is essentially the major precipitating phase in numerous high-temperature high-strength alloys. (The γ' Ni_3Al and Ni_3Ti phases are isomorphous.) In the Ni–Al binary system the γ' is the equilibrium phase whereas in the Ni–Ti binary precipitation system the equilibrium phase is an Ni_3Ti (η) hexagonal phase which is preceded by the formation of a coherent γ' Ni_3Ti phase during aging. We will focus our attention on the formation of this metastable γ' in Ni–Ti alloys containing 10–15 atomic percent Ti because extensive experimental evidence is available indicating a complex interplay between clustering and ordering effects during the decomposition of supersaturated solid solutions in this system. There appears to be a synergism between ordering instabilities and spinodal decomposition during the precipitation of the $\gamma'Ni_3Ti$ phase. These experimental studies include magnetic measurements (Israel and Fine, 1963), electron microscopy and diffraction (Saito and Watanabe, 1969; Ardell, 1970; Laughlin, 1976; Kompatscher et al., 2003), atom probe field ion microscopy (Sinclair et al., 1974; Grune, 1988) and small-angle neutron scattering (Kostorz et al., 1999; Kompascher et al., 2000). The results clearly point to a complex interplay between continuous ordering and phase separation/spinodal decomposition. The following analysis is based heavily on the thermodynamic analyses of Soffa and Laughlin (1989) and Khachaturyan et al. (1988).

In **Figure 101** a schematic phase diagram showing a metastable γ' solvus along with loci of thermodynamic instability with respect to ordering (T_i^-) and phase separation (T_S) is depicted. Also delineated is a region of congruent ordering between T_0 and T_i^- wherein a supersaturated fcc disordered solid solution can lower its free energy by ordering via a nucleation and growth process at constant composition and subsequently spinodally decompose. The T_S is a conditional spinodal mapping out a region between T_0 and T_S where a nonstoichiometric ordered state becomes unstable with respect to phase separation subsequent to ordering of an initially metastable disordered solid solution. For example, if an Ni–Ti alloy containing ~12–14 atomic percent Ti (C_o in **Figure 101**) is rapidly quenched to room temperature and then aged at 600 °C, the resulting supersaturated state α_o (A) depicted in **Figure 102** may become unstable with respect to $L1_2$ ordering and is expected to continuously order to an imperfectly ordered, nonstoichiometric solid solution decreasing the free energy as shown. This ordered state at B is now phase separation and a spinodal process involving selective amplification of composition modulations within the ordered solution resulting in the continuous evolution of a metastable two-phase mixture composed of α' terminal solid solution and $\gamma'(Ni_3Ti; L1_2)$. During the

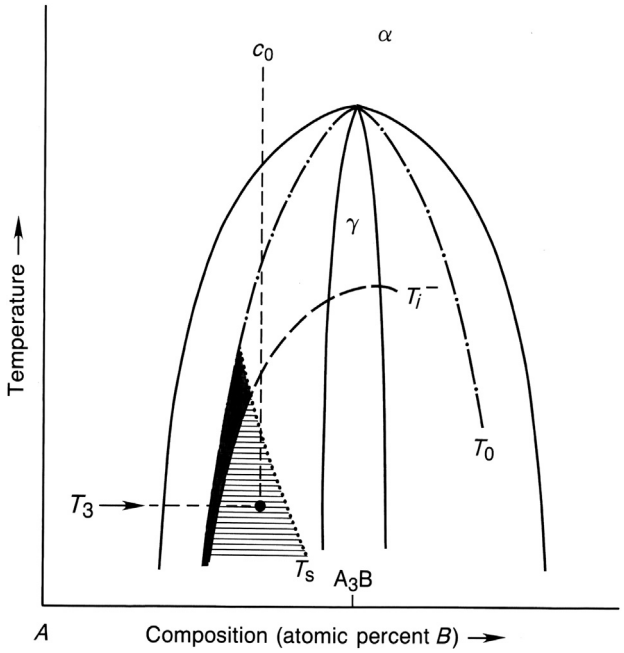

Figure 101 Schematic phase diagram showing a metastable γ' phase including a spinodal region (shaded) as well as a region of ordering instability below T_i^-. After Soffa and Laughlin (1989).

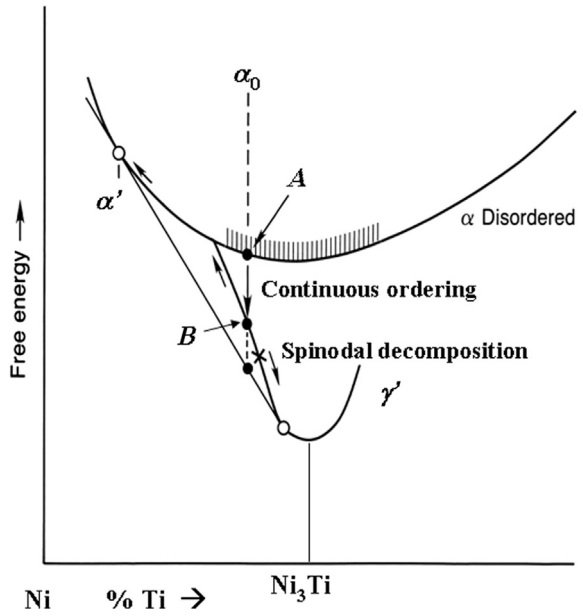

Figure 102 Hypothetical free energy–composition diagram that is consistent with the decomposition process in Ni–Ti alloys. A supersaturated α_0 solid solution will first order continuously and then decompose spinodally into the ordered γ' and disordered α' two-phase mixture.

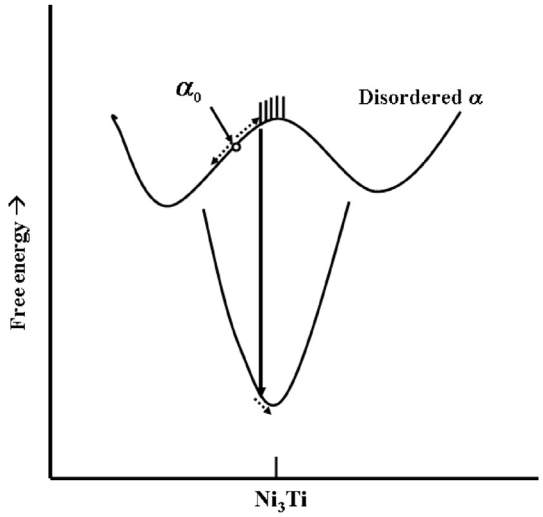

Figure 103 Precipitation reaction whereby the initial supersaturated solid solution α_0 begins to decompose spinodally and the solute-enriched regions become unstable with respect to atomic ordering (continuous ordering) leading to the formation of a two-phase mixture resulting from consecutive continuous transformations.

early stages of decomposition the alloy exhibits a so-called modulated structure and "sideband" state as composition waves develop preferentially along the ⟨100⟩ directions of the cubic matrix (~100A spacing) resulting in a periodic array of γ' particles aligned along the ⟨100⟩ directions. There is strong experimental evidence as well as computational thermodynamic analysis that an ordered state precedes the amplification of the concentration waves within this synergistic process involving ordering and clustering (Kompascher et al., 2000 and Soffa et al., 2010) consistent with the decomposition path shown in the free energy–composition scheme of **Figure 102**. The reaction path involving a conditional spinodal phase separation similar is to that discussed by Allen and Cahn (1976) and Ino (1978) cited earlier but in this case a first-order ordering transformation (A1 → $L1_2$) is involved rather than a second-order/higher order (A2 → B2) ordering. However, another decomposition path has been suggested (Laughlin, 1975) as depicted in the free energy–composition scheme in **Figure 103**. In this scenario the initial supersaturated disordered solid solution begins to phase separate spinodally into solute-enriched and solute-depleted regions with the solute-enriched regions becoming unstable with respect to ordering and continuously order to form the $L1_2$-based ordered phase. In both cases there is an interplay between ordering and clustering tendencies and continuous transformation involved in the precipitation of an ordered phase within a supersaturated solid solution. Generally, this behavior derives from solution energetics involving pairwise interactions beyond first nearest neighbors (Richards and Cahn, 1971; Ino, 1978; Soffa et al., 2010).

The Al–Li binary system is the basis for the development of a series of light-weight, high-strength precipitation-hardened alloys and the strengthening precipitate, δ′, is a metastable Al_3Li ($L1_2$) phase characterized by a small misfit (<0.1%) between the matrix and precipitate. The δ′ phase can form coherently with the matrix with a very low interfacial free energy $\sigma_{M-P} \sim 20$ erg/cm^2 to produce fine homogeneous dispersions of quasi-spherical particles throughout the matrix after suitable heat treatment. (Sometimes so-called precipitate-free zones can develop near grain boundaries resulting from vacancy depletion or solute depletion near grain boundaries (Kelly and Nicholson, 1963).) The equilibrium

δ phase has the B32 cubic structure and nucleates and grows primarily at the grain boundaries after prolonged aging. Baumann and Williams (1985) have applied CNT to describe the homogeneous nucleation of the metastable δ′ phase and Wang and Shiflet (1998) have quantitatively described nucleation and growth of δ′ on dislocations. Radmilovic, Fox and Thomas (1989) in their HREM and X-ray studies of Al–Li alloys containing ~8–11 atomic percent Li called attention to an atomic ordering within the supersaturated state preceding precipitation of the δ′ phase and explicitly suggested that the ordering was followed by spinodal decomposition similar to the conditional spinodal discussed earlier. Their observation is in agreement with the earlier report by Sato et al. (1988) that the early stages of decomposition in similar alloys exhibited imperfectly ordered domains that percolated throughout the microstructure before formation of a fully developed discrete $L1_2$ precipitate phase. These experimental studies were followed by a theoretical treatment by Khachaturyan et al. (1988) that indicated an interplay of ordering and spinodal phase separation in the precipitation of ordered intermetallic phases consistent with a generalized graphical thermodynamic description by Soffa and Laughlin (1989) as cited previously. Poduri and Chen (1997) subsequently reported a computer simulation of ordering and phase separation in the Al–Li alloys associated with δ′ formation and were able to delineate the different regimes of behavior discussed earlier as well as revealing a regime of nonclassical nucleation involving fluctuations in composition and order parameter.

Copper–titanium alloys containing 1–6 atomic percent Ti can be age hardened to develop physical and mechanical properties comparable with the widely used high-strength Cu–Be alloy series. In the 1960s and 1970s the Cu–Ti alloys were recognized to be prototypical "sideband alloys" (see **Figure 90**) and it was suggested by various investigators that these alloys undergo spinodal decomposition during age hardening (Hakkarainen, 1971; Cornie et al., 1973; Laughlin and Cahn, 1976; Datta and Soffa, 1976; Soffa and Laughlin, 2004). The strengthening precipitate is a tetragonal Cu_4Ti $\left(D1_a; Ni_4Mo - \text{type}/I\frac{4}{m}\right)$ phase which forms below approximately 700–800 °C. At aging temperatures in the range 350–500 °C ultrahigh strengths can be achieved through the formation of fine-scale dispersions of coherent $D1_a$ precipitates aligned along the ⟨100⟩ matrix directions exhibiting a quasi-periodic microstructure. The precipitates are elongated along the *c*-axis of the tetragonal phase which is parallel to the cube directions of the matrix. See **Figure 104**. The equilibrium phase is a $Cu_4Ti(\beta)$ orthogonal (Pnma) phase above about 400–500 °C whereas at lower temperatures the $D1_a(\beta')$ phase is the stable phase. Relevant portions of the Cu–Ti binary phase diagram are shown in **Figure 105**. During prolonged aging at low and moderate temperatures (350–500 °C) a coarse cellular lamellar microconstituent composed of terminal solid solution and the equilibrium phase forms at the grain boundaries and grows out consuming the fine dispersion of coherent/semicoherent $D1_a$ particles. See **Figure 106**. At high aging temperatures ~700 °C the equilibrium orthorhombic phase forms via classic Widmanstatten precipitation with platelets lying along the {111} matrix planes as shown in **Figure 106**. Ecob et al. (1980) have suggested that the Widmanstatten plates in the vicinity of the grain boundaries can catalyze the formation of the cellular colonies at the higher aging temperatures.

The decomposition of supersaturated Cu–Ti alloys containing 1–6 atomic percent Ti embodies a very complex synergy of ordering, clustering and precipitation behavior associated with the formation of the $D1_a$ phase. During decomposition there is a subtle interplay between SRO and LRO as well as phase separation and precipitation of an ordered intermetalic phase. The early stage ordering effects have been widely studied in Ni_4Mo-type systems for stoichiometric and off-stoichiometric compositions including effects of radiation (Bellon and Martin, 1988). The concentration wave approach shown in **Figure 107** has proven very useful for describing the SRO and LRO effects. Interestingly, the dilute

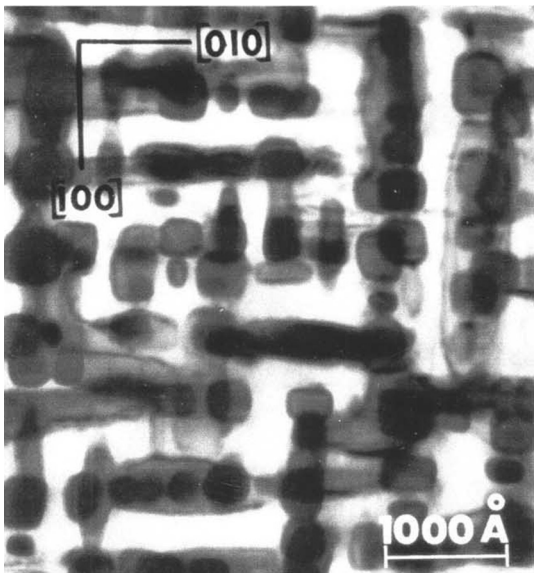

Figure 104 TEM microstructure of age-hardened Cu-4wt % Ti alloy aged at 500 °C for 2000 min. After Soffa and Laughlin (2004).

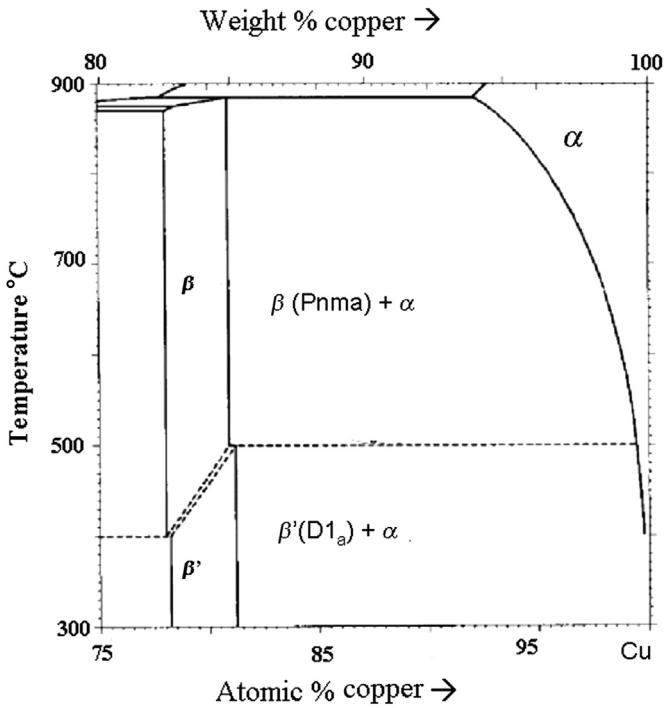

Figure 105 Detailed portion of Cu–Ti phase diagram showing the polymorphic transformation temperatures of Cu_4Ti phase. After Soffa and Laughlin (2004) and Brun et al. (1983).

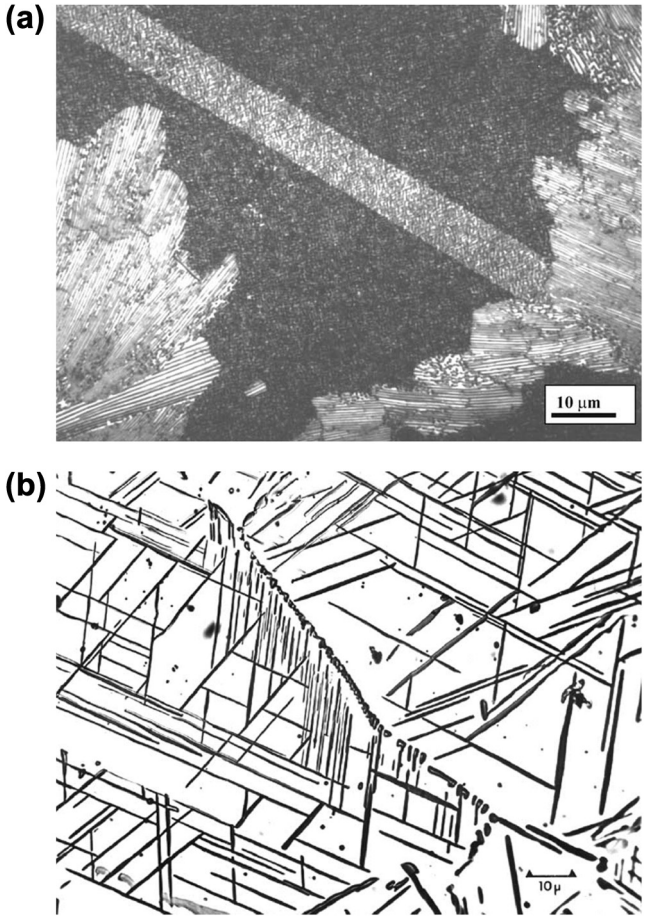

Figure 106 (a) Cellular microconstituent growing into the coherent/semicoherent fine-scale two-phase mixture ($\alpha' + \beta'$) near peak hardness of a Cu-4w/0 Ti alloy aged at 600 °C for 1000 min. (b) Widmanstätten precipitation in a Cu 3 wt.% Ti alloys held at 730 °C for 600 min. After Soffa and Laughlin (2004).

Cu–Ti alloys very early in the decomposition process during aging show diffuse diffracted intensity at reciprocal lattice locations $\langle 1½\ 0\rangle$ deriving from the amplification of concentration waves along the {420} planes having a wave vector ¼ ⟨420⟩ producing modulations of the type AABBAA.... This rapid amplification of "ordering waves" stems from an ordering instability associated with so-called special points in the k-space representation of the solution energetics (de Fontaine, 1975; Bellon and Martin, 1980). These early stage atomic rearrangements (SRO) are followed by the emergence of an imperfectly ordered $D1_a$ structure producing diffuse superlattice reflectons (LRO) at the positions $1/5\langle 420\rangle$ (Hakkarainen, 1971; Laughlin and Cahn, 1975) which then gives rise to discrete coherent $Cu_4Ti/D1_a$ precipitates aligned along the ⟨100⟩ matrix directions. It is important to point out that the free energy–composition curve which is central to conventional thermodynamic discussions of metastability and instability in supersaturated solid solutions is subject to change as atomic rearrangements on various length scales within a nonequilibrium solid solution occur. The free energy curve evolves as the

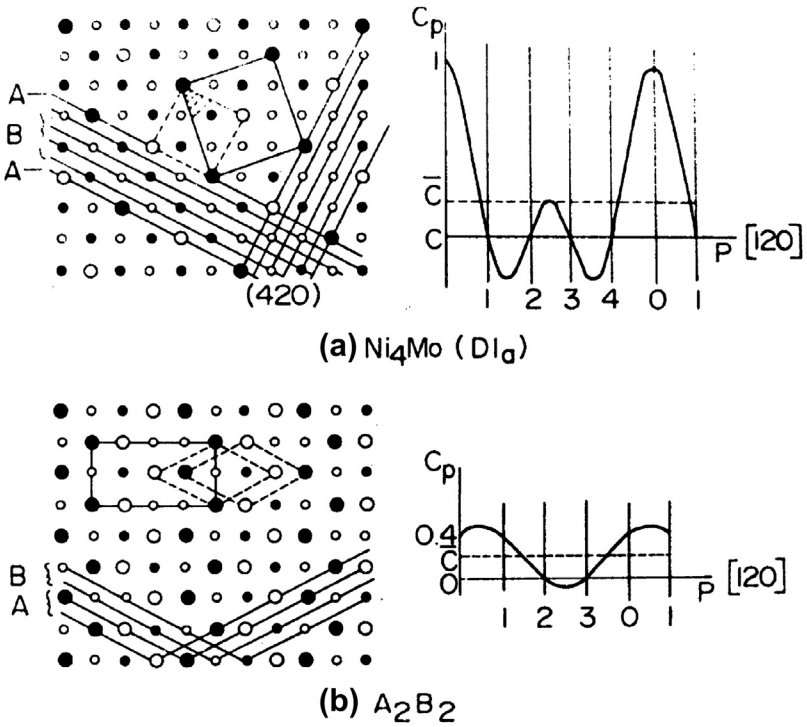

Figure 107 Concentration wave description of LRO (a) and SRO (b) in an Ni_4Mo-type system depicted as modulation in atomic arrangement of {420} planes. After Banerjee and Sundaraman (1992).

solution energetics are changed by local ordering (or clustering) and distort giving rise to regions of negative curvature and changes in thermodynamic stability with respect to ordering and phase separation (Liu and Loh, 1971). See **Figure 108**. Thus, a disordered solid solution which is initially metastable when passing through the SRO → LRO states described above can lower the free energy from P to Q and render the imperfectly ordered state unstable with respect to phase separation and lead to spinodal decomposition and continuous formation of the nearly stoichiometric $D1_a$ phase. This is a conditional spinodal reaction similar to the reaction paths discussed above and consistent with the apparent amplification of concentration waves within an imperfectly ordered state and the unambiguous appearance of a sideband state. It is concluded here that the decomposition of dilute Cu–Ti alloys at high supersaturations generally involves a conditional spinodal process resulting from the SRO → LRO atomic rearrangements occurring during the earliest stages of aging resulting in the precipitation of an intermetallic phase (Laughlin and Cahn, 1975; Datta and Soffa, 1973, 1976; Soffa and Laughlin 1982). However, Borchers (1999) in studies of a Cu-0.9 at.%Ti alloy using electron microscopy (TEM) and thermodynamic calculations analyzed the nucleation energetics and suggests that the copious formation of coherent ellipsoidal or oblong $D1_a$ particles from the onset of decomposition in this alloy was most likely the result of nonclassical nucleation or "big bang"/"catastrophic" nucleation. The analysis using classical nucleation indicates a nucleation barrier ΔG^* of approximately k_BT for an estimated interfacial free energy $\sigma \sim 30$ erg cm^{-2} including an Eshelby estimate of the strain energy. Borchers concludes that the apparent modulated structures emerge through concomitant

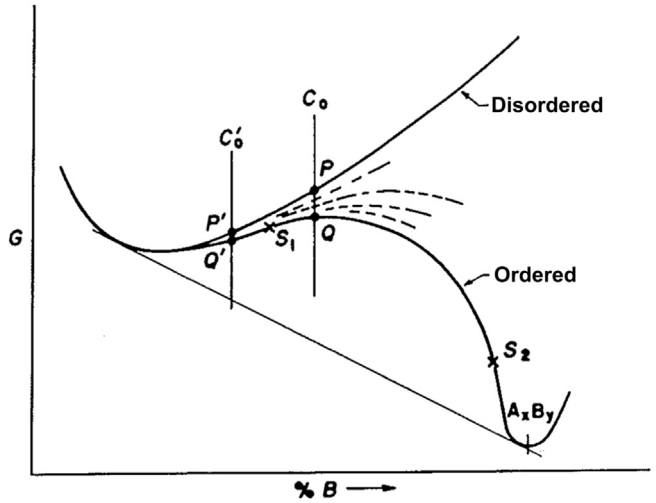

Figure 108 Hypothetical free energy–composition diagram for homogeneous disordered and ordered solid solution, showing a hierarchy of free energy curves. An alloy of composition C_0 first orders homogeneously (from P to Q), and then phase separates into two ordered phases until the solute lean phase disorders. After Soffa and Laughlin (1982).

growth and coarsening under the influence of elastic interaction from the earliest stages of decomposition.

Kahlweit (1970) and Kampmann and Kahlweit (1967, 1970) suggested that at high supersaturations separating a precipitation reaction into distinct stages of nucleation, growth and coarsening may not be applicable to describing the evolution of the particle density during aging. They analyzed a supersaturated system wherein nucleation, growth and coarsening were concomitant and competitive processes showing that the density of precipitate particles during decomposition rises to a maximum and then tends to decrease while the matrix is still markedly supersaturated as a result of competitive coarsening. Langer and Schwarz (1980) later approached the problem and found a similar behavior. Wendt (1981) and Wendt and Haasen (1983) also revealed such a trend in his studies of precipitation in an Ni-14 at.% Al alloy. Wagner and Kampmann (1991) proposed a modified Langer–Schwartz model and a detailed numerical formulation to predict the evolution of the size distribution of precipitate particles and applied it to a Cu-1.9 wt % alloy.

Spinodal decomposition has been identified in high-strength Cu–Ni–Sn alloys which also results in the precipitation of an ordered phase (Zhao and Notis, 1998). In these ternary alloys the initial disordered supersaturated state appears to undergo spinodal decomposition into two disordered phases with the solute-rich phase then lowering its free energy by ordering to form the ordered precipitate phase as discussed earlier.

8.7 Crystallography and Microstructure

8.7.1 Introduction

There are many ways that the symmetry of the parent and/or new phases comes into play in determining the microstructure of an alloy that has undergone a phase transformation. For example, it is well

known that if the new phase has an arrangement of atoms on a plane that is the same as or similar to a plane in the parent phase, it is expected that the planes may be in contact with each other and determine the orientation relation between the new and parent phases. When an HCP Co alloy phase forms from an FCC Co alloy phase we find that the $(0001)_{HCP}$ planes are parallel to the $\{111\}_{FCC}$ planes. If the environmental fields (stress fields, magnetic fields, etc.) are isotropic, or non existent, we expect all the $\{111\}_{FCC}$ planes to have HCP particles of Co with their basal planes parallel to them. If however a field is applied in a specific direction one or more of the orientations of the new HCP phase may be missing.

The shape of the new phase is another way that symmetry controls microstructure. For example, a phase with one long direction and two unequal short directions will give rise to a distinctive microstructure.

Another effect of symmetry has to do with the relationship between the symmetry groups of the parent and new phases. When a phase undergoes a *disorder to order transition*, the phase with the lower symmetry (the ordered phase) can exist in two or more regions, called variants or *domains*, that are related to each other by one of the symmetry operations that was lost in the transition. In atomic ordering transitions, regions differing by a translation vector are called *antiphase domains* and regions differing by a rotation or reflection are called *orientational domains*.

Disorder to Order Transformations include

- Atomic Order
- Magnetic Order
- Displacive Order
- Ferroelectric Order

Subsequently, we will only discuss atomic ordering. See Dahmen (1987) for a full discussion of the role of symmetry on phase transformations.

8.7.2 Habit Planes and Orientation Relationships

The number of variants of a phase that exist in the microstructure of a transformed alloy can be determined by use of the symmetry of the parent phase if the orientation relationship is known. The example mentioned earlier of a plate-like HCP Co alloy phase precipitating from an FCC Co alloy phase will first be discussed. It was stated that the close-packed planes were parallel to each other. There are eight $\{111\}$ planes in the FCC structure, as the digits 1 or -1 can be placed in any of the three positions of the Miller indices. These are

$$(111), (\overline{1}11), (11\overline{1}), (\overline{1}\overline{1}1), (1\overline{1}1), (\overline{1}1\overline{1}), (\overline{1}\overline{1}1) \text{ and } (1\overline{1}\overline{1})$$

However, both the HCP and FCC phases contain a center of symmetry and so there are only four distinguishable orientations of the variants. For example, in this case, the $(0001)_{HCP}//(111)_{FCC}$ cannot be differentiated from the case of $(0001)_{HCP}//(\overline{1}\overline{1}\overline{1})_{FCC}$.

For the general case of an $\{hkl\}$ habit plane in a cubic phase with m$\overline{3}$m symmetry it can determined that there are 24 distinct orientation relationships that a plate-like new phase with that of the parent phase if the new phase has a center of symmetry. The $\pm h$ index could be placed in any of the three positions (six ways), the $\pm k$ index could then be placed in any of two positions (four ways) and the $\pm l$ index can only go in the remaining position (two ways). The product of these ways of indexing $\{hkl\}$ planes is 48 (the order of the cubic point group). However if the structures of the new phase contains

a center of symmetry, only 24 of these is distinguishable. This method can also be used for parent phases of lower symmetry.

8.7.3 Shape of the Precipitate

The orientation relationship does not necessarily completely determine the number of ways that a new phase may appear in the parent matrix. If the shape of the new phase allows for additional degrees of freedom more orientations are possible. Consider a lath-shaped particle forming in a cubic matrix, where one dimension of the particle is much longer than the other two unequal dimensions. See Figure 109. The long dimension of the precipitate can be along any of the ⟨100⟩ directions of the cubic phase. However there are two ways for each ⟨100⟩ direction that the precipitate may align itself. See for example particles 5 and 6 of Figure 109. These particles have their larger flat surfaces perpendicular to the [010] and [100] directions, respectively.

In this case there are three possible habit planes and two orientations per habit producing six possible orientations of the particle. If the flat faces of the particles are along {hk0} of the cubic matrix, there are six possible planes and 2 orientations of the particle per habit yielding 12 possible orientations of the particles. For habit planes along {*hkl*} planes there are 24 possible orientations of the particles. In all these cases it was assumed that both the particle and matrix contained a center of symmetry. If either the particle or the matrix does not contain a center of symmetry (or if neither does) the above number of orientations should be multiplied by 2.

An interesting feature of the precipitations of particles with specific orientation relationships with the matrix can be seen in Figure 110. Here two hexagonal phases have precipitated in an Al alloy 6022. It can be seen that the overall symmetry of the selected area electron pattern (SAD) retains its 4 mm symmetry when all the variants of the new phases are present. This is quite general and shows that when all variants are present the symmetry of the parent phase is retained in the SAD if the diffracting region is large enough.

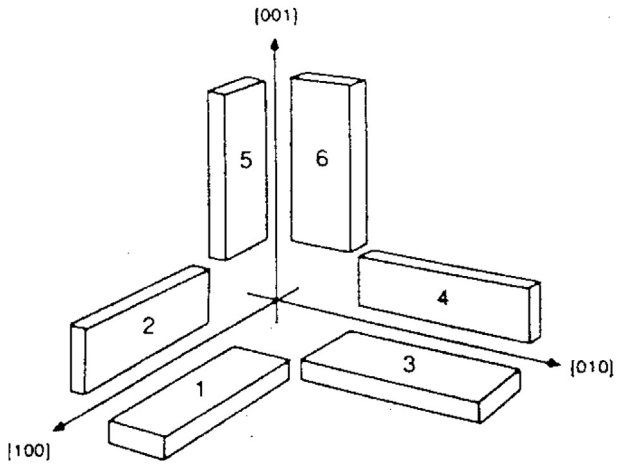

Figure 109 Possible arrangement of a lath with its face perpendicular to ⟨100⟩ directions of a cubic matrix. After Hugo and Muddle (1989).

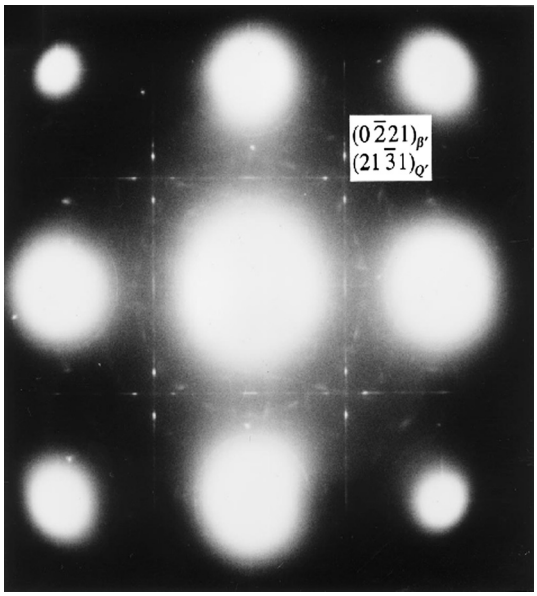

Figure 110 An [001] electron diffraction pattern from an Al–Mg–Si Cu alloy (6022) which has both *Q′* and *b′* precipitates. Both precipitates have their basal planes parallel to ⟨001⟩ of Al matrix. After Miao and Laughlin (2000).

8.7.4 Atomic Disorder to Order Transitions

All disorder to order phase transitions give rise to regions in the microstructure that are called domains. The domains exist as a necessary consequence of the lowering of the symmetry during the ordering process. For atomic ordering the usual cases involve a lowing of the translational symmetry, a lowing of the point symmetry or both translational and point symmetry being lowered. We will look at some examples.

8.7.4.1 Lowering of the Translational Symmetry

A common atomic ordering transformation in binary alloys is the FCC to $L1_2$ transformation. See Figure 111.

This transformation is an isostructural one in that the structure of both phases is cubic. What has changed during the atomic ordering is the translational symmetry: In the FCC structure, the smallest translation of the unit cell which leaves the crystal unchanged (i.e. to identical sites) is $\frac{1}{2}\langle 110\rangle a$, whereas in the $L1_2$ structure the shortest translation to translation of the unit cell which leaves the crystal unchanged is $\langle 100\rangle a$. This decrease in the translational symmetry gives rise to four possible domains, where the red atoms may be placed on any of the four equivalent sites of the FCC structure. See Figure 112.

These domains should arise with equal probabilities unless there is an outside influence on the transformation.

Another example of an isostructural transformation is the BCC to B2 transformation.

Because the ordering arrangements of the four domains displayed in Figure 110 are out of phase with each other a defect called an antiphase domain boundary (APB) is produced when the domains impinge on each other. These APBs will influence many of the physical properties of the ordered phase.

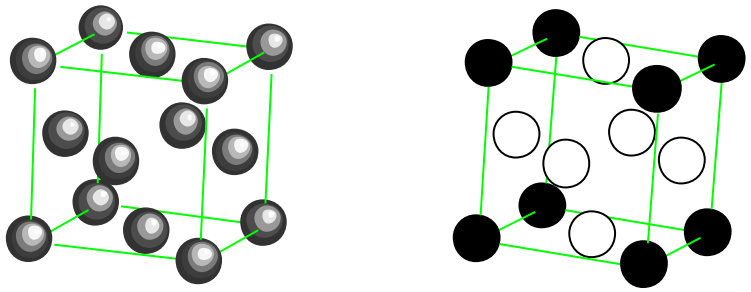

Figure 111 Unit cell of an FCC (Cu prototype, A1, cF4) phase transforming to a $L1_2$ (Cu_3Au prototype cP4). In the disordered cell, the probability of occupancy of all sites by a red atom is 25%, in other words the red atoms and blue atoms are assumed to be randomly arranged on the FCC Bravais lattice.

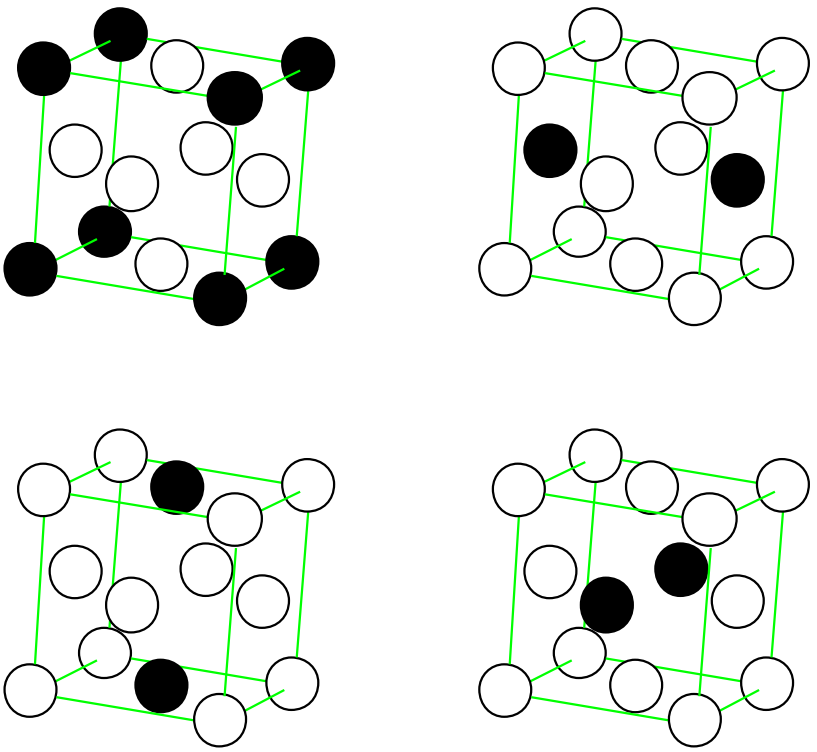

Figure 112 The four possible translational domains that may arise from the FCC to $L1_2$ disorder to order transformation.

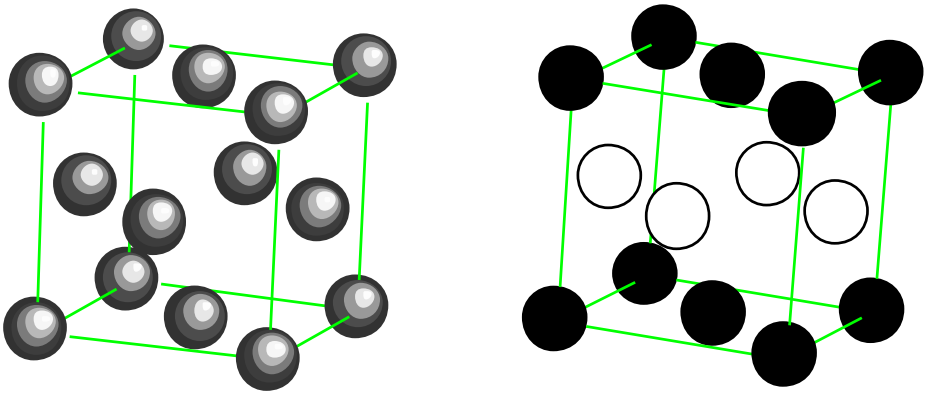

Figure 113 FCC structure to L10 structure. Note the $L1_0$ structure is no longer cubic (it is tetragonal) and can no longer be classified as a face centered cell.

8.7.4.2 Lowering of the Point Group Symmetry

In some disorder to order transitions the point group of the high symmetry disordered phase decreases on ordering. A well-known example of a disorder to order transformation is FCC to $L1_0$. See Figure 113.

This transformation has lowered the point group symmetry of the unit cell from $m\bar{3}m$ to $\frac{4}{m}$mm. It can be readily seen that the *c*-axis of the ordered phase could be parallel to any of the $\langle 100 \rangle$ directions of the parent FCC structure. Since both of the structures contain a center of symmetry, there are three ways to do this since $[001]_{L1_0}//[100]_{FCC}$ is the same as $[001]_{L1_0}//[\bar{1}00]_{FCC}$. More generally this can be determined by the ratio of the orders of the point groups of the two structures: 48 for the cubic structure and 16 for the tetragonal one.

This transformation has a new aspect to it. Adjacent domains may not have parallel *c*-axes. See Figure 114. In this case the domains are called *structural domains* or *variants* of the new phase. Sometimes they have been called twin domains, but that is not the best description, since the underlying disordered structure is not in a twin relationship. Clearly this microstructural feature will affect many of the physical properties of the ordered phase.

This transformation actually changes both the translational symmetry and the point group symmetry. The FCC Bravais lattice with four equivalent sites was changed to a simple tetragonal lattice (with two atoms in it) of one half the volume. This means that there would be not only the *structural domains* or *variants* of the ordered phase but also domains in antiphase with one another. Thus, there would be a total six domains of $L1_0$ arising from the disordered FCC structure. This also can be obtained by multiplying the ratio of the order of the points groups (which we found above to be 3) by the factor 2, which is the ratio (per unit volume) of the number of equivalent points in the disordered phase to that of the ordered phase.

8.8 Massive Transformation

The massive transformation is a distinct genre of diffusional solid-state phase transformation involving a compositionally invariant nucleation and growth process producing a change in crystal structure and/

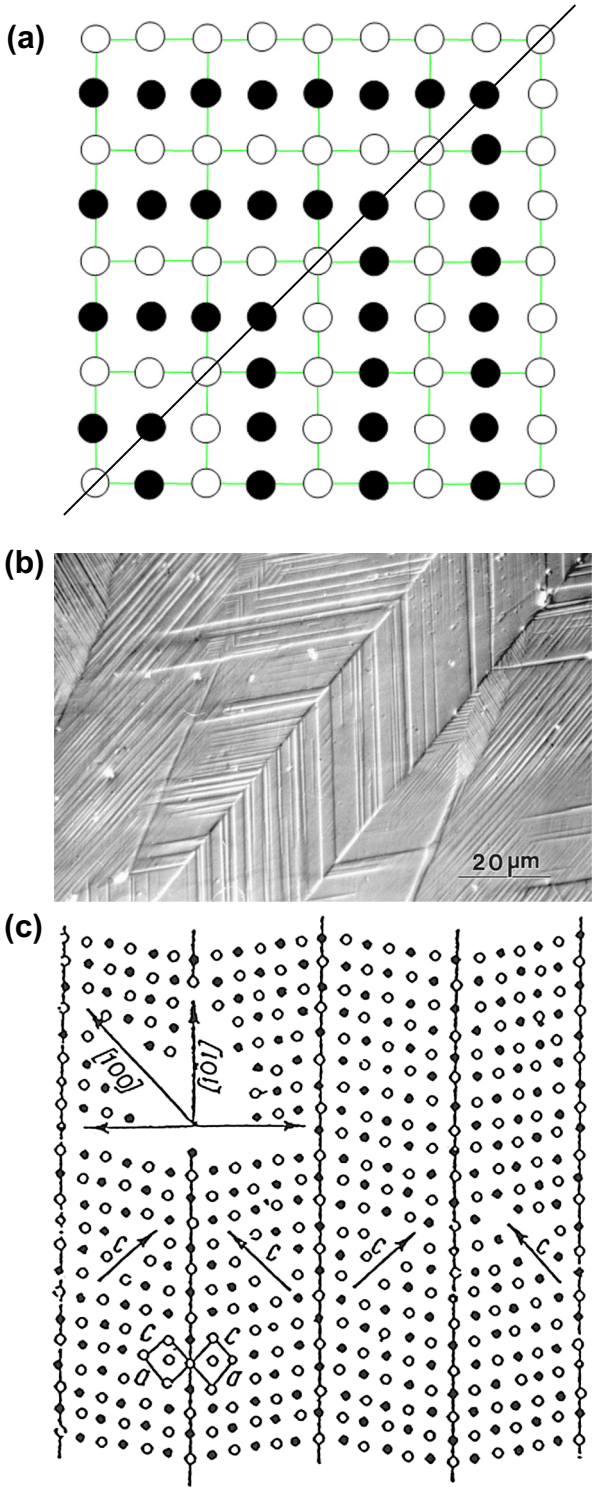
(a)
(b)
20 μm
(c)
[001]
[101]
c
a

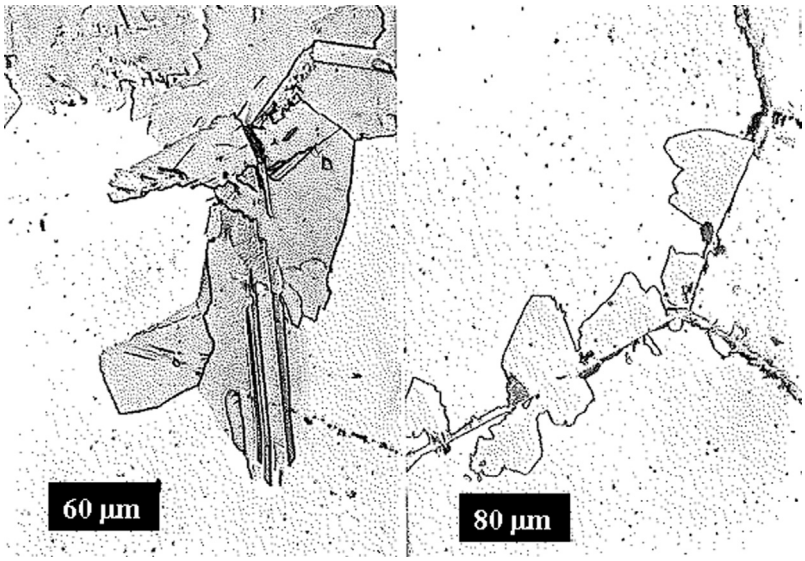

Figure 115 Massive transformation $\beta \rightarrow \alpha$ in β-brass. After Hull and Garwood (1956).

or degree of LRO. This partitionless change of phase is propagated by the migration of interphase interfaces controlled by interphase boundary diffusion processes and these interfaces are generally incoherent across which no systematic crystallographic orientation relationship is established and maintained between the parent and product phases. This mode of transformation occurs in pure metals, ferrous and nonferrous solid solutions and ceramic materials (Massalski, 1970; Fung et al., 1994; Aaronson et al., 2010). The transformation was first documented in studies of Cu–Zn and Cu–Al alloys during the 1930s (Phillips, 1930; Greninger, 1939), and later examined, in detail, by Hull and Garwood (1956) and Massalski (1958) in the 1950s. **Figure 115** shows the massive transformation product in the seminal β-brass alloys. A Symposium on the Mechanism of the Massive Transformaion was held in St. Louis, MO, at the Fall 2000 TMS/ASM Meeting as the transformation was recognized to occur in a growing number of technological contexts such as in TiAl-based alloys (Wang et al., 2002; Wittig, 2002).

Let us look briefly at the thermodynamic aspects of this compositionally invariant transformation in a binary system. We consider the classic β(bcc) $\rightarrow$ α_m(fcc) massive transformation in a Cu- 38 at.% Zn solid solution occurring when the high-temperature β phase is quenched to room temperature or below with the α_m(fcc) massive product appearing at the grain boundaries of the parent phase. See **Figure 115**. A set of schematic free energy–composition curves are shown for the α and β phases in **Figure 116** exhibiting the important crossing of the free energy curves at the composition Cu-38 Zn at 700 °C. This

Figure 114 (a) Two domains of the $L1_0$ structure with perpendicular *c*-axes. These are called variants of the phase and the boundary is a structure domain boundary. For this case the boundary mirrors the structure of one domain into that of the other. (b) Optical micrograph showing polytwinned structure in Fe-Pd alloy resulting from stress-affected growth and coarsening of tetragonal L1o phase. (courtesy of H. Okumura). (c) Schematic of polytwinned microstructure with modulation of the c-axis across variant related c-domains. After Vlasova et al. (1969).

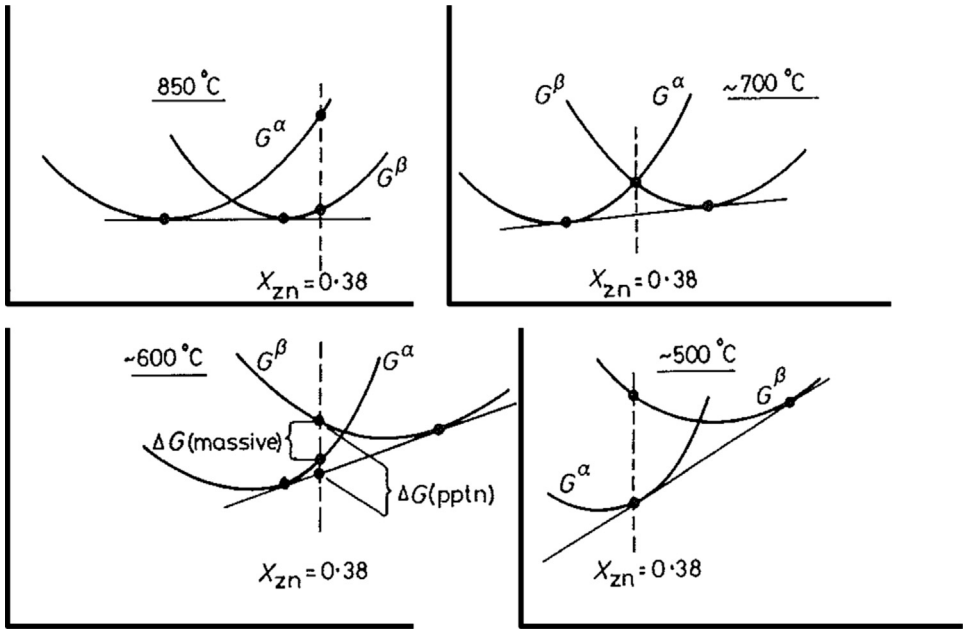

Figure 116 Free energy–composition diagrams showing the thermodynamics of the massive transformation $\beta \rightarrow \alpha$ in Cu–Zn (β-brass) delineating the temperature $T = T_0 \approx 700\,^{\circ}\text{C}$ for the composition $X_{Zn} = 0.38$. After Porter and Easterling (1992).

intersection defines the temperature T_0 for this composition because it is clear that at any temperature below 700 °C this particular alloy can lower its free energy by transforming at constant composition by $\Delta G_{massive}$ as the free energy of the solution falls from one curve to another ($\beta \rightarrow \alpha$) with an attendant change in crystal structure. This massively transformed state α_m is metastable with respect to an $\alpha + \beta$ phase mixture that would lower the free energy to a point on the common tangent. A general set of free energy–composition curves are shown in **Figure 117** where regions between X^{α}_{eq} and X_0 allow for the

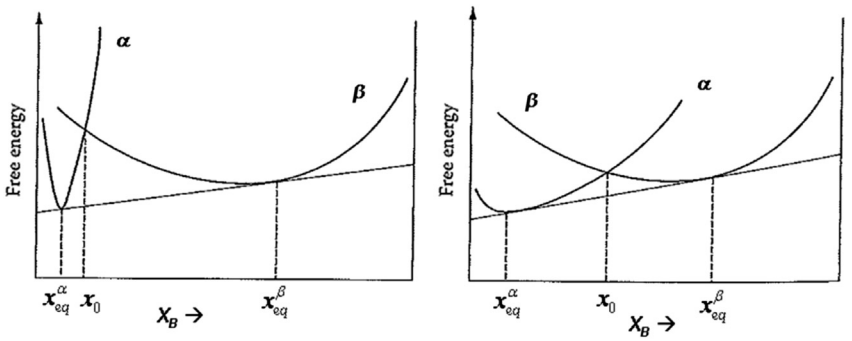

Figure 117 General free energy–composition schemes delineating regions of possible massive transformation of $\beta \rightarrow \alpha$ between compositions $X_{eq}(\alpha)$ and X_0. Note the importance of the crossover point at $X = X_0$ in both figures. After Aaronson et al. (2010).

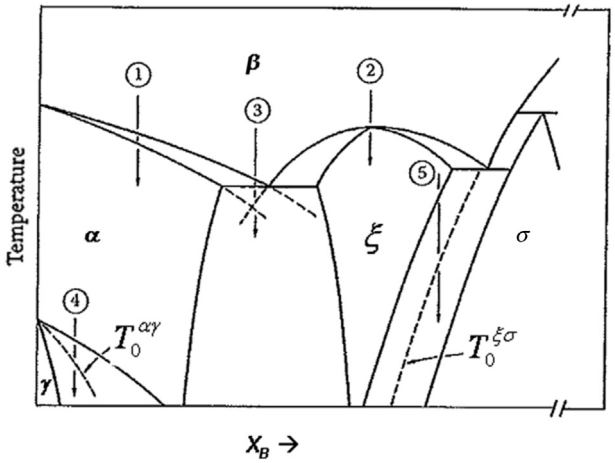

Figure 118 General phase diagram showing T_0 loci and regions of possible massive transformation. After Aaronson et al. (2010).

possibility of a compositionally invariant $\beta \rightarrow \alpha$ transformation (massive or martensitic as mentioned earlier). The T_0 concept is of paramount importance in mapping regions of possible compositionally invariant transformation below this temperature. The T_0 loci are depicted in a general hypothetical binary phase diagram in Figure 118.

The massive transformation product almost invariably nucleates heterogeneously at the grain boundaries of the high-temperature phase generally establishing an orientation relationship and a low-energy coherent or semicoherent interphase interface with one of the grains and an incoherent interface with the adjacent grain. Subsequent growth occurs virtually exclusively into the parent phase by migration of the disordered/incoherent boundary. However, it is sometimes found that the migrating interphase boundaries develop facets and serrated morphologies even in the absence of any orientation relationship with the parent phase and it appears that this results from the nature of the surface energetics and atomic attachment processes specific to the growing phase and not from constraints associated with crystallographic matching at the interface (Yanar et al., 2002).

The heterogeneous nucleation of the massive transformation product at grain boundaries has been treated quantitatively by several investigators over the years using CNT (Yanar et al., 2002; Veeraraghavan et al., 2003). The growth kinetics appear to follow a modified Burke–Turnbull description allowing for continuous atomic attachment or a ledge mechanism at the advancing interface. The activation energy for growth is typically found to be about 1/4 to 2/3 that for bulk diffusion in the system consistent with the notion of growth mediated by boundary or interface diffusion. Atomic attachment at the migrating interface can result in profuse twinning and faulting of the massive transformation product (Veeraraghavan et al., 1999; Yanar et al., 2002).

Buckley (1975) and Rajkovic and Buckley (1981) have revealed and analyzed a massive mode involved in the order–disorder transformation (A2 → B2) in Fe–Co and Fe–Co–X alloys. See Figure 119. At high transformation temperatures the ordering appears to occur via homogeneous or continuous ordering controlled by volume diffusion but at low temperatures where volume diffusion becomes sluggish the ordered phase nucleates at the grain boundaries of the parent-disordered bcc phase and grows behind an advancing incoherent interface utilizing the enhanced diffusivity at the

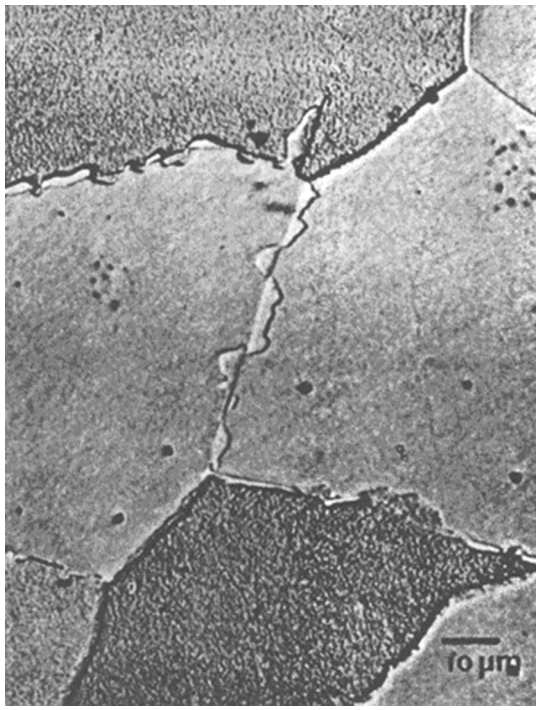

Figure 119 Massive transformation mode in the disorder → order transformation in Fe–Co alloy. After Rajkovic and Buckley (1981).

phase boundary. As mentioned earlier, the nuclei are coherent with respect to the adjacent grain into which growth of the ordered phase is negligible. It is important to note that the A2 → B2 is thermodynamically HIGHER ORDER making this a particularly interesting case.

8.9 Closure

Phase transformations in materials (metallic and nonmetallic) provide the metallurgist and materials scientist/engineer with one of the most effective tools for tailoring the structure and properties of engineering materials for application in modern technology. Understanding the fundamentals (thermodynamics, kinetics, crystallography and mechanistics, etc.) governing the evolution of material structure during synthesis, heat treatment and thermomechanical processing substantially removes the production and manufacture of materials from the realm of inefficient and unnecessarily expensive quasi-empiricism—albeit sometimes sophisticated empiricism—and allows for intelligent engineering design of structure–property relations in high-strength aluminum alloys, high-strength low-alloy steels and high-temperature nickel-base alloys. Ceramic materials are toughened by controlled precipitation from solid solution of a dispersed phase in an oxide matrix which inhibits crack propagation. It must be appreciated that the wide variety of structure–property relationships attainable with conventional steels more often than not involves controlling the distribution of carbides within an Fe-rich matrix or controlling the ferrite grain size resulting from the proeutectoid reaction in low-carbon steels. In

quenched and tempered steels the important tempering step really involves precipitation from a supersaturated bcc or bct phase. If steels were the substance of the industrial revolution of the nineteenth and early twentieth century we might say that the Fe–C phase diagram with its eutectoid and associated phase transformations underpinned this cultural transformation. Extraordinary combinations of properties can now be achieved in age hardenable alloys through our understanding of metastability and the role of vacancies and trace elements in controlling the formation of phases during commercial heat treatments. Furthermore, our understanding and control of deleterious effects of fine-scale precipitation reactions during exposures of alloys to critical temperature ranges such as in the case ferritic and austenitic stainless steels have greatly enhanced our control over the properties of these materials in important engineering applications. The remarkable properties of Ni-base precipitation hardened superalloys (and they are indeed super) in turbine blades stems from a comprehensive understanding of the nucleation, growth and coarsening of the $\gamma'(Ni_3Ti, Al)$ phase during processing and in-service (as well as single-crystal growth during solidification). Over the past two decades or so a great deal of attention has focused on the nature of the disorder $\rightarrow$order transformation in ferromagnetic alloys because of the growing applications of ordered alloys, (for example, FePt) in a plethora of applications in magnetic thin films including futuristic spintronic materials. Furthermore, with the emergence of nanotechnology new fundamental challenges have arisen related to our lack of understanding of the thermodynamics and kinetics of transformations in small systems compared with bulk behavior and this realm will be a rich area for study well into the future.

Computational methodologies and computer simulations have had an enormous impact on the field of phase transformations and microstructural evolution in materials from both a scientific point of view and in the realm of practical application to the design of material structure and properties. CALPHAD and THERMOCALC and associated databases have been of tremendous value to systematizing phase equilibria in a myriad of alloy systems and Monte Carlo simulations and phase field approaches have provided insights into a wide range of issues related to transformation behavior. In this treatise we have not attempted to review this area because of space limitations, not because these contributions were deemed peripheral to the subject matter.

The field of phase transformations is a uniquely broad field of scientific endeavor and fundamental issues which have arisen in the analysis of pearlite growth and spinodal decomposition reach to the cutting edge of some of the most challenging problems in the thermodynamics and statistical mechanics of matter such as nonequilibrium thermodynamics and statistical mechanics, irreversible processes, self-assembly or self-organization, dissipative structures, critical phenomena, and so on. The Nobel Prize winner Prigogine (1980) has called attention to the important difference between BEING (thermodynamic equilibrium) and BECOMING (transformation) and THERMOSTATICS versus THERMODYNAMICS in the physical sciences and the domain of phase transitions is a marvelous example where these two dimensions come together to define the evolution of structure. Another eminent scientist and Nobel Prize recipient Steven Weinberg in his short book "The First Three Minutes" describing the "big bang" and the origins of the universe in virtually layman's terms relates the unfolding of this event essentially as a cascade of phase transitions.

References

Aaronson, H.I., Enomoto, M., Lee, J.K., 2010. Mechanisms of Diffusional Phase Transformations in Metals an Alloys. CRC Press, Baca Raton FL.
Abe, T., Brenner, S.S., Soffa, W.A., 1991. Decomposition of a Cu-Ni-Cr Ternary Alloy. Surf. Sci. 246 (1-3), 266–271.
Allen, S.M., Cahn, J.W., 1976. Mechanisms of Phase Transformations Within the Miscibility Gap of Fe-Rich Fe-Al Alloys. Acta. Met. 24, 425–437.

Ardell, A.J., 1988. Precipitate Coarsening in Solids: Modern Theories, Chronic Disagreement With Experiment. In Phase Transformations '87. Institute of Metals, Cambridge, 485–494.
Ardell, A.J., Nicholson, R.B., 1966. On modulated structure of aged Ni–Al alloys. Acta Metall. 14 (10), 1295–1309.
Ardell, A.J., 1970. The growth of gamma prime precipitates in aged Ni–T alloys. Metall. Trans. 1, 525–534.
Ardell, A.J., 1972. Effect of volume fraction on particle coarsening: theoretical considerations. Acta Metall. 20 (1), 61–71.
Ardell, A.J., Maheshwari, A., 1995. Coherent equilibrium in alloys containing spherical precipitates. Acta Metall. Mater. 43, 1825–1835.
Ardell, A.J., 1988. Precipitate Coarsening in Solids: Modern Theories, Chronic Disagreement With Experiment. Phase Transformations '87. Institute of Metals, Cambridge, 485–494.
Archer, R.S., Jeffries, Z., 1925. New developments in high-strength aluminum alloys. Trans. Am. Inst. Min. Metall. Eng. 71, 828–845.
Asimow, R., 1963. Clustering kinetics in binary alloys. Acta Metall. 11 (1), 72–73.
Avrami, M., 1939. Kinetics of phase change. I: general theory. J. Chem. Phys. 7, 1103–1112.
Avrami, M., 1940. Kinetics of phase change. II: transformation–time relations for random distribution of nuclei. J. Chem. Phys. 8, 212–224.
Avrami, M., 1941. Granulation, phase change and microstructure: kinetics of phase change. III. J. Chem. Phys. 9, 177–184.
Bain, E.C., 1923. Crystal structure of solid solutions. Trans. AIME 68, 625–639.
Banerjee, S., Sundaraman, M., 1992. Kinetics of order-disorder transformation under irradiation. In: Chen, H., Vasudevan, V.K. (Eds.), Kinetics of Ordering Transformations in Metals. The Minerals, Metals and Materials Society, pp. 227–253.
Barmak, K., 2010. A commentary on: Reaction kinetics in the processes of nucleation and growth. Met. Trans. A. 41, 2711–2712 by W. A. Johnson, R. F. Mehl, Trans. AIME 35, 416–458(1939).
Barrett, C.S., Massalski, T.B., 1966. The Structure of Metals. McGraw-Hill, NY, NY.
Baumann, S.F., Williams, D.B., 1985. Experimental observations on the nucleation and growth of Delta prime (Al_3Li) in dilute Al–Li alloys. Metall. Trans. A 16 (7), 1203–1211.
Becker, R., Doring, W., 1935. Kinetic treatment of grain formation in supersaturated vapours. Ann. Phys. 24, 719–752.
Becker, R., 1937. Über den Aufbau binarer Legierungen (On the constitution of binary alloys). Z. Metallk. 29, 245–249.
Becker, R., 1938. Die Keimbildung bei der Ausscheidung in metallischen Mischkristallen. Ann. Physik. 32, 128–140.
Bellon, P., Martin, G., 1988. Irradiation-induced formation of metastable phases-A master equation approach. Phys. Rev. B 38 (940), 2570–2582.
Bethe, H.A., 1935. Statistical theory of superlattices. Proc. Roy. Soc. London 150A, 552–575.
Borchers, C., 1999. Catastrophic nucleation during decomposition of Cu-0.9%Ti, Phil. Mag 79 (3), 537–547.
Borelius, G., 1937. Ann. Phys. 280, 507–??
Borchers, C., 1999. Catastrophic nucleation during decomposition of Cu-0.9%Ti, Phil. Mag 79 (3), 537–547.
Bradley, A.J., 1940. X- ray evidence of intermediate stages during precipitation from solid solution. Proc. Phys. Soc. vol. 52, 80–85.
Bradley, A.J., Taylor, A., 1940. An X-ray Investigation of Aluminum-rich iron nickel aluminum alloys after slow cooling. J. Institute of Metals 66, 53–65.
Bragg, W.L., Williams, E.J., 1934. The effect of thermal agitation on atomic arrangement in alloys. Proc. Roy. Soc. London 145A, 699–730.
Brenner, S.S., Miller, M.E., Soffa, W.A., 1982. Spinodal decomposition of iron-32 at. % chromium at 470 °C. Scr. Metall. 16, 831–836.
Brenner, S.S., Camus, P.P., Miller, M.E., Soffa, W.A., 1984. Phase separation and coarsening in Fe–Cr–Co alloys. Acta Metall. 32, 1217–1227.
Brun, J.Y., Hamar-Thilbault, S.J., Allibert, C.H., 1983. Cu-Ti and Cu-Ti-Al solid-state phase-equilibria in the cu-rich region. Zeitschrift Fur Metallkunde 74 (8), 525–529.
Buckley, R.A., 1975. Microstructure and kinetics of the ordering transformation in iron–cobalt alloys, FeCo, FeCo 0.4%Cr and FeCo 2.5% V. Metal Sci. 9, 243–247.
Buckley, R.A., Rajkovic, M., 1979. Order–Disorder Transformations, and the Metallography and Kinetics of Ordering in Fe-50% Co Based Alloys. Institution of Metallurgists, London.
Buerger, M.J., 1948. The role of temperature in minerology. Am. Mineral. 33 (3–4), 101–121.
Buerger, M.J., 1951. Crystallographic aspects of phase transformations. In: Phase Transformations in Solids. Wiley and Sons, New York, pp. 183–211.
Burgers, W.G., Groen, J., 1957. Mechanism and Kinetics of the Allotropic Transformation of Tin. Discuss. Faraday Soc. 23, 183–195.
Burke, J.E., Turnbull, D., 1952. Recrystallization and grain growth. Prog. Metals Phys. 3, 220–292.
Butler, E.P., Thomasp, G, 1970. Structure and properties of spinodally decomposed Cu-Ni-Fe alloys. Acta. Met. vol. 18, 347–365.
Cahn, J.W., 2006. Introduction to "A solid Solution Model for Inhomogeneous Systems". In: Agren, John, Brechet, Y., Hutchinson, C., . Philbert, J., Purdy, G. (Eds.), Thermodynamics and Phase Transformations: Selected works of mats Hillert. EDP Sciences.
Cahn, J.W., 1956. The kinetics of grain boundary nucleated reactions. Acta Metall. 4, 449–459.
Cahn, J.W., 1957. Nucleation on dislocations. Acta Metall. 5, 169–172.
Cahn, J.W., Hilliard, J.E., 1958. Free energy of a nonuniform system. 1. Interfacial free energy. J. Chem. Phys. 28 (2), 258–267.
Cahn, J.W., 1959. Free energy of a nonuniform system. 2. Thermodynamic basis. J. Chem. Phys. 30 (5), 1121–1124.
Cahn, J.W., Hilliard, J.E., 1959. Free energy of a nonuniform system. 3. Nucleation in a 2-component incompressible fluid. J. Chem. Phys. 31 (3), 688–699.

Cahn, J., 1961. On spinodal decomposition. Acta Metall. 9 (9), 795–801.
Cahn, J.W., 1962a. On spinodal decomposition in cubic crystals. Acta Metall. 10, 179–183.
Cahn, J.W., 1962b. Coherent fluctuations and nucleation in coherent solids. Acta Metall. 10, 907–913.
Cahn, J.W., 1966. The later stages of spinodal decomposition nad the beginnings of particle coarsening. Acta Metall. 14, 1685–1692.
Cahn, J.W., 1968. Spinodal decomposition. Trans. TMS AIME 242, 166–180.
Carslaw, H.S., Jaeger, J.C., 1946. Conduction of Heat in Solids, second ed. 1959. Oxford at the Claredon Press, Oxford.
Cheong, B., Laughlin, D.E., 1994. Thermodynamic consideration of the tetragonal lattice distortion of the $L1_0$ ordered phase. Acta Metall. Mater. 42 (6), 2123–2132.
Chou, A., Datta, A., Meier, G.H., Soffa, W.A., 1978. Microstructural behaviour and mechanical hardening in a Cu–Ni–Cr alloy. J. Mater. Sci. 13, 541–552.
Christian, J.W., 2002. The Theory of Transformation in Metals and Alloys. Pergamon Press.
Corey, C.L., Rosenblum, B.Z., Greene, G.M., 1973. Ordering transition in Ni_3Al alloys. Acta Metall. 21 (7), 837–844.
Cornie, J.A., Datta, A., Soffa, W.A., 1973. Electron microscopy study of precipitation in Cu–Ti sideband alloys. Metall. Trans. 4 (3), 727–733.
Dahmen, U., 1987. Phase Transformations, Crystallographic Aspects. In: Encyclopedia of Physical Science and Technology. Academic Press, San Diego, pp. 319–354.
Daniel, V., Lipson, H., 1943. An X-ray study of the dissociation of an alloy of copper, iron and nickel. Proc. Royal Soc. A 181, 368–378.
Daniel, V., Lipson, H., 1944. The dissociation of copper, iron and nickel: further X-ray work. Proc. Royal Soc. A 182, 378–387.
Danoix, F., Auger, P., 2000. Atom probe studies of the Fe–Cr system and stainless steels aged at intermediate temperature: a review. Mater. Charact. 44 (1–2), 177–201.
Datta, A., Soffa, W.A., 1976. Structure and properties of age hardened Cu–Ti alloys. Acta Metall. 24, 987–1001.
Dehlinger, U., 1937. Dei verschiedenen Arten der Ausscheidung. Z. Metallk 29, 401–403.
Dehlinger, U., 1939. Chemische Physik der Metalle und Legierungen. Akademische verlagsgesellschaft m.b.h.
DeNys, T., Gielen, P.M., 1971. Spinodal decompositionin the Fe–Cr system. Metall. Trans. 2, 1423–1428.
de Fontaine, D., 1973. In: Phase Transitions. Pergamon Press, New York.
de Fontaine, D., 1975. K-space symmetry rules for order-disorder reactions. Acta. Met. 23 (5), 553–571.
Ditchek, B., Schwartz, L., 1979. Applications of spinodal alloys. Ann. Rev. Mater. Sci. 9, 219–253.
Doi, M., Miyazaki, T., Wakatsuki, T., 1984. The effect of elastic interaction energy on the morphology of γ′ precipitates in nickel-based alloys. Mater. Sci. Eng. 67, 247–253.
Dollins, C.C., 1970. Nucleation on dislocations. Acta Metall. 18, 1209–1215.
Ecob, R.C., Bee, J.V., Ralph, B., 1980. The cellular reaction in dilute copper-titanium alloys. Metallurgical Transactions A 11 (8), 1407–1414.
Ehrenfest, P., 1933. Phasenumwandlungen im ueblichen und erweiterten Sinn, classifiziert nach dem entsprechenden Singularitaeten des thermodynamischen Potentiales, vol. 36. Verhandlingen derKoninklijke Akademie van Wetenschappen, Amsterdam, pp. 153–157.
Eshelby, J.D., 1957. The determination of the elastic field of an ellipsoidal inclusion, and related problems. Proc. Royal Soc. A 241, 376–396.
Eyring, H., Glasstone, S., Laidler, K.J., 1939. Application of the theory of absolute reaction rates to overvoltage. J. Chem. Phys. 7 (12), 1053–1065.
Farkas, L., 1927. The speed of germinitive formation in over saturated vapours. Z. physikalische chemie–stochiometrie verwandtschaftslehre 125 (3/4), 236–242.
Finniston, H.M., 1971. Structural characteristics of materials. Elsevier materials science series, Amsterdam.
Fisher, R.M., Dulis, E.J., Carroll, K.G., 1953. Identification of the precipitate accompanying 885 °F embrittlement in Cr steels. Trans. AIME 197 (5), 690–695.
Fournelle, R.A., Clarke, J.B., 1972. The Genesis of the cellular precipitation reaction. Met. Trans. 3, 2757–2767.
Fung, K.Z., Vikar, A.V., Drobeck, D.L., 1994. Massive transformation in the Y_2O_3–Bi_2O_3 system. J. Amer. Ceram. Soc. 77, 1638–1648.
Gentry, W.O., Fine, M.E., 1972. Precipitation in Ni-11.1 at percent A1 and Ni-13.8 at percent A1 alloys. Acta Metall. 20 (2), 181–190.
Gibbs, J.W., 1873. Graphical methods in the thermodynamics of fluids. Trans. Conn. Acad. 2, 309–342. Also in Collected Works 1928, Vol. 1. Longmans, Green and Co., New York. 1–32.
Gibbs, J.W., 1875. On the Equilibrium of heterogeneous Substances. Trans. Conn. Acad. 3, 108–248, 1875–76; 343–524, 1877–78. Also in Collected Works, (1928) vol. 1. Longmans, Green and Co., New York. 55–349.
Ginzburg, V.L., Landau, L.D., 1950. J. Exptl. Theoret. Phys. (USSR) 20, 1064ff.
Ginzburg, V.L., Levanyuk, A.P., Sobyanin, A.A., 1987. Comments on the region of applicability of the Landau theory for structural phase transitions. Ferroelectrics 73, 171–182.
Girifalco, L.A., 1971. Statistical Physics of Materials. Wiley and Sons, NY, NY.
Glasstone, S., Laidler, K.J., Eyring, H., 1941. The Theory of Rate Processes; the Kinetics of Chemical Reactions, Viscosity, Diffusion and Electrochemical Phenomena. McGraw-Hill Book Company, New York; London.
Glicksman, M.E., 2000. Diffusion in Solids: Field Theory, Solid State Principals and Applications. Wiley, NY, NY.
Gomez-Ramirez, R., Pound, G.M., 1973. Nucleation of a second solid-phase along dislocations. Metall. Trans. 4, 1563–1570.

Greenwood, G.W., 1956. The growth of dispersed precipitates in solution. Acta Metall. 4, 243–248.
Greenwood, G.W., 1969. The mechanism of Phase Transformations in Crystalline solids. London UK, 103–108.
Greninger, A.B., 1939. The martensitic transformation in beta copper–aluminum alloys. Trans. AIME 133, 204–229.
Grune, R., 1988. Decomposition of Ni-12 at.% Ti by atom probe field-ion microscopy. Acta Metallurgica 36 (10), 2797–2809.
Guggenheim, E.A., 1952. Mixtures. Clarenden Press, Oxford.
Guinier, A., 1938a. Un nouveau type de diagrammes de rayons X, (A new type of X-ray diagram). Comptes Rendus Hebdomadaires Séances l'Académie Sci. 206, 1641–1643.
Guinier, A., 1938b. Structure of age-hardened Aluminium–Copper alloys. Nature 142, 569–570.
Gust, W., 1979. Discontinuous Precipitation in Binary Metallic Systems. In: Phase Transformations, vol. 1 II-27–68. Institution of Metallurgists, London.
Guy, A.G., Hren, J.L., 1974. Elements of Physical Metallurgy. Addison-Wesley series in metallurgy and materials.
Haasen, P., 2001. Physical Metallurgy. Cambridge University Press.
Hakkarainen, T., 1971. Formation of Coherent Cu_4Ti Precipitates in Copper-rich Copper–Titanium Alloys. Helsinki University of Technology, Helsinki.
Ham, F.S., 1959. Diffusion limited growth of precipitate particles. J. Appl. Phys. 30 (10), 1518–1525.
Hardy, H.K., Heal, T.J., 1954. Report on precipitation. Prog. Metals Phys. 5, 143–278.
Hermann, C., 1934. Tensors and crystal symmetry. Zeit. Kritallographie 89 (1), 32–48.
Hilliard, J.E., 1970. Spinodal decomposition. In: Phase Transformations. American Society for Metals, ASM, Park OH, pp. 497–560.
Hillert, M., 1956. A Theory of Nucleation for Solid Metallic Solutions, D. Sc. Thesis, Mass. Inst. Tech.
Hillert, M., 1957. The role of interfacial energy during solid state phase transformation. Jernkontorets Annaler 141, 757–789.
Hillert, M., 1961. A solid solution model for inhomogeneous systems. Acta Metall. 9, 525–536.
Hillert, M., Cohen, M., Averbach, 1961. Formation of modulated structures in copper–nickel–iron alloys. Acta Metall. 9 (6), 536–546.
Hillert, M., Jarl, M., 1978. Model for alloying effects in ferromagnetic metals. Calphad-Computer Coupling of Phase Diagrams and Thermochemistry 2 (3), 227–238.
Hillert, M., 2011. Discussion of A Commentary on Reaction Kinetics in Processes of Nucleation and Growth. Metall. Mats. Trans. 42A, 3241.
Howe, J.M., 1997. Interfaces in Materials: Atomic Structure, Thermodynamics and Kinetics of Solid–Vapor. In: Solid–Liquid and Solid–Solid Interfaces. John Wiley & Sons Inc, New York.
Hugo, G.R., Muddle, B.G., 1989. The role of symmetry in determining precipitate morphology. Mater. Forum 13, 147–152.
Hull, D., Garwood, R.D., 1956. The Diffusionless Transformations of metastable beta brass. In: The Mechanism of Phase Transformations in Metals. Institute of Metals, London, pp. 219–227.
Hyde, J.M., Miller, M.K., Hetherinton, M.G., Cerezo, A., Smith, G.D.W., Elliott, C.M., 1995a. Spinodal decomposition in fe-cr alloys - experimental-study at the atomic-level and comparison with computer-models .2. Development of domain size and composition amplitude. Act. Met. et. Mat. 43 (9), 3403–3413.
Hyde, J.M., Miller, M.K., Hetherinton, M.G., Cerezo, A., Smith, G.D.W., Elliott, C.M., 1995b. Spinodal decomposition in fe-cr alloys - experimental-study at the atomic-level and comparison with computer-models, 3. Development of morphology. Act Met. et. Mat. 43 (9), 3414–3426.
Imai, Y., Izumiyama, M., Masumoto, T., 1966. Phase Transformations of Fe–Cr Binary System at about 5000C, vol. 18. Sci. Rep. Res. Inst. Tohoku University, Ser. A, p. 56.
Ino, H., 1978. Pairwise interaction-model for decomposition and ordering processes in Bcc binary-alloys and its application to Fe–Be system. Acta Metall. 26 (5), 827–834.
Israel, D.H.B., Fine, M.E., 1963. Precipitation studies in Ni-10 at. Percent Ti. Acta Metall. 11 (9), 1051–1059.
Inden, G., 1976. Project Meeting CALPHAD V, 21–25 June 1976. Max-Planck –Inst. Eisenforschung, G.m.b.H, Dusseldorf/West Germany, pp. 111, 4-1.
Inden, G., 1981. The role of magnetism in the calculation of phase diagrams. Physica B & C 103 (1), 82–100.
Inden, G., 1982. The effect of continuous transformations on phase diagrams. Bull. Alloy Phase Diagrams 2, 412–422.
International Tables for Crystallography, 2006. Volume D, Physical Properties of Crystals. http://dx.doi.org/10.1107/9780955360206000104, International Union of Crystallography.
Jena, A.K., Chaturvedi, M.C., 1992. Phase Transformations in Materials. Prentice Hall, Englewood Cliffs, NJ.
Johansson, C.H., Linde, J.O., 1925. X-ray determination of the atomic structure of the Au–Cu and Pd–Cu mixed crystal series. Ann. Physik 78 (21), 439–460.
Johnson, C.A., 1965. Generalization of Gibbs–Thomson equation. Surf. Sci. 3 (5), 429–444.
Johnson, W.A., Mehl, R.F., 1939. Reaction kinetics in processes of nucleation and growth. Trans. AIME 135, 416–458.
Johnson, W.C., Voorhees, P.W., 1987. Phase equilibria in two-phase solids. Metall. Trans. 18A, 1213–1228.
Johnson, W.C., Mueller, W.H., 1991. Characteristics of phase equilibria in coherent solids. Acta Metall. Mater. 39, 89–103.
Kahlweit, M., 1970. Precipitation and Aging, in PHYSICAL CHEMISTRY: an Advanced Treatise. In: Jost, Wilhelm (Ed.), Solid State, vol. X. Academic Press, New York/London, pp. 719–759.
Kampmann, L., Kahlweit, M., 1967. Zur Theorie Von Fallungen. Berichte Der Bunsen-Gesellschaft Fur Physikalische Chemie 71 (1), 78.

Kampmann, L., Kahlweit, M., 1970. On theory of precipitations. 2. Ber. Bunsen Gesell Phys. Chem. 74 (5), 456–462.
Kashyap, K.T., Koppad, P.G., 2011. Small-angle scattering from GP zones in Al–Cu alloy. Bull. Mater. Sci. 34 (7), 1455–1458.
Khachaturyan, A.G., Airapetya, V.M., 1974. Spatially periodic distributions of new phase inclusions caused by elastic distortions. Physica Status Solidi (A) 28, 61–70.
Khachaturyan, A.G., 1978. Ordering in substitutional and interstitial solid solutions. Prog. Mater. Sci. 22 (1–2), 1–150.
Khachaturyan, A.G., 1983. Theory of Stuctural Transformations in Solids. John Wiley & Sons Inc, New York.
Khachaturyan, A.G., Semenovskaya, S.V., Morris, J.W., 1988. Theoretical analysis of strain-induced shape changes in cubic precipitates during coarsening. Acta Metallurgica 36 (6), 1563–1572.
Khachaturyan, A.G., Lindsey, T.F., Morris, J.W., 1988. Theoretical Investigation Of The Precipitation Of Delta. In Al-Li. Metallurgical Transactions A-physical Metallurgy and Materials Science 19 (2), 249–258.
Kashchiev, D., 2000. Nucleation: Basic Theory with Applications. Butterworths-Heinemann, Oxford.
Kaufman, L., Weiss, R.J., Clougherty, E.V., 1963. Lattice stability of metals-III- iron. Acta Metall. 11 (4), 323–328.
Kelly, A., Nicholson, R.B., 1963. Prog. Mater. Sci. 10, 151–391.
Kelton, K.F., Greer, A.L., 2010. Nucleation in Condensed Matter, Pergamon Materials Series. Elsevier, Netherlansds.
Kirkaldy, J.S., Young, D.J., 1987. Diffusion in the Condensed State. Institute of Metals, London.
Kirkwood, D.H., 1970. Precipitate number density in a Ni–Al alloy at early stages of ageing. Acta Metall. 18, 563–570.
Kokorin, V.V., Chuistov, K.V., 1976. Spinodal Decomposition in ordering Solid Solutions. Fizika Metallov Metallovedenie 42 (5), 1114–1117.
Kolmogorov, A.N., 1937. The statistical theory of metal crystallization. Izv. Akad. Nauk SSSR, Ser. Mater. 3, 355–360.
Kompascher, M., Schonfeld, B., Heinrich, H., Kostorz, G., 2000. Small-angle neutron scattering investigation of the early stages of decomposition in Ni-rich Ni–Ti alloys. J. Appl. Cryst. 33, 488–490.
Kompatscher, M., Schonfeld, B., Heinrich, H., Kostorz, G., 2003. Phase separation in Ni-rich Ni–Ti alloys; metastable states. Acta Mater. 51, 165–175.
Kostorz, G., Kompatscher, M., Schonfeld, B., 1999. Coherent precipitates in Ni-rich Ni–Ti single crystals. In: Koiwa, M., Otsuka, K., Miyasaki, T. (Eds.), Proceedings of the International Conference on Solid–Solid Phase Transformations'99 (JIMIC-3). JIM, Tokoyo, pp. 305–312.
Kubo, H., Wayman, C.M., 1980. Theoretical basis for spinodal decomposition in ordered alloys. Acta Metall. 28 (3), 395–404.
Kurnakow, N., Zemczuzny, S., Zasedatelev, M., 1916. The transformations in alloys of gold with copper. J. Inst. Metals 15, 305–331.
Laughlin, D.E., 1976a. Spinodal decomposition in Ni based Ni–Ti alloys. Acta Metall. 24, 53–58.
Laughlin, D.E., Cahn, J.W., 1975. Spinodal decomposition in age hardening Cippoer–Titanium alloys. Acta Metall. 23, 329–339.
Laughlin, D.E., Soffa, W.A., 1988. In: Salje, E.K.H. (Ed.), Exsolution, Ordering and Structural Transformations: Systematics and Synergistics. Physical Properties and Thermodynamic Behaviour of Minerals, NATO ASI Series C, vol. 225. D. Reidel Publishing Company, pp. 213–264.
Laughlin, D.E., Soffa, W.A., 1985. Spinodal Structures Metals Handbook. In: Metallography and Microstructures, Ninth ed., vol. 9. American Society for Metals. 652–654.
Landau, L.D., 1937. In: Collected Papers, D. ter Haar, (Ed.) Oxford.
Langer, J.S., Schwartz, A.J., 1980. Kinetics of Nucleation in near critical fluids. Phys. Rev. A21, 948–958.
Larche', F., Cahn, J.W., 1973. A linear theory of thermochemical equilibrium of solids under stress. Acta Metall. 21, 1051–1063.
Larche', F.C., 1979. In: Dislocations in Solids, edited by F.R.N. Nabarro. North-Holland Publishing Company, Amsterdam, Holland, vol. 4. Pergamon Press.
Larikov, L.N., Geichenko, V.V., Falchenko, V.M., 1975. Diffusional Processes in Ordered Alloys. Izdatel'stvo Naukova Dumka, Kiev.
Legoues, F.K., Aaronson, H.I., 1984. Influence of crystallography upon critical nucleus shapes and kinetics of homogeneous fcc–fcc nucleation .4. Comparisons between theory and experiment in Cu–Co alloys. Acta Metall. 32, 1855–1870.
Linde, A.D., 1982. A new inflationary universe scenario: a possible solution of the horizon, flatness, homogeneity, isotropy and primordial monopole problems. Phys. Lett. B108, 389–393.
Lifshitz, I.M., Slyozov, V.V., 1961. The kinetics of precipitation from supersaturated solid solutions. J. Phys. Chem. Solids 19, 35–50.
Liu, C.T., Loh, B.T.M., 1971. Solid Solution Theory and Spinodal Decomposition. Phil. Mag. 24, 367–380.
Livak, R.J., Thomas, G., 1971. Spinodally Decomposed Cu-Ni-Fe Alloys Of Asymmetrical Compositions Acta. Met. 19 (6), 497–505.
Livingston, J.D., Cahn, J.W., 1975. Discontinuous coarsening of aligned eutectoids. Acta Metall. 22 (4), 495–503.
Lukas, H.L., Fries, S.G., Sundman, Bo, 2007. Computational Thermodynamics (Calphad Method). Cambridge University Press.
Lyubov, B.Y., Solovyov, V.A., 1965. The possible existence of stable segregations of solute atoms and the formation of coherent nuclei of a new phase of the elastic field of edge dislocations. Fiz. Met. Metallov 19, 333–342.
Manna, I., Pabi, S.K., Gust, W., 2001. Discontinuous reactions in Solids. Int. Mater. Rev. 46 (2), 53–91.
Martin, J.W., Doherty, R.D., Cantor, B., 1997. Stability of microstructure in metallic systems. Cambridge University Press, NY, USA.
Martin, J.W., 1998. Precipitation Hardening: Theory and Applications. Butterworth-Heinemann, Oxford.
Massalski, T.B., 1958. The mode and morphology of massive transformations in Cu–Ga, Cu–Zn, Cu–Zn–Ga and Cu–Ga–Ge alloys. Acta Metall. 6 (4), 243–253.
Massalski, T.B., 1970. Massive transformations. In: Phase Transformations. American Society for Metals, ASM Park OH.

Massalski, T.B., Laughlin, D.E., 2009. The surprising role of magnetism on the phase stability of Fe (Ferro). CALPHAD: Comput. Coupling Phase Diagrams Thermochem. 33, 3–7.
Massalski, T.B., Soffa, W.A., Laughlin, D.E., 2006. The nature and role of incoherent interphase interfaces in diffusional solid-solid phase transformations. Metall. Mater. Trans. 37A, 825–831.
Mehl, R.F. and Jetter, L.K., (1940). American society for metals Symposium, Age Hardening of Metals, 342–317.
Meijering, J.L., 1952. Calculs thermodynamiques concernant la nature des zones Guinier-Preston dans les alliages aluminum-cuivre. Revue de Metallurgie. 49 (12), 906–910.
Meijering, J.L., 1963a. Miscibility gaps in ferromagnetic alloy systems. Philips Res. Rep. 18, 318–330.
Meijering, J.L., 1963b. Usefulness of the $1/\gamma$ plot in the theory of thermal faceting. Acta Metall. 11, 847–849.
Merica, P.D., Waltenberg, R.G., Scott, H., 1921. Heat treatment and constitution of duralumin. Trans. Am. Inst. Min. Metall. Eng. 64, 41–77.
Miao, W.F., Laughlin, D.E., 2000. Effects of Cu content and preaging on precipitation characteristics in aluminum alloy 6022. Metall. Mater. Trans. 31A, 361–371.
Miller, M.K., Hyde, J., Hetherington, M.G., Cerezo.A., Smith, G.D.W., Elliott, C.M., 1996. Spinodal decomposition in Fe-Cr alloys: Experimental study at the atomic level and comparison with computer models—I. Introduction and methodology. Act Met. et. Mat. 43 (9), 3385–3401.
Miyazaki, T., Imamura, H., Kozakai, T., 1982. The formation of g′ precipitate doublets in Ni–A1 alloys and their energetic stability. Mater. Sci. Eng. 54, 9–15.
Mott, N.F., Nabarro, F.R.N., 1940. An attempt to estimate the degree of precipitation hardening, with a simple model. Proc. Phys. Soc. 52, 86–89.
Nabarro, F.R.N., 1940. The influence of elastic strain on the shape of particles segregating in an alloy. Proc. Phys. Soc. 52, 90–93 and The strains produced by precipitation in alloys. Proc. R. Soc. A, 175, 519–538.
Nembach, E., 1996. Particle Strengthening of Metals and Alloys. John Wiley and Sons, NY, NY.
Nicholson, R.B., Nutting, J., 1958. Direct observation of the strain field produced by coherent precipitated particles in an age-hardened alloy. Philos. Mag. 3 (29), 531–535.
Nicholson, R.B., Thomas, G., Nutting, J., 1959. Electron-microscopic studies of precipitation in aluminium alloys. J. Inst. Metals 87 (12), 429–438.
Nicholson, R.B., 1970. Nucleation at imperfections. In: Phase Transformations. American Society for Metals, ASM Park OH.
Nishizawa, T., Hasebe, M., Ko, M., 1979. Thermodynamic analysis of solubility and miscibility gap alpha iron alloys. Acta Metall. 21, 817–828.
Nix, F.C., Shockley, W., 1938. Order–disorder transformations in alloys. Rev. Mod. Phys. 10, 1–71.
Novotny, G.M., Ardell, A.J., 2001. Precipitation of Al_3Sc in Al–Sc alloys. Mater. Sci. Eng. A318, 144–154.
Orowan, E., 1948. Theory of Yield Strength without Particle Shear. Institute of Metals Symposium on Internal Stress, London, p. 451.
Pfeifer, M.J., Voorhees, P.W., 1991. A graphical method for constructing coherent phase diagrams. Acta Metall. Mater. 39, 2001–2012.
Phillips, A.J., 1930. The alpha to beta transformation in brass. Trans. AIME 89, 194–200.
Pippard, A.B., 1966. Elements of Classical Thermodynamics. Cambridge University Press, Cambridge.
Poduri, R., Chen, L.-Q., 1997. Computer simulation of the kinetics of order-disorder and phase separation during precipitation of delta' (Al3Li) in Al-Li alloys. Acta. Mater. 45 (1), 245–255.
Porter, D.A., Easterling, K.E., 1992. Phase Transformations in Metals and Alloys. Chapman Hall, London.
Preston, G.D., 1938a. The diffraction of X-rays by age-hardening aluminium copper alloys. Proc. R. Soc. A167, 526–538.
Preston, G.D., 1938b. The diffraction of X-rays by an age-hardening alloy of aluminium and copper. Struct. Intermediate Phase Philos. Mag. 26, 855–871.
Preston, G.D., 1938c. Structure of age-hardened aluminium–copper alloys. Nature 142, 570.
Prigogine, I., 1980. From being to becoming: time and complexity in the physical sciences. W. H. Freeman, San Francisco.
Putnis, A., 1992. Introduction to Mineral Sciences. Cambridge University Press.
Radmilovic, V., Fox, A.G., Thomas, G., 1989. Spinodal decomposition of Al rich Al–Li alloys. Acta Metall. 37 (9), 2385–2394.
Rajkovic, M., Buckley, R.A., 1981. Ordering transformations in Fe 50Co based alloys. Metal Sci. 81 (1), 21–29.
Reed-Hill, R.E., 1972. Physical Metallurgy Principles, second ed. Van Nostrand.
Richards, M.J., Cahn, J.W., 1971. Pairwise interactions and ground state of orderd binary alloys. Acta Metall. 19 (11), 163–1277.
Rioja, R.J., Laughlin, D.E., 1977. The early stages of G. P. zone formation in Naturally aged Al-4w/o Cu alloys. Met. Trans. 8A, 1257–1261.
Robin, P.Y., 1974. Thermodynamic equilibrium across a coherent interface in a stressed crystal. Am. Mineral. 59, 1286–1298.
Rollins, C.C., 1970. Nucleation on dislocations. Acta. Met. 18, (11), 1209–1215.
Rossiter, P.I., Houghton, M.E., 1984. Contemporary Fe–Cr–Co and Mn–Al–C permanent magnet alloys: a review. Metals Forum 7 (3), 187–208.
Russell, K.C., 1970. Nucleation in solids. In: Phase Transformations. American Society for Metals, ASM Park OH, pp. 219–268.
Sato, T., Tanaka, N., Takahashi, T., 1988. High Resolution Lattice Images of Ordered Structures in Al–Li Alloys. Transactions of the Japan Institute of Metals. 29 (1), 17–25.
Saito, K., Watanabe, R., 1969. Precipitation in Ni-12at.% Ti. Jap. J. Appl. Phys. 83, 14–23.
Shewmon, P., 1963. Diffusion in Solids. Mcgraw-Hill, Ny. NY.
Sinclair, R., Ralph, B., Leake, J.A., 1974. Spinodal decomposition of a nickel–titanium alloy. Phys. Stat. Solidi (A) 26, 285–298.
Singh, A.K., Lele, S., 1991. Ground state structures of ordered binary HCP alloys. Philos. Mag. B 64 (3), 275–297.

Sirotin, Y.I., Shaskolskaya, M.P., 1982. Fundamentals of Crystal Physics. Mir Publishers, Moscow.
Smallman, R.E., 1963. Modern Physical Metallurgy. Butterworths.
Soffa, W.A., Laughlin, D.E., 1982. Recent experimental studies of continuous transformations in alloys: an overview. Proceedings of an International Conference on Solid–Solid Phase Transformations. AIME, 159–183.
Soffa, W.A., Laughlin, D.E., 1989. Decomposition and ordering processes involving thermodynamically first-order order->disorder transformations. Acta Metall. 37, 3019–3029.
Soffa, W.A., Laughlin, D.E., 2004. High-strength age hardening copper-titanium alloys: redivivus. Prog. Mater. Sci. 49, 347–366.
Soffa, W., Laughlin, D.E., Singh, N., 2010. Interplay of ordering and spinodal decomposition in the formation of ordered precipitates in binary fcc alloys: role of second nearest-neighbor interactions. Philos. Mag. 90 (1–4), 287–304.
Soffa, W., Laughlin, D.E., Singh, N., 2011. Re-examination of A1 → $L1_0$ ordering: generalized Bragg-Williams model with elastic relaxation. Solid State Phenomena 172, 608–616.
Soffa, W.A., 1985. Structures Resulting from Precipitation from Solid Solution, Metallography and Microstructures. In: ASM Handbook, ASM International, pp. 646–650.
Stanley, H.E., 1971. Introduction to Phase Transitions and Critical Phenomena. Oxford University Press, Oxford and New York.
Stowell, M.J., 2002. Precipitate nucleation: does capillarity theory work? Mater. Sci. Technol. 18 (2), 139–144.
Stubican, V.S., Schultz, A.H., 1970. Phase Separation by Spinodal Decomposition in the Tetragonal System 53 (4), 211–214.
Tammann, G., 1919. Die chemischen und galvanischen Eigenscaften von Mischkristallrein und ihre Atomverteilung. Zeits. F. Anorg. Allgem. Chemie 107 (1/3), 1–239.
Trivedi, R., 1970. The role of interfacial free energy and interface kinetics during the growth of precipitate plates and needles. Met. Trans 1 (4), 921–927.
Trivedi, R., 1975. The effects of crystallographic anisotropy on the growth kinetics of Widmanstatten precipitates. Acta Met 23, 713–722.
Trivedi, R., 1999. Theory of capillarity. In: Aaronson, H.I. (Ed.), Lectures on the Theory of Phase Transformations, second ed. TMS, Warrendale, PA.
Turnbull, D., 1956. Phase changes. In: Seitz, Turnbull (Eds.), Solid State Physics, vol. 3. Academic Press, New York, pp. 226–308.
Turnbull, D., Fischer, J.C., 1949. Rate of nucleation in condensed systems. J. Chem. Phys. 17 (1), 71–73.
Turnbull, D., 1950a. Correlation of liquid-solid interfacial energies calculated from supercooling of small droplets. J. Chem. Phys. 18 (5), 769.
Turnbull, D., 1950b. Isothermal rate of solidification of mercury droplets. J. Chem. Phys. 18 (5), 448, 448.
Turnbull, D., Tu, K.N., 1970. The cellular and pearlite reactions. In: Phase Transformations. American Society for Metals, ASM Park OH.
Van der Waals, J. D. and Kohnatamm, P. (1908). Lehrbuch der Thermodynamik. Maas und Suchtelen.
Veeraraghavan, D., Wang, P., Vasudevan, V.K., 1999. Kinetics and thermodynamics of the alpha->gamma(m), massive transformation in a Ti-47.5 at.% Al alloy. Acta Mater. 47 (11), 3313–3330.
Veeraraghavan, D., Wang, P., Vasudevan, V.K., 2003. Nucleation kinetics of the alpha->gamma(M) massive transformation in a Ti-47.5 at.% Al alloy. Acta Mater. 51 (6), 1721–1741.
Vineyard, G.H., 1957. Frequency factors and isotope effects in solid state rate processes. J. Phys. Chem. Solids 3, 121–127.
Vintaykin, Y.Z., Loshmanov, A.A., 1966. The character of embrittlement in Fe–Cr alloy at 475 °C. Fiz. Metallov. Metalloved 22, 473–476.
Vintaykin, Y.Z., Dmitiyov, V.N., Kolontsov, Y., 1970. Kinetic study of phase separation of Fe–Cr solid solutions by neutron diffraction analysis. Phys. Metals Metall. 29 (6), 1257–1267.
Vlasova, Y.Y., Vintaykin, Y.Z., 1969. Study of the fine structure of FePt alloys. Phys. Met. Metallogr. 27, 60–64.
Volmer, M., Weber, A., 1926. Nuclei-formation in supersaturated alloys. Z. Phys. Chem. 119, 227–301.
Vonnegut, B.J., 1948. Variation with temperature of the nucleation rate of supercooled liquid tin and water drops. Colloid Sci. 3, 563–569.
Voorhees, P.W., Johnson, W.C., 2004. Thermodynamics of elastically stressed crystals. Solid State Phys. 59, 1–201.
Voss, K.J., 1969. Alnico permanent magnet alloys. Chapter IX. In: Berkowitz, A., Kneller, E. (Eds.), Metallurgy and Magnetism, vol. 1. Academic Press, New York and London, pp. 473–512.
Wagner, C., 1961. Theorie der Alterrung von Niederschlägen durch Umlösen. Z. Electrochem., 581–591.
Wagner, R., Kampmann, R., 1991. Homogeneous Second Phase Precipitation, in Phase Transformations. In: Haasen, Peter (Ed.), Materials/Materials Science And Technology, Chapter 4, vol. 5. VCH Publishers, Weinheim and New York, p. 213.
Wagner, R., Kampmann, 1991. Homogeneous second phase precipitation, In: Cahn, R.W., Haasen, P., Kramer, E.J. (Eds.), Materials, Materials Science and Technology, vol. 5, Phase Transformations in Materials, P. Haasen, (Chapter 4), pp. 213–303.
Wang, P., Veeraraghavan, D., Vasudevan, V.K., 2002. Massive-parent interphase boundaries and their implications on the mechanisms of the alpha -> gamma (M) massive transformation in Ti–Al alloys. Metall. Mater. Trans. 33A (8), 2353–2371.
Wang, Z.M., Shiflet, G.J., 1998. Growth of Delta on dislocations in a dilute Al–Li alloy. Met. Maters. Trans. 29 (8), 2073–2085.
Weiss, R.J., Tauer, K.J., 1956. Components of the thermodynamic functions of iron. Phys. Rev. 102 (6), 1490–1495.
Weiss, P., 1907. L'Hypothèse du champ moléculaire et du propriété ferromagnétique. J. Physique 6, 661–690.
Wendt, H., 1981. Ph.D. Thesis, Univ.Goettingen.
Wendt, H., Haasen, P., 1983. Nucleation and growth of γ'-precipitates in Ni-14 at-percent Al. Acta Metall. 31, 1649–1659.
Wert, C., Zener, C., 1950. Interference of growing spherical precipitate particles. J. Appl. Phys. 21 (1), 5–8.

Wilm, A., 1911. Physikalisch-metallurgische Untersuchungen über magnesiumhaltige Aluminiumlegierungen. Metallurgie: Z. gesamte Hüttenkunde 8 (8), 225–227.
Wilkinson, D.S., 2000. Mass Transport in Solids and Fluids. In: Cambridge Solid State Science Series. Cambridge University Press.
Williams, D.B., Butler, E.P., 1981. Grain boundary discontinuous precipitation reactions. Int. Metals Rev. 26 (3), 153–183.
Williams, R.O., Paxton, H.W., 1957. The nature of aging of binary iron chromium alloys around 500C. J. Iron Steel Inst. 185, 358–374.
Williams, R.O., 1980. Long-period superlattices in the copper–gold system as two-phase systems. Metall. Trans. 11A, 247–253.
Williams, R.O., 1984. Calculation of coherent phase equilibria. CALPHAD 8 (1), 1–14.
Wittig, J.E., 2002. Mater. Trans. A (2002), vol. 33A, p. 2373. The massive transformation in titanium aluminides: Initial stages of nucleation and growth. Met. Mater. Trans. A 33 (8), 2373–2379.
Yanar, C., Wiezorek, J.M.K., Radmilovic, V., Soffa, W.A., 2002. Massive transformation and the formation of the ferromagnetic L1(0) phase in manganese–aluminum-based alloys. Met. Mater. Trans. A 33 (8), 2413–2423.
Zackay, V.F., Aaronson, H.I., 1962. The Decomposition of Austenite by Diffusional Processes. TMS of AIME, Interscience Publishers, NY.
Zeldovich, J.B., 1943. On the Theory of New Phase formation.
Zener, C., 1946. Kinetics of the decomposition of austenite. Trans. AIME 167, 550–595.
Zener, C., 1955. Impact of magnetism upon metallurgy. Trans. AIME 203, 619–630.
Zhao, J.C., Notis, M.R., 1998. Spinodal decomposition, ordering transformation and discontinuous precipitation in a Cu–15Ni–8Sn alloy. Acta Mater. 46 (12), 4203–4218.

Further Reading

Aaronson, H.I. (Ed.), 1999. Lectures on the Theory of Phase Transformations. TMS, Warrendale PA.
Aaronson, H.I., Enomoto, E., Lee, J.K., 2010. Mechanisms of Diffusional Phase Transformations in Metals and Alloys. CRC Press, Baca Raton.
Balluffi, R.W., Allen, S.M., Carter, W.C., 2005. Kinetics of Materials. Wiley, Hoboken, NJ.
Banerjee, S., Mukhopadhyay, P., 2007. Phase Transformations: Examples from Titanium and Zirconium Alloys. ELSEVIER, Amsterdam.
Burke, J., 1965. The Kinetics of Phase Transformations in Metals. Pergamon Press, Oxford.
Christian, J.W., 2002. The Theory of Transformation in Metals and Alloys. Pergamon Press.
Fine, M.E., 1964. Phase Transformations in Condensed Systems. Macmillian, NY.
Kelton, K.F., Greer, A.L., 2010. Nucleation in Condensed Matter. In: Pergamon Materials Series. Elsevier, Oxford.
Khachaturyan, A.G., 1983. Theory of Structural Transformations in Solids. John Wiley & Sons, NY, NY.
Kostorz, G. (Ed.), 2001. Phase Transformations in Materials. Wiley-VCH, Weinhem.
Machlin, E.S., 1991. An Introduction to Aspects of Thermodynamics and Kinetics Relevant to Materials Science. Giro press, Croton-on-Hudson, NY.
Martin, J.W., Doherty, R.D., Cantor, B., 1997. Stability of Microstructure in Metallic Systems. Cambridge University Press.
Rao, C.N.R., Rao, K.J., 1978. Phase Transitions in Solids. McGraw-Hill, NY.
Sharma, R.C., 2002. Phase Transformations in Materials. CBS Publishers, India.
Shewmon, P.G., 1969. Transformations in Metals. McGraw–Hill, NY, NY.
Wagner, R., Kampmann, L., 1991. Homogeneous second phase precipitation. In: Cahn, R.W., Haasen, P., Kramer, E.J. (Eds.), Phase Transformations in Materials, Materials Science and Technology, Phase Transformations in Materials (Volume Editor, P. Haasen), vol. 5, pp. 213–303 (Chapter 4).

Conferences/Symposia on Phase Transformations (in chronological order)

Age hardening of Metals, 1940. American Society for Metals. Cleveland, OH.
Smoluchowski, R., Mayer, J.E., Wehl, W.A. (Eds.), 1951. Phase Transformations in Solids. John Wiley and Sons, London.
The Mechanism of Phase Transformations in Metals, 1955. Institute of Metals, London.
Precipitation from Solid Solution, 1959. American Society for Metals. Cleveland, OH.
Zackay, V.F., Aaronson, H.I., 1962. The Decomposition of Austenite by Diffusional Processes. TMS of AIME, Interscience Publishers, NY.
Phase Transformations, 1969. American Society for Metals. ASM Park, OH.
The Mechanism of Phase Transformations in Crystalline Solids. Monograph and Report Series No. 33. 1969. Institute of Metals, London.
Russell, K.C., Aaronson, H.I., 1978. Precipitation Processes in Solids. Metallurgical Society of AIME, Warendale, PA.
Solid State Phase Transformations in Metals and Alloys: Ecole d'été d'Aussois, 3–15 septembre 1978, 1980. Orsay: Editions de Physique.
Aaronson, H.I., Laughlin, D.E., Sekerka, R.F., Wayman, C.M., 1982. Proceedings of an International Conference on Solid [to] Solid Phase Transformations. Metallurgical Society of AIME, Warrendale, Pa.

Hassen, P., Gerold, V., Wagner, R., Ashby, M.F., 1984. Decomposition of Alloys: Early Stages. Pergamon Press, Oxford.
Lorimer, G.W., 1988. Phase Transformations '87. Institute of Metals, London.
Johnson, W.C., Howe, J.M., Laughlin, D.E., Soffa, W.A. (Eds.), 1994. Proceedings of an International Conference on Solid [to] Solid Phase Transformations. Metallurgical Society of AIME, Warrendale, Pa.
Koiwa, M., Otsuka, K., Miyazaki, T., 1999. Solid [to] solid phase transformations. Jpn. Inst. Metals Proc. 12 (I & II).
Howe, J.M., Laughlin, D.E., Lee, J.K., Dahman, U., Soffa, W.A., 2005. Proceedings of an International Conference on Solid [to] Solid Phase Transformations in Inorganic Materials. Metallurgical Society of AIME, Warrendale, Pa.
Brechet, Y., Clouet, E., Deschamps, A., Finel, A., Soisson, F., 2011. Solid [to] Solid Phase Transformations in Inorganic Materials. Trans tech Publications, Zurich.

Biography

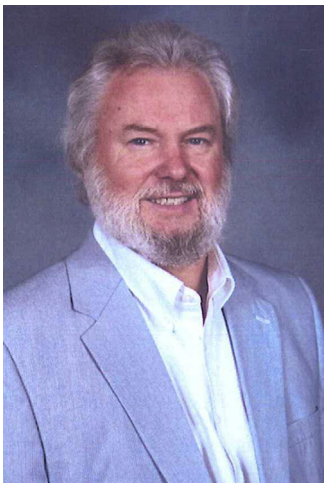

Professor Soffa received his B.S. in Metallurgy/Metallurgical Engineering from Carnegie Institute of Technology (CMU) in 1961 and his M.S. in Materials Engineering from Rensselaer Polytechnic Institute (RPI) in 1963. He completed his Ph.D. in Metallurgical Engineering/Physical Metallurgy at Ohio State University in 1967 after which he was granted a N.A.T.O Postdoctoral Fellowship to study at Oxford University in the Department of Metallurgy and Materials Science. Following his post-doctoral work at Oxford he joined the faculty in the Department of Materials Science and Engineering at the University of Pittsburgh in 1968 where he taught and did research for over thirty years. He was Department Chair at Pitt from 1995–2000. He was a Visiting Humboldt Scholar at the Institut fur Metallphysik at the University of Goettingen in 1979 and a Visiting Professor in the Department Materials Science at Berkeley (U of Cal) in 1987. While at Pitt he was also Director of the Engineering Physics Program. In 2000–2001 Professor Soffa was a Visiting Professor in the Department of Physics at the University of Vienna and at the Department of Applied Physics/ ETH-Zurich. In 2004 he joined the Department of Materials Science and Engineering at the University of Virginia becoming Professor Emeritus in 2012. Professor Soffa has published over 100 papers in archival journals and refereed conference proceedings in the areas of phase transformations, magnetic materials and materials physics.

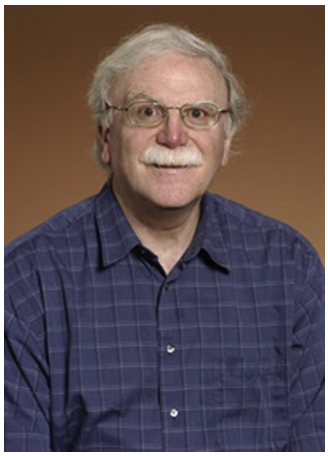

David E. Laughlin is the ALCOA Professor of Physical Metallurgy in the Department of Materials Science and Engineering at Carnegie Mellon University, Pittsburgh, PA. He obtained his B.S. in Metallurgical Engineering from Drexel University in 1969 and his Ph.D. in Metallurgy and Materials Science from MIT in 1973. He has taught at CMU since 1974. He is Principal Editor of *Metallurgical and Materials Transactions* and has co-edited eight books. His research has centered on the structure of materials as observed by electron microscopy, phase transformations and magnetic materials. He has published more than 450 peer reviewed research papers and is co-inventor on eleven US patents. Laughlin is a Fellow of TMS and ASM International.